

A two-scale homogenization scheme for the prediction of magneto-electric product properties

Von der Fakultät für Ingenieurwissenschaften,
Abteilung Bauwissenschaften
der Universität Duisburg-Essen
zur Erlangung des akademischen Grades

Doktor-Ingenieur
genehmigte Dissertation

von

Matthias Labusch, M.Sc.

Hauptberichter: Prof. Dr.-Ing. habil. J. Schröder
Korreferenten: Prof. Dr. rer. nat. D.C. Lupascu
Prof. Dipl.-Ing. B. Kiefer, Ph.D.

Tag der Einreichung: 31. Juli 2018
Tag der mündlichen Prüfung: 14. November 2018

Fakultät für Ingenieurwissenschaften,
Abteilung Bauwissenschaften
der Universität Duisburg-Essen
Institut für Mechanik
Prof. Dr.-Ing. habil. J. Schröder

Herausgeber:

Prof. Dr.-Ing. habil. J. Schröder

Organisation und Verwaltung:

Prof. Dr.-Ing. habil. J. Schröder
Institut für Mechanik
Fakultät für Ingenieurwissenschaften
Abteilung Bauwissenschaften
Universität Duisburg-Essen
Universitätsstraße 15
45141 Essen
Tel.: 0201 / 183 - 2682
Fax.: 0201 / 183 - 2680

© Matthias Labusch
Institut für Mechanik
Abteilung Bauwissenschaften
Fakultät für Ingenieurwissenschaften
Universität Duisburg-Essen
Universitätsstraße 15
45141 Essen

Alle Rechte, insbesondere das der Übersetzung in fremde Sprachen, vorbehalten. Ohne Genehmigung des Autors ist es nicht gestattet, dieses Heft ganz oder teilweise auf fotomechanischem Wege (Fotokopie, Mikrokopie), elektronischem oder sonstigen Wegen zu vervielfältigen.

ISBN-10 3-9818074-6-4
ISBN-13 978-3-9818074-6-2
EAN 9783981807462

Vorwort

Die vorliegende Arbeit entstand während meiner Tätigkeit als wissenschaftlicher Mitarbeiter am Institut für Mechanik an der Universität Duisburg-Essen im Rahmen des durch die Deutsche Forschungsgemeinschaft (DFG) geförderten Forschungsprojekts SCHR 570/12-2 (FOR 1509 “Ferroic Functional Materials”). Ich möchte mich an dieser Stelle bei der DFG für die finanzielle Unterstützung bedanken und meinen persönlichen Dank einigen Menschen aussprechen, die zum Gelingen dieser Arbeit beigetragen haben.

Mein größter Dank gilt meinem geschätzten Doktorvater Professor Jörg Schröder. Durch die gute Zusammenarbeit und intensive Förderung gab er mir die Möglichkeit unter seiner Leitung zu promovieren. Dabei möchte ich mich für die Unterstützung und Betreuung während meiner gesamten Promotionszeit sowie das mir entgegengebrachte Vertrauen bedanken. Ein besonderer Dank gilt Herrn Professor Doru C. Lupascu für die Übernahme des Korreferates und die besonders gute Zusammenarbeit. Seine experimentelle Betrachtungsweise gab mir ein tieferes Verständnis meines Themengebiets. Weiterhin möchte ich Herrn Professor Björn Kiefer für die Übernahme des externen Gutachtens und die erfolgreiche Zusammenarbeit im Rahmen der Forschungsgruppe danken. Ein großer Dank gilt Herrn Juniorprofessor Marc-André Keip. Seine Fachkompetenz und die hervorragende Fähigkeit komplizierte Sachverhalte verständlich zu erklären haben mir bei der Fertigstellung dieser Arbeit sehr geholfen. Weiterhin möchte ich mich bei Herrn Professor Joachim Bluhm bedanken, der sich jederzeit gerne für fachliche Angelegenheiten Zeit nahm. Ebenfalls danke ich allen ehemaligen und derzeitigen Kollegen am Institut für Mechanik, Solveigh Averweg, Daniel Balzani, Julia Bergmann, Dominik Brands, Moritz Bloßfeld, Sarah Brinkhues, Bernhard Eidel, Simon Fausten, Ashutosh Gandhi, Markus von Hoegen, Veronika Jorisch, Simon Kugai, Veronica Lemke, Petra Lindner-Roullé, Sascha Maassen, Simon Maike, Rainer Niekamp, Paulo Nigro, Carina Nisters, Yasemin Özmen, Mangesh Pise, Sabine Ressel, Mohammad Sarhil, Thomas Schmidt, Alexander Schwarz, Serdar Serdaş, Steffen Specht, Karl Steeger, Huy Ngoc Thai, Sonja Uebing, Vera Vetrov und Nils Viehbahn für die tolle Arbeitsatmosphäre, hilfreichen Diskussionen und gute Zusammenarbeit. An dieser Stelle möchte ich mich besonders bei Lisa Scheunemann und Maximilian Igelbüscher für die humorvollen Unterhaltungen und uneingeschränkte Unterstützung bedanken.

Ein herzliches Dankeschön gilt meinen Freunden Sebastian Napierski-Heide und Christian Ulrich für die notwendige und humorvolle Ablenkung nach der Arbeit. Abschließend danke ich meiner gesamten Familie, die mich in schwierigen Phasen meiner Promotion sowie in jeglicher Lebenslage unterstützt.

Essen, im November 2018

Matthias Labusch

Abstract

The present work focuses on the theoretical basics of mechanically coupled magneto-electric properties and the simulation of composite materials in the framework of the Finite Element Method. Since magneto- and electro-mechanically coupled materials find applications in many technical devices and their fields of application could be improved and extended through the magneto-electric coupling, the interest in such materials has increased in the last decades. The goal of this work is the development of microscopically motivated material models in order to reflect the experimentally measured magneto-electric coupling behavior of two-phase composites as precisely as possible. Since the effective properties not only significantly depend on the morphology of the underlying microstructure, but also result from it, the material models were implemented in the framework of a multiscale homogenization scheme, the so-called FE²-method. The performed numerical examples demonstrate the accuracy of the different models used. Furthermore, it is shown that additional defects, such as an increased porosity of the composite, substantially influence the magneto-electric properties.

Zusammenfassung

Die vorliegende Arbeit befasst sich mit den theoretischen Grundlagen mechanisch vermittelter magneto-elektrischer Kopplungseigenschaften und Simulationen von Kompositmaterialien im Rahmen der Finiten Elemente Methode. Da magneto- und elektro-mechanisch koppelnde Materialien in vielen technischen Bauteilen Anwendung finden und das Anwendungsfeld durch magneto-elektrische Kopplungen verbessert und erweitert werden kann, ist in den letzten Jahrzehnten das Interesse an solchen Materialien stark angestiegen. Ziel dieser Arbeit ist es, mikroskopisch motivierte Materialmodelle zu entwickeln um das experimentell gemessene magneto-elektrische Kopplungsverhalten von Zwei-Phasen-Kompositen so exakt wie möglich widerzuspiegeln. Da diese effektiven Eigenschaften nicht nur stark von der Morphologie der Mikrostruktur abhängen sondern ebenfalls daraus resultieren, werden die Materialmodelle im Rahmen eines multi-skalen Homogenisierungsverfahrens, der sogenannten FE²-Methode, implementiert. Die durchgeführten numerischen Beispiele zeigen die Genauigkeit der verwendeten unterschiedlichen Modelle. Weiterhin wird gezeigt, dass zusätzliche Störungen, wie beispielsweise eine erhöhte Porosität des Komposites, die magneto-elektrischen Eigenschaften stark beeinflussen können.

Contents

1	Introduction and Motivation	1
2	Brief introduction to electro-magneto-statics	5
2.1	Electric and magnetic fields in vacuum	5
2.2	Electric and magnetic fields in matter	9
2.3	Maxwell Equations	11
2.4	Maxwell Stress Tensor	13
3	Introduction to continuum mechanics	15
3.1	Kinematics of continuum bodies	15
3.2	Concept of stress	16
3.3	Balance of mass	16
3.4	Balance of linear momentum	17
3.5	Balance of angular momentum	17
3.6	First law of thermodynamics (Balance of energy)	18
3.7	Second law of thermodynamics (Entropy inequality)	19
3.8	Thermodynamic potentials	20
3.9	Representation of anisotropic materials with isotropic tensor functions	22
4	Ferroic materials	24
4.1	Introduction to magnetic materials	24
4.1.1	Origin of magnetism	24
4.1.2	Different types of magnetism	27
4.1.3	Magnetostrictive effect	32
4.2	The ferroelectric effect	32
4.3	The ferroelastic effect	35
4.4	The ferrotoroidic effect	36
4.5	Magneto-electric materials	37
4.5.1	Single-phase magneto-electric materials	37
4.5.2	Magneto-electric composite materials	39
4.5.3	Why are there so few magneto-electric single-phase materials?	43
5	Finite element formulation	44
5.1	Boundary value problem for the magneto-electro-mechanical case	44
5.2	Weak formulation for the magneto-electro-mechanical case	45

5.3	Linearization of the weak forms	47
5.4	Vector-matrix (Voigt) notation	48
5.5	Discretization with finite elements	50
5.6	Isoparametric concept	50
5.7	Approximations with finite elements	51
5.8	Discretization of the weak forms and linearizations	52
5.9	Assembling procedure for the boundary value problem	53
6	Two-scale homogenization of magneto-electro-mechanical problems	55
6.1	Overview on homogenization approaches	55
6.2	Homogenization based on the FE ² -method	56
6.2.1	Macroscopic magneto-electro-mechanical boundary value problem .	58
6.2.2	Microscopic magneto-electro-mechanical boundary value problem .	59
6.2.3	Scale transition and definitions of microscopic boundary conditions	59
6.2.4	Consistent linearization of macroscopic field quantities	61
7	Material models	68
7.1	Linear piezoelectric/piezomagnetic material model	71
7.2	Nonlinear magnetostrictive material model	72
7.3	Ferroelectric/-elastic switching model	76
7.4	Three-dimensional Preisach model	81
7.4.1	Classical Preisach model	81
7.4.2	Application of the Preisach operator to ferroelectrics	82
7.4.3	Magnetostrictive Preisach model	86
8	Numerical examples	90
8.1	Piezomagnetic-piezoelectric composite	90
8.2	Magnetostrictive-piezoelectric composite	95
8.3	Ferroelectric/ferroelastic-piezomagnetic composite	98
8.4	Magnetostrictive-ferroelectric/ferroelastic composite	103
8.5	Influence of the microstructure on the magneto-electric coupling	107
8.6	Simulation of a porous magneto-electric composite	109
9	Conclusion and Outlook	114
	References	116

1 Introduction and Motivation

Smart materials are used in many modern technical devices. They are capable of changing one of their properties due to the stimulation of another. An example are *piezoelectric* materials, which can change their shape due to an externally applied electric field. There are many further smart materials which couple two material properties. *Magnetostrictive* materials perform a deformation caused by an applied magnetic field or magnetize due to mechanical stresses. A change in temperature depending on a magnetic field is observable in *magnetocaloric* materials or *magnetic shape memory alloys* change their shape under the influence of magnetic fields. Due to the coupling between different material properties, smart materials are used in a variety of technical applications. In the following we take a closer look at ferroic materials, which can have ferroelastic, ferroelectric, ferromagnetic and/or ferrotoroidic properties. The diagram shown in Figure 1.1 depicts possible interactions of different fields of ferroic materials. Piezoelectric materials respond with a deformation ϵ due to an applied electric field \mathbf{E} . Otherwise they exhibit a change in the dielectric displacement \mathbf{D} by an applied pressure σ on the body. The ferroelectric hysteresis is used in ferroelectric memories. The piezoelectric effect is used in hearing aids with piezoelectric transducers or piezo-inline injection systems in automobile engines and all ultrasonics.

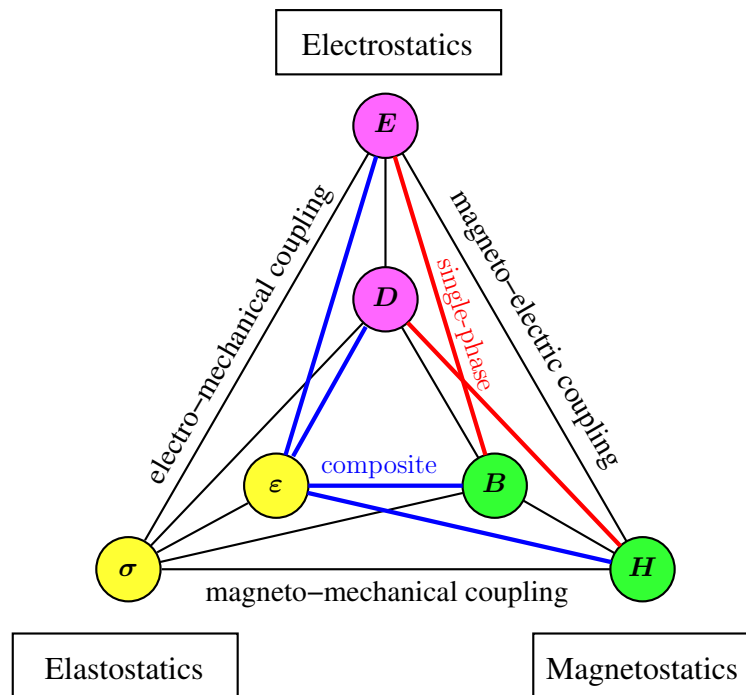


Figure 1.1: Heckmann diagram for functional materials. The magneto-electric coupling of single-phase materials is highlighted with a red line and the strain-induced magneto-electric coupling of composite materials with blue lines.

Additional to ferroelectric devices, magnetic and ferromagnetic components are also frequently used in technical applications. Magnetic materials are employed in data storage devices, where microscopic magnetization directions are used to store the information. The coupling in ferromagnets is given between magnetic fields and mechanical deformations. An applied magnetic field \mathbf{H} yields a deformation of the body, also called magnetostric-

tion, and an applied pressure causes a magnetic induction \mathbf{B} . Such materials are for example used as magnetostrictive linear position sensors. A further special phenomenon which has gained particular attention in the last decades is magneto-electric (ME) coupling. This property is characterized by an interaction between magnetic and electric fields and is investigated in more detail in the framework of the present doctoral thesis. Materials which combine two or more ferroic characteristics are called multiferroic. If an electric field is applied to such a magneto-electric multiferroic, this material responds with a change in magnetization. On the other hand an applied magnetic field causes a change of the electric polarization. Such ME multiferroics allow for new applications in sensor or actuator technology, high-end equipment for automobile, aircraft and spacecraft, medical and information technology. One example is a Magneto-Electric Random Access Memory (MERAM), see EERENSTEIN ET AL. [41], SPALDIN AND FIEBIG [196], VOPSAROIU ET AL. [213] or BIBES AND BARTHÉLÉMY [19].

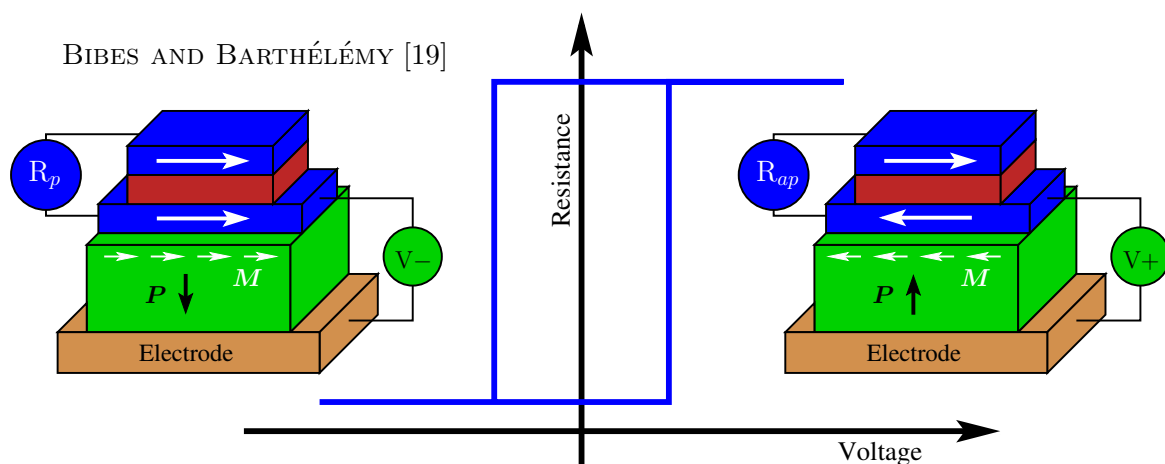


Figure 1.2: Illustration of a Magneto-Electric Random Access Memory (MERAM), adopted from BIBES AND BARTHÉLÉMY [19].

This data storage device can combine the advantages of Ferroelectric Random Access Memories (FeRAMs) and Magnetic Random Access Memories (MRAM). Typically, magnetic storage devices are characterized by their better access time but also by a high writing energy. The idea is to combine the positive properties of FeRAMs and MRAMs through the construction of multiple layers, which is illustrated in Figure 1.2. On the top, two separated magnetic layers (blue) change their resistance according to their relative spin orientation. Either the magnetic layers are magnetized in the same direction or they are magnetized in the opposite directions. Thus, the information is stored as a binary code. Due to this construction the better access time of magnetic memories is used. In order to avoid high writing energies, the advantage of FeRAMs is used, by writing the information through an electric voltage applied across the multiferroic ferroelectric-antiferromagnetic layer (green) below the bottom magnetic layer. An applied electric field switches the direction of the polarization in the multiferroic layer. Due to the magneto-electric coupling its magnetization direction is also changed accordingly, which influences the magnetization direction of the bordering magnetic layer. Therefore, the information is written due to a polarization change which requires a lower writing energy. A further technical application of the magneto-electric coupling is the magnetoencephalography. Human brain activity can be recorded by measuring small magnetic fields which are produced by natural electric

currents inside the brain. Such non-invasive investigations are highly preferred in order to protect the sensitive brain from invasive measurements. However, the natural magnetic field strengths are extremely small and only measurable by so-called superconducting quantum interference devices (SQUIDS). Due to quantum mechanical reasons, which are not described here in detail, only a magnetic field strength which is a multiple of the magnetic fluxon can flow through a superconducting material. With the help of electrical contacts the jumps of the magnetic field strengths are observed through measurable electric voltages. The brain activity can be captured without loss of time and can be spatially allocated due to the helmet shape of the device, which is placed around the human head. However, to obtain superconducting properties the used magnetic material has to be cooled down to extremely low temperatures between about 9 K and 40 K (-264.15°C and -233.15°C). Therefore, liquid helium is used for the cooling process, which requires elaborate constructions and high operating cost. A financial and manufacturing advantage of such devices could be given by magneto-electric materials. However, the magneto-electric coupling in ME single-phase materials is weak and mostly occurs at cryogenic temperatures, which makes it unfavorable for most technical applications. Thus, the idea is to manufacture composite materials, which obtain their magneto-electric coupling due to the interaction of the constituents. Such composites can operate at room temperature and do not require cryogenic cooling as well as show a sensitivity to very low magnetic fields, see SCOTT [190]. In the framework of the present contribution the magneto-electric coupling coefficient is determined through numerical simulations. With appropriate material models, which reflect the realistic behavior of the individual constituents, the effective properties are calculated with a two-scale homogenization approach. The results are compared with experimental measurements and an evaluation of different approaches for material models is given. The document is structured as follows:

- **Chapter 2** gives a brief introduction to the basic relations in magneto-electrostatics and the fundamental electric and magnetic quantities. Its properties and the influences between them are described with the four Maxwell Equations and the electromagnetic Lorentz force.
- **Chapter 3** introduces the continuum mechanical basics, which are necessary for the simulations of the materials in the framework of the Finite Element Method (FEM). Here, the basics are restricted to the linear theory and the fundamental principles of the balance laws are explained. In view of magneto-electro-mechanically coupled problems, a general thermodynamic framework is derived and several thermodynamic potentials are provided for the description of coupled systems.
- In **Chapter 4** the properties of different kinds of ferroic materials are described. For the understanding of these phenomena we also consider the origin of magnetism which includes some aspects of quantum mechanics. Such fundamentals are also important to describe the ME coupling in single-phase materials and to answer the question why ME single-phase materials are so rare in nature. As an alternative, possible structures of composite materials are shown, which outperform the magneto-electric characteristics of single-phase materials.
- In order to perform numerical simulations of such ferroic and composite materials, **Chapter 5** outlines the Galerkin-method based on the principle of virtual work.

The weak formulations and its linearizations are derived with respect to magneto-electro-mechanically coupled boundary value problems. Then the Finite Element Method is used and additional treatments, such as the isoparametric concept and the discretizations of the weak forms and linearizations are discussed.

- **Chapter 6** starts with an overview of possible homogenization procedures. In the framework of this contribution we derive a two-scale Finite Element homogenization scheme, the so-called FE²-method, for magneto-electro-mechanically coupled problems. Two boundary value problems, one on the macroscale and the other on the microscale, are solved with the FEM and connected via scale bridging. Thereby, the influence of the microscopic morphology on the macroscopic effective properties is inspected. Since the magneto-electric coupling significantly depends on the microstructure, the FE²-method is a suitable tool to investigate such effects.
- Further important influences on the ME properties are the material models used. In **Chapter 7** different approaches are shown to approximate the electro-mechanical and magneto-mechanical materials. We start with the derivative of a linear model for both phases, then derive a nonlinear magnetostrictive material model, extend a ferroelectric/ferroelastic switching model based on a switching criterion to the magneto-electro-mechanical case and finally derive a three-dimensional magnetostrictive Preisach model.
- The influence of the different material models on the ME coupling is demonstrated in **Chapter 8** by performing several numerical examples with different combinations of the implemented models. The resulting magneto-electric coefficients are then compared with experimental measurements. Furthermore, additional effects are investigated, such as the influence of the microscopic morphology, the effect of applied mechanical stresses as well as the influence of defects at the interface between the composite constituents.
- **Chapter 9** concludes the document and gives a short outlook on future work.

2 Brief introduction to electro-magneto-statics

The following section gives a brief introduction to the basic relations of electro-magneto-statics, which are used to describe the considered ferroelectric and ferromagnetic material properties. We start with the introduction of the fundamental equations of electric and magnetic fields in vacuum, which includes moving charges and thus time dependent effects. However, since we do not consider free charge carriers in the materials, the necessary time independent electro-magnetic relations in matter are described. For a detailed explanation of the fundamental magneto-electric equations we refer to FROHNE [53], JILES [85], LEHNER [122] and J.D.JACKSON [84].

2.1 Electric and magnetic fields in vacuum

Two different electric loading states are known, the positive and negative electric charge. Only the elementary particles can be charged either positively or negatively and are called protons (+ e) or electrons ($-e$), respectively. The absolute value of their amount of charge is called the elementary charge

$$e = 1.602 \cdot 10^{-19} \text{ C} , \quad (2.1)$$

where the unit Coulomb is denoted by the symbol C and defined by the amount of electric charges that pass one point in one second s due to the electric current of one Ampere A , with $C = As$. If a body is electrically charged, its amount of charge is thus always a multiple of the elementary charge e . Considering two charges with two different or equal charge states a force is acting between them. In the case of equal charges they repel each other, whereas for different charge states both charges attract each other. The force acting on a charge q is described by the **Lorentz force** \mathbf{F}_L and is defined as

$$\mathbf{F}_L = q\mathbf{E} + q\mathbf{v} \times \mathbf{B} \quad (2.2)$$

with the electric field \mathbf{E} , the velocity vector \mathbf{v} of the point charge q and the vector of magnetic induction \mathbf{B} . We first consider in more detail the first part of the Lorentz force $\mathbf{F}_L^C = q\mathbf{E}$, which is also denoted as the Coulomb force and describes the influence due to an electric field. This part of the Lorentz force is proportional to the square of the distance between two electric charges q_i and q_j as

$$\mathbf{F}_{L,ij}^C = \frac{q_i q_j}{4\pi\epsilon_0 r_{ij}^2} \frac{\mathbf{r}_{ij}}{\|\mathbf{r}_{ij}\|} \quad (2.3)$$

with the vector \mathbf{r}_{ij} pointing from the location of one charge to the position of the other charge, such that the norm $\|\mathbf{r}_{ij}\|$ denotes the distance and $\mathbf{r}_{ij}/\|\mathbf{r}_{ij}\|$ the unit vector between both charges. The factor $1/(4\pi\epsilon_0)$ is also denoted as the electrostatic constant with the permittivity of free space $\epsilon_0 = 1/(\mu_0 c^2)$, including the vacuum permeability $\mu_0 = 4\pi \cdot 10^{-7} N/A^2$ and the speed of light c resulting in $\epsilon_0 \approx 8.854 \cdot 10^{-12}$. The phenomenon of the *electrical* part of the Lorentz force can be observed in an electric circuit, where the electrons move through the wire from the negative electric pole to the positive electric pole. Furthermore, the influence of a single point charge q on another point charge can be expressed with the electric field as

$$\mathbf{E} = \frac{\mathbf{F}_L^C}{q} = \frac{q}{4\pi\epsilon_0} \frac{\mathbf{r}}{\|\mathbf{r}\|^2 \|\mathbf{r}\|} . \quad (2.4)$$

The definition of the latter equation means that the charge q generates the electric field strength \mathbf{E} at a point with distance $\|\mathbf{r}\|$ and is therefore independent of the other point charge. The work which is needed to move an electric point charge over an infinitesimal distance is given by

$$d\mathcal{W} = -\mathbf{F}_L^C \cdot d\mathbf{s} = -q \mathbf{E} \cdot d\mathbf{s} , \quad (2.5)$$

with the amount of work over the distance l as

$$\mathcal{W} = - \int_l \mathbf{F}_L^C \cdot d\mathbf{s} = -q \int_l \mathbf{E} \cdot d\mathbf{s} . \quad (2.6)$$

By considering a closed path of the electron movement for time independent states, then the amount of work which is needed to move the point charge from one position of the path to an arbitrary other position is equal to the amount of work which is needed to move the electron back to the initial position on another path, such that we obtain the following relation

$$\oint \mathbf{E} \cdot d\mathbf{s} = 0 \quad \text{or} \quad \text{curl} \mathbf{E} = 0 . \quad (2.7)$$

It has to be emphasized that the latter relation holds for time independent (static) states, which are assumed in this work. However, for time dependent processes the rotation of \mathbf{E} is not equal zero, which can be seen later in the Maxwell equations.

The work between a starting point \mathbf{r}_0 and an arbitrary point \mathbf{r} can also be described by an electric potential ϕ as

$$\phi(\mathbf{r}) = - \int_{\mathbf{r}_0}^{\mathbf{r}} \mathbf{E}(\mathbf{r}) \cdot d\mathbf{s} . \quad (2.8)$$

Then the potential difference between two points \mathbf{r}_1 and \mathbf{r}_2 is given by

$$\phi_2 - \phi_1 = - \int_{\mathbf{r}_0}^{\mathbf{r}_2} \mathbf{E} \cdot d\mathbf{s} + \int_{\mathbf{r}_0}^{\mathbf{r}_1} \mathbf{E} \cdot d\mathbf{s} = - \int_{\mathbf{r}_1}^{\mathbf{r}_2} \mathbf{E} \cdot d\mathbf{s} \quad (2.9)$$

resulting in the expression for the electric field

$$\boxed{\mathbf{E} = -\text{grad}\phi} . \quad (2.10)$$

For the explanation of the second part of the Lorentz force we have to introduce the magnetic induction \mathbf{B} , which is also called the magnetic flux density, and take a closer look at its definition in the following. For simplicity, we consider the generation of the magnetic induction in vacuum or simply in air and take a closer look at the magnetic induction in matter in Section 2.2. Then a point charge q with the velocity vector \mathbf{v} produces a magnetic field \mathbf{H} and a magnetic induction in free space as

$$\mathbf{H} = \frac{1}{4\pi} \frac{q\mathbf{v} \times \mathbf{r}/\|\mathbf{r}\|}{\|\mathbf{r}\|^2} \quad \text{and} \quad \mathbf{B} = \frac{\mu_0}{4\pi} \frac{q\mathbf{v} \times \mathbf{r}/\|\mathbf{r}\|}{\|\mathbf{r}\|^2} \quad \text{with} \quad \mathbf{B} = \mu_0 \mathbf{H} \quad (2.11)$$

with the radius \mathbf{r} describing the distance between the point charge and the produced point of application of the magnetic induction. Here it has to be emphasized that the latter equations for \mathbf{B} are valid for the free space. The resulting magnetic induction

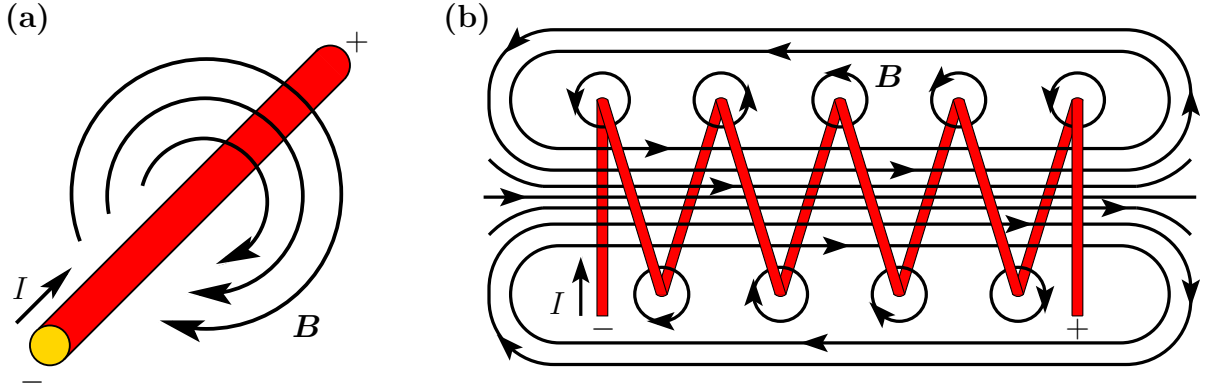


Figure 2.1: (a) Magnetic field produced by moving charge carriers in a straight wire. (b) Superposition of multiple magnetic field lines in a circular conductor loop.

vector is perpendicular to the velocity vector of the point charge and the unit vector of the radius, with $\mathbf{r}/\|\mathbf{r}\|$, see Figure 2.1(a).

This means that an electron moving in one direction produces a magnetic induction in form of concentric circles around the directional movement. Furthermore, the norm of the magnetic induction \mathbf{B} is proportional to the point charge q and the norm of the velocity \mathbf{v} . Based on the angle θ between the velocity vector and the displacement vector \mathbf{r} the magnetic induction is proportional to $\sin(\theta)$, such that the magnetic induction vanishes in the direction of the velocity vector. Additionally, the magnetic induction decreases with the square of the norm of the distance. If we now consider a number n of point charges in a cross section \mathbf{A} and in an infinitesimal part $d\mathbf{l}$ of a conductor, which displays the moving direction of the point charge, as

$$q\mathbf{v} n \mathbf{A} d\mathbf{l} = I d\mathbf{l} , \quad (2.12)$$

we obtain with the electric current density $\mathbf{J} = nq\mathbf{v}$ and the strength of the electric current

$$I = \int_A \mathbf{J} \cdot d\mathbf{A} . \quad (2.13)$$

With the integration over the cross section of the conductor, the incremental expression of the magnetic induction is given as

$$\boxed{d\mathbf{B} = \frac{\mu_0}{4\pi} \frac{I d\mathbf{l} \times \mathbf{r}/\|\mathbf{r}\|}{\|\mathbf{r}\|^2}} . \quad (2.14)$$

The latter equation is denoted as the **Biot-Savart law**. In the following we want to consider the resulting magnetic field in the center of a conductor loop. Since the resulting field at an observed position is perpendicular to the point charge movement and the displacement vector between the point charge and the observed position, for the center of the conductor loop the magnetic induction results in

$$d\mathbf{B} = \frac{\mu_0}{4\pi} \frac{I d\mathbf{l} \sin(\theta)}{\|\mathbf{R}\|^2} \quad (2.15)$$

with the vector of radius \mathbf{R} of the conductor loop and the angle θ between $d\mathbf{l}$ and \mathbf{R} . Then, the vector of the magnetic induction points along the axis of the conductor loop. After the integration over the complete conductor loop, where $\sin(\theta) = 1$ at every position in a circular loop, we obtain the overall magnetic induction in the center of the loop as

$$\mathbf{B} = \oint d\mathbf{B} = \frac{\mu_0}{4\pi} \frac{I}{\|\mathbf{R}\|^2} \oint d\mathbf{l} = \frac{\mu_0}{4\pi} \frac{I}{\|\mathbf{R}\|^2} 2\pi R = \frac{\mu_0 I}{2R} \quad (2.16)$$

with the circumference of the conductor loop $\oint d\mathbf{l} = 2\pi R$. In order to determine the magnetic induction produced by a conductor loop at a position with the distance \mathbf{r} to the incremental part of the conductor, we obtain

$$|d\mathbf{B}| = \frac{\mu_0}{4\pi} \frac{I \left| d\mathbf{l} \times \frac{\mathbf{r}}{\|\mathbf{r}\|} \right|}{\|\mathbf{r}\|^2}. \quad (2.17)$$

However, a summation of $d\mathbf{B}$ over all increments of the conductor loop shows that inside the loop only a remaining magnetic induction in the direction of the axis (here, x-axis) remains, in this case

$$dB_x = \frac{\mu_0}{4\pi} \frac{Idl}{(x^2 + R^2)} \frac{R}{\sqrt{x^2 + R^2}} = \frac{\mu_0}{4\pi} \frac{Idl}{(x^2 + R^2)^{3/2}}, \quad (2.18)$$

where the distance to the point of interest r now depends on the radius of the conductor loop with $r = \sqrt{x^2 + R^2}$. The integration over the complete conductor loop yields

$$B_x = \oint \frac{\mu_0}{4\pi} \frac{IR}{(x^2 + R^2)^{3/2}} dl = \frac{\mu_0 R^2 I}{2(x^2 + R^2)^{3/2}}. \quad (2.19)$$

In an electromagnetic coil the generated magnetic field is a result of the superposition of multiple magnetic fields of layered conductor loops. Then, the magnetic field strength depends on the number of coils of the wire within an incremental length and the current intensity.

With the definition of the magnetic induction the second part of the Lorentz force including the cross product $q\mathbf{v} \times \mathbf{B}$ can be explained. Then the force is proportional to the point charge q , the velocity vector \mathbf{v} and the vector of the magnetic induction. As described with the cross product the Lorentz force acts perpendicular to the velocity vector and the magnetic induction. For a positive and a negative point charge $+q$ and $-q$ moving with the same velocity vector, the Lorentz forces point in their opposite directions. With the definition of the Lorentz force, which is produced by a moving charge q_1 and acts on another point charge q_2 , the magnetic force can be determined as

$$\mathbf{F}_{12} = q_2 \mathbf{v}_2 \times \mathbf{B}_1 = q_2 \mathbf{v}_2 \times \left(\frac{\mu_0}{4\pi} \frac{q_1 \mathbf{v}_1 \times \mathbf{r}_{12} / \|\mathbf{r}_{12}\|}{\|\mathbf{r}_{12}\|^2} \right), \quad (2.20)$$

where \mathbf{B}_1 denotes the magnetic induction produced by point charge q_1 at the position of the point charge q_2 , \mathbf{F}_{12} the force acting from point charge q_1 on point charge q_2 and \mathbf{r}_{12} the distance between both particles. Simultaneously, the force produced by point charge q_2 acting on q_1 is given as

$$\mathbf{F}_{21} = q_1 \mathbf{v}_1 \times \mathbf{B}_2 = q_1 \mathbf{v}_1 \times \left(\frac{\mu_0}{4\pi} \frac{q_2 \mathbf{v}_2 \times \mathbf{r}_{21} / \|\mathbf{r}_{21}\|}{\|\mathbf{r}_{21}\|^2} \right). \quad (2.21)$$

The direction of the Lorentz force for positive point charges $+q$ can be determined with the right-hand rule. Then, the forefinger points into the direction of the velocity vector, the middle finger in the direction of the magnetic induction and the thumb in the direction of the resulting Lorentz force. For negative point charges the left hand can be taken using the same principle. If we consider an electric conductor of the length l and the cross section A with the number of point charges n in an magnetic induction \mathbf{B} and neglect the influence of electric fields, then we obtain the Lorentz force density as

$$\mathbf{f}_L = (q\mathbf{v} \times \mathbf{B}) n A l , \quad (2.22)$$

where we neglect the electric part of the Lorentz force due to the fact that no electric fields are present in this example. With the electric current density $\mathbf{J} = nq\mathbf{v}$ we obtain

$$\mathbf{f}_L = \mathbf{J} A l \times \mathbf{B} . \quad (2.23)$$

With the strength of electric current

$$I = \int_A \mathbf{J} \cdot d\mathbf{A} \quad (2.24)$$

we get the relations

$$\mathbf{f}_L = I \mathbf{l} \times \mathbf{B} \quad \text{and} \quad d\mathbf{f}_L = I d\mathbf{l} \times \mathbf{B} , \quad (2.25)$$

where the second relation is a generalized incremental statement considering an infinitesimal small part of the electric conductor.

2.2 Electric and magnetic fields in matter

For the consideration of the electric and magnetic fields in matter, further quantities depending on material properties have to be defined. First, we take a closer look at the magnetic induction \mathbf{B} . A moving electric charge generates a magnetic field and using the magnetic permeability a magnetic induction in a medium. Therefore, the magnetic induction depends on the corresponding material properties, where the magnetic field is present. The relation between the magnetic field and the relative magnetic permeability $\mu_r = \hat{\mu}_r(\mathbf{H})$ of the material is given as

$$\mathbf{B} = \mu_0 \mu_r \cdot \mathbf{H} = \mu_0 (\mathbf{I} + \chi_m) \cdot \mathbf{H} = \mu_0 (\mathbf{H} + \chi_m \cdot \mathbf{H}) = \mu_0 \mathbf{H} + \mathbf{M} \quad (2.26)$$

with the magnetic susceptibility $\chi_m = \hat{\chi}_m(\mathbf{H})$ describing the magnetizability and $\mathbf{M} = \hat{\mathbf{M}}(\mathbf{H})$ the magnetization of the material. Different notations are used in literature for the representation of the magnetic induction. In order to get an analogous representation to the dielectric displacement we use the representation in Equation (2.26), see also the work of SCHOLTEN [179] to this topic. Depending on the material properties the magnetizability of different substances can vary largely. In case of a vacuum, which is not magnetizable, χ completely vanishes and the magnetic induction only depends on the magnetic field and the vacuum permeability with $\mathbf{B} = \mu_0 \mathbf{H}$. Additionally, some materials can modify the ratio between the applied magnetic field and the resulting magnetic induction in the medium, such that the magnetic induction can be smaller or larger than the applied

field. These materials can be distinguished with the magnetic susceptibility and thus the magnetic permeability. For instance in water, copper or silver, the magnetic susceptibility is between $-1 < \chi_m < 0$. With the relation $\mathbf{B} = \mu_0 \mathbf{H} + \mu_0 \chi_m \cdot \mathbf{H}$ it can be seen that the magnetic induction inside such materials is lower than in the surrounding area. Furthermore, the created magnetic induction is in opposite direction to the applied field so that the material is repelled by the magnetic field.

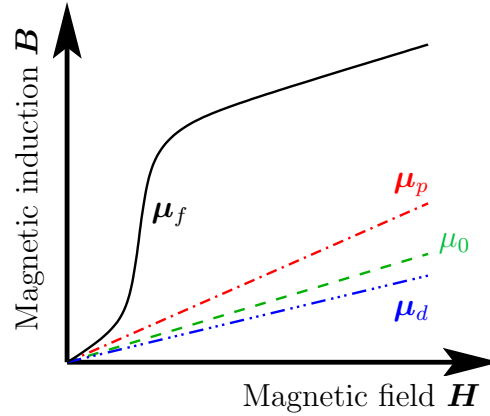


Figure 2.2: Resulting magnetic induction with respect to an applied magnetic field in different magnetic materials, where the magnetic permeability is denoted as μ_f for ferromagnetic materials, μ_p for paramagnetic materials, μ_0 for vacuum and μ_d for diamagnetic materials.

Such materials have so-called diamagnetic properties. A special case are superconducting materials with a magnetic susceptibility of $\chi_m = -1$. Then inside the material no magnetic field is present. Figure 2.2 depicts simplified relations between the applied magnetic field and the resulting magnetic inductions in the corresponding materials, where the magnetic permeability is denoted as μ_f for ferromagnetic materials, μ_p for paramagnetic materials, μ_0 for vacuum and μ_d for diamagnetic materials. If the susceptibility is slightly larger than zero with $\chi_m > 0$ the material shows a small magnetization in the direction of the applied field. Such materials are called paramagnetic materials and show a linear behavior between the applied field and the resulting magnetization. If the susceptibility is significantly larger than 1 with $\chi_m \gg 1$, which is the case in ferri-, antiferro- and ferromagnetic materials, a nonlinear increase of the magnetic induction with respect to the applied field is observable. Additionally, a remaining (remanent) magnetization is present after removing the magnetic field. Further characteristics of the different kinds of magnetic materials and the origin of their properties are discussed in detail in Section 4.1.

Analogously to the magnetic induction we have to introduce the dielectric displacement \mathbf{D} , which describes the polarization of a material depending on the electric permittivity ϵ as

$$\mathbf{D} = \epsilon \cdot \mathbf{E} , \quad (2.27)$$

where the electric permittivity can be decomposed into $\epsilon = \epsilon_0 \epsilon_r$. Here, ϵ_0 is the vacuum permittivity and ϵ_r the relative permittivity such that we obtain

$$\mathbf{D} = \epsilon_0 \epsilon_r \cdot \mathbf{E} = \epsilon_0 (1 + \chi_e) \cdot \mathbf{E} = \epsilon_0 \mathbf{E} + \epsilon_0 \chi_e \cdot \mathbf{E} \quad (2.28)$$

with the electric susceptibility χ_e . This quantity describes the current polarization state of the material depending on the applied electric field, such that we obtain

$$\mathbf{D} = \epsilon_0 \mathbf{E} + \mathbf{P} . \quad (2.29)$$

The polarization $\mathbf{P} = \hat{\mathbf{P}}(\mathbf{E})$ of the material is generated by charge carriers. At this point we have to differentiate between the density of free charge carriers ρ_f and the density of bound charge carriers ρ_b . Free charge carriers can be free electrons or for example ions which move through electrolytes. Bound charge carriers however are for example ions which are fixed in the lattice structure and a possible displacement of the positive and negative charge centers produce a polarization of the crystal. The determination of the divergence of Equation (2.29) yields an expression depending on the free ρ_f and bound ρ_b charge carrier densities as

$$\operatorname{div}(\epsilon_0 \mathbf{E}) = \rho \Leftrightarrow \operatorname{div}(\epsilon_0 \mathbf{E}) = \rho_f + \rho_b \Leftrightarrow \rho_f + \rho_b = \operatorname{div} \mathbf{D} - \operatorname{div} \mathbf{P} \quad (2.30)$$

such that we obtain the two relations

$$\operatorname{div} \mathbf{D} = \rho_f \quad \text{and} \quad \operatorname{div} \mathbf{P} = -\rho_b, \quad (2.31)$$

where Equation (2.31)₁ is one of the four Maxwell equations and known as the **Gauss law of electrostatics**. In this thesis, I consider the dielectric material barium titanate with very low doping level, which has no electrically conducting properties at or near room temperature such that approximately no free charge carriers are present in the material resulting in the following expression for the divergence of the dielectric displacement

$$\operatorname{div} \mathbf{D} = 0. \quad (2.32)$$

2.3 Maxwell Equations

As shown in the expression of the Biot-Savart law in Equation (2.14) a moving point charge produces a magnetic induction in form of concentric circles around the moving direction of this point charge. Such circles can be described by a rotation of a vector field with the curl-operator $\operatorname{curl}(\bullet)$. Furthermore, the rotation of the vector field can be associated with the strength of the electric current with **Ampère's circuital law**

$$\operatorname{curl} \mathbf{H} = \mathbf{J} \quad (2.33)$$

with the vector of current density \mathbf{J} . However, in Equation (2.33) the time independent state is considered. For the time dependent case the change of the current density with time

$$\mathbf{J} = \rho_f n \mathbf{v} \quad (2.34)$$

and the time dependent change of the dielectric displacement $\partial \mathbf{D} / \partial t$ are taken into account resulting in the **1. Maxwell Equation** as

$$\boxed{\operatorname{curl} \mathbf{H} = \mathbf{J} + \frac{\partial \mathbf{D}}{\partial t}}. \quad (2.35)$$

Additional to the coherence between a change of the dielectric displacement and the magnetic field, we can also observe a correlation between a change of the magnetic induction in time and the resulting electric field as

$$\boxed{\operatorname{curl} \mathbf{E} = -\frac{\partial \mathbf{B}}{\partial t}}. \quad (2.36)$$

The latter equation is called the **2. Maxwell Equation** and is also known as the electromagnetic induction, which was first discovered in 1831 by the English scientist Michael Faraday. It describes the induction of electric currents in a material by applying a magnetic induction which changes in time.

The **3. Maxwell Equation**, also denoted as the Gauss law of magnetostatics, states that the divergence of the magnetic induction is equal to zero as

$$\boxed{\operatorname{div}\mathbf{B} = 0} . \quad (2.37)$$

From the physical perspective, the latter equation shows that the magnetic field lines have no sources and sinks and therefore as a consequence that no magnetic monopoles exist. It is often stated in literature, that the magnetic field lines are closed or run to infinity. However, there are indeed some examples which show that magnetic field lines are neither closed nor run to infinity, see LEHNER [122](chapter 5.11.2) for an example.

In contrast to magnetism where no magnetic monopoles exist, the electric field lines depend on electrically charged monopoles. We differentiate between the density of free charge carriers ρ_f and the density of bounded charge carriers ρ_b , where we obtain the relation

$$\boxed{\operatorname{div}\mathbf{D} = \rho_f} , \quad (2.38)$$

which is known as the **4. Maxwell Equation** or the Gauss law of electrostatics. The following Table 2.1 summarizes the four Maxwell equations and their physical description.

Maxwell Equation	equation	physical description
1. Maxwell equation (Ampère's circuital law)	$\operatorname{curl}\mathbf{H} = \mathbf{J} + \frac{\partial\mathbf{D}}{\partial t}$	The rotation of the magnetic field can be associated with the strength of the electric current.
2. Maxwell equation (Faraday's law of induction)	$\operatorname{curl}\mathbf{E} = -\frac{\partial\mathbf{B}}{\partial t}$	A temporally changing field of the magnetic flux density generates an electric eddy current field.
3. Maxwell equation (Gauss law of magnetostatics)	$\operatorname{div}\mathbf{B} = 0$	No magnetic sources and sinks (solenoidality) and therefore no magnetic monopoles exist.
4. Maxwell equation (Gauss law of electrostatics)	$\operatorname{div}\mathbf{D} = \rho_f$	The source of the electric field is the free electric charge.

Table 2.1: Summary of the four Maxwell equations with their physical description.

Since we in the framework of the present contribution performed time independent simulations and neglected free charge carriers in the materials, we use the following two relations

$$\operatorname{div}\mathbf{D} = 0 \quad \text{and} \quad \operatorname{div}\mathbf{B} = 0 . \quad (2.39)$$

2.4 Maxwell Stress Tensor

In classical small strain continuum mechanics, where purely mechanical boundary value problems are taken into account, the stress tensor $\boldsymbol{\sigma}^{mech}$ depends on the mechanical deformations $\boldsymbol{\varepsilon}$. However, by considering electromagnetic boundary value problems, it can be necessary to take into account electromagnetic forces which influence the stress tensor. The so called Maxwell stress tensor $\boldsymbol{\sigma}^{maxw}$ represents the influence of the electromagnetic force on the stress tensor as

$$\boldsymbol{\sigma} = \boldsymbol{\sigma}^{mech} + \boldsymbol{\sigma}^{maxw} . \quad (2.40)$$

For the derivative of the Maxwell stresses we start with the definition of the Lorentz force \mathbf{F}_L for a single point charge

$$\mathbf{F}_L = q(\mathbf{E} + \mathbf{v} \times \mathbf{B}) \quad \text{with} \quad \mathbf{F}_L = \int_{\mathcal{B}} \mathbf{f}_L \, dv . \quad (2.41)$$

Here, the volume of a single charge carrier is used. More generally, if multiple charge carriers per volume are taken into account, we consider the charge density ρ_f and the resulting current density $\mathbf{J} = \rho_f n \mathbf{v}$ and obtain the Lorentz force density \mathbf{f}_L as

$$\mathbf{f}_L = \rho_f \mathbf{E} + \mathbf{J} \times \mathbf{B} . \quad (2.42)$$

For the following numerical reformulation of the latter equation we consider the first Maxwell equations with $\mathbf{J} = \text{curl} \mathbf{H} - \partial_t \mathbf{D}$ and the fourth Maxwell equation and obtain

$$\mathbf{f}_L = (\text{div} \mathbf{D}) \mathbf{E} + (\text{curl} \mathbf{H} \times \mathbf{B}) - \left(\frac{\partial \mathbf{D}}{\partial t} \times \mathbf{B} \right) . \quad (2.43)$$

The last term of the previous equation can be expressed using the product rule

$$\frac{\partial}{\partial t} (\mathbf{D} \times \mathbf{B}) = \frac{\partial \mathbf{D}}{\partial t} \times \mathbf{B} + \mathbf{D} \times \frac{\partial \mathbf{B}}{\partial t} \quad \Leftrightarrow \quad \frac{\partial \mathbf{D}}{\partial t} \times \mathbf{B} = \frac{\partial}{\partial t} (\mathbf{D} \times \mathbf{B}) - \mathbf{D} \times \frac{\partial \mathbf{B}}{\partial t} \quad (2.44)$$

such that the Lorentz force density results in the following equation

$$\mathbf{f}_L = (\text{div} \mathbf{D}) \mathbf{E} + (\text{curl} \mathbf{H} \times \mathbf{B}) - \frac{\partial}{\partial t} (\mathbf{D} \times \mathbf{B}) + \mathbf{D} \times \frac{\partial \mathbf{B}}{\partial t} . \quad (2.45)$$

Now we take into account the second Maxwell equation $\text{curl} \mathbf{E} = -\partial_t \mathbf{B}$, the relation $\text{curl} \mathbf{H} \times \mathbf{B} = -\mathbf{B} \times \text{curl} \mathbf{H}$ and add the term $(\text{div} \mathbf{B}) \mathbf{H} = 0$. After some algebraic modulations we obtain the following expression of the Lorentz force density as

$$\mathbf{f}_L = [(\text{div} \mathbf{D}) \mathbf{E} - \mathbf{D} \times \text{curl} \mathbf{E}] + [(\text{div} \mathbf{B}) \mathbf{H} - \mathbf{B} \times \text{curl} \mathbf{H}] - \frac{\partial}{\partial t} (\mathbf{D} \times \mathbf{B}) . \quad (2.46)$$

In order to get rid of the curl-operator, we apply the next reformulation for the electric field and analogously to the magnetic field as

$$\text{curl} \mathbf{E} = \nabla \times \mathbf{E} \quad \Leftrightarrow \quad \mathbf{D} \times \nabla \times \mathbf{E} = (\text{grad} \mathbf{E})^T \mathbf{D} - (\text{grad} \mathbf{E}) \mathbf{D} . \quad (2.47)$$

Then the Lorentz force density results in

$$\begin{aligned} \mathbf{f}_L = & [(\text{div} \mathbf{D}) \mathbf{E} - (\text{grad} \mathbf{E})^T \mathbf{D} + (\text{grad} \mathbf{E}) \mathbf{D}] \\ & + [(\text{div} \mathbf{B}) \mathbf{H} - (\text{grad} \mathbf{H})^T \mathbf{B} + (\text{grad} \mathbf{H}) \mathbf{B}] - \frac{\partial}{\partial t} (\mathbf{D} \times \mathbf{B}) . \end{aligned} \quad (2.48)$$

The last two modulations $\operatorname{div}(\mathbf{E} \otimes \mathbf{D}) = (\operatorname{div}\mathbf{D})\mathbf{E} + (\operatorname{grad}\mathbf{E})\mathbf{D}$ and $(\operatorname{grad}\mathbf{E})^T\mathbf{D} = \frac{1}{2}\epsilon_0\operatorname{div}(\|\mathbf{E}\|^2)\mathbf{I}$ with $\mathbf{D} = \epsilon_0\mathbf{E}$ as well as $\mathbf{B} = \mu_0\mathbf{H}$ and the analogous modulations for the magnetic quantities yield the final expression of the Lorentz force density as

$$\mathbf{f}_L = \underbrace{\epsilon_0\operatorname{div}\left[\mathbf{E} \otimes \mathbf{E} - \frac{1}{2}\|\mathbf{E}\|^2\mathbf{I}\right]}_{\operatorname{div}\boldsymbol{\sigma}_{elec}^{maxw}} + \underbrace{\mu_0\operatorname{div}\left[\mathbf{H} \otimes \mathbf{H} - \frac{1}{2}\|\mathbf{H}\|^2\mathbf{I}\right]}_{\operatorname{div}\boldsymbol{\sigma}_{magn}^{maxw}} - \frac{\partial}{\partial t}(\mathbf{D} \times \mathbf{B}), \quad (2.49)$$

where the first and second term represent the divergence of the electric and magnetic part of the Maxwell stresses, respectively. With the correlation of the Lorentz force density and the Maxwell stresses as $\mathbf{f}_L = \operatorname{div}\boldsymbol{\sigma}^{maxw}$ we obtain the Maxwell stresses as

$$\boldsymbol{\sigma}^{maxw} = \epsilon_0\left[\mathbf{E} \otimes \mathbf{E} - \frac{1}{2}\|\mathbf{E}\|^2\mathbf{I}\right] + \mu_0\left[\mathbf{H} \otimes \mathbf{H} - \frac{1}{2}\|\mathbf{H}\|^2\mathbf{I}\right]. \quad (2.50)$$

However, the Maxwell stresses become important in materials with moving charge carriers or in order to incorporate magnetic or electric body forces. In dielectric materials, such as barium titanate used in the investigated composites, the maxwell stresses are less important and have only a small impact on the overall stresses. Thus, the Maxwell stresses are not regarded in the performed numerical simulations in the framework of this doctoral thesis. The Maxwell stresses are indeed important in, for example, magnetorheological elastomers or electroactive polymers (EAPs), where magnetic forces between particles or moving ions are responsible for the deformations of the body, see for example KEIP AND RAMBAUSEK [94].

3 Introduction to continuum mechanics

Every material consist of atomic particles and is characterized by its microstructural properties. Theories considering the material structure on the atomic level are *molecular* and *atomistic theories*. In contrast, **continuum mechanics** considers the material as a macroscopic body supposed to have a continuous distribution of matter and the properties are described by a few quantities. Thus, the body is considered as an average of the properties of much smaller scales. In the framework of continuum mechanics we investigate the **kinematics**, describing the motion and deformation of the body, the **concept of stress**, and the **balance principles** governing the fundamental laws of physics. Since the present contribution considers small deformations of the bodies, only the geometrically linear theory of solid mechanics will be presented. For a detailed description of continuum mechanics the reader is referred to ERINGEN AND MAUGIN [43], HOLZAPFEL [70], TRUESDELL AND NOLL [209], or WRIGGERS [221].

3.1 Kinematics of continuum bodies

Each considered body $\mathcal{B}_0 \in \mathbb{R}^3$ consists of a set of material points, whereas the individual points can be characterized by the position vector \mathbf{X} in the undeformed (reference) configuration. We are furthermore interested in the description of the deformations of the body, such that we additionally introduce a deformed (current) configuration, where the material points are described by the position vectors \mathbf{x} . The new positions of the material points are then described by the transformation

$$\mathbf{x} = \varphi(\mathbf{X}) . \quad (3.1)$$

Furthermore, the displacement which each particle undergoes is described by the displacement vector \mathbf{u} as

$$\mathbf{u} = \mathbf{x} - \mathbf{X} . \quad (3.2)$$

Since we are not only interested in the current position of each particle, but also on the deformation of the body, which can be described by the distances between neighboring particles, we determine the deformation gradient \mathbf{F} with

$$\mathbf{F} = \frac{\partial \mathbf{x}}{\partial \mathbf{X}} = \frac{\partial \mathbf{X}}{\partial \mathbf{X}} + \frac{\partial \mathbf{u}}{\partial \mathbf{X}} = \mathbf{1} + \nabla \mathbf{u} \quad (3.3)$$

with the identity tensor $\mathbf{1}$ and the gradient-operator ∇ with respect to \mathbf{X} . Using the deformation gradient \mathbf{F} the mappings from the reference configuration to the current configuration of an infinitesimal line element $d\mathbf{X}$, an infinitesimal area element $d\mathbf{A}$ and an infinitesimal volume element dV can be determined with the following transformations

$$d\mathbf{x} = \mathbf{F} \cdot d\mathbf{X} , \quad d\mathbf{a} = \det[\mathbf{F}] \mathbf{F}^{-T} \cdot d\mathbf{A} \quad \text{and} \quad dv = J dV \quad \text{with} \quad J = \det[\mathbf{F}] . \quad (3.4)$$

In the latter equation J denotes the Jacobian determinant. The deformation gradient can be multiplicatively decomposed into a rotation tensor \mathbf{R} and a left and right stretch tensor \mathbf{V} and \mathbf{U} , respectively, as

$$\mathbf{F} = \mathbf{R} \cdot \mathbf{U} \quad \text{and} \quad \mathbf{F} = \mathbf{V} \cdot \mathbf{R} . \quad (3.5)$$

Based on the square of the deformation gradient we define the right and left Cauchy-Green tensor as

$$\mathbf{C} = \mathbf{F}^T \cdot \mathbf{F} \quad \text{and} \quad \mathbf{b} = \mathbf{F} \cdot \mathbf{F}^T, \quad (3.6)$$

which include no rigid body motions due to the orthogonal properties of the rotation tensor with $\mathbf{R}^{-1} = \mathbf{R}^T$ and the properties $\det \mathbf{R} = 1$ and $\mathbf{R} \cdot \mathbf{R}^{-1} = \mathbf{1}$. With the right Cauchy-Green tensor \mathbf{C} we can determine the Green-Lagrange strain tensor as

$$\mathbf{E} = \frac{1}{2}(\mathbf{C} - \mathbf{1}) = \frac{1}{2}(\nabla \mathbf{u} + \nabla^T \mathbf{u} + \nabla^T \mathbf{u} \cdot \nabla \mathbf{u}). \quad (3.7)$$

Since we only consider bodies undergoing small deformations, the higher order terms can be neglected, such that the linear strain tensor $\boldsymbol{\varepsilon}$ is defined as

$$\boldsymbol{\varepsilon} = \frac{1}{2}(\text{Grad} \mathbf{u} + \text{Grad}^T \mathbf{u}). \quad (3.8)$$

3.2 Concept of stress

If a statically supported body is loaded with external mechanical forces the body reacts with deformations and internal stresses. Such stresses can be determined in arbitrary cross-sections of the body. Depending on the orientation of the cross-section, with the normal vector \mathbf{n} , we introduce the traction or stress vector \mathbf{t} with the so-called **Cauchy theorem** as

$$\mathbf{t} = \boldsymbol{\sigma} \cdot \mathbf{n} \quad (3.9)$$

with the Cauchy stress tensor $\boldsymbol{\sigma}$. This stress tensor is independent of the orientation of the cross-section and is defined as

$$\boldsymbol{\sigma} = \mathbf{t} \otimes \mathbf{n} = \begin{bmatrix} \sigma_{11} & \sigma_{12} & \sigma_{13} \\ \sigma_{21} & \sigma_{22} & \sigma_{23} \\ \sigma_{31} & \sigma_{32} & \sigma_{33} \end{bmatrix} \mathbf{e}_i \otimes \mathbf{e}_j. \quad (3.10)$$

The Cauchy stress tensor represents the stresses associated to the current configuration. Since the simulations in this doctoral thesis are restricted to small deformations, further stress quantities are not described.

3.3 Balance of mass

The balance of mass states that the mass of a considered body is constant and the amount of the material entering and leaving the system has to be the same. In the framework of this work we consider closed systems and the conservation of mass implies that mass can not be created or destroyed, such that the mass change over time is equal to zero as

$$m = \int_{\mathcal{B}} \rho \, dv \quad \text{with} \quad m = \text{const.} \quad \text{and} \quad \dot{m} = \frac{d}{dt} \int_{\mathcal{B}} \rho \, dv \quad \text{with} \quad \dot{m} = 0. \quad (3.11)$$

With the material time derivative, the volume mapping $dv = JdV$ and the time derivative of the Jacobi-determinant with $\dot{J} = J \text{div} \dot{\mathbf{x}}$ we obtain

$$\dot{m} = \int_{\mathcal{B}} \dot{\rho} + \rho \text{div} \dot{\mathbf{x}} \, dv. \quad (3.12)$$

Since the balance law is also valid for each individual part of the considered body we formulate the local form of the balance of mass as

$$\dot{\rho} + \rho \operatorname{div} \dot{\mathbf{x}} = 0 \quad (3.13)$$

with the velocity $\dot{\mathbf{x}} = \partial_t \mathbf{x}$ of a material point at the position \mathbf{x} .

3.4 Balance of linear momentum

The balance of linear momentum postulates that the change over time of the linear momentum \mathbf{I} of a system is equal to the external forces \mathbf{k} acting on the considered body with the statement

$$\dot{\mathbf{I}} = \mathbf{k} \quad \text{with} \quad \mathbf{I} = \int_{\mathcal{B}} \rho \dot{\mathbf{x}} \, dv \quad \text{and} \quad \dot{\mathbf{I}} = \int_{\mathcal{B}} \rho \ddot{\mathbf{x}} \, dv \quad (3.14)$$

using the local form of the balance of mass (3.13). The external forces include the body forces $\int_{\mathcal{B}} \mathbf{f} \, dv$ acting on the entire body as well as traction forces $\int_{\partial \mathcal{B}} \mathbf{t} \, da$ operating on the boundary of the body with

$$\mathbf{k} = \int_{\mathcal{B}} \mathbf{f} \, dv + \int_{\partial \mathcal{B}} \mathbf{t} \, da . \quad (3.15)$$

With Cauchy's theorem and the divergence theorem the balance of linear momentum is given as

$$\int_{\mathcal{B}} \rho \ddot{\mathbf{x}} \, dv = \int_{\mathcal{B}} \mathbf{f} \, dv + \int_{\mathcal{B}} \operatorname{div} \boldsymbol{\sigma} \, dv \quad (3.16)$$

with the following local form of the balance of linear momentum

$$\operatorname{div} \boldsymbol{\sigma} + \mathbf{f} - \rho \ddot{\mathbf{x}} = \mathbf{0} . \quad (3.17)$$

3.5 Balance of angular momentum

The balance of angular momentum states that the time derivative of the angular momentum \mathbf{H}_0 , with respect to the fixed point of origin (0), of a body is equal to the moment \mathbf{M}_0 resulting from all external forces acting on the body, with $\dot{\mathbf{H}}_0 = \mathbf{M}_0$. The angular momentum of the body and the moment resulting from external forces are defined as

$$\mathbf{H}_0 = \int_{\mathcal{B}} \rho \mathbf{x} \times \dot{\mathbf{x}} \, dv \quad \text{and} \quad \mathbf{M}_0 = \int_{\mathcal{B}} \mathbf{x} \times \mathbf{f} \, dv + \int_{\partial \mathcal{B}} \mathbf{x} \times \mathbf{t} \, da . \quad (3.18)$$

The time derivative of the angular momentum $\dot{\mathbf{H}}_0$ with $\rho \dot{\mathbf{x}} \times \dot{\mathbf{x}} = \mathbf{0}$ yields

$$\dot{\mathbf{H}}_0 = \int_{\mathcal{B}} \rho \mathbf{x} \times \ddot{\mathbf{x}} \, dv \quad (3.19)$$

resulting in the following expression of the balance of angular momentum as

$$\int_{\mathcal{B}} \rho \mathbf{x} \times \ddot{\mathbf{x}} \, dv = \int_{\mathcal{B}} \mathbf{x} \times \mathbf{f} \, dv + \int_{\partial \mathcal{B}} \mathbf{x} \times \mathbf{t} \, da . \quad (3.20)$$

With the Cauchy theorem $\mathbf{t} = \boldsymbol{\sigma} \cdot \mathbf{n}$ and the divergence theorem $\int_{\partial\mathcal{B}} \mathbf{x} \times \boldsymbol{\sigma} \cdot \mathbf{n} \, da = \int_{\mathcal{B}} \mathbf{x} \times \operatorname{div} \boldsymbol{\sigma} + \mathcal{E} : \boldsymbol{\sigma}^T \, dv$ we obtain the representation

$$\int_{\mathcal{B}} \mathbf{x} \times \operatorname{div} \boldsymbol{\sigma} - \mathbf{x} \times \rho \ddot{\mathbf{x}} + \mathbf{x} \times \mathbf{f}_0 \, dv + \int_{\mathcal{B}} \mathcal{E} : \boldsymbol{\sigma}^T \, dv = \mathbf{0} \quad (3.21)$$

with the third-order permutation tensor \mathcal{E} . Taking into account the balance of linear momentum $\operatorname{div} \boldsymbol{\sigma} - \rho \ddot{\mathbf{x}} + \mathbf{f}_0 = \mathbf{0}$ we obtain the following expressions

$$\int_{\mathcal{B}} \mathcal{E} \times \boldsymbol{\sigma}^T \, dv = \mathbf{0} \quad \text{with} \quad \boldsymbol{\sigma} = \boldsymbol{\sigma}^T. \quad (3.22)$$

The latter part is a result of the determination with the permutation tensor.

3.6 First law of thermodynamics (Balance of energy)

The first law of thermodynamics, also denoted as the balance of energy, states that the change of the total energy of a considered system is equal to the energy which enters and leaves the system.

$$\dot{\mathcal{U}} + \dot{\mathcal{K}} = \mathcal{W}_{mech} + \mathcal{W}_{magn} + \mathcal{W}_{elec} + \mathcal{Q}. \quad (3.23)$$

Thereby, the total energy can be decomposed into the internal energy \mathcal{U} , depending on the specific internal energy $\hat{\mathcal{U}}$, and the kinetic energy \mathcal{K} , which are defined as

$$\mathcal{U} = \int_{\mathcal{B}} \rho \hat{\mathcal{U}} \, dv \quad \text{and} \quad \mathcal{K} = \frac{1}{2} \int_{\mathcal{B}} \rho \dot{\mathbf{x}} \cdot \dot{\mathbf{x}} \, dv. \quad (3.24)$$

With the use of the balance of mass (3.13), the balance of linear momentum (3.17) as well as the relations $\int_{\mathcal{B}} \operatorname{div} \boldsymbol{\sigma} \cdot \dot{\mathbf{x}} \, dv = \int_{\partial\mathcal{B}} \mathbf{t} \cdot \dot{\mathbf{x}} \, da - \int_{\mathcal{B}} \boldsymbol{\sigma} : \nabla \dot{\mathbf{x}} \, dv$ and $\boldsymbol{\sigma} : \nabla \dot{\mathbf{x}} = \boldsymbol{\sigma} : \dot{\boldsymbol{\varepsilon}}$ we obtain the rates of change of the internal and kinetic energies as

$$\dot{\mathcal{U}} = \int_{\mathcal{B}} \rho \dot{\hat{\mathcal{U}}} \, dv \quad \text{and} \quad \dot{\mathcal{K}} = \int_{\mathcal{B}} \mathbf{f} \cdot \dot{\mathbf{x}} \, dv + \int_{\partial\mathcal{B}} \mathbf{t} \cdot \dot{\mathbf{x}} \, da - \int_{\mathcal{B}} \boldsymbol{\sigma} : \dot{\boldsymbol{\varepsilon}} \, dv. \quad (3.25)$$

The energies which enter or leave the system can be mechanical, thermal, magnetic, electric, chemical, or other forms of energy. In this contribution we restrict ourselves to mechanical \mathcal{W}_{mech} , magnetic \mathcal{W}_{magn} , electric \mathcal{W}_{elec} and thermal \mathcal{Q} rates of change of energies, given by the expressions

$$\begin{aligned} \mathcal{W}_{mech} &= \int_{\mathcal{B}} \mathbf{f} \cdot \dot{\mathbf{x}} \, dv + \int_{\partial\mathcal{B}} \mathbf{t} \cdot \dot{\mathbf{x}} \, da, & \mathcal{W}_{magn} &= \int_{\mathcal{B}} \dot{\mathbf{B}} \cdot \mathbf{H} \, dv, \\ \mathcal{W}_{elec} &= \int_{\mathcal{B}} \dot{\mathbf{D}} \cdot \mathbf{E} \, dv & \text{and} & \quad \mathcal{Q} = \int_{\mathcal{B}} \rho \hat{r} \, dv - \int_{\partial\mathcal{B}} \mathbf{q} \cdot \mathbf{n} \, da, \end{aligned} \quad (3.26)$$

where \hat{r} is the internal heat source and \mathbf{q} the heat flux vector. With the rates of the internal and kinetic energies we obtain the balance of energy as follows

$$\int_{\mathcal{B}} \rho \dot{\hat{\mathcal{U}}} \, dv - \int_{\mathcal{B}} \boldsymbol{\sigma} : \dot{\boldsymbol{\varepsilon}} \, dv = \int_{\mathcal{B}} \dot{\mathbf{B}} \cdot \mathbf{H} \, dv + \int_{\mathcal{B}} \dot{\mathbf{D}} \cdot \mathbf{E} \, dv + \int_{\mathcal{B}} \rho \hat{r} \, dv - \int_{\partial\mathcal{B}} \mathbf{q} \cdot \mathbf{n} \, da, \quad (3.27)$$

where the mechanical energy \mathcal{W}_{mech} vanishes due to the mechanical part in the rate of the kinetic energy $\dot{\mathcal{K}}$. The local form of the balance of energy then results in

$$\rho \dot{\hat{U}} = \boldsymbol{\sigma} : \dot{\boldsymbol{\varepsilon}} + \dot{\mathbf{B}} \cdot \mathbf{H} + \dot{\mathbf{D}} \cdot \mathbf{E} + \rho \hat{r} - \operatorname{div} \mathbf{q} , \quad (3.28)$$

where the divergence theorem is applied to the heat flux vector as $\int_{\mathcal{B}} \operatorname{div} \mathbf{q} \, dv = \int_{\partial \mathcal{B}} \mathbf{q} \cdot \mathbf{n} \, da$.

3.7 Second law of thermodynamics (Entropy inequality)

The German physicist R.J.E. Clausius formulated the second law of thermodynamics, namely that the single outcome of a system change can not be the heat transfer from a colder body to a warmer body. Therefore, an inequality is set up which describes the change of entropy of a system, where the entropy change is equal to zero for lossless reversible conversions of energy and greater zero for irreversible conversions of energy. This means that the entropy in a closed system can not be zero and not decrease. We introduce the entropy \mathcal{S} of a body in terms of the specific entropy $\hat{\eta}$ as

$$\mathcal{S} = \int_{\mathcal{B}} \rho \hat{\eta} \, dv . \quad (3.29)$$

The rate of the entropy change is equal or greater than the contribution from an internal heat source and the heat flux over the boundary of the considered body as

$$\int_{\mathcal{B}} \rho \dot{\hat{\eta}} \, dv \geq \int_{\mathcal{B}} \frac{1}{\vartheta} \rho \hat{r} \, dv - \int_{\partial \mathcal{B}} \frac{1}{\vartheta} \mathbf{q} \cdot \mathbf{n} \, da , \quad (3.30)$$

where ϑ denotes the temperature. With the divergence theorem the heat flux on the surface is transferred to the volume, such that the local form is given as

$$\rho \dot{\hat{\eta}} \geq \frac{1}{\vartheta} \rho \hat{r} - \operatorname{div} \left(\frac{\mathbf{q}}{\vartheta} \right) , \quad (3.31)$$

which is also known as the **Clausius-Duhem-Inequality**. The divergence term of the latter equation is reformulated to

$$\operatorname{div} \left(\frac{\mathbf{q}}{\vartheta} \right) = \frac{1}{\vartheta} \operatorname{div} \mathbf{q} - \mathbf{q} \cdot \frac{1}{\vartheta^2} \operatorname{grad} \theta \quad (3.32)$$

such that we get the following expression of the local form of the entropy inequality as

$$\vartheta \rho \dot{\hat{\eta}} \geq \rho \hat{r} - \operatorname{div} \mathbf{q} + \mathbf{q} \cdot \frac{1}{\vartheta} \operatorname{grad} \theta . \quad (3.33)$$

Together with the local form of the first law of thermodynamics, the restriction to isothermal processes with $\operatorname{grad} \theta = 0$ and the introduction of the volume specific counterparts of the internal energy $U = \rho \hat{U}$, the internal heat source $r = \rho \hat{r}$ and internal entropy $\eta = \rho \hat{\eta}$ the local form of the entropy inequality results in

$$-\dot{U} + \boldsymbol{\sigma} : \dot{\boldsymbol{\varepsilon}} + \mathbf{E} \cdot \dot{\mathbf{D}} + \mathbf{H} \cdot \dot{\mathbf{B}} + \vartheta \dot{\eta} \geq 0 . \quad (3.34)$$

In the following section, some reformulations of the entropy inequality are shown in order to obtain different thermodynamic potentials for the description of magneto-electro-mechanically coupled systems.

3.8 Thermodynamic potentials

In the following section, an overview of thermodynamic potentials will be given. Such potentials can be derived with the help of *Legendre transformations* of the internal energy and can be used to derive thermodynamic descriptions of thermo-magneto-electro-mechanically coupled systems. Here, the magneto-electric enthalpy function is derived as an example. For the transformation to the different potentials we generally start with the definition of the internal energy U , which depends on the extensive variables. Extensive variables are defined as quantities which depend on the size of the considered system and change if the size of the system is modified. Such variables are for instance, the volume V , the mass m , the strain $\boldsymbol{\varepsilon}$, or the entropy η . In contrast to that, intensive variables are independent on the size of the system and do not change if the system is modified. Examples for intensive variables are the temperature ϑ or the density ρ . In the case of thermo-magneto-electro-mechanical systems the internal energy is given as a function of the strain $\boldsymbol{\varepsilon}$, the dielectric displacement \mathbf{D} , the magnetic induction \mathbf{B} , and the entropy η as $U := U(\boldsymbol{\varepsilon}, \mathbf{D}, \mathbf{B}, \eta)$ with the rate of the internal energy as

$$\dot{U} = \frac{\partial U}{\partial \boldsymbol{\varepsilon}} : \dot{\boldsymbol{\varepsilon}} + \frac{\partial U}{\partial \mathbf{D}} \cdot \dot{\mathbf{D}} + \frac{\partial U}{\partial \mathbf{B}} \cdot \dot{\mathbf{B}} + \frac{\partial U}{\partial \eta} \dot{\eta}. \quad (3.35)$$

The latter equation is inserted into the entropy inequality (3.34) as

$$-\frac{\partial U}{\partial \boldsymbol{\varepsilon}} : \dot{\boldsymbol{\varepsilon}} - \frac{\partial U}{\partial \mathbf{D}} \cdot \dot{\mathbf{D}} - \frac{\partial U}{\partial \mathbf{B}} \cdot \dot{\mathbf{B}} - \frac{\partial U}{\partial \eta} \dot{\eta} + \boldsymbol{\sigma} : \dot{\boldsymbol{\varepsilon}} + \mathbf{E} \cdot \dot{\mathbf{D}} + \mathbf{H} \cdot \dot{\mathbf{B}} + \vartheta \dot{\eta} \geq 0 \quad (3.36)$$

and can be reformulated to

$$\left(\boldsymbol{\sigma} - \frac{\partial U}{\partial \boldsymbol{\varepsilon}} \right) : \dot{\boldsymbol{\varepsilon}} + \left(\mathbf{E} - \frac{\partial U}{\partial \mathbf{D}} \right) \cdot \dot{\mathbf{D}} + \left(\mathbf{H} - \frac{\partial U}{\partial \mathbf{B}} \right) \cdot \dot{\mathbf{B}} + \left(\vartheta - \frac{\partial U}{\partial \eta} \right) \dot{\eta} \geq 0. \quad (3.37)$$

The stress, the electric field, the magnetic field, and the temperature can be identified as the partial derivative of the internal energy as

$$\boldsymbol{\sigma} = \frac{\partial U}{\partial \boldsymbol{\varepsilon}}, \quad \mathbf{E} = \frac{\partial U}{\partial \mathbf{D}}, \quad \mathbf{H} = \frac{\partial U}{\partial \mathbf{B}}, \quad \text{and} \quad \vartheta = \frac{\partial U}{\partial \eta}. \quad (3.38)$$

resulting in the following expression of the rate of the internal energy as

$$\dot{U} = \boldsymbol{\sigma} : \dot{\boldsymbol{\varepsilon}} + \mathbf{E} \cdot \dot{\mathbf{D}} + \mathbf{H} \cdot \dot{\mathbf{B}} + \vartheta \dot{\eta}. \quad (3.39)$$

However, for the modeling of magneto-electro-mechanics we use a thermodynamic potential depending on the strains $\boldsymbol{\varepsilon}$, the electric field \mathbf{E} and the magnetic field \mathbf{H} and apply a displacement field \mathbf{u} , an electric potential ϕ , and a magnetic potential φ . In order to reformulate the equation (3.39) we apply a *Legendre transformation* with $\mathbf{E} \cdot \dot{\mathbf{D}} = \overline{\mathbf{E} \cdot \dot{\mathbf{D}}} - \mathbf{D} \cdot \dot{\mathbf{E}}$ and $\mathbf{H} \cdot \dot{\mathbf{B}} = \overline{\mathbf{H} \cdot \dot{\mathbf{B}}} - \mathbf{B} \cdot \dot{\mathbf{H}}$ and obtain the following expression

$$\dot{U} = \boldsymbol{\sigma} : \dot{\boldsymbol{\varepsilon}} + \overline{\mathbf{E} \cdot \dot{\mathbf{D}}} - \mathbf{D} \cdot \dot{\mathbf{E}} + \overline{\mathbf{H} \cdot \dot{\mathbf{B}}} - \mathbf{B} \cdot \dot{\mathbf{H}} + \vartheta \dot{\eta}. \quad (3.40)$$

With the help of the next conversion into

$$\overline{\mathbf{E} \cdot \dot{\mathbf{D}}} - \mathbf{H} \cdot \dot{\mathbf{B}} = \boldsymbol{\sigma} : \dot{\boldsymbol{\varepsilon}} - \mathbf{D} \cdot \dot{\mathbf{E}} - \mathbf{B} \cdot \dot{\mathbf{H}} + \vartheta \dot{\eta} \quad (3.41)$$

we can identify the magneto-electric enthalpy function $H_4 = U - \mathbf{E} \cdot \mathbf{D} - \mathbf{H} \cdot \mathbf{B}$ depending on the process variables $\boldsymbol{\varepsilon}$, \mathbf{E} , \mathbf{H} , and η . The determination of the rate of the magneto-electric enthalpy function with respect to the process variables yields

$$\dot{H}_4 = \boldsymbol{\sigma} : \dot{\boldsymbol{\varepsilon}} - \mathbf{D} \cdot \dot{\mathbf{E}} - \mathbf{B} \cdot \dot{\mathbf{H}} + \vartheta \dot{\eta} \quad (3.42)$$

with the partial derivatives

$$\boldsymbol{\sigma} = \frac{\partial H_4}{\partial \boldsymbol{\varepsilon}}, \quad \mathbf{D} = -\frac{\partial H_4}{\partial \mathbf{E}}, \quad \mathbf{B} = -\frac{\partial H_4}{\partial \mathbf{H}}, \quad \text{and} \quad \vartheta = \frac{\partial H_4}{\partial \eta}. \quad (3.43)$$

Further thermodynamic potentials can be derived analogously and the following Table 3.1 gives an overview of some possible potentials, see also LINES AND GLASS [126], LUPASCU ET AL. [127].

Thermodynamic potential	Natural variables	Rate equation of potential
Internal energy U	$\boldsymbol{\varepsilon}, \mathbf{D}, \mathbf{B}, \eta$	$\dot{U} = \boldsymbol{\sigma} : \dot{\boldsymbol{\varepsilon}} + \mathbf{E} \cdot \dot{\mathbf{D}} + \mathbf{H} \cdot \dot{\mathbf{B}} + \vartheta \dot{\eta}$
Free energy $\psi = U - \vartheta \eta$	$\boldsymbol{\varepsilon}, \mathbf{D}, \mathbf{B}, \vartheta$	$\dot{\psi} = \boldsymbol{\sigma} : \dot{\boldsymbol{\varepsilon}} + \mathbf{E} \cdot \dot{\mathbf{D}} + \mathbf{H} \cdot \dot{\mathbf{B}} - \eta \dot{\vartheta}$
Enthalpy $H = U - \boldsymbol{\sigma} : \boldsymbol{\varepsilon} - \mathbf{E} \cdot \mathbf{D} - \mathbf{H} \cdot \mathbf{B}$	$\boldsymbol{\sigma}, \mathbf{E}, \mathbf{H}, \eta$	$\dot{H} = -\boldsymbol{\varepsilon} : \dot{\boldsymbol{\sigma}} - \mathbf{D} \cdot \dot{\mathbf{E}} - \mathbf{B} \cdot \dot{\mathbf{H}} + \vartheta \dot{\eta}$
Elastic enthalpy $H_1 = U - \boldsymbol{\sigma} : \boldsymbol{\varepsilon}$	$\boldsymbol{\sigma}, \mathbf{D}, \mathbf{B}, \eta$	$\dot{H}_1 = -\boldsymbol{\varepsilon} : \dot{\boldsymbol{\sigma}} + \mathbf{E} \cdot \dot{\mathbf{D}} + \mathbf{H} \cdot \dot{\mathbf{B}} + \vartheta \dot{\eta}$
Electric enthalpy $H_2 = U - \mathbf{E} \cdot \mathbf{D}$	$\boldsymbol{\varepsilon}, \mathbf{E}, \mathbf{B}, \eta$	$\dot{H}_2 = \boldsymbol{\sigma} : \dot{\boldsymbol{\varepsilon}} - \mathbf{D} \cdot \dot{\mathbf{E}} + \mathbf{H} \cdot \dot{\mathbf{B}} + \vartheta \dot{\eta}$
Magnetic enthalpy $H_3 = U - \mathbf{H} \cdot \mathbf{B}$	$\boldsymbol{\varepsilon}, \mathbf{D}, \mathbf{H}, \eta$	$\dot{H}_3 = \boldsymbol{\sigma} : \dot{\boldsymbol{\varepsilon}} + \mathbf{E} \cdot \dot{\mathbf{D}} - \mathbf{B} \cdot \dot{\mathbf{H}} + \vartheta \dot{\eta}$
Magneto-electric enthalpy $H_4 = U - \mathbf{E} \cdot \mathbf{D} - \mathbf{H} \cdot \mathbf{B}$	$\boldsymbol{\varepsilon}, \mathbf{E}, \mathbf{H}, \eta$	$\dot{H}_4 = \boldsymbol{\sigma} : \dot{\boldsymbol{\varepsilon}} - \mathbf{D} \cdot \dot{\mathbf{E}} - \mathbf{B} \cdot \dot{\mathbf{H}} + \vartheta \dot{\eta}$
Gibbs energy $G = U - \boldsymbol{\sigma} : \boldsymbol{\varepsilon} - \mathbf{E} \cdot \mathbf{D} - \mathbf{H} \cdot \mathbf{B} - \eta \vartheta$	$\boldsymbol{\sigma}, \mathbf{E}, \mathbf{H}, \vartheta$	$\dot{G} = -\boldsymbol{\varepsilon} : \dot{\boldsymbol{\sigma}} - \mathbf{D} \cdot \dot{\mathbf{E}} - \mathbf{B} \cdot \dot{\mathbf{H}} - \eta \dot{\vartheta}$
Elastic Gibbs energy $G_1 = U - \boldsymbol{\sigma} : \boldsymbol{\varepsilon} - \eta \vartheta$	$\boldsymbol{\sigma}, \mathbf{D}, \mathbf{B}, \vartheta$	$\dot{G}_1 = -\boldsymbol{\varepsilon} : \dot{\boldsymbol{\sigma}} + \mathbf{E} \cdot \dot{\mathbf{D}} + \mathbf{H} \cdot \dot{\mathbf{B}} - \eta \dot{\vartheta}$
Electric Gibbs energy $G_2 = U - \mathbf{E} \cdot \mathbf{D} - \eta \vartheta$	$\boldsymbol{\varepsilon}, \mathbf{E}, \mathbf{B}, \vartheta$	$\dot{G}_2 = \boldsymbol{\sigma} : \dot{\boldsymbol{\varepsilon}} - \mathbf{D} \cdot \dot{\mathbf{E}} + \mathbf{H} \cdot \dot{\mathbf{B}} - \eta \dot{\vartheta}$
Magnetic Gibbs energy $G_3 = U - \mathbf{H} \cdot \mathbf{B} - \eta \vartheta$	$\boldsymbol{\varepsilon}, \mathbf{D}, \mathbf{H}, \vartheta$	$\dot{G}_3 = \boldsymbol{\sigma} : \dot{\boldsymbol{\varepsilon}} + \mathbf{E} \cdot \dot{\mathbf{D}} - \mathbf{B} \cdot \dot{\mathbf{H}} - \eta \dot{\vartheta}$
Magneto-electric Gibbs energy $G_4 = U - \mathbf{E} \cdot \mathbf{D} - \mathbf{H} \cdot \mathbf{B} - \eta \vartheta$	$\boldsymbol{\varepsilon}, \mathbf{E}, \mathbf{H}, \vartheta$	$\dot{G}_4 = \boldsymbol{\sigma} : \dot{\boldsymbol{\varepsilon}} - \mathbf{D} \cdot \dot{\mathbf{E}} - \mathbf{B} \cdot \dot{\mathbf{H}} - \eta \dot{\vartheta}$

Table 3.1: Thermodynamic potentials.

3.9 Representation of anisotropic materials with isotropic tensor functions

In order to describe the material behavior in the framework of continuum mechanics, tensor functions of different orders are used. Such tensor functions should represent the anisotropic material response of magneto-mechanically and electro-mechanically coupled solids. However, the description of the material behavior must satisfy the principle of material symmetry, which states that the constitutive response must be independent of transformations $\mathbf{Q} \in \mathcal{G}_k$, with the symmetry group \mathcal{G}_k . If the material is independent of any transformations \mathbf{Q} , where \mathcal{G}_k is the special orthogonal group $SO(3)$, the material is called isotropic. An isotropic tensor function $\hat{\psi}$ depending on the strains is formulated as

$$\hat{\psi}(\boldsymbol{\varepsilon}) = \hat{\psi}(\mathbf{Q}\boldsymbol{\varepsilon}\mathbf{Q}^T) \quad \forall \quad \mathbf{Q} \in SO(3) . \quad (3.44)$$

The thermodynamic functions can then be described with isotropic tensor functions. For a general representation of isotropic functions we consider a scalar-valued function $\hat{f}(\mathbf{v}_i, \mathbf{V}_j)$, a vector-valued function $\hat{\mathbf{f}}(\mathbf{v}_i, \mathbf{V}_j)$, and a tensor-valued function $\hat{\mathbf{F}}(\mathbf{v}_i, \mathbf{V}_j)$, depending on the vector-valued arguments \mathbf{v}_i and the tensor-valued arguments \mathbf{V}_j . Based on the transformations of the special orthogonal group $SO(3)$, the isotropic tensor functions are defined as

$$\left. \begin{aligned} \hat{f}(\mathbf{v}_i, \mathbf{V}_j) &= \hat{f}(\mathbf{Q}\mathbf{v}_i, \mathbf{Q}\mathbf{V}_j\mathbf{Q}^T) \\ \mathbf{Q}\hat{\mathbf{f}}(\mathbf{v}_i, \mathbf{V}_j) &= \hat{\mathbf{f}}(\mathbf{Q}\mathbf{v}_i, \mathbf{Q}\mathbf{V}_j\mathbf{Q}^T) \\ \mathbf{Q}\hat{\mathbf{F}}(\mathbf{v}_i, \mathbf{V}_j)\mathbf{Q}^T &= \hat{\mathbf{F}}(\mathbf{Q}\mathbf{v}_i, \mathbf{Q}\mathbf{V}_j\mathbf{Q}^T) \end{aligned} \right\} \quad \forall \quad \mathbf{Q} \in SO(3) . \quad (3.45)$$

As mentioned above, electro- and magneto-mechanically coupled solids are often characterized by an anisotropic behavior. Therefore, isotropic tensor functions which describe an anisotropic material behavior are considered in the following.

Anisotropic materials are characterized by a direction-dependent behavior, which means that an arbitrary rotation of the neighborhood of a material point leads to a different material response for the same unrotated loading. These anisotropies are based on the preferred directions \mathbf{a}_i of the material. With the help of these vectors the so-called structural tensors $\mathbf{m}_i = \hat{\mathbf{m}}_i(\mathbf{a}_i)$ can be determined. An anisotropic free energy function $\hat{\psi}(\boldsymbol{\varepsilon}, \mathbf{a}_i, \mathbf{m}_j)$ in a coordinate invariant setting has to satisfy

$$\hat{\psi}(\boldsymbol{\varepsilon}) = \hat{\psi}(\mathbf{Q}\boldsymbol{\varepsilon}\mathbf{Q}^T, \mathbf{a}_i, \mathbf{m}_j) \quad \forall \quad \mathbf{Q} \in \mathcal{G}_k , \quad (3.46)$$

where the tensor functions are extended by the preferred directions \mathbf{a}_i and the structural tensors \mathbf{m}_i . The used structural vectors and tensors have to fulfill the requirements of the symmetry group $SO(3)$, such that we obtain the following general representation of anisotropic tensor functions as

$$\left. \begin{aligned} \hat{f}(\mathbf{v}_i, \mathbf{V}_j, \mathbf{a}_i, \mathbf{m}_j) &= \hat{f}(\mathbf{Q}\mathbf{v}_i, \mathbf{Q}\mathbf{V}_j\mathbf{Q}^T, \mathbf{Q}\mathbf{a}_i, \mathbf{Q}\mathbf{m}_j\mathbf{Q}^T) \\ \mathbf{Q}\hat{\mathbf{f}}(\mathbf{v}_i, \mathbf{V}_j, \mathbf{a}_i, \mathbf{m}_j) &= \hat{\mathbf{f}}(\mathbf{Q}\mathbf{v}_i, \mathbf{Q}\mathbf{V}_j\mathbf{Q}^T, \mathbf{Q}\mathbf{a}_i, \mathbf{Q}\mathbf{m}_j\mathbf{Q}^T) \\ \mathbf{Q}\hat{\mathbf{F}}(\mathbf{v}_i, \mathbf{V}_j, \mathbf{a}_i, \mathbf{m}_j)\mathbf{Q}^T &= \hat{\mathbf{F}}(\mathbf{Q}\mathbf{v}_i, \mathbf{Q}\mathbf{V}_j\mathbf{Q}^T, \mathbf{Q}\mathbf{a}_i, \mathbf{Q}\mathbf{m}_j\mathbf{Q}^T) \end{aligned} \right\} \quad \forall \quad SO(3) . \quad (3.47)$$

An illustration of this concept is given in Figure 3.1.

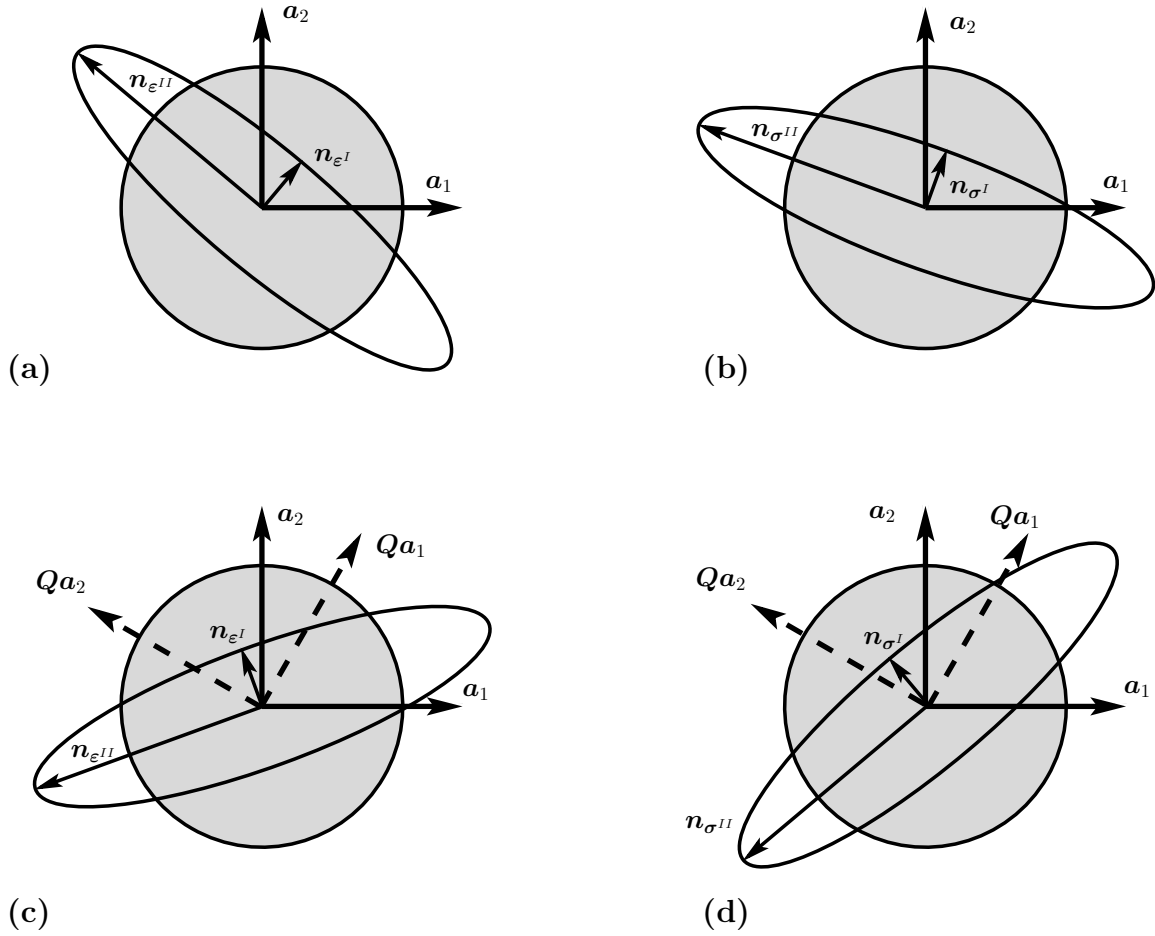


Figure 3.1: Illustration of the concept of isotropic tensor functions for anisotropic materials. The initial state of the body is depicted with a circle. (a) Principle directions of the deformation for a given mechanical loading. (b) Due to the material anisotropy the principle directions of the stresses do not coincide with the directions of the deformation. (c) Main directions of the deformations and (d) stresses after the application of a transformation $Q \in SO(3)$. Adopted from KEIP [93].

The unloaded reference state of the body is depicted with a circle, whereas the deformed state with the corresponding main deformation directions n_{ϵ^I} and $n_{\epsilon^{II}}$ is illustrated with an ellipsoid in Figure 3.1(a). Due to the anisotropy the main directions of the stress response n_{σ^I} and $n_{\sigma^{II}}$ display different orientations, see Figure 3.1(b). For any transformations $Q \in SO(3)$, the preferred directions undergo these transformations as well, resulting in the corresponding correct deformation and stress response, shown in Figure 3.1(c) and 3.1(d).

The isotropic tensor functions used for the description of the material behavior can be represented by a defined number of scalar-valued invariants. For an introduction to the invariant theory in the framework of continuum mechanics see for instance the works of BOEHLER [22], SMITH [193; 194], SPENCER [198], TRUESDELL AND NOLL [209], WINE-MAN AND PIPKIN [220], or SCHRÖDER [183]. An invariant formulation for transversely isotropic electro-mechanically coupled functions, which is applied to the electrical phase in this thesis, is derived in SCHRÖDER AND GROSS [184].

4 Ferroic materials

For the strain-induced generation of magneto-electric product properties in composite materials different ferroic characteristics for each phase of the composite are needed. Therefore, we first have to introduce the term ferroic and therefore provide a definition based on the work of AIZU [3]. It states that, a crystal has ferroic properties when two or more stable orientation (tensor) states are possible without the application of an electric field, a magnetic field, or mechanical stresses on the body. This intrinsic ordering typically arises at a temperature dependent phase transition of the material. Four different ferroic properties are known, which are the **ferroelasticity**, **ferroelectricity**, **ferromagnetism** and **ferrotoroidicity**. Ferroelastic properties are characterized by a spontaneous strain in one or more directions. The orientation can be changed by an applied mechanical stress, such that the spontaneous strain rotates into another direction and remains after removing the mechanical stress. Locally this transformation is typically discontinuous because crystal physics prescribes a few axes of anisotropy in the material. In ferroelectric materials, the crystal is characterized by a spontaneous, remanent electric polarization. Often this is due to a displacement of positively and negatively charged ions. The polarization direction can be changed by an applied electric field in another direction. Analogously, ferromagnetic materials show a spontaneous remanent magnetization in a specific direction (or more complex forms of ordering), which can be reoriented by an applied magnetic field. The fourth ferroic state is the ferrotoroidicity, which can be characterized by a vortex of microscopic magnetic moments, which continue over multiple crystals. Some materials exhibit more than one ferroic characteristics and are then called **higher-order ferroics** or **multiferroics**. Barium titanate is an example of a higher-order ferroic material since it shows ferroelectric and ferroelastic properties. In the framework of this doctoral thesis the materials barium titanate and cobalt ferrite are investigated in more detail. Some ferroic properties are explained with the help of the crystal structure of barium titanate in Section 4.2.

4.1 Introduction to magnetic materials

In this section the basic principles of the origin of magnetism and the arising different types of magnetism and the magnetostrictive effect are explained. For a detailed overview in the literature see for example CHIKAZUMI [30], ERINGEN AND MAUGIN [43], FABRIZIO AND MORRO [49], HUBERT AND SCHÄFER [76], IDA AND BASTOS [80], J.D.JACKSON [84], JILES [85], LEHNER [122], MAUGIN [133], TIPLER [207].

4.1.1 Origin of magnetism

In order to explain the effect of magnetostriction and the following argumentation why the magneto-electric effect is so rare in natural materials, a closer look has to be taken at the atomic orbital structures. Therefore, a very brief introduction to some aspects in the quantum mechanical theory is given. The German physicist Werner Heitler and the American-German physicist Fritz Wolfgang London described the interaction of atoms based on new aspects in the theory of quantum mechanics, see HEITLER AND LONDON [64]. However, the development of the orbital model is based on the some important scientific discoveries including for example the physical insights of the Austrian physicist

Erwin Schrödinger, the French physicist Louis-Victor de Broglie or the German physicist Werner Karl Heisenberg. In 1923 Louis De Broglie postulated that any moving particle can be described by its *phase wave*, see BROGLIE [26], with the definition of the wave frequency ν as

$$\nu = (m c^2) / \left(\hbar \sqrt{1 - \frac{v^2}{c^2}} \right) , \quad (4.1)$$

where m denotes the mass of the considered particle, c the speed of light, v the velocity of the particle and \hbar the Planck constant. The latter one, \hbar , relates the energy of a particle with the frequency of the wave and has the value of $\hbar = 6.62606957 \cdot 10^{-34}$ Js. Considering a macroscopic body from our daily life, with a relatively small velocity compared to the speed of light, then the wavelength $\lambda = v/\nu$ of this body is approximately zero and therefore not measurable. In contrast, the velocity of an electron is relatively high compared to a macroscopic body. The same applies for the small mass of the electron, such that the wavelength of an electron can be determined. As a result, fast moving particles can be described in terms of wave properties. This conjunction between particle and wave characteristics is called *wave-particle duality*. The double-slit experiment is capable of showing the wave properties of light or even electrons. In 1801, the English physicist Thomas Young performed the double-slit experiment in the following way. A beam of light is sent through an aperture with two slits next to each other. Due to the bending of the light waves around the corners of the slits, which is denoted as diffraction, the light spreads out in the three dimensional space behind the aperture. The light waves behind the two slits superimpose and arrive at an observation screen. Because of the superposition of the waves an interference pattern on the screen is observable. A simplified depiction of the experimental setup is given in Figure 4.1.

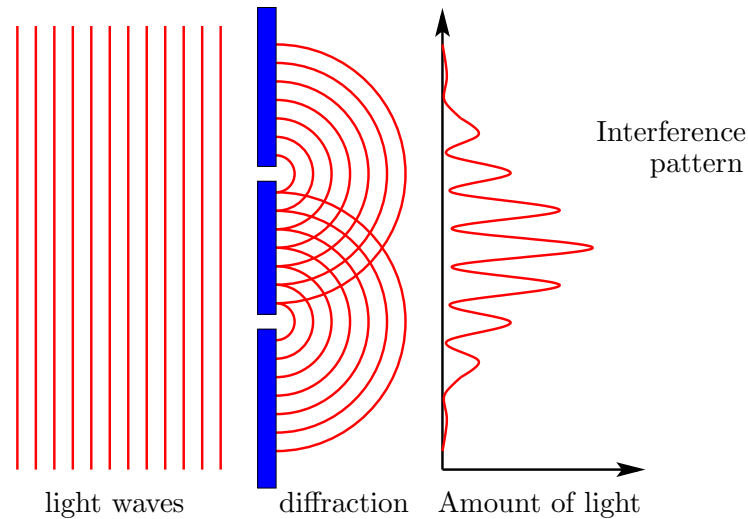


Figure 4.1: Illustration of the double slit experiment. The diffraction of the light waves, after passing the aperture with two slits, result in a superposition of the bended waves. Such superposition is shown on an observation screen, where an interference pattern of the arrived light waves is visible.

In 1927, the double slit experiment was performed again by the American physicists Clinton Davisson and Lester Germer, see DAVISSON AND GERMER [35], this time investigating electrons instead of light. If the electrons were particles without wave properties

no interference pattern would have been observed and a roughly regular distribution of the number of electrons should have passed through both slits. However, in the case of electrons the screen again showed an interference pattern, which demonstrated the wave properties of matter. With the help of the double-slit experiment, it was shown that an electron is neither a particle with a specific shape or its motion be described by a wave. Due to the wave-particle duality an electron and its condition can be described by wave functions. Because of this spatial extension it is not possible to clearly determine the position and momentum of the particle at the same time. If the momentum, and therefore the velocity, is known, then the exact position is unknown and vice versa in the same spatial direction. This relation is called the **Heisenberg's uncertainty principle**, see HEISENBERG [63]. Here, the difference between quantum physics and classical physics becomes clear, since a quantum state describes a probability distribution for a quantum mechanically measured parameter. In order to describe now the quantum mechanical properties of an elementary particle, for example an electron, the **Schrödinger equation** is taken into account. Erwin Schrödinger published the derivation of this equation in 1926, see SCHRÖDINGER [189]. One solution of this equation is a complex-valued wave function describing a quantum state. With the help of such wave functions the probabilities for possible results can be determined. In other words, the most probable positions of the electrons around the atomic nucleus can be computed. All possible positions with probabilities over 90% build areas which are called **orbitals**. Depending on the number of protons and neutrons of the nucleus and therefore on the number and energy states of the electrons, an atom can consist of several orbitals. In order to define the complete states of the electrons in the atoms four quantum numbers are used. The *principle quantum number* (n) describes the main energy level of the electron and therefore in which orbital it is present. The *azimuthal quantum number* (l) defines the shape of the orbital. A further characteristic of the electron, which is interesting in the framework of this thesis, is described by the *magnetic quantum number* (m_l). It denotes the spatial orientation of the orbital angular momentum, which generates a magnetic moment. Additionally to the orbital angular momentum, the electron also produces a magnetic moment due to its spin, which is described with the *spin quantum number* (m_s). The spin of the electron can have two different states, clockwise and counter-clockwise, and therefore only two values for the spin quantum number are possible for the electron. The magnetic moment of an electron produced by its orbital angular momentum and spin depends on the *spin-orbit coupling*. However, due to the Pauli principle two electrons in one atom can not occupy the same energy state given by the same four quantum numbers. This physical law is the *Pauli exclusion principle* formulated by the Austrian physicist Wolfgang Ernst Pauli in 1925. Hence, if two electrons are characterized by the same first three quantum numbers (n, l, m_l) only two electrons can be located in the same orbital, which must be different in the spin quantum number. This results in two different magnetic states of an atomic orbital. First, if the orbital is partially occupied with one electron, then a magnetic moment results due to its spin and spin-orbit coupling. In the second magnetic state, the orbital is completely filled with two electrons. In this case the magnetic moments cancel each other due to the opposite spin direction and no magnetization remains. It can be seen that the requirements for a resulting magnetization are the spin-orbit coupling of the electrons as well as **partially occupied orbitals**. However, the magnetic moments of the individual electrons are not sufficient to produce a macroscopically measurable magnetization, they have to interact with each other. The energy which causes the interactions

of the electrons in one atom and between the neighboring atoms is called the **quantum mechanical exchange energy**. Since a minimization of the total energy is the referred state, the exchange energy only dominates, if orbitals with specific energy levels are partially filled, namely the d- and f-orbitals. If this is the case, the magnetic moments in the different orbitals align in the same direction. This yields a domain structure, which is the basis for an overall magnetization. The direction of the alignment is influenced by the exchange energy between the neighboring orbitals. A minimization of these interacting energies produces a preferred magnetization direction in the crystal, the **easy magnetization direction**. Depending on the crystallographic properties of different magnetic materials, for instance in ferromagnets, which are discussed in more detail in the following section, the easy magnetization direction can also vary among them.

4.1.2 Different types of magnetism

After the analysis of origin of magnetism, a closer look is taken at the different types of magnetic ordering. The magnetic moments generated by the electrons in the partially filled orbitals can interact in various ways. It can be distinguished between **diamagnetism**, **paramagnetism**, **ferromagnetism**, **antiferromagnetism**, and **ferrimagnetism**. The effect of diamagnetism is also visible in materials with filled orbitals. Figure 4.2 shows simplifications of the arrangement of multiple magnetic moments due to their interaction with each other.

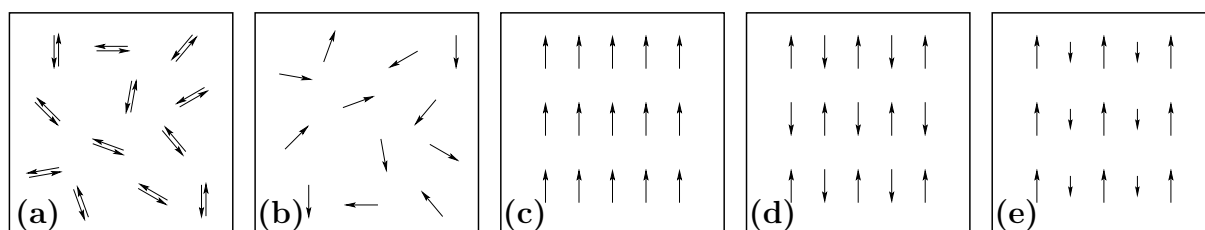


Figure 4.2: Simplified depiction of the arrangement of the microscopic magnetic moments in (a) diamagnetism, (b) paramagnetism, (c) ferromagnetism, (d) antiferromagnetism, and (e) ferrimagnetism.

In the following subsections the reason for these orientation distributions are explained in more detail.

Diamagnetism. Basically, diamagnetism is present in every material. However, since this effect is much smaller than the other magnetic effects, diamagnetism becomes visible in materials which are not paramagnetic, ferromagnetic, ferrimagnetic or antiferromagnetic. The main characteristic of diamagnetic materials is the negative magnetic susceptibility, which only appears in completely occupied orbitals, see JÄGER AND PERTHEL [83]. In these orbitals, the magnetic moments of the two electrons compensate each other resulting in no remaining magnetization, see Figure 4.2(a). If a magnetic field is applied, the generated magnetic field inside the material points in opposite direction to the applied field and the material is repelled. The resulting opposed magnetic field can be explained by the second Maxwell equation $\text{curl}\mathbf{E} = -\partial\mathbf{B}/\partial t$, also called Faraday's law of induction, and the resulting Lenz's law, which is shown by the negative sign in the latter equation. Then, an applied magnetic induction changing over time produces *electric currents* in the material. In diamagnetism, such *electric currents* are specific electron movements in-

side the atomic orbitals. Then, the electron movement generates a magnetic moment in opposite direction to the applied field. As mentioned before, this field is very small and only becomes visible if no other dominant magnetic effects are present. Perfect diamagnetic properties are obtained through superconductivity. Then, the generated magnetic field has the same field strength as the applied field and no remaining magnetic field is visible. However, under superconducting properties only a magnetic field strength which is a multiple of the magnetic fluxon can flow through the material. The generated electric current also depends on multiples of the magnetic fluxon, such that very small changes in the magnetic field can be measured. These properties are used through superconducting quantum interference devices (SQUIDS), for example in the magnetoencephalography.

Paramagnetism. The disorganized orientation distribution of the magnetic moments in the paramagnetic phase appears at high temperatures. In this framework, high temperatures means temperatures above the material specific Curie temperature T_C , also called Néel temperature for antiferromagnetic materials, which is for example $T_C = 790\text{K}$ for cobalt ferrite. Above T_C , the thermal energy inside the material is higher than the quantum mechanical exchange energy. The magnetic moments produced by the electron spins are not aligned in the same direction, resulting in a disordered and random orientation distribution, see Figure 4.2(b). In this case no remanent macroscopic magnetization can be measured and even domain structures are not visible. However, the magnetic moments can be aligned by an applied external magnetic field on the body, such that an overall magnetization can be observed. Once the applied magnetic field is removed, a demagnetization of the material takes place and no remanent magnetization is obtained. The dependency between the applied magnetic field and the magnetization is linear.

Ferromagnetism. Ferromagnetic materials are in the paramagnetic phase at temperatures above the Curie temperature and show a random orientation distribution of the magnetic moments as explained before.

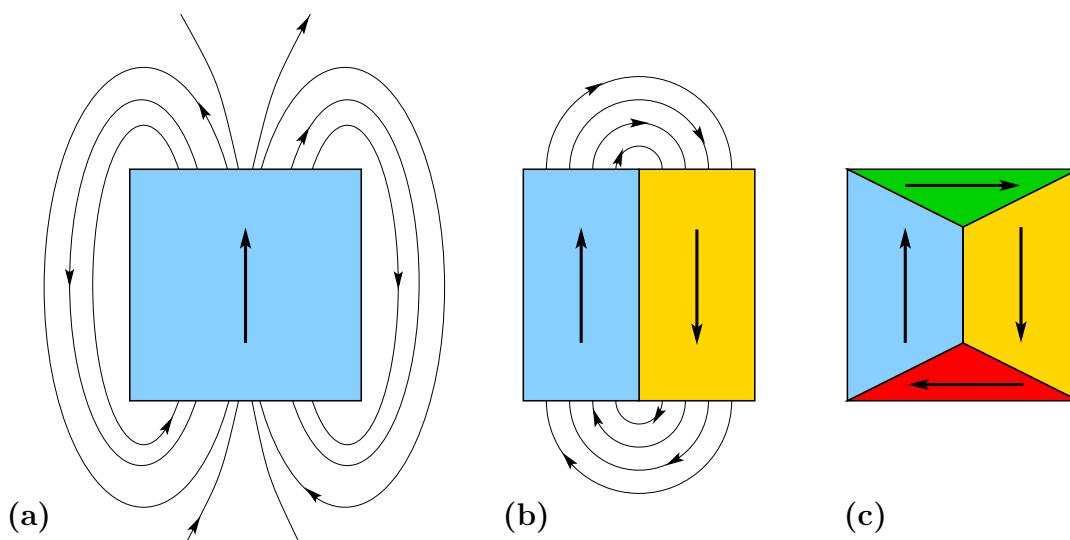


Figure 4.3: Magnetic stray fields of different magnetic bodies. (a) In the case of a magnetized body reaching the saturation magnetization, the stray field energy is maximized. (b) Reduced stray field energy due to domain wall formation. The different magnetic domains are highlighted in different colors. (c) Minimized stray field energy due to complex domain structure.

When the temperature decreases below the Curie temperature, the quantum mechanical exchange energy between the magnetic moments of the electrons is higher than the thermal energy. This results in a parallel alignment of the spontaneous magnetizations and in a lower energy state compared to a disorganized distribution, see Figure 4.2(c). However, the exchange energy rapidly (exponentially) decreases for an increasing distance between the atoms and is only effective for the nearest neighbors. This magnetic alignment continues over multiple atoms and is interrupted for example at crystallographic defects. At such points, other easy magnetization directions can be energetically preferable, resulting in a change in the magnetization direction and therefore in the development of magnetic domains, which are visually observable with the help of a Kerr microscope. Magnetic domains, also denoted as **Weiss domains**, can have widths of several μm . Another reason for the development of domains is the magnetic stray field energy. A magnetic stray field is created outside the material due to the magnetization of the sample, see Figure 4.3(a). The stray field energy gets maximized with the saturation magnetization of the material and reduces through the formation of domain walls. With a complex domain structure without magnetic fields outside the material, the stray field energy is minimized, see Figure 4.3(c). An interaction between the quantum mechanical exchange energy, the magnetocrystalline anisotropy and the stray field energy yield the energetically most preferable domain structure. From the macroscopic point of view, all domain magnetizations cancel out such that no overall magnetization is measurable. These magnetic domains with different magnetization directions are separated by magnetic domain walls. **Bloch Walls** and **Néel Walls** can be distinguished. In these transition zones, the magnetization continuously varies from one direction to another direction and changes its magnetization direction by 90° or 180° or even more complex scenarios. Figure 4.4 depicts possible 180° transitions in a Bloch wall and a Néel wall.

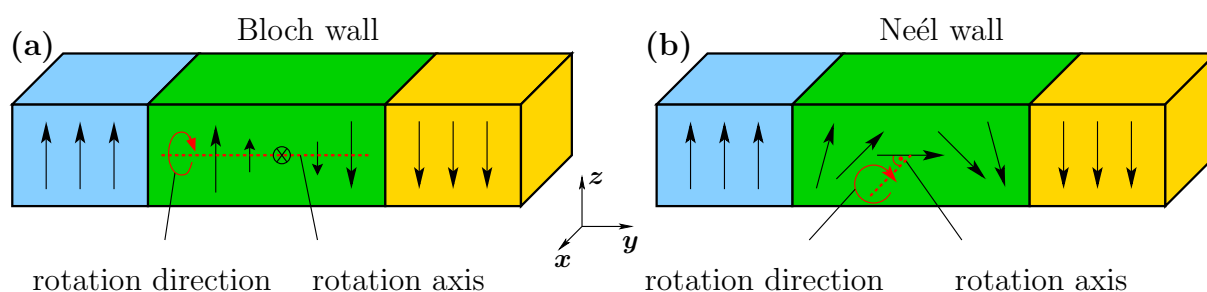


Figure 4.4: (a) Rotation of the magnetization direction by 180° in a Bloch wall (green). The rotation proceeds around an axis parallel to the y-axis of coordinates. (b) Magnetization rotation in a Néel wall (green), where the rotation axis is parallel to the x-axis of coordinates. The domains at the left and right, with opposite magnetization directions, are highlighted in blue and yellow.

In the domains on the left hand side, the magnetic moments point in positive vertical direction and switch their orientations into negative vertical directions in the domain on the right hand side. The difference between both domain wall types is the rotation direction of the magnetic moments. In Bloch walls, the rotation proceeds in the plane of the domain wall.

In contrast, the magnetization in Néel walls rotates around an axis perpendicular to the domain surface. Domain walls can move and increase or decrease the size of the domains by changing the orientation of the magnetic moments. As a consequence, an increasing

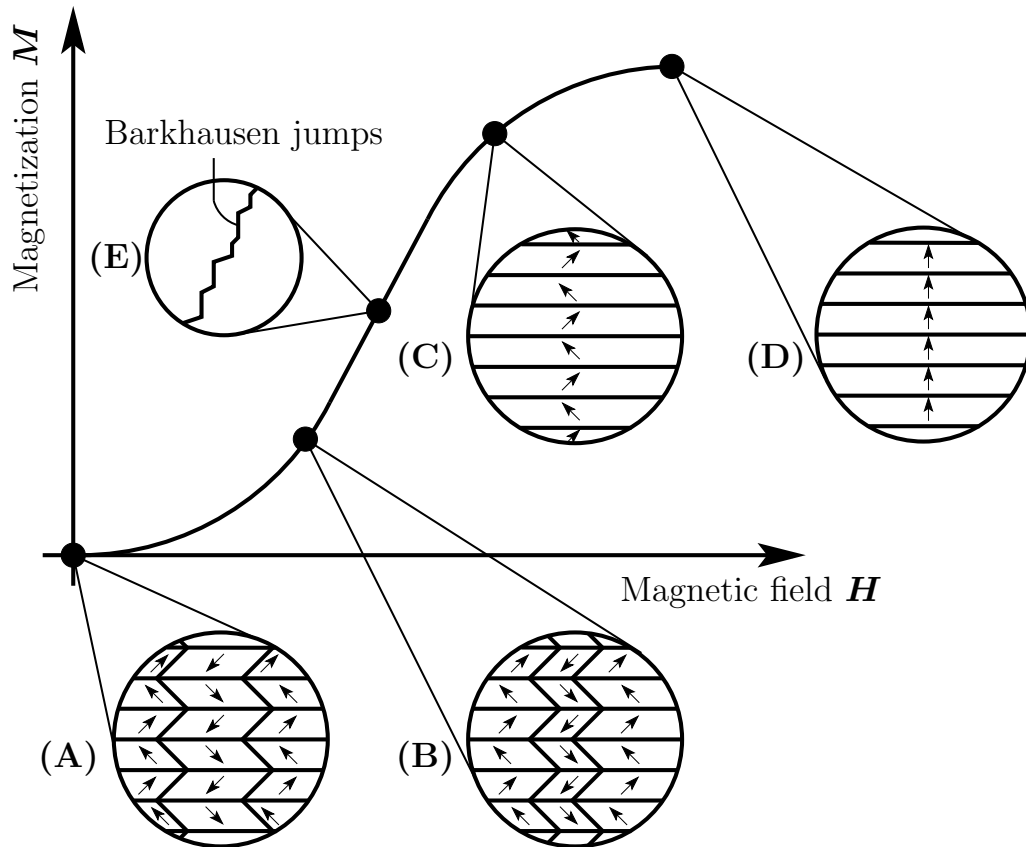


Figure 4.5: Magnetization curve due to domain wall movements and Barkhausen jumps. (A) Magnetic domain structure with 90° and 180° domain walls. (B) Domain wall movement due to an applied magnetic field. (C) All domain wall movements are completed and the magnetizations of the domains point roughly in the direction of the applied field. (D) The magnetic moments rotate into the direction of the applied field and the saturation magnetization is reached. (E) Illustration of Barkhausen jumps (vertical lines), due to crystallographic defects and collective jumps of multiple domain walls. The increase of the magnetization between the Barkhausen jumps is triggered by domain wall movements.

magnetic field generates an overall magnetization. An alternating magnetic field then yields the typical magnetization hysteresis loop. A change of the overall magnetization has the following three main reasons:

- **Domain wall movements:** An increasing applied magnetic field causes a change of the magnetic moments in the transition zones, the so called domain walls. Here, the required energy for a rotation of the individual magnetic moments inside the domain walls is lower than the energy which is necessary to rotate all the aligned magnetic moments inside a domain. A movement of the domain walls is observable. Thereby, the domains, whose magnetization orientations point roughly in the direction of the applied magnetic field, grow, whereas the other domains shrink. Such domain wall motions are mostly irreversible processes.
- **Barkhausen jumps:** Domain wall movements do not always proceed very smoothly, but are hindered by crystallographic defects in the lattice structure. Therefore, higher magnetic fields are necessary to displace the domain walls, resulting in small jumps of the magnetization change. These discontinuously irreversible

changes of the magnetization are called Barkhausen jumps, see the cascaded increase in Figure 4.5.

- **Rotation of overall magnetization:** The final increase of the overall magnetization is a reversible process and requires the highest energy from the applied field. After the domain wall movements are completed including the Barkhausen jumps, the domain magnetizations are not necessarily aligned in the exact direction of the applied field and can still show deviations between the directions, since the crystallographically easy magnetization direction only points roughly in the applied field direction. For high magnetic fields, whose strength depends on the material properties, a pure rotation of the domain magnetizations from the easy direction to the applied field direction is obtained until the saturation magnetization is reached. This final rotation to the saturation state requires a comparably large magnetic field to overcome the magnetic anisotropy and its magnitude depends on the crystallographic easy direction.

Once the magnetic field decreases, the magnetization rotates back to the crystallographic easy direction. A further decrease of the applied field to zero involves on the one hand side domain wall movements to an energetically preferable position, which does not necessarily have to be the initial position, and on the other hand side very few Barkhausen jumps due to crystallographic defects. Depending on the magnetic material, a high or low remanent magnetization can be observed. By applying a magnetic field in the opposite direction the domain wall movements and Barkhausen jumps decrease the magnetization until the overall magnetization vanishes. The necessary magnetic field to demagnetize the material is called the **coercivity field** H_c and depends on the material properties. It can be distinguished between soft and hard ferromagnetic materials. In soft ferromagnetic materials, the coercivity field is comparatively low $H_c \approx 1 \text{ kA/m}$ resulting in a narrow hysteresis loop, whereas in hard ferromagnetic materials a high coercivity field $H_c \approx 10 \text{ kA/m}$ as well as a wide hysteresis curve are observable. Therefore, soft magnetic materials are for example used in alternating current (AC) applications such as transformers or motors. Hard magnetic materials are used in storage devices, where a high magnetic coercivity field is preferable. If the applied magnetic field is further decreased, the magnetization saturates in the opposite direction. For alternating fields, the magnetization proceeds on the hysteresis loops.

Antiferromagnetism. In antiferromagnetic materials the exchange energy causes an antiparallel alignment of the magnetic moments in contrast to a parallel alignment. An illustration of the antiferromagnetism is given in Figure 4.2(d). The antiparallel magnetizations neutralize each other such that no remanent macroscopic magnetization is measurable. An applied magnetic field changes this state, since the magnetic moments rotate into the direction of the external field. However, if the field is removed, the magnetic moments return to their original position.

Ferrimagnetism. Similar to antiferromagnetism the exchange energy yields an antiparallel orientation of the magnetic moments. However, as shown in Figure 4.2(e), they do not neutralize each other completely since the magnetic moments of the one direction are slightly larger than the magnetic moments in the opposite direction. As a consequence, a macroscopic magnetization is measurable. The crystal system used in this thesis

is characterized by an inverse spinel structure, where 1/3 of the FE-ions (Fe^{2+}) occupy tetrahedral sites and 2/3 of the Fe-ions (1/3 Fe^{3+} and 1/3 Fe^{2+}) occupy octahedral sites. The magnetic moments of the Fe^{3+} ions point in opposite directions and compensate each other. The net magnetization is only generated by the alignment of the magnetic moments in the Fe^{2+} -ions. Figure 4.6 illustrates the spin arrangement of the ferrimagnetic material magnetite (Fe_3O_4), see BAYREUTHER [15].

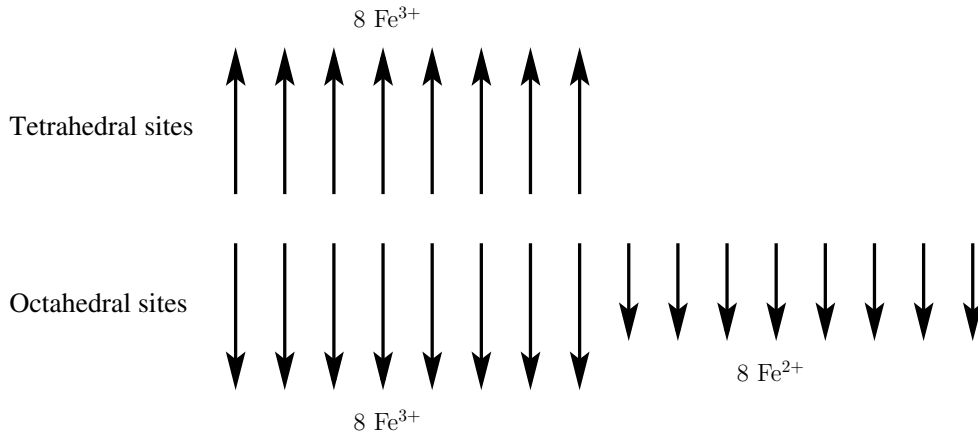


Figure 4.6: Spin arrangement of the ferrimagnetic material magnetite (Fe_3O_4), see BAYREUTHER [15]. The crystal consists of tetrahedral and octahedral sites occupied with Fe-ions. The net magnetization results from the magnetic moments of the Fe^{2+} -ions.

A further example of a ferrimagnetic material is cobalt ferrite (CoFe_2O_4), which is considered in the present contribution in more detail.

4.1.3 Magnetostrictive effect

The origin of the magnetostrictive effect is the spontaneous deformation of each crystal towards the easy magnetization direction, which can be a contraction, the so-called negative magnetostriction, or an elongation, the positive magnetostriction. The material performs a deformation due to the rotations of the crystallographic magnetization directions, which continue over the whole domain due to domain wall motions. The superposition of all domain deformations yield a macroscopically measurable magnetostriction with the magnitude of about $\epsilon \approx 10^{-6}$ to $\epsilon \approx 10^{-5}$, see CHIKAZUMI [30]. After all domain wall motions, the magnetization rotates from the crystallographic easy direction to the direction of the applied field, such that the saturation magnetostriction is reached. In this case, the rotation of the magnetization direction again causes a change in the crystallographic lattice, resulting in magnetostriction. The piezomagnetic effect is a simplified linear approximation of the real nonlinear magnetostrictive behavior.

4.2 The ferroelectric effect

An electric polarization can be obtained by positive and negative charge carriers with a small distance between them. The special characteristic in ferroelectric materials is a polarization of the crystal structure without the application of an applied electric field. These crystal polarizations are called remanent or spontaneous polarizations and are generated due to a displacement of positively and negatively charged ions. In order to explain

the ferroelectric effect in more detail we take a look at the material properties of barium titanate. This material undergoes several phase transitions for different temperature ranges, starting with a hexagonal phase for high temperatures above $T > \approx 1460^\circ\text{C}$. In this state, the material is paraelectric and no remanent electric polarization is present in the unit cell. In contrast to paramagnetic properties, where the magnetic moments of the electrons point in arbitrary directions due to the thermal energy, an electric polarization in the individual unit cells is not present in the paraelectric state, since a displacement between positively and negatively charged ions does not exist or cancels out dynamically. Below this temperature ($T < \approx 1460^\circ\text{C}$) the crystal changes to the cubic lattice, still with paraelectric properties. A visualization of this unit cell is given in Figure 4.7(a).

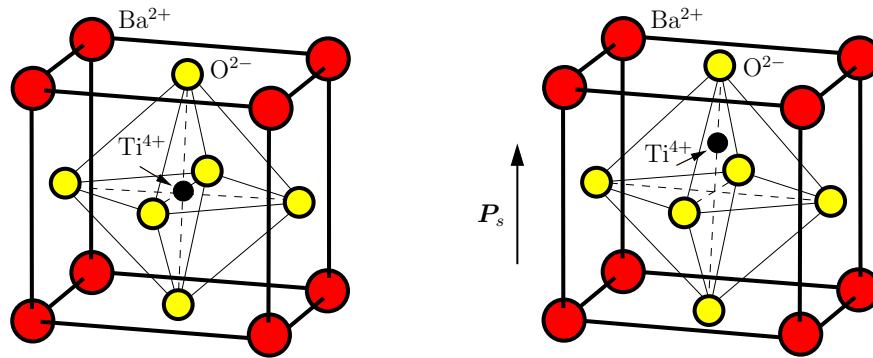


Figure 4.7: Barium titanate unit cell, (a) above the Curie temperature $> T_c = 120^\circ\text{C}$ and (b) below the Curie temperature, adopted from KEIP [93].

It can be seen that the center of the positively (red, black) and negatively (yellow) charged ions is located at the same position, such that no remanent electric polarization is created, see Figure 4.7(a) for an illustration of the cubic lattice. If the material cools down below the Curie temperature of $T_c = 120^\circ\text{C}$ the unit cell changes to a tetragonal structure, see Figure 4.7(b). In this state, the titanate ion is shifted in one direction of the three crystal axes, with the result that the centers of the positively and negatively charged ions do not coincide any longer and a remanent polarization P_s is present. Additionally, the unit cell shows a spontaneous strain ε_s along the direction of the polarization. In this state, the unit cells show the highest amount of spontaneous polarization, which is preferable for technical applications. Below $T \approx 0^\circ\text{C}$, a phase transition to the orthorhombic state takes place and a further transition to the trigonal phase below $T \approx -90^\circ\text{C}$. In both states, the unit cell is characterized by a spontaneous electric polarization, but with lower values of the polarization compared to the tetragonal phase. However, in order to obtain a macroscopic polarization the unit cells have to align in similar direction. Similar to ferromagnetic materials, ferroelectric materials build domain structures on the microscopic level when the material is cooled under the materials specific Curie temperature T_c . In such domains, the spontaneous polarizations of the unit cells point into the same direction. The domains next to each other are separated by domain walls, where the polarization direction can switch their orientation by 90° or 180° in the case of barium titanate, see the domain constellation at (A) in Figure 4.8. In some other ferroelectric materials, different angles between the domain polarizations can be possible. On the mesoscopic level, different grains are observable, where each grain includes several domains. However, the interaction energy between the unit cells, which build the domains and result in domain walls, do not proceed over different grains. In Figure 4.8, the different grains are highlighted with different colors

and the angle between the polarization directions of two domains in neighboring grains at the grain boundary is arbitrary. Due to the different polarization directions of the domains no macroscopic polarization of the body is observable, see point (A) in Figure 4.8. If an increasing macroscopic electric field is applied on the body, the unit cells begin to switch into the direction of the applied field. During this process, the unit cells begin to reorient and the domain walls move.

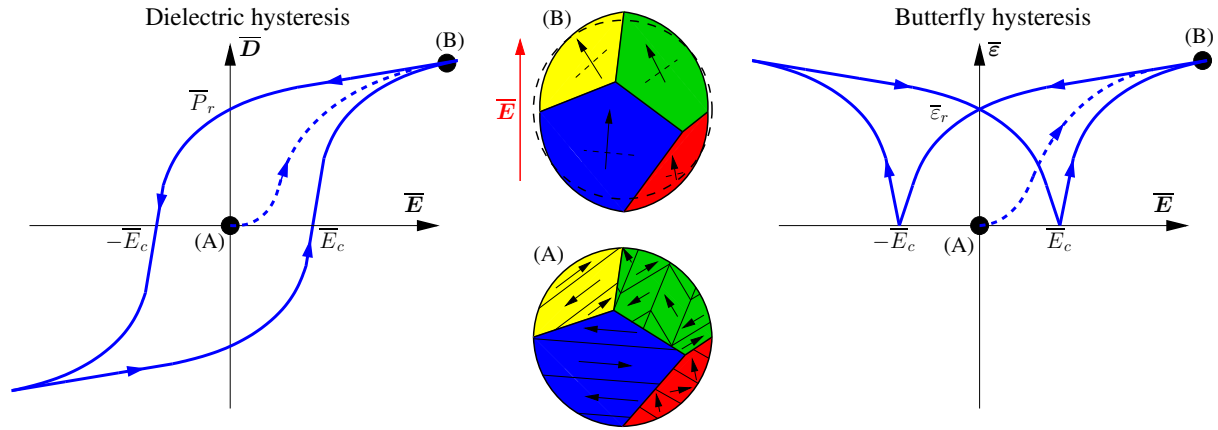


Figure 4.8: Dielectric and butterfly hysteresis curves of barium titanate. The initial domain structure at point (A) shows a random distribution of the domain polarizations. After the application of an electric field, the spontaneous polarizations perform 90° and 180° switchings into the field direction, resulting in an overall polarization and deformation. Adopted from KEIP [93].

The domains with a polarization direction close to the applied field direction increase in size, until the saturation polarization is reached, see point (B) in Figure 4.8. At this state, all domain movements are completed and the linear increase of the dielectric displacement is only triggered by the stretch of the unit cells, where the positively and negatively charged ions are pulled apart by the electric field. However, even after reaching the saturation polarization not all domains are perfectly aligned with the macroscopic field, since only 90° and 180° switchings are possible, due to the crystallographic structure of the barium titanate unit cells. If the electric field is removed, some unit cells switch back to their original orientation, where the energy level is lower. However, multiple domains remain in their new polarization state, such that the material shows a macroscopic remanent polarization \overline{P}_r . The remanent polarization can be removed by applying an electric field in the opposite direction until the remaining quantities vanish. This electric field is called the coercive field \overline{E}_c . If the field is further increased, the material polarizes in the opposite direction until the saturation state is reached. For an alternating electric field a point symmetric dielectric hysteresis curve with respect to the origin of the coordinate system is obtained, see Figure 4.8.

Since a spontaneous polarization of the unit cell involves a deformation of the same lattice, a change of the overall polarization state is associated with a change of the overall deformation state, resulting in an **electro-mechanical coupling**. An applied electric field induces ferroelectric switching and domain wall movements on the microscopic level as described previously. This leads to a non-linear increase of the overall deformation state until a saturation of the deformation is reached, which coincides with the saturation polarization, see point (b) in the butterfly hysteresis loop in Figure 4.8. The resulting stretch of the unit cells linearly depends on the increasing electric field. Such linear

electro-mechanical coupling is denoted as the **inverse piezoelectric effect**. The **direct piezoelectric effect**, which is described in Section 4.3, marks the linear coupling between an applied pressure and the resulting change in electric polarization. After removing the electric field, an overall remanent strain $\bar{\epsilon}_r$ is observable. An applied electric field in the opposite direction causes a decrease of the deformation until the strains completely vanish at the coercive field strength \bar{E}_c . A further increase of the electric load indeed yields a polarization in the opposite direction but again an elongation of the material. This results in the axisymmetric strain hysteresis loop, also denoted as the butterfly hysteresis loop, for an alternating electric field, see Figure 4.8.

4.3 The ferroelastic effect

The crystals in ferroelastic materials have more than one stable orientation state. In the case of barium titanate, six different preferred polarization directions resulting in three orientation directions are possible, which are characterized by a remanent strain in the respective direction, due to a deformation of the unit cell. The transverse direction typically contracts due to Poisson's number of the elastic unit cell. The direction of remanent strain can be changed due to applied mechanical stresses. However, the preferred ferroelastic directions in barium titanate can only switch by 90° reorientations. The resulting ferroelastic hysteresis curves are depicted in Figure 4.9. At the beginning, an electrically poled material is considered, where the polarization directions of the domains in the individual grains point in the same direction, which is more or less the direction of the applied electric field, see Figure 4.9(a).

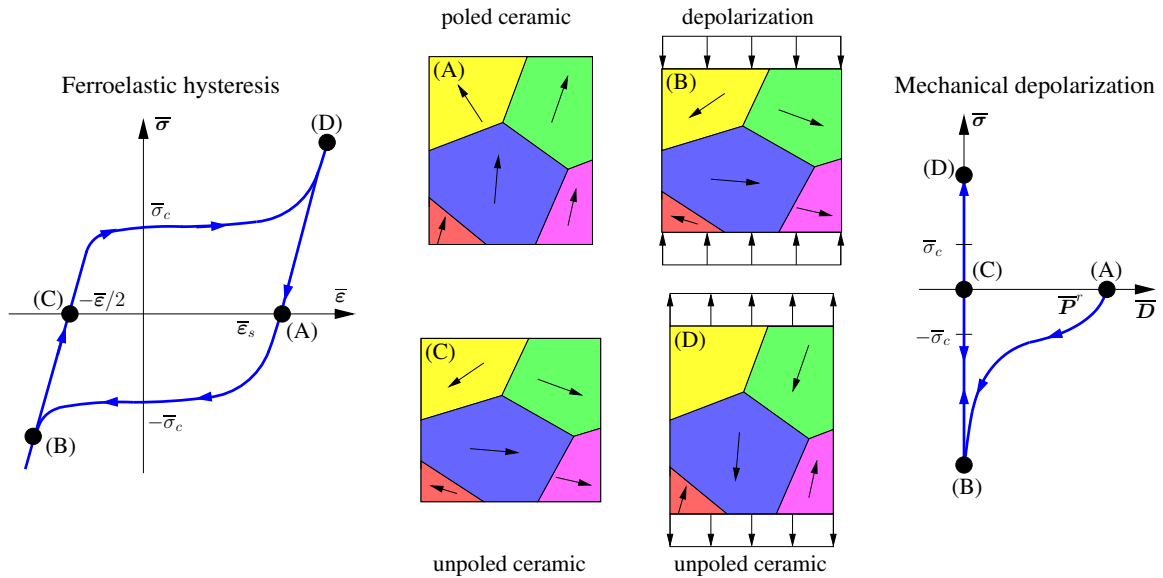


Figure 4.9: Barium titanate unit cell, (a) above the Curie temperature $> T_c$ and (b) below the Curie temperature. Adopted from KEIP [93].

If a mechanical pressure is applied on the specimen, the orientations perform 90° switchings and point into one of four possible directions vertical to the applied pressure. Due to the crystal structure of barium titanate, six preferred directions are possible, since the Ti-ion can displace in one of the six spatial directions. For the ferroelastic switching the four orientations perpendicular to the original direction are possible. The orientation in

opposite direction can be excluded, since the resulting remanent deformation is the same in the opposed preferred orientations. Due to the slightly different deviations between the grain polarizations and the applied pressure, different mechanical forces are necessary for the switching process, resulting in a nonlinear ferroelastic hysteresis curve, see Figure 4.9(e). The strains of the material with respect to the applied pressure are plotted in Figure 4.9(e). After removing the mechanical pressure the unit cells remain in their new orientation state and a remanent compression of the material is obtained, see the illustration in Figure 4.9(c). In the framework of small deformations, the magnitude of the contraction of the specimen is half the value of the elongation. If then a mechanical traction force in the same vertical direction is applied on the body, the unit cells perform 90° switching into the direction of the vertical axis. As a consequence, the material shows an overall elongation in traction direction and a contraction in perpendicular direction. This deformation state essentially remains after removing the applied force only contracting elastically, resulting in a closed hysteresis loop. Additional to the ferroelastic hysteresis, a mechanical depolarization curve is obtained due to the electro-mechanical coupling. In the initial state, the material is polarized in one direction. After applying a mechanical pressure in polarization direction, the domains change their orientations in perpendicular direction to the applied force. However, they switch into the energetically most preferable directions, which are not the same for all domains and are therefore more or less equally distributed in the four possible directions. Thus, the material gets depolarized, see the mechanical depolarization curve in Figure 4.9(f). Even a mechanical traction force can not polarize the material in traction direction. The unit cells switch again more or less uniformly distributed in the up and down orientations with respect to the traction direction. Due to this depolarization no hysteresis loop is obtained and the curve remains at zero polarization.

4.4 The ferrotoroidic effect

A further ferroic property, which was discovered much later than the other ferroic properties, is the ferrotoroidicity, see for example AKEN ET AL. [4], EERENSTEIN ET AL. [40], PAPASIMAKIS ET AL. [156], PLANES ET AL. [157], RABE [161], RESSOUCHE ET AL. [165], SPALDIN ET AL. [197], TOLÉDANO ET AL. [208], VIGNESH ET AL. [211], ZIMMERMANN ET AL. [229]. This property is characterized by a circular (toroidal) arrangement of electric polarizations or magnetizations on the microscopic level.

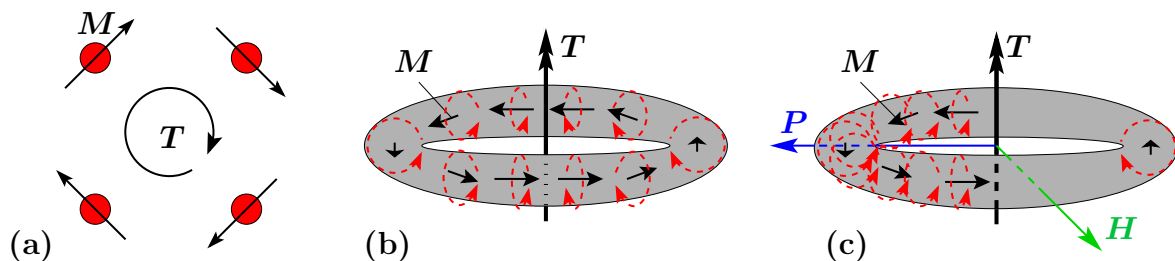


Figure 4.10: (a) Vortex configuration of microscopic magnetizations generating a toroidal moment T . (b) Ring-shaped solenoid where the magnetizations are produced by electric currents. (c) Possible magneto-electric coupling by a shift of the electric currents due to a magnetic field resulting in an electric polarization.

In the case of electric ferrotoroidicity, the polarization vectors are results of different charges organized in a corresponding distribution, whereas the magnetic ferrotoroidicity is characterized by a vortex configuration of magnetic moments, see Figure 4.10(a) for a simplified depiction of possible ferrotoroidic properties. A classical example of a generated toroidal moment is a ring-shaped solenoid with an even number of current windings, see Figure 4.10(b). In this context the reader is referred to the work of AKEN ET AL. [4]. In such structures it is also possible to induce an electric polarization with an applied magnetic field. This magneto-electric coupling is illustrated in Figure 4.10(c), where the current loops are shifted by the magnetic field to one side of the solenoid resulting in a polarization. This characteristic leads to the high interest in toroidic materials, recently. The generated magneto-electric properties due to ferrotoroidicity are not investigated in more detail in this thesis.

4.5 Magneto-electric materials

Magneto-electric (ME) materials are characterized by a coupling of electric and magnetic properties. They change their magnetization due to an applied electric field and show a change of their electric polarization under magnetic loading. The interest to use the magneto-electric coupling phenomena in technical applications goes back to the mid-twentieth century. Since then several materials have been discovered, which exhibit an interaction between electric polarization and magnetization. However, the origin of the discovery of the magneto-electric coupling phenomena goes back to the end of the eighteenth century when the German physicist Wilhelm Conrad Röntgen discovered that a moving dielectric material in an electric field influences a magnetic needle, see RÖNTGEN [171]. Further experiments, for example in the work of WILSON [219] in 1905, showed the existence of the magneto-electric coupling and in the works of DEBYE [36] or DZYALOSHINSKII [39], the authors supposed by theoretical considerations that a magneto-electric coupling should emerge in single-phase materials. However, the magneto-electric coupling is very rare in nature and only present in a minority of natural materials. More often the ME effect appears in synthetic materials, where single-phase and composite materials can be distinguished. In the following two Sections 4.5.1 and 4.5.2 both kinds of ME materials are investigated in more detail. For an overview of the arising ME coupling effect the reader is, for instance referred, to the works of FIEBIG AND SPALDIN [51].

4.5.1 Single-phase magneto-electric materials

In this thesis the term single-phase denotes materials consisting of one single crystal phase. To be precise a single-phase ME material can be further classified into two different groups.

- **Single-phase ME multiferroics:** Multiferroic materials combine two or more ferroic properties, for example ferroelectricity, ferromagnetism and ferroelasticity. However, antiferroic properties are also included in the class of multiferroics, see EERENSTEIN ET AL. [40]. In magneto-electric multiferroics, the electric and magnetic properties are linked and can be influenced by each other. The ME properties can on the one hand be created from the same ions or on the other hand from different ions, which are connected due to the crystal lattice. An example for the first phenomena is given by the material LuFe_2O_4 . Here, the Fe-ions are differently

charged in the lattice layers. Due to the charge deviations of the Fe^{2+} - and Fe^{3+} -ions, a polarization in the material is observed. Additionally, ferrimagnetic properties are caused by the Fe-ions. The second phenomenon is exhibited for example by bismuth ferrite (BiFeO_3). Here, the ferroelectric properties arise in the Bi-ion and the antiferromagnetism in the Fe-ion. However, there are indeed multiferroic materials exhibiting polarizations and magnetizations but do not couple to each other generating a magneto-electric effect. An example is given by barium cobalt fluoride (BaCoF_4).

- **Single-phase ME non-multiferroics:** It is not a requirement for a material to have ferroic or antiferroic characteristics, and thus multiferroic properties, in order to generate a magneto-electric coupling. In addition, the magneto-electric coupling can also occur in materials which have for example paramagnetic properties. An example for a non-multiferroic ME material is given by the paramagnetic ferroelectric $\text{Tb}_2(\text{MoO}_4)_3$, see PONOMAREV ET AL. [158].

Such materials can be found in nature or can be created synthetically. However, only very few natural materials with ME properties are known, which are for instance congolite ($\text{Fe}_2\text{B}_7\text{O}_{13}\text{Cl}$), huebnerite (MnWO_4) or chambersite ($\text{Mn}_3\text{B}_7\text{O}_{13}\text{Cl}$), see Figure 4.11.

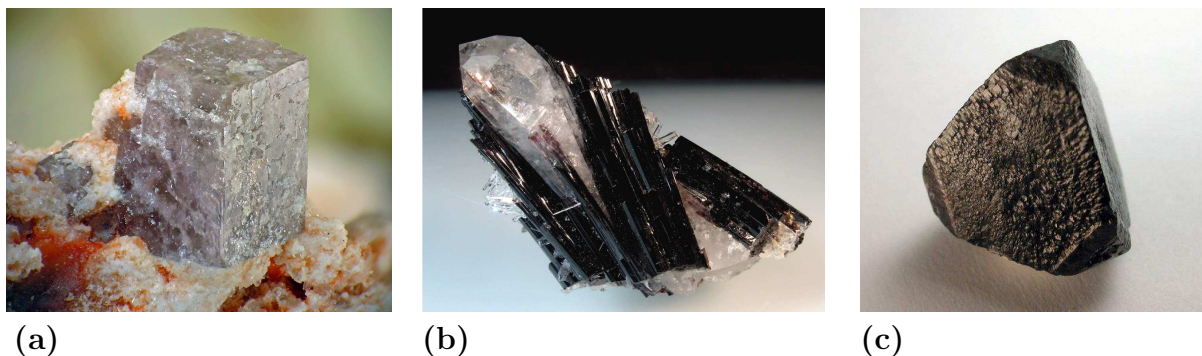


Figure 4.11: Natural magneto-electric single-phase materials: a) congolite ($\text{Fe}_2\text{B}_7\text{O}_{13}\text{Cl}$), b) huebnerite (MnWO_4) and c) chambersite ($\text{Mn}_3\text{B}_7\text{O}_{13}\text{Cl}$), taken from www.mindat.org, www.surreyminerals.com and www.mindat.org, respectively.

They are characterized by a very low ME coefficient appearing at cryogenic temperatures. However, in the work of DZIALOSHINSKII [39] the author explicitly mentioned the material chromium(III)-oxide (Cr_2O_3) as a possible candidate for a material with ME properties. Shortly afterwards, LANDAU AND LIFSHITZ [118] showed that a magneto-electric effect may occur in some antiferromagnetic crystals. These assumptions were proven a few years later with the successful evidences of an ME coupling in Cr_2O_3 , see for example ASTROV [8; 9], RADO AND FOLEN [163] or FOLEN ET AL. [52]. In the following decades, various investigations on Cr_2O_3 were reported and further materials with magneto-electric properties have been observed. Table 4.1 gives an overview of ME-coefficients arising at the given temperatures. More detailed investigations on the ME coupling regarding the lattice structure of the corresponding material are for example given in KIMURA ET AL. [100], LAWES ET AL. [120], YAMASAKI ET AL. [223]. A comprehensive historical overview can be found in FIEBIG [50]. However, due to physical reasons, only very few natural materials with magneto-electric properties exist. A more detailed description of the reasons is given in section 4.5.3, where the work of HILL [65] has to be mentioned explicitly.

Furthermore, the magneto-electric properties in single-phase materials mostly arise far below room temperature, see Table 4.1.

single-phase magneto-electric materials				
Year	Material	ME coef. s/m	Temp.	Reference
1961	Cr ₂ O ₃	$1.43 \cdot 10^{-12}$	293.15 K	ASTROV [9]*, ASTROV [8], RADO AND FOLEN [163], FOLEN ET AL. [52], RIVERA [167], MARTIN AND ANDERSON [131], WIEGELMANN ET AL. [217]
1963	Ti ₂ O ₃	$0.033 \cdot 10^{-12}$	165 K	AL'SHIN AND ASTROV [6]
1964	GaFeO ₃	$1 \cdot 10^{-12}$	77.0 K	RADO [162]
1966	Ni ₃ B ₇ O ₁₃ I	$1.1 \cdot 10^{-12}$	15.0 K	ASCHER ET AL. [7]
1967	Y ₃ Fe ₅ O ₁₂	—	—	O'DELL [154]
1984	TbPO ₄	$36.7 \cdot 10^{-12}$	1.9 K	RADO ET AL. [164]
1989	(YBi) ₃ (FeGa) ₅ O ₁₂	$\approx 33 \cdot 10^{-12}$	294.0 K	KRICHEVTSOV ET AL. [105]
1989	PbFe _{0.5} Nb _{0.5} O ₃	$\approx 0.0038 \cdot 10^{-12}$	≈ 5 K	WATANABE AND KOHN [216]
1994	LiCoPO ₄	$30.6 \cdot 10^{-12}$	4.2 K	RIVERA [167]*, RIVERA [168]
1994	Cr ₃ B ₇ O ₁₃ Cl	$0.05 \cdot 10^{-12}$	4.2 K	YE ET AL. [224]
1997	BiFeO ₃	$0.52 \cdot 10^{-12}$	18.0 K	RIVERA AND SCHMID [169]
1997	Mn ₃ B ₇ O ₁₃ I	$0.095 \cdot 10^{-12}$	4.2 K	CROTTAZ ET AL. [34]
2002	V ₂ O ₃	$0.01 \cdot 10^{-12}$	8.0 K	MATTEO AND JANSEN [132]

Table 4.1: Measured ME coefficients of single-phase materials. Some materials were investigated by different authors and the measured ME-values could slightly differ. The reference which is marked by a star (*) is the corresponding work to the listed ME coefficient.

A promising single-phase material is Cr₂O₃, which also shows an ME coefficient at room temperature. Therefore, many investigations for this material have been made. However, the ME coefficient quickly decreases for slightly higher temperatures and finally vanishes at a Néel temperature of about $T_n = 307$ K, see ASTROV [9].

The overview of the measured ME coefficients of single-phase materials in Table 4.1 shows, that the ME coupling is on the one hand too low for technical applications and on the other hand mostly occurring at cryogenic temperatures in the range of 4 to 18 Kelvin. In order to produce technical devices which show a sufficiently high ME coupling coefficient near room temperature, two phase composites are highly preferable.

4.5.2 Magneto-electric composite materials

The considered magneto-electric composite materials consist of a ferroelectric and a ferromagnetic phase. They generate the magneto-electric coupling as a **strain-induced product property**, see EERENSTEIN ET AL. [40], NAN [150], NAN ET AL. [152], PRIYA ET AL. [160], RYU ET AL. [176], SRINIVASAN [199], WANG ET AL. [215]. VAN SUCHTELEN [210] introduced the term **product property** and denoted it as a property that is not present in the individual constituents itself, but arises effectively in the composite due to the interaction of the single components. In the case of magneto-electric composites, the

direct and converse ME effects can be distinguished

$$\begin{aligned} \text{direct ME effect} &= \frac{\text{magnetic}}{\text{mechanical}} \times \frac{\text{mechanical}}{\text{electrical}} \\ \text{converse ME effect} &= \frac{\text{electrical}}{\text{mechanical}} \times \frac{\text{mechanical}}{\text{magnetic}} \end{aligned} \quad (4.2)$$

see e.g. FIEBIG [50], NAN [150] or MA ET AL. [129]. The direct ME effect denotes a magnetically induced electric polarization. An applied magnetic field yields a deformation of the magnetostrictive phase. This deformation is transferred to the ferroelectric phase responding with a change of its electric polarization.

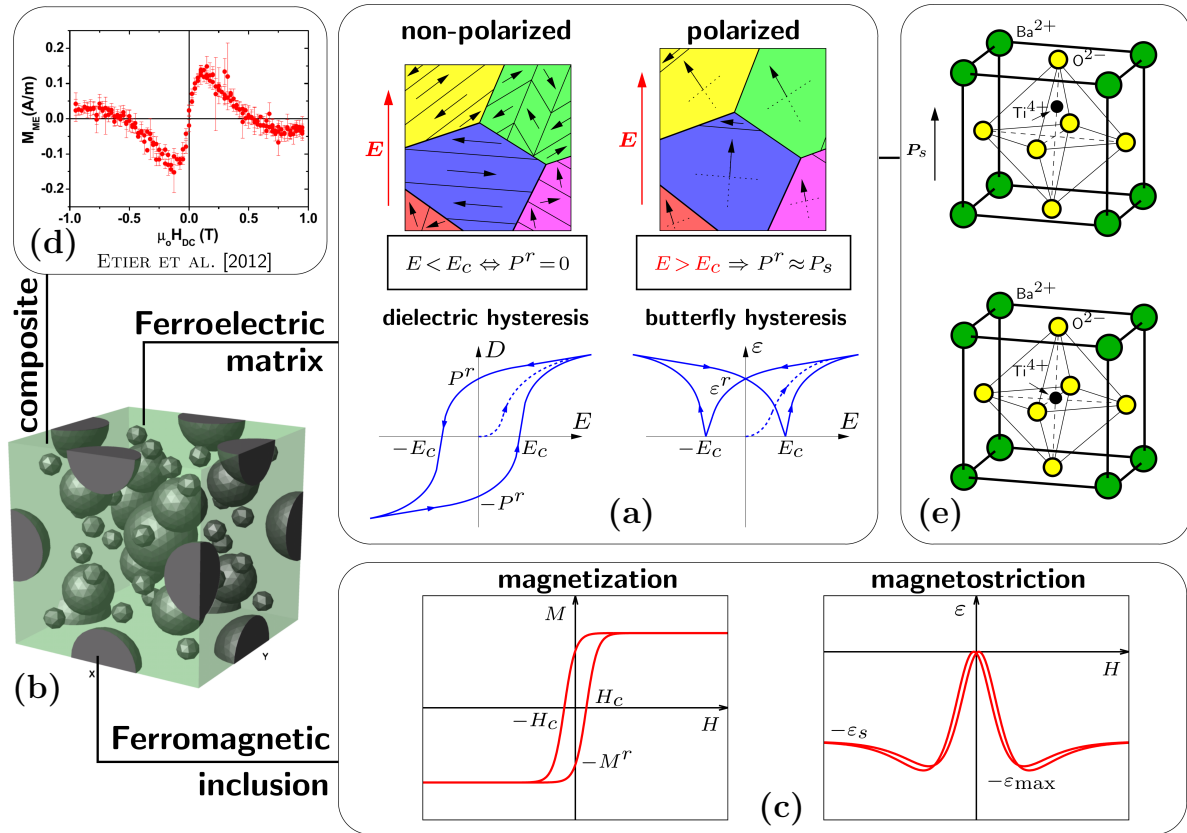


Figure 4.12: Design of two-phase magneto-electric composites: a) Typical macroscopic dielectric and butterfly hysteresis of BaTiO₃, resulting from microscopic domain movements, b) two-phase composite, c) typical magnetization and magnetostriction of CoFe₂O₄, d) measured magneto-electric response, e) BaTiO₃ unit cell below (illustration on top) and above the Curie temperature. Taken from LABUSCH ET AL. [116].

Due to this mechanical coupling as shown in Equation (4.2)₁ a strain-induced magneto-electric effect is generated. Additionally, in the same composite the converse ME effect could be produced by applying an electric field. Then, the ferroelectric phase reacts and transfers the deformations to the magnetic phase. The result is an electrically induced change in the magnetization, see equation (4.2)₂. Figure 4.12 shows an example of a composite, consisting of an electro-mechanically coupled barium titanate (BaTiO₃) matrix with idealized spherical magneto-mechanically coupled cobalt ferrite (CoFe₂O₄) inclu-

sions. The considered materials are characterized by typical dielectric and butterfly hysteresis curves for the ferroelectric phase as well as magnetization and magnetostriction curves for the magnetostrictive phase, which are qualitatively depicted in Figure 4.12(a) and Figure 4.12(c). Changes of the ferroelectric hysteresis curves depend on the reorientations of the spontaneous polarizations of the barium titanate unit cells on the nanoscopic level, shown in Figure 4.12(e). Similarly, changes in the ferromagnetic hysteresis loops are results of reorientations of the magnetic moments produced by the electron movements in the atomic orbitals. Due to the fact that the effective magneto-electric coupling in composite materials is a strain-induced property, it is obvious that it strongly depends on the ferroic characteristics of the individual phases. In Figure 4.12(d), a curve of an experimentally measured direct ME coefficient of a composite material depending on an alternating magnetic field is depicted. A highly nonlinear ME behavior with an inversion of sign for an increasing magnetic field can be observed. These nonlinear characteristics are a result of the polycrystalline character of the material. In a single crystal, magnetostriction is monotonic. Due to transverse contraction and magnetization rotation the mean value yields a reduction of the absolute value of magnetostriction at high magnetic fields. Since the strain-induced ME properties are a result of the interaction of the different phases on the microscopic level, a further significant influence on the ME coupling is given by the microscopic morphology. The shape and assembly of both phases affect the transmission of the deformations and influence the ME properties. Common composite structures in the field of magneto-electric materials are the following three different structures shown in Figure 4.13.

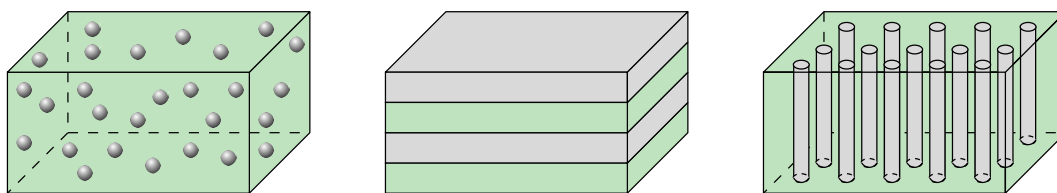


Figure 4.13: Typical 0–3 (particulate), 2–2 (lamine, lamellar), and 1–3 (columnar) ME composites (from left to right). Taken from SCHRÖDER AND KEIP [185].

In the notation of the different composites the first number indicates the spatial connectivity of the magneto-mechanical phase and the second number indicates the spatial connectivity of the electro-mechanical phase.

- **Particular (0-3) ME composites:** In (0-3) composites, see Figure 4.13(a), the magneto-active inclusions have no spatial connectivity and are completely embedded in the electro-active matrix. It can be assumed that the inclusions roughly have a spherical shape.
- **ME composite laminar (2-2) structures:** The laminar (2-2) composites, shown in Figure 4.13(b), consist of stacked magneto- and electro-active layers, which have spatial connectivities in two dimensions. Due to the large joint face between the different layers, such composites are characterized by good strain transmissions resulting in the largest measurable ME coefficients among these three types of composites.
- **Nanopillar (1-3) ME composites:** Such composites are characterized by magneto-active nanopillars which grow on a substrate in an electro-active matrix

material. They are denoted as (1-3) composites since the inclusions have one axis spatial connectivity, see Figure 4.13(c).

For the numerical simulations in this thesis (0-3) and (1-3) two-phase composites are considered, see Section 8.

Several experiments on ME composites showed remarkable ME coefficients, which are orders of magnitudes higher than those of single-phase materials, see e.g. FIEBIG [50]. Thus, composite materials are a promising solution to obtain a large ME coupling at room temperature and were first created in 1972, see VAN SUCHTELEN [210]. A small overview of magneto-electric two-phase composites and their generated ME coefficients is given in Table 4.2.

composite magneto-electric materials			
Year	Material	ME coef. s/m	Reference
1974	CoFe ₂ O ₄ -BaTiO ₃	31.1 · 10 ⁻¹²	RUN ET AL. [172]
1974	CoFe ₂ O ₄ -BaTiO ₃ +TiO ₂	305.0 · 10 ⁻¹²	RUN ET AL. [172]
1976	CoFe ₂ O ₄ -BaTiO ₃ -CoTi ₂ O ₄	733.3 · 10 ⁻¹²	BOOMGAARD ET AL. [24]
1978	BaTiO ₃ - Ni _{0.97} Co _{0.03} Mn _{0.1} Fe _{1.9} O ₄	≈ 330.0 · 10 ⁻¹²	BOOMGAARD AND BORN [23]
2001	PbZr _x Ti _{1-x} O ₃ - NiCo _{0.02} Mn _{0.1} Fe _{1.8} O ₄	≈ 779.0 · 10 ⁻¹²	RYU ET AL. [174]
2002	Tb _{0.28} Dy _{0.72} Fe _{1.95} - PbZr _x Ti _{1-x} O ₃ -C ₂ H ₂ F ₂	≈ 104.5 · 10 ⁻¹²	NAN ET AL. [151]
2006	FeBSiC-PZT	400000 · 10 ⁻¹²	DONG ET AL. [38]
2011	CoFe ₂ O ₄ -BaTiO ₃	22.0 · 10 ⁻¹²	SHVARTSMAN ET AL. [191]
2013	CoFe ₂ O ₄ -BaTiO ₃	4.4 · 10 ⁻¹²	ETIER ET AL. [46]

Table 4.2: Measured ME coefficients at room temperature of composite materials.

All ME coefficients of the listed composites are obtained at room temperature. The ME coupling of composite structures is several orders of magnitude higher than the coupling in single-phase materials, especially shown in the work of DONG ET AL. [38], which showed an ME coupling of about 400000 · 10⁻¹² s/m in a laminate structure composite. It has been discovered in several investigations that laminate composites yield the highest magneto-electric coefficients. Further publications which show remarkable ME coefficients and have to be mentioned here, are BOOMGAARD ET AL. [25], CAI ET AL. [29], DONG ET AL. [37], GREVE ET AL. [58], ISLAM AND PRIYA [81], ISLAM ET AL. [82], MA ET AL. [128], MORI AND WUTTIG [148], NAN ET AL. [149], RYU ET AL. [173; 175], SRINIVASAN ET AL. [200; 201], which are not listed in Table 4.2 due to other units of the ME coupling coefficient. For a conversion of the units, the dielectric permittivity of the composite must be known and is not always mentioned in the works. In this thesis the experimentally measured ME coefficients of CoFe₂O₄-BaTiO₃ composites in the works of SHVARTSMAN ET AL. [191] as well as ETIER ET AL. [46] are compared with the ME coefficients obtained by numerical simulations. Further investigations of CoFe₂O₄-BaTiO₃ composites are given in ETIER ET AL. [47] or SCHMITZ-ANTONIAK ET AL. [178].

4.5.3 Why are there so few magneto-electric single-phase materials?

In ferroelectric materials, the electric polarization arises due to a displacement of the positively and negatively charged ions in the crystal lattice, see Section 4.2 for a detailed explanation. Then, the center of the positively and negatively charged ions do not coincide and generate a spontaneous polarization. This off-center displacement can be influenced by applied stresses or electric fields. Such ferroelectric properties (off-center distortion) arise due to a balance between short-range repulsion, due to overlapping orbitals, which favor the nonpolar cubic structure, and long-range Coulomb forces, which favor the ferroelectric state. In barium titanate d-orbitals of the Ti-ion build a connection with corresponding orbitals of the O-ions, a so-called orbital hybridization, resulting in an overlap of these orbitals and the tetragonal distortion of the unit cell. For an explanation of atomic orbitals including d-orbitals, see Section 4.1.1. The new energy state of these orbitals, caused by the hybridization, yields a minimization of the overall energy. Without this Ti-O hybridization the cubic phase is more stable, see COHEN [33]. In most ferroelectric oxide perovskites, the lowest unoccupied energy levels are d-orbitals, for instance in Ti-, Nb- or Zr-ions, yielding d-hybridization with the O-ion. In contrast to the off-center displacement of the differently charged ions, a magnetization has its origin in the atomic orbitals which are partially filled with electrons. These electrons, which generate a magnetic moment due to their spin and orbital movements, interact with each other based on the quantum mechanical exchange energy and align in the same direction. These interactions proceed between different atoms resulting in magnetic domains. Here, the d-orbital occupancies are necessary for the generation of magnetic moments since the energy state of the d-orbitals is preferable for the exchange energy in order to align the magnetic moments of the different electrons in one direction. In magneto-electric materials both electric and magnetic ordering have to be present, which includes materials with ferroic and antiferroic properties. On the one hand, an off-center displacement of the positively and negatively charged ions has to be present and, on the other hand, partially filled atomic d-orbitals are necessary. Since in most ferroelectric perovskite structures the Ti-, Nb- or Zr-ions have no electrons in the d-orbitals, they perform an orbital hybridization with the O-ions resulting in an off-center distortion. However, since partially filled d-orbitals are a requirement for magnetization, the driving force for an off-center distortion is no longer preferable. The associated mechanisms for the generation of both properties are mutually orthogonal to each other and therefore rare in single-phase materials. However, there is a further fact which reduces the number of materials with magneto-electric properties. To obtain ferroelectricity, the material has to be an insulator in order to produce a polarization instead of an electric current. But many ferromagnets are conductors instead of insulators and therefore reduce the number of possible ME candidates. However, most ferrimagnets, antiferromagnets or weak ferromagnets are indeed insulators. Thus only a very small number of natural ME multiferroics exists. For a more detailed explanation of the ferroelectric and ferromagnetic origins we refer to HILL [65].

5 Finite element formulation

In the framework of engineering applications, numerical simulations are of great importance. However, most mathematical descriptions are not solvable analytically due to their complex boundary value problems. The Finite Element Method (FEM) is a common and popular tool to solve static and dynamic problems. Based on balance equations the equilibrium conditions are given with geometric (Dirichlet) and static (Neumann) boundary conditions. The considered body is then discretized with a finite number of elements, which approximate the shape of the body as well as the degrees of freedom. The solution of an assembled global system of equations, with an appropriate iterative solution algorithm, yield the result of the complex boundary value problem. For the iterative solution the Newton-Method is used and for the volume integration of the individual finite elements the Gaussian quadrature is applied. A detailed description of the finite element method is for example given in HUGHES [78], WRIGGERS [221]. Since ferroelectric and magnetostrictive materials are simulated in this thesis, an extension to electric and magnetic fields is necessary. The first approach for the finite element method for piezoelectric problems was given in ALLIK AND HUGHES [5]. For more works in this field and detailed discussions the reader is referred to BENJEDDOU [16], KAMLAH AND BÖHLE [91], MACKERLE [130].

5.1 Boundary value problem for the magneto-electro-mechanical case

In order to solve a boundary value problem with the Finite Element Method, suitable balance equations have to be fulfilled. For the magneto-electro-mechanically coupled case these are the balance of linear momentum, the Gauss' law of electrostatics and the Gauss' law of magnetostatics as

$$\operatorname{div} \boldsymbol{\sigma} + \mathbf{f}_{mech} + \mathbf{f}_L = \mathbf{0} , \quad \operatorname{div} \mathbf{D} = \rho_f \quad \text{and} \quad \operatorname{div} \mathbf{B} = 0 . \quad (5.1)$$

The balance of linear momentum depends on the mechanical body force density \mathbf{f}_{mech} , caused by the gravitational acceleration, and the electromagnetic body force density \mathbf{f}_L . The latter one can be identified as the Lorentz force density, which was explained in Section 2.4. As mentioned in Section 2.4 the Maxwell stresses can be derived from the Lorentz force density. However, since Maxwell stresses only become important in materials with moving charge carriers, which are neglected in the framework of this contribution, we also neglect the influences of electromagnetic body forces with $\mathbf{f}_L = \mathbf{0}$. With the same assumption the density of free charge carriers ρ_f in Gauss' law of electrostatics can be neglected with $\operatorname{div} \mathbf{D} = 0$. These balance equations depend on the mechanical strain, the electric field, and the magnetic field which are defined as

$$\boldsymbol{\varepsilon} = \operatorname{sym}[\operatorname{grad}_{\mathbf{x}} \mathbf{u}] , \quad \mathbf{E} = -\operatorname{grad} \phi \quad \text{and} \quad \mathbf{H} = -\operatorname{grad} \varphi . \quad (5.2)$$

The balance equations given in Equation (5.1) have to be fulfilled for applied boundary conditions. Possible boundary conditions are Dirichlet and Neumann conditions. In the first case the unknown mechanical, electric or magnetic quantities at the boundary are directly defined and the Dirichlet boundary conditions are given as

$$\mathbf{u} = \mathbf{u}_0 \quad \text{on} \quad \partial \mathcal{B}_u , \quad \phi = \phi_0 \quad \text{on} \quad \partial \mathcal{B}_\phi \quad \text{and} \quad \varphi = \varphi_0 \quad \text{on} \quad \partial \mathcal{B}_\varphi . \quad (5.3)$$

In the second case the boundary conditions due to surface forces and surface fluxes can be applied, resulting in the following Neumann boundary conditions

$$\mathbf{t} = \boldsymbol{\sigma} \cdot \mathbf{n} \text{ on } \partial\mathcal{B}_\sigma, \quad -Q_0 = \mathbf{D} \cdot \mathbf{n} \text{ on } \partial\mathcal{B}_D \quad \text{and} \quad -\zeta_0 = \mathbf{B} \cdot \mathbf{n} \text{ on } \partial\mathcal{B}_B, \quad (5.4)$$

where \mathbf{n} denotes the outward unit normal vector, see Figure 5.1. With these two types of boundary conditions the boundary of the body can be decomposed into

$$\partial\mathcal{B} = \partial\mathcal{B}_u \cup \partial\mathcal{B}_\sigma \quad \text{and} \quad \partial\mathcal{B}_u \cap \partial\mathcal{B}_\sigma = \emptyset \quad (5.5)$$

for the mechanical part,

$$\partial\mathcal{B} = \partial\mathcal{B}_\phi \cup \partial\mathcal{B}_D \quad \text{and} \quad \partial\mathcal{B}_\phi \cap \partial\mathcal{B}_D = \emptyset \quad (5.6)$$

for the electrical part and

$$\partial\mathcal{B} = \partial\mathcal{B}_\varphi \cup \partial\mathcal{B}_B \quad \text{and} \quad \partial\mathcal{B}_\varphi \cap \partial\mathcal{B}_B = \emptyset \quad (5.7)$$

for the magnetical part.

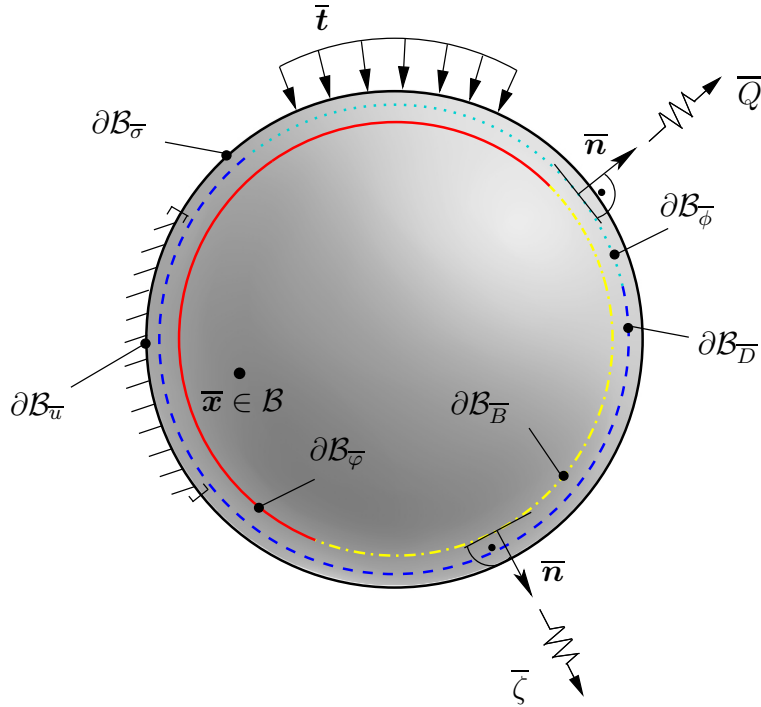


Figure 5.1: The boundary of the considered two dimensional body is decomposed into different areas, representing mechanical, electrical, and magnetical Dirichlet and Neumann boundary conditions.

5.2 Weak formulation for the magneto-electro-mechanical case

In order to solve a defined boundary value problem, the Galerkin method is employed using the principle of virtual work. Thus, the balance equations have to be multiplied with appropriate test functions. For the mechanical case the balance of linear momentum

is multiplied with the test function $\delta \mathbf{u}$, which fulfills the mechanical boundary conditions. The balance equation for the electrical boundary value problem, Gauss' law of electrostatics, is multiplied by the test function $\delta \phi$, and the Gauss' law of magnetostatics is multiplied with the test function $\delta \varphi$ resulting in the following expressions of the weak forms

$$\begin{aligned} G_u &= - \int_{\mathcal{B}} (\operatorname{div} \boldsymbol{\sigma} + \mathbf{f}_{mech}) \cdot \delta \mathbf{u} \, dv = 0 , \\ G_\phi &= - \int_{\mathcal{B}} (\operatorname{div} \mathbf{D} - \rho_f) \delta \phi \, dv = 0 , \\ G_\varphi &= - \int_{\mathcal{B}} \operatorname{div} \mathbf{B} \delta \varphi \, dv = 0 . \end{aligned} \quad (5.8)$$

Using the product rule as $\operatorname{div}(\boldsymbol{\sigma}^T \cdot \delta \mathbf{u}) = \operatorname{div} \boldsymbol{\sigma} \cdot \delta \mathbf{u} + \boldsymbol{\sigma} : \operatorname{grad} \delta \mathbf{u}$ for the mechanical part with the relation $\boldsymbol{\sigma}^T = \boldsymbol{\sigma}$, the product rule as $\operatorname{div}(\mathbf{D} \delta \phi) = \operatorname{div} \mathbf{D} \delta \phi + \mathbf{D} \cdot \operatorname{grad} \phi$ for the electrical part, as well as $\operatorname{div}(\mathbf{B} \delta \varphi) = \operatorname{div} \mathbf{B} \delta \varphi + \mathbf{B} \cdot \operatorname{grad} \varphi$ for the magnetical part we obtain

$$\begin{aligned} G_u &= \int_{\mathcal{B}} \boldsymbol{\sigma} : \operatorname{grad} \delta \mathbf{u} \, dv - \int_{\mathcal{B}} \operatorname{div}(\boldsymbol{\sigma} \cdot \delta \mathbf{u}) \, dv - \int_{\mathcal{B}} \mathbf{f}_{mech} \cdot \delta \mathbf{u} \, dv = 0 , \\ G_\phi &= \int_{\mathcal{B}} \mathbf{D} \cdot \operatorname{grad} \delta \phi \, dv - \int_{\mathcal{B}} \operatorname{div}(\mathbf{D} \delta \phi) \, dv + \int_{\mathcal{B}} \rho_f \delta \phi \, dv , \\ G_\varphi &= \int_{\mathcal{B}} \mathbf{B} \cdot \operatorname{grad} \delta \varphi \, dv - \int_{\mathcal{B}} \operatorname{div}(\mathbf{B} \delta \varphi) \, dv . \end{aligned} \quad (5.9)$$

With the use of the divergence theorem we can map the second integrals of the equations (5.9)₁₋₃ on the boundary of the body and can apply the Cauchy theorems $\mathbf{t} = \boldsymbol{\sigma} \cdot \mathbf{n}$, $-Q = \mathbf{D} \cdot \mathbf{n}$ and $-\zeta = \mathbf{B} \cdot \mathbf{n}$. Furthermore, in the first integral in equation (5.9)₁ only the symmetric part of $\operatorname{grad}_{sym} \delta \mathbf{u} = \delta \boldsymbol{\varepsilon}$ is considered due to the symmetry of the stress tensor. The gradient of the electric and magnetic potentials in (5.9)₂₋₃ can be replaced by $\delta \mathbf{E} = -\operatorname{grad} \delta \phi$ and $\delta \mathbf{H} = -\operatorname{grad} \delta \varphi$, respectively. Then, equations (5.9)₁₋₃ can be written as

$$\begin{aligned} G_u &= \underbrace{\int_{\mathcal{B}} \boldsymbol{\sigma} : \delta \boldsymbol{\varepsilon} \, dv}_{G_u^{int}} - \underbrace{\int_{\partial \mathcal{B}_\sigma} \mathbf{t} \cdot \delta \mathbf{u} \, da}_{G_u^{ext}} - \int_{\mathcal{B}} \mathbf{f}_{mech} \cdot \delta \mathbf{u} \, dv = 0 , \\ G_\phi &= \underbrace{- \int_{\mathcal{B}} \mathbf{D} \cdot \delta \mathbf{E} \, dv}_{G_\phi^{int}} + \underbrace{\int_{\partial \mathcal{B}_D} Q \delta \phi \, da + \int_{\mathcal{B}} \rho_f \delta \phi \, dv}_{G_\phi^{ext}} , \\ G_\varphi &= \underbrace{- \int_{\mathcal{B}} \mathbf{B} \cdot \delta \mathbf{H} \, dv}_{G_\varphi^{int}} + \underbrace{\int_{\partial \mathcal{B}_B} \zeta \delta \varphi \, da}_{G_\varphi^{ext}} \end{aligned} \quad (5.10)$$

with the internal and external virtual work G_u^{int} and G_u^{ext} for the mechanical quantities, G_ϕ^{int} and G_ϕ^{ext} for the electric quantities, and G_φ^{int} and G_φ^{ext} for the magnetic quantities.

By using the software FEAP the internal part has to be programmed with an appropriate material model and the external part is defined through the applied boundary conditions.

5.3 Linearization of the weak forms

The weak forms can be of nonlinear nature such that an iterative method is required for the solution of the problem. Here we use the Newton-Raphson method, which requires a linearization of the weak forms with respect to a given point $\mathbf{u} = \tilde{\mathbf{u}}$, $\phi = \tilde{\phi}$ and $\varphi = \tilde{\varphi}$ as

$$\begin{aligned}
\text{Lin}G_u(\tilde{\mathbf{u}}, \tilde{\phi}, \tilde{\varphi}, \Delta\mathbf{u}, \Delta\phi, \Delta\varphi, \delta\mathbf{u}) &= G_u(\tilde{\mathbf{u}}, \tilde{\phi}, \tilde{\varphi}, \delta\mathbf{u}) + \Delta G_u(\tilde{\mathbf{u}}, \Delta\mathbf{u}, \delta\mathbf{u}) \\
&\quad + \Delta G_u(\tilde{\phi}, \Delta\phi, \delta\mathbf{u}) + \Delta G_u(\tilde{\varphi}, \Delta\varphi, \delta\mathbf{u}) , \\
\text{Lin}G_\phi(\tilde{\mathbf{u}}, \tilde{\phi}, \tilde{\varphi}, \Delta\mathbf{u}, \Delta\phi, \Delta\varphi, \delta\phi) &= G_\phi(\tilde{\mathbf{u}}, \tilde{\phi}, \tilde{\varphi}, \delta\phi) + \Delta G_\phi(\tilde{\mathbf{u}}, \Delta\mathbf{u}, \delta\phi) \\
&\quad + \Delta G_\phi(\tilde{\phi}, \Delta\phi, \delta\phi) + \Delta G_\phi(\tilde{\varphi}, \Delta\varphi, \delta\phi) , \\
\text{Lin}G_\varphi(\tilde{\mathbf{u}}, \tilde{\phi}, \tilde{\varphi}, \Delta\mathbf{u}, \Delta\phi, \Delta\varphi, \delta\varphi) &= G_\varphi(\tilde{\mathbf{u}}, \tilde{\phi}, \tilde{\varphi}, \delta\varphi) + \Delta G_\varphi(\tilde{\mathbf{u}}, \Delta\mathbf{u}, \delta\varphi) \\
&\quad + \Delta G_\varphi(\tilde{\phi}, \Delta\phi, \delta\varphi) + \Delta G_\varphi(\tilde{\varphi}, \Delta\varphi, \delta\varphi)
\end{aligned} \tag{5.11}$$

with the incremental quantities $\Delta\mathbf{u}$, $\Delta\phi$ and $\Delta\varphi$. In order to obtain the incremental parts of the linearization, a directional derivative has to be performed with respect to the corresponding field quantity. For example, we obtain the mechanical increment ΔG_u with

$$\Delta G_u(\tilde{\mathbf{u}}, \Delta\mathbf{u}, \delta\mathbf{u}) = \text{D}G_u(\tilde{\mathbf{u}}, \delta\mathbf{u}) \cdot \Delta\mathbf{u} = \left. \frac{\text{d}}{\text{d}\epsilon} [G_u(\tilde{\mathbf{u}} + \epsilon\Delta\mathbf{u}, \delta\mathbf{u})] \right|_{\epsilon=0} . \tag{5.12}$$

The other incremental parts are obtained analogously. We assume that the external loadings, the mechanical traction density \mathbf{t} , the mechanical body force density \mathbf{f}_{mech} , the electric flux density Q , and the magnetic flux density ζ , are conservative loadings and their directional derivatives vanish as

$$\Delta G_u^{ext} = 0 , \quad \Delta G_\phi^{ext} = 0 \quad \text{and} \quad \Delta G_\varphi^{ext} = 0 . \tag{5.13}$$

Linearizing the weak forms (5.10) we obtain only the linearizations of the internal parts as

$$\Delta G_u = \int_{\mathcal{B}} \Delta\boldsymbol{\sigma} : \delta\boldsymbol{\varepsilon} \, \text{d}v , \quad \Delta G_\phi = - \int_{\mathcal{B}} \Delta\mathbf{D} \cdot \delta\mathbf{E} \, \text{d}v , \quad \text{and} \quad \Delta G_\varphi = - \int_{\mathcal{B}} \Delta\mathbf{B} \cdot \delta\mathbf{H} \, \text{d}v . \tag{5.14}$$

Due to the considered composite materials with a magneto-electro-mechanical coupling behavior, the stress, dielectric displacement, and magnetic induction depend on the strains, the electric field, and the magnetic field with $\boldsymbol{\sigma} = \hat{\boldsymbol{\sigma}}(\boldsymbol{\varepsilon}, \mathbf{E}, \mathbf{H})$, $\mathbf{D} = \hat{\mathbf{D}}(\boldsymbol{\varepsilon}, \mathbf{E}, \mathbf{H})$

and $\mathbf{B} = \hat{\mathbf{B}}(\boldsymbol{\varepsilon}, \mathbf{E}, \mathbf{H})$. Thus, we obtain the following linearizations of the weak forms

$$\begin{aligned}\Delta G_u &= \int_{\mathcal{B}} \delta \boldsymbol{\varepsilon}^T : \partial_{\boldsymbol{\varepsilon}} \boldsymbol{\sigma} : \Delta \boldsymbol{\varepsilon} \, dv + \int_{\mathcal{B}} \delta \boldsymbol{\varepsilon}^T : \partial_{\mathbf{E}} \boldsymbol{\sigma} \cdot \Delta \mathbf{E} \, dv + \int_{\mathcal{B}} \delta \boldsymbol{\varepsilon}^T : \partial_{\mathbf{H}} \boldsymbol{\sigma} \cdot \Delta \mathbf{H} \, dv \\ \Delta G_\phi &= - \int_{\mathcal{B}} \delta \mathbf{E} \cdot \partial_{\boldsymbol{\varepsilon}} \mathbf{D} : \Delta \boldsymbol{\varepsilon} \, dv - \int_{\mathcal{B}} \delta \mathbf{E} \cdot \partial_{\mathbf{E}} \mathbf{D} \cdot \Delta \mathbf{E} \, dv - \int_{\mathcal{B}} \delta \mathbf{E} \cdot \partial_{\mathbf{H}} \mathbf{D} \cdot \Delta \mathbf{H} \, dv \\ \Delta G_\varphi &= - \int_{\mathcal{B}} \delta \mathbf{H} \cdot \partial_{\boldsymbol{\varepsilon}} \mathbf{B} : \Delta \boldsymbol{\varepsilon} \, dv - \int_{\mathcal{B}} \delta \mathbf{H} \cdot \partial_{\mathbf{E}} \mathbf{B} \cdot \Delta \mathbf{E} \, dv - \int_{\mathcal{B}} \delta \mathbf{H} \cdot \partial_{\mathbf{H}} \mathbf{B} \cdot \Delta \mathbf{H} \, dv .\end{aligned}\tag{5.15}$$

The partial derivatives of the stress, dielectric displacement, and magnetic induction with respect to the strains, electric field, and magnetic field result in the tangent moduli

$$\begin{aligned}\partial_{\boldsymbol{\varepsilon}} \boldsymbol{\sigma} &= \mathbb{C} , & \partial_{\mathbf{E}} \boldsymbol{\sigma} &= -\mathbf{e}^T , & \partial_{\mathbf{H}} \boldsymbol{\sigma} &= -\mathbf{q}^T , & \partial_{\boldsymbol{\varepsilon}} \mathbf{D} &= \mathbf{e} , & \partial_{\mathbf{E}} \mathbf{D} &= \boldsymbol{\varepsilon} , \\ \partial_{\mathbf{H}} \mathbf{D} &= \boldsymbol{\alpha}^T , & \partial_{\boldsymbol{\varepsilon}} \mathbf{B} &= \mathbf{q} , & \partial_{\mathbf{E}} \mathbf{B} &= \boldsymbol{\alpha} , & \partial_{\mathbf{H}} \mathbf{B} &= \boldsymbol{\mu} .\end{aligned}\tag{5.16}$$

Writing down the resulting tangent moduli in compact matrix notation we obtain the expression

$$\begin{bmatrix} \boldsymbol{\sigma} \\ \mathbf{D} \\ \mathbf{B} \end{bmatrix} = \begin{bmatrix} \mathbb{C} & -\mathbf{e}^T & -\mathbf{q}^T \\ -\mathbf{e} & -\boldsymbol{\varepsilon} & -\boldsymbol{\alpha}^T \\ -\mathbf{q} & -\boldsymbol{\alpha} & -\boldsymbol{\mu} \end{bmatrix} \begin{bmatrix} \boldsymbol{\varepsilon} \\ \mathbf{E} \\ \mathbf{H} \end{bmatrix} .\tag{5.17}$$

5.4 Vector-matrix (Voigt) notation

For the following finite element formulation, the Voigt notation is introduced. Second-order tensors are rewritten in reduced vector form and all higher-order tensors will be written in reduced matrices. Matrices and vectors in Voigt-notation will be denoted with an underline as $\underline{\bullet}$. First, the non-reduced vectors are given for the strain and stress tensor as

$$\underline{\boldsymbol{\varepsilon}}^{9 \times 1} = [\varepsilon_{11}, \varepsilon_{22}, \varepsilon_{33}, \varepsilon_{12}, \varepsilon_{23}, \varepsilon_{13}, \varepsilon_{21}, \varepsilon_{32}, \varepsilon_{31}]^T\tag{5.18}$$

and

$$\underline{\boldsymbol{\sigma}}^{9 \times 1} = [\sigma_{11}, \sigma_{22}, \sigma_{33}, \sigma_{12}, \sigma_{23}, \sigma_{13}, \sigma_{21}, \sigma_{32}, \sigma_{31}]^T .\tag{5.19}$$

The mechanical stiffness tensor \mathbb{C} is written in non-reduced matrix notation as

$$\underline{\mathbb{C}}^{9 \times 9} = \begin{bmatrix} \mathbb{C}_{1111} & \mathbb{C}_{1122} & \mathbb{C}_{1133} & \mathbb{C}_{1112} & \mathbb{C}_{1123} & \mathbb{C}_{1113} & \mathbb{C}_{1121} & \mathbb{C}_{1132} & \mathbb{C}_{1131} \\ \mathbb{C}_{2211} & \mathbb{C}_{2222} & \mathbb{C}_{2233} & \mathbb{C}_{2212} & \mathbb{C}_{2223} & \mathbb{C}_{2213} & \mathbb{C}_{2221} & \mathbb{C}_{2232} & \mathbb{C}_{2231} \\ \mathbb{C}_{3311} & \mathbb{C}_{3322} & \mathbb{C}_{3333} & \mathbb{C}_{3312} & \mathbb{C}_{3323} & \mathbb{C}_{3313} & \mathbb{C}_{3321} & \mathbb{C}_{3332} & \mathbb{C}_{3331} \\ \mathbb{C}_{1211} & \mathbb{C}_{1222} & \mathbb{C}_{1233} & \mathbb{C}_{1212} & \mathbb{C}_{1223} & \mathbb{C}_{1213} & \mathbb{C}_{1221} & \mathbb{C}_{1232} & \mathbb{C}_{1231} \\ \mathbb{C}_{2311} & \mathbb{C}_{2322} & \mathbb{C}_{2333} & \mathbb{C}_{2312} & \mathbb{C}_{2323} & \mathbb{C}_{2313} & \mathbb{C}_{2321} & \mathbb{C}_{2332} & \mathbb{C}_{2331} \\ \mathbb{C}_{1311} & \mathbb{C}_{1322} & \mathbb{C}_{1333} & \mathbb{C}_{1312} & \mathbb{C}_{1323} & \mathbb{C}_{1313} & \mathbb{C}_{1321} & \mathbb{C}_{1332} & \mathbb{C}_{1331} \\ \mathbb{C}_{2111} & \mathbb{C}_{2122} & \mathbb{C}_{2133} & \mathbb{C}_{2112} & \mathbb{C}_{2123} & \mathbb{C}_{2113} & \mathbb{C}_{2121} & \mathbb{C}_{2132} & \mathbb{C}_{2131} \\ \mathbb{C}_{3211} & \mathbb{C}_{3222} & \mathbb{C}_{3233} & \mathbb{C}_{3212} & \mathbb{C}_{3223} & \mathbb{C}_{3213} & \mathbb{C}_{3221} & \mathbb{C}_{3232} & \mathbb{C}_{3231} \\ \mathbb{C}_{3111} & \mathbb{C}_{3122} & \mathbb{C}_{3133} & \mathbb{C}_{3112} & \mathbb{C}_{3123} & \mathbb{C}_{3113} & \mathbb{C}_{3121} & \mathbb{C}_{3132} & \mathbb{C}_{3131} \end{bmatrix} .\tag{5.20}$$

Applying the Voigt notation we obtain the reduced form of the symmetric strain and stress tensors in the following form

$$\underline{\boldsymbol{\varepsilon}} = [\varepsilon_{11}, \varepsilon_{22}, \varepsilon_{33}, 2\varepsilon_{12}, 2\varepsilon_{23}, 2\varepsilon_{13}]^T \quad \text{and} \quad \underline{\boldsymbol{\sigma}} = [\sigma_{11}, \sigma_{22}, \sigma_{33}, \sigma_{12}, \sigma_{23}, \sigma_{13}]^T. \quad (5.21)$$

Fourth order tensors, like the mechanical stiffness tensor \mathbb{C} with the symmetry conditions $\mathbb{C}_{ijkl} = \mathbb{C}_{jikl} = \mathbb{C}_{ijlk}$, can be reduced to matrices as

$$\underline{\mathbb{C}}_{(Voigt)}^{6 \times 6} = \begin{bmatrix} \mathbb{C}_{1111} & \mathbb{C}_{1122} & \mathbb{C}_{1133} & \frac{1}{2}(\mathbb{C}_{1112} + \mathbb{C}_{1121}) & \frac{1}{2}(\mathbb{C}_{1123} + \mathbb{C}_{1132}) & \frac{1}{2}(\mathbb{C}_{1113} + \mathbb{C}_{1131}) \\ \mathbb{C}_{2211} & \mathbb{C}_{2222} & \mathbb{C}_{2233} & \frac{1}{2}(\mathbb{C}_{2212} + \mathbb{C}_{2221}) & \frac{1}{2}(\mathbb{C}_{2223} + \mathbb{C}_{2232}) & \frac{1}{2}(\mathbb{C}_{2213} + \mathbb{C}_{2231}) \\ \mathbb{C}_{3311} & \mathbb{C}_{3322} & \mathbb{C}_{3333} & \frac{1}{2}(\mathbb{C}_{3312} + \mathbb{C}_{3321}) & \frac{1}{2}(\mathbb{C}_{3323} + \mathbb{C}_{3332}) & \frac{1}{2}(\mathbb{C}_{3313} + \mathbb{C}_{3331}) \\ \frac{1}{2}(\mathbb{C}_{1211} + \mathbb{C}_{2111}) & \frac{1}{2}(\mathbb{C}_{1222} + \mathbb{C}_{2122}) & \frac{1}{2}(\mathbb{C}_{1233} + \mathbb{C}_{2133}) & \frac{1}{4}(\mathbb{C}_{1212} + \mathbb{C}_{2112} + \mathbb{C}_{1221} + \mathbb{C}_{2121}) & \frac{1}{4}(\mathbb{C}_{1223} + \mathbb{C}_{2123} + \mathbb{C}_{1232} + \mathbb{C}_{2132}) & \frac{1}{4}(\mathbb{C}_{1213} + \mathbb{C}_{2113} + \mathbb{C}_{1231} + \mathbb{C}_{2131}) \\ \frac{1}{2}(\mathbb{C}_{2311} + \mathbb{C}_{3211}) & \frac{1}{2}(\mathbb{C}_{2322} + \mathbb{C}_{3222}) & \frac{1}{2}(\mathbb{C}_{2333} + \mathbb{C}_{3233}) & \frac{1}{4}(\mathbb{C}_{2312} + \mathbb{C}_{3212} + \mathbb{C}_{2321} + \mathbb{C}_{3221}) & \frac{1}{4}(\mathbb{C}_{2323} + \mathbb{C}_{3223} + \mathbb{C}_{2332} + \mathbb{C}_{3232}) & \frac{1}{4}(\mathbb{C}_{2313} + \mathbb{C}_{3213} + \mathbb{C}_{2331} + \mathbb{C}_{3231}) \\ \frac{1}{2}(\mathbb{C}_{1311} + \mathbb{C}_{3111}) & \frac{1}{2}(\mathbb{C}_{1322} + \mathbb{C}_{3122}) & \frac{1}{2}(\mathbb{C}_{1333} + \mathbb{C}_{3133}) & \frac{1}{4}(\mathbb{C}_{1312} + \mathbb{C}_{3112} + \mathbb{C}_{1321} + \mathbb{C}_{3121}) & \frac{1}{4}(\mathbb{C}_{1323} + \mathbb{C}_{3123} + \mathbb{C}_{1332} + \mathbb{C}_{3132}) & \frac{1}{4}(\mathbb{C}_{1313} + \mathbb{C}_{3113} + \mathbb{C}_{1331} + \mathbb{C}_{3131}) \end{bmatrix}. \quad (5.22)$$

Analogously, third order tensors, as the electro-mechanical coupling tensor \mathbf{e} , with the symmetry conditions $e_{ijk} = e_{ikj}$, can be written as

$$\underline{\mathbf{e}}_{(Voigt)}^{3 \times 6} = \begin{bmatrix} e_{111} & e_{122} & e_{133} & \frac{1}{2}(e_{112} + e_{121}) & \frac{1}{2}(e_{123} + e_{132}) & \frac{1}{2}(e_{113} + e_{131}) \\ e_{211} & e_{222} & e_{233} & \frac{1}{2}(e_{212} + e_{221}) & \frac{1}{2}(e_{223} + e_{232}) & \frac{1}{2}(e_{213} + e_{231}) \\ e_{311} & e_{322} & e_{333} & \frac{1}{2}(e_{312} + e_{321}) & \frac{1}{2}(e_{323} + e_{332}) & \frac{1}{2}(e_{313} + e_{331}) \end{bmatrix} \quad (5.23)$$

and the magnetomechanical coupling tensor \mathbf{q} , with the symmetry conditions $q_{ijk} = q_{ikj}$, can be derived as

$$\underline{\mathbf{q}}_{(Voigt)}^{3 \times 6} = \begin{bmatrix} q_{111} & q_{122} & q_{133} & \frac{1}{2}(q_{112} + q_{121}) & \frac{1}{2}(q_{123} + q_{132}) & \frac{1}{2}(q_{113} + q_{131}) \\ q_{211} & q_{222} & q_{233} & \frac{1}{2}(q_{212} + q_{221}) & \frac{1}{2}(q_{223} + q_{232}) & \frac{1}{2}(q_{213} + q_{231}) \\ q_{311} & q_{322} & q_{333} & \frac{1}{2}(q_{312} + q_{321}) & \frac{1}{2}(q_{323} + q_{332}) & \frac{1}{2}(q_{313} + q_{331}) \end{bmatrix}. \quad (5.24)$$

All vectors and scalar valued quantities are not modified in Voigt-notation.

5.5 Discretization with finite elements

In order to solve the boundary value problem with the Finite-Element-Method, the body has to be discretized with finite elements, see Figure 5.2.

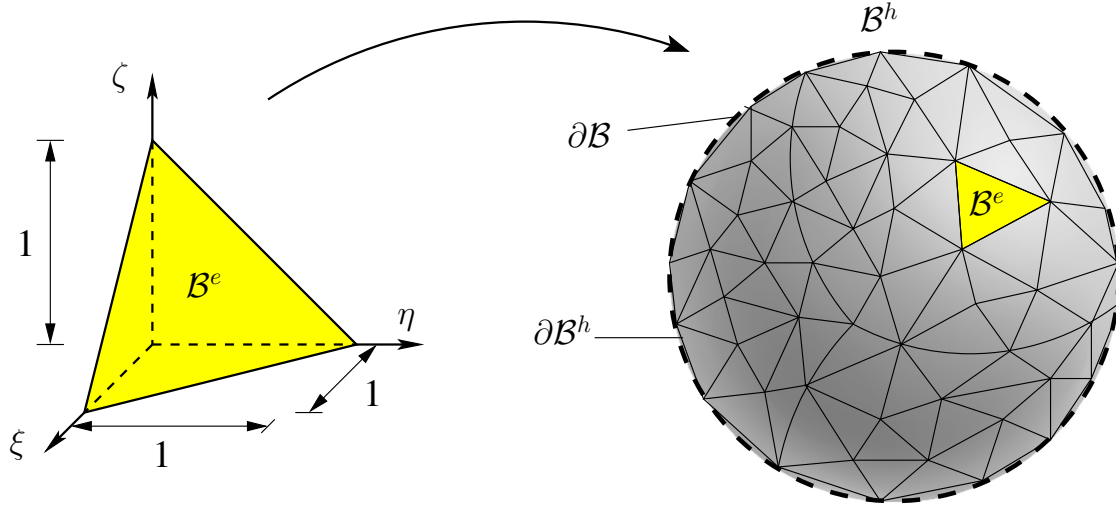


Figure 5.2: Example of a discretized body \mathcal{B}^h with tetrahedron finite elements \mathcal{B}^e . The mesh refinement controls the accuracy of the boundary reproduction of the discretized boundary $\partial\mathcal{B}^h$ with respect to the original geometry of the boundary $\partial\mathcal{B}$.

We consider a body \mathcal{B} which is discretized with finite elements \mathcal{B}^e . The higher the number of used finite elements the more precise is the reproduction of the geometry. However, an increasing number of finite elements also increases the computational cost and is very time consuming. Therefore, an appropriate number of finite elements has to be chosen in order to reproduce the original body in a sufficient manner. The discretized body \mathcal{B}^h then consists of the number of finite elements \mathcal{B}^e as

$$\mathcal{B} \approx \mathcal{B}^h = \bigcup_{e=1}^{num_{ele}} \mathcal{B}^e, \quad (5.25)$$

where $(\bullet)^h$ is an indicator for the approximated domain and num_{ele} for the number of finite elements. Figure 5.2 shows the approximation of the discretized boundary $\partial\mathcal{B}^h$ with respect to the original shape of the boundary $\partial\mathcal{B}$.

5.6 Isoparametric concept

The main idea of the isoparametric concept is that the shape of the considered body as well as the unknown quantities are discretized with the same interpolation functions. These interpolation functions, the so called shape functions N , are defined in a parameterized space with the natural coordinates $\boldsymbol{\kappa} = (\xi, \eta, \zeta)$. Through such shape functions the original geometry

$$\underline{\boldsymbol{x}}^h = \sum_{I=1}^{n_{node}} N^I(\boldsymbol{\kappa}) \underline{\boldsymbol{x}}^I \quad (5.26)$$

and unknown quantities are approximated as

$$\underline{\mathbf{u}}^h = \sum_{I=1}^{n_{node}} N^I(\boldsymbol{\kappa}) \underline{\mathbf{d}}_u^I, \quad \phi^h = \sum_{I=1}^{n_{node}} N^I(\boldsymbol{\kappa}) d_\phi^I \quad \text{and} \quad \varphi^h = \sum_{I=1}^{n_{node}} N^I(\boldsymbol{\kappa}) d_\varphi^I \quad (5.27)$$

with the number of element nodes n_{node} and the mechanical, electric and magnetic degrees of freedoms for each node $\underline{\mathbf{d}}_u^I$, d_ϕ^I and d_φ^I . Since the physical coordinates and unknown quantities are derived in the physical coordinates $\underline{\mathbf{x}}$, the shape functions have to be transferred from the parameterized space to the physical space through the application of the chain rule as

$$\frac{\partial N^I(\boldsymbol{\kappa})}{\partial \underline{\mathbf{x}}} = \frac{\partial N^I(\boldsymbol{\kappa})}{\partial \boldsymbol{\kappa}} \frac{\partial \boldsymbol{\kappa}}{\partial \underline{\mathbf{x}}} = \underline{\mathbf{J}}^{-T} \frac{\partial N^I(\boldsymbol{\kappa})}{\partial \boldsymbol{\kappa}} \quad (5.28)$$

with the Jacobian matrix $\underline{\mathbf{J}}$ including the derivatives of the shape functions with respect to $\boldsymbol{\kappa}$. The connection to the physical space is obtained by an approximation with the shape functions as

$$\underline{\mathbf{J}} = \frac{\partial \underline{\mathbf{x}}^h}{\partial \boldsymbol{\kappa}} = \frac{\partial}{\partial \boldsymbol{\kappa}} \sum_{I=1}^{n_{node}} N^I(\boldsymbol{\kappa}) \underline{\mathbf{x}}^I. \quad (5.29)$$

The Jacobi matrix can then be written as

$$\underline{\mathbf{J}} = \sum_{I=1}^{n_{node}} \begin{bmatrix} x_1^I N_{,\xi}^I & x_1^I N_{,\eta}^I & x_1^I N_{,\zeta}^I \\ x_2^I N_{,\xi}^I & x_2^I N_{,\eta}^I & x_2^I N_{,\zeta}^I \\ x_3^I N_{,\xi}^I & x_3^I N_{,\eta}^I & x_3^I N_{,\zeta}^I \end{bmatrix}. \quad (5.30)$$

5.7 Approximations with finite elements

As mentioned in the isoparametric concept, the unknown fields are approximated through appropriate shape functions. Additionally, the virtual and incremental counterparts are also described with these shape functions and for the mechanical fields appear as

$$\underline{\mathbf{u}}^h = \sum_{I=1}^{n_{node}} N^I \underline{\mathbf{d}}_u^I, \quad \delta \underline{\mathbf{u}}^h = \sum_{I=1}^{n_{node}} N^I \delta \underline{\mathbf{d}}_u^I \quad \text{and} \quad \Delta \underline{\mathbf{u}}^h = \sum_{I=1}^{n_{node}} N^I \Delta \underline{\mathbf{d}}_u^I, \quad (5.31)$$

for the electric fields as

$$\phi^h = \sum_{I=1}^{n_{node}} N^I d_\phi^I, \quad \delta \phi^h = \sum_{I=1}^{n_{node}} N^I \delta d_\phi^I \quad \text{and} \quad \Delta \phi^h = \sum_{I=1}^{n_{node}} N^I \Delta d_\phi^I, \quad (5.32)$$

and for the magnetic fields as

$$\varphi^h = \sum_{I=1}^{n_{node}} N^I d_\varphi^I, \quad \delta \varphi^h = \sum_{I=1}^{n_{node}} N^I \delta d_\varphi^I \quad \text{and} \quad \Delta \varphi^h = \sum_{I=1}^{n_{node}} N^I \Delta d_\varphi^I \quad (5.33)$$

with the discrete nodal displacement, electric potential and magnetic potential $\underline{\mathbf{d}}_u^I$, d_ϕ^I and d_φ^I . Since the Voigt notation is applied, we use B-matrices, denoted as $\underline{\mathbb{B}}$, for the discretizations of the mechanical strains as

$$\underline{\boldsymbol{\varepsilon}}^h = \sum_{I=1}^{n_{node}} \underline{\mathbb{B}}_u^I \underline{\mathbf{d}}_u^I, \quad \delta \underline{\boldsymbol{\varepsilon}}^h = \sum_{I=1}^{n_{node}} \underline{\mathbb{B}}_u^I \delta \underline{\mathbf{d}}_u^I \quad \text{and} \quad \Delta \underline{\boldsymbol{\varepsilon}}^h = \sum_{I=1}^{n_{node}} \underline{\mathbb{B}}_u^I \Delta \underline{\mathbf{d}}_u^I, \quad (5.34)$$

for the electric fields as

$$\underline{\mathbf{E}}^h = \sum_{I=1}^{n_{node}} \mathbb{B}_\phi^I d_\phi^I, \quad \delta \underline{\mathbf{E}}^h = \sum_{I=1}^{n_{node}} \mathbb{B}_\phi^I \delta d_\phi^I \quad \text{and} \quad \Delta \underline{\mathbf{E}}^h = \sum_{I=1}^{n_{node}} \mathbb{B}_\phi^I \Delta d_\phi^I, \quad (5.35)$$

and for the magnetic fields as

$$\underline{\mathbf{H}}^h = \sum_{I=1}^{n_{node}} \mathbb{B}_\phi^I d_\phi^I, \quad \delta \underline{\mathbf{H}}^h = \sum_{I=1}^{n_{node}} \mathbb{B}_\phi^I \delta d_\phi^I \quad \text{and} \quad \Delta \underline{\mathbf{H}}^h = \sum_{I=1}^{n_{node}} \mathbb{B}_\phi^I \Delta d_\phi^I. \quad (5.36)$$

The B-matrices for each node are defined as

$$\underline{\mathbb{B}}_u^I = \begin{bmatrix} N_{,x_1}^I & 0 & 0 \\ 0 & N_{,x_2}^I & 0 \\ 0 & 0 & N_{,x_3}^I \\ N_{,x_2}^I & N_{,x_1}^I & 0 \\ 0 & N_{,x_3}^I & N_{,x_2}^I \\ N_{,x_3}^I & 0 & N_{,x_1}^I \end{bmatrix}, \quad \mathbb{B}_\phi^I = \begin{bmatrix} -N_{,x_1}^I \\ -N_{,x_2}^I \\ -N_{,x_3}^I \end{bmatrix} \quad \text{and} \quad \underline{\mathbb{B}}_\varphi^I = \begin{bmatrix} -N_{,x_1}^I \\ -N_{,x_2}^I \\ -N_{,x_3}^I \end{bmatrix}. \quad (5.37)$$

5.8 Discretization of the weak forms and linearizations

The weak forms and their linearizations have to be discretized with the introduced approximations. Then we obtain the expression for the virtual mechanical work

$$G_u^h = \sum_{I=1}^{n_{node}} (\partial \underline{\mathbf{d}}_u^I)^T \underbrace{\left\{ \int_{\mathcal{B}^e} (\underline{\mathbb{B}}_u^I)^T \underline{\boldsymbol{\sigma}} \, dv - \int_{\partial \mathcal{B}_\sigma^e} N^I \underline{\mathbf{t}} \, da - \int_{\mathcal{B}^e} N^I \underline{\mathbf{f}}_{mech} \, dv \right\}}_{\underline{\mathbf{r}}_u^I}. \quad (5.38)$$

Due to the definition of the B-matrix for the electric quantities a change of the sign occurs for the virtual electrical work as

$$-G_\phi^h = \sum_{I=1}^{n_{node}} \delta d_\phi^I \underbrace{\left\{ - \int_{\mathcal{B}^e} (\mathbb{B}_\phi^I)^T \underline{\mathbf{D}} \, dv + \int_{\partial \mathcal{B}_D^e} N^I Q \, da + \int_{\mathcal{B}^e} N^I \rho_f \, dv \right\}}_{\underline{\mathbf{r}}_\phi^I}. \quad (5.39)$$

Finally, the discretization of the virtual magnetical work can be written as

$$-G_\varphi^h = \sum_{I=1}^{n_{node}} \delta d_\varphi^I \underbrace{\left\{ - \int_{\mathcal{B}^e} (\underline{\mathbb{B}}_\varphi^I)^T \underline{\mathbf{B}} \, dv + \int_{\partial \mathcal{B}_B^e} N^I \zeta \, da \right\}}_{\underline{\mathbf{r}}_\varphi^I}. \quad (5.40)$$

Analogously, we discretize the linearizations of the weak forms with the same principle and obtain the linearized mechanical weak form as

$$\Delta G_u^h = \sum_{I=1}^{n_{node}} \sum_{J=1}^{n_{node}} (\delta \underline{\mathbf{d}}_u^I)^T \left\{ \underbrace{\int_{\mathcal{B}^e} (\mathbb{B}_u^I)^T \underline{\mathbf{C}} \mathbb{B}_u^J dv \Delta \underline{\mathbf{d}}_u^J}_{\underline{\mathbf{k}}_{uu}^{IJ}} - \underbrace{\int_{\mathcal{B}^e} (\mathbb{B}_u^I)^T \underline{\mathbf{e}}^T \mathbb{B}_\phi^J dv \Delta d_\phi^J}_{\underline{\mathbf{k}}_{u\phi}^{IJ}} - \underbrace{\int_{\mathcal{B}^e} (\mathbb{B}_u^I)^T \underline{\mathbf{q}}^T \mathbb{B}_\varphi^J dv \Delta d_\varphi^J}_{\underline{\mathbf{k}}_{u\varphi}^{IJ}} \right\}, \quad (5.41)$$

the linearization of the electrical weak form as

$$\Delta G_\phi^h = \sum_{I=1}^{n_{node}} \sum_{J=1}^{n_{node}} \delta d_\phi^I \left\{ \underbrace{- \int_{\mathcal{B}^e} (\mathbb{B}_\phi^I)^T \underline{\mathbf{e}} \mathbb{B}_u^J dv \Delta \underline{\mathbf{d}}_u^J}_{\underline{\mathbf{k}}_{\phi u}^{IJ}} - \underbrace{\int_{\mathcal{B}^e} (\mathbb{B}_\phi^I)^T \underline{\mathbf{e}} \mathbb{B}_\phi^J dv \Delta d_\phi^J}_{k_{\phi\phi}^{IJ}} - \underbrace{\int_{\mathcal{B}^e} (\mathbb{B}_\phi^I)^T \underline{\mathbf{\alpha}}^T \mathbb{B}_\varphi^J dv \Delta d_\varphi^J}_{k_{\phi\varphi}^{IJ}} \right\}, \quad (5.42)$$

and the linearization of the magnetical weak form as

$$\Delta G_\varphi^h = \sum_{I=1}^{n_{node}} \sum_{J=1}^{n_{node}} \delta d_\varphi^I \left\{ \underbrace{- \int_{\mathcal{B}^e} (\mathbb{B}_\varphi^I)^T \underline{\mathbf{q}} \mathbb{B}_u^J dv \Delta \underline{\mathbf{d}}_u^J}_{\underline{\mathbf{k}}_{\varphi u}^{IJ}} - \underbrace{\int_{\mathcal{B}^e} (\mathbb{B}_\varphi^I)^T \underline{\mathbf{\alpha}} \mathbb{B}_\phi^J dv \Delta d_\phi^J}_{k_{\varphi\phi}^{IJ}} - \underbrace{\int_{\mathcal{B}^e} (\mathbb{B}_\varphi^I)^T \underline{\mathbf{\mu}} \mathbb{B}_\varphi^J dv \Delta d_\varphi^J}_{k_{\varphi\varphi}^{IJ}} \right\}. \quad (5.43)$$

5.9 Assembling procedure for the boundary value problem

For the solution of the complete boundary value problem with the number of finite elements num_{ele} , an assembling of the complete system of equations has to be done. We start with the element vectors for the virtual and incremental mechanical displacements, and electric and magnetic potentials

$$\delta \underline{\mathbf{d}}_u^e = \begin{bmatrix} \delta \underline{\mathbf{d}}_u^1 \\ \delta \underline{\mathbf{d}}_u^2 \\ \vdots \\ \delta \underline{\mathbf{d}}_u^n \end{bmatrix}, \quad \delta \underline{\mathbf{d}}_\phi^e = \begin{bmatrix} \delta d_\phi^1 \\ \delta d_\phi^2 \\ \vdots \\ \delta d_\phi^n \end{bmatrix} \quad \text{and} \quad \delta \underline{\mathbf{d}}_\varphi^e = \begin{bmatrix} \delta d_\varphi^1 \\ \delta d_\varphi^2 \\ \vdots \\ \delta d_\varphi^n \end{bmatrix}, \quad (5.44)$$

where the index n denotes the number of nodes for a finite element. Analogously, the element-wise right hand sides are allocated as

$$\underline{\mathbf{r}}_u^e = \begin{bmatrix} \underline{\mathbf{r}}_u^1 \\ \underline{\mathbf{r}}_u^2 \\ \vdots \\ \underline{\mathbf{r}}_u^n \end{bmatrix}, \quad \underline{\mathbf{r}}_\phi^e = \begin{bmatrix} r_\phi^1 \\ r_\phi^2 \\ \vdots \\ r_\phi^n \end{bmatrix} \quad \text{and} \quad \underline{\mathbf{r}}_\varphi^e = \begin{bmatrix} r_\varphi^1 \\ r_\varphi^2 \\ \vdots \\ r_\varphi^n \end{bmatrix}. \quad (5.45)$$

The element stiffness matrices are given as follows

$$\underline{\mathbf{k}}_{xy}^e = \begin{bmatrix} \underline{\mathbf{k}}_{xy}^{11} & \underline{\mathbf{k}}_{xy}^{12} & \underline{\mathbf{k}}_{xy}^{13} & \cdots & \underline{\mathbf{k}}_{xy}^{1n} \\ \underline{\mathbf{k}}_{xy}^{21} & \underline{\mathbf{k}}_{xy}^{22} & \underline{\mathbf{k}}_{xy}^{23} & \cdots & \underline{\mathbf{k}}_{xy}^{2n} \\ \underline{\mathbf{k}}_{xy}^{31} & \underline{\mathbf{k}}_{xy}^{32} & \underline{\mathbf{k}}_{xy}^{33} & \cdots & \underline{\mathbf{k}}_{xy}^{3n} \\ \vdots & \vdots & \vdots & \ddots & \vdots \\ \underline{\mathbf{k}}_{xy}^{n1} & \underline{\mathbf{k}}_{xy}^{n2} & \underline{\mathbf{k}}_{xy}^{n3} & \cdots & \underline{\mathbf{k}}_{xy}^{nn} \end{bmatrix} \quad \text{for} \quad \begin{array}{l} x = \{u, \phi, \varphi\} \\ y = \{u, \phi, \varphi\} \end{array}, \quad (5.46)$$

where the indices x and y denote the mechanical, electric, and magnetic parts. By combining the element stiffness matrices and right hand sides of the mechanical, electric and magnetic fields we allocate the complete element vectors and matrices as

$$\delta \underline{\mathbf{d}}^e = \begin{bmatrix} \delta \underline{\mathbf{d}}_u^e \\ \delta \underline{\mathbf{d}}_\phi^e \\ \delta \underline{\mathbf{d}}_\varphi^e \end{bmatrix}, \quad \Delta \underline{\mathbf{d}}^e = \begin{bmatrix} \Delta \underline{\mathbf{d}}_u^e \\ \Delta \underline{\mathbf{d}}_\phi^e \\ \Delta \underline{\mathbf{d}}_\varphi^e \end{bmatrix}, \quad \underline{\mathbf{r}}^e = \begin{bmatrix} \underline{\mathbf{r}}_u^e \\ \underline{\mathbf{r}}_\phi^e \\ \underline{\mathbf{r}}_\varphi^e \end{bmatrix}, \quad \underline{\mathbf{k}}^e = \begin{bmatrix} \underline{\mathbf{k}}_{uu}^e & \underline{\mathbf{k}}_{u\phi}^e & \underline{\mathbf{k}}_{u\varphi}^e \\ \underline{\mathbf{k}}_{\phi u}^e & \underline{\mathbf{k}}_{\phi\phi}^e & \underline{\mathbf{k}}_{\phi\varphi}^e \\ \underline{\mathbf{k}}_{\varphi u}^e & \underline{\mathbf{k}}_{\varphi\phi}^e & \underline{\mathbf{k}}_{\varphi\varphi}^e \end{bmatrix}. \quad (5.47)$$

In order to solve the complete boundary value problem with the Newton-Raphson method, a global system of equation is needed. Therefore, a global right hand side vector $\underline{\mathbf{R}}$ and a global stiffness matrix $\underline{\mathbf{K}}$ have to be used with the following assembling procedures

$$\underline{\mathbf{K}} = \mathbf{A} \sum_{e=1}^{num_{ele}} \underline{\mathbf{k}}^e, \quad \underline{\mathbf{R}} = \mathbf{A} \sum_{e=1}^{num_{ele}} \underline{\mathbf{r}}^e \quad \text{and} \quad \Delta \underline{\mathbf{D}} = \mathbf{A} \sum_{e=1}^{num_{ele}} \Delta \underline{\mathbf{d}}^e, \quad (5.48)$$

where $\Delta \underline{\mathbf{D}}$ is the global solution vector. Then, the global system of equations results in

$$\underline{\mathbf{K}} \Delta \underline{\mathbf{D}} = -\underline{\mathbf{R}}, \quad (5.49)$$

which has to be solved iteratively for nonlinear boundary value problems.

6 Two-scale homogenization of magneto-electro-mechanical problems

From a technical point of view, often only the macroscopic response of a device is of interest. Depending on the kind of application, the goal is to obtain enhanced macroscopic material properties. These can for example be high strength and good formability in dual-phase steels for the automotive industry, hard magnetic material properties for reliable data storage devices, soft magnetorheological elastomers for magnetic actuators or vibration dampers, or enhanced magneto-electric characteristics for modern smart applications. Such enhanced effective material properties are a result of the interaction between different phases on the microscopic level in composite materials. For instance, the enhanced effective properties of dual-phase steels are a result of the assembly of hard and soft mechanical properties of martensitic inclusions, with a high tensile strength, and a ferrite matrix with preferable yield strength characteristics. The properties of soft magnetorheological elastomers are obtained by a combination of the magnetic properties of the inclusions and the elastic properties of an elastomer matrix. Due to the interaction of the magnetic particles the composite reacts with a deformation and a change of the mechanical stiffness. In the case of magneto-electric composites the effective ME coupling only arises macroscopically and is not present in the individual phases. Such characteristics are called product properties.

The development of suitable macroscopic material models for micro-heterogeneous materials is a challenging task and therefore several homogenization approaches have been developed. The application of homogenization schemes for dual-phase steels or magnetorheological elastomers was for example performed in KEIP AND RAMBAUSEK [94; 95]. With the application of homogenization strategies it is not necessary to derive a suitable macroscopic material model. Instead, the overall material moduli are determined based on the properties of the individual constituents. Especially for the simulation of magneto-electric composites such approaches are a powerful tool, since the overall ME response highly depends on the phase properties, the type of the composite, as well as small variations of the microscopic morphology. Small changes of such microscopic characteristic result in different macroscopic responses, which can hardly be captured by one macroscopic model. Influences by microscopic morphologies or defects, such as pores, can easily be incorporated within homogenization approaches, such as multi-level finite element simulations, by simply varying the microscopic finite element mesh. In the following chapter several homogenization approaches are presented.

6.1 Overview on homogenization approaches

This chapter presents a small overview on some developed homogenization schemes for the determination of effective properties. Analytical homogenization strategies are for example the *dilute distribution* method, see CHRISTENSEN [31], the *Mori-Tanaka*-method, see TANAKA AND MORI [203], or *self-consistent* methods, see for instance BUDIANSKY [28], CHRISTENSEN AND LO [32], HILL [68], KRÖNER [106], WILLIS [218], ZHENG AND DU [227]. For a general overview the reader is referred to ABOUDI [2], HASHIN [60]. Such homogenization approaches are mainly based on Eshelby's equivalent eigenstrain solution, see ESHELBY [44], but are restricted to specific inclusion geometries and volume fractions. Two further well known approximation approaches of the effective properties are given

by Voigt and Reuss. In the case of the Voigt approximation, the macroscopic material moduli is determined depending on the assumption of a constant strain distribution on the microscopic level, see VOIGT [212]. In contrast to that, a constant microscopic stress distribution on the microscopic level is assumed in the Reuss approximation, see REUSS [166]. Due to the simplified assumptions of the constant stress or strain distributions, both approximations build the upper (Voigt) and lower (Reuss) bounds of the effective properties. HILL [66] postulated that the arithmetic mean of both values gives more accurate results. The three mentioned approximations of the effective elastic modulus $\bar{\mathbb{C}}$ are given by

$$\bar{\mathbb{C}}^V = \frac{1}{V} \int_{\mathcal{RVE}} \mathbb{C} \, dV, \quad \bar{\mathbb{C}}^R = \frac{1}{V} \left(\int_{\mathcal{RVE}} \mathbb{C}^{-1} \right)^{-1}, \quad \text{and} \quad \bar{\mathbb{C}}^{VRH} = \frac{1}{2} (\bar{\mathbb{C}}^V + \bar{\mathbb{C}}^R), \quad (6.1)$$

where the index VRH denotes the Voigt-Reuss-Hill arithmetic mean. Further approximations for the effective properties are given by the Hashin-Shtrikman bound, see HASHIN AND SHTRIKMAN [61], BRUGGEMAN [27], HUBER AND SCHMID [75] or BOAS [21].

In order to simulate the effect of microstructural influences on the macroscopic material behavior more precisely, multi-scale methods based on a homogenization of a much smaller length scale are quite common. Thereby, boundary value problems on the macro- and microscale are solved, where the microscopic boundary value problem is driven by the macroscopic kinematic quantities. Both scales are coupled via a macro-homogeneity condition for the homogenization of the microscopic quantities. If the finite element method is used on both scales, such method is also denoted as the FE^2 -method, which is explained in the following Section 6.2 in more detail. First-order multi-scale homogenization approaches were performed by GHOSH ET AL. [57], GUEDES AND KIKUCHI [59], KOUZNETSOVA ET AL. [101], MIEHE AND BAYREUTHER [139], MIEHE AND KOCH [141], MIEHE ET AL. [143; 144; 145], SCHRÖDER [181], SMIT ET AL. [192], TERADA ET AL. [205] or TEMIZER AND WRIGGERS [204]. The mentioned first-order homogenization schemes concern mechanical problems in the field of, for instance, nonlinear problems, finite plasticity, or viscoplasticity. Due to the large length scale separation, the macroscopic point with the attached representative volume element is assumed to be homogeneous. The macroscopic kinematic quantities are then applied homogeneously across the RVE. Second-order homogenization approaches additionally include geometric size effects and strain gradients, which are not considered in the before mentioned first-order techniques. Applications of second-order extensions are performed in, for example, GEERS ET AL. [54; 55], KACZMARCZYK ET AL. [86], KOUZNETSOVA ET AL. [102]. Extensions to multiphysics problems of multi-scale homogenization approaches were performed, for instance, in ÖZDEMİR ET AL. [155] for thermo-mechanically coupled problems, SCHRÖDER AND KEIP [185] for electro-mechanically coupled problems, KEIP AND RAMBAUSEK [94; 95] for magnetorheological elastomers, or SCHRÖDER ET AL. [188] for magneto-electro-mechanically coupled problems. For an overview and the trends in computational homogenization the reader is referred to GEERS ET AL. [56].

6.2 Homogenization based on the FE^2 -method

In this doctoral thesis a two-scale finite element homogenization scheme, the FE^2 -method, is used. For the simulation of the investigated composites the FE^2 -method is extended

to magneto-electro-mechanically coupled problems, see SCHRÖDER ET AL. [188], and described in the following. The macroscopic body of interest is discretized with a finite element mesh and considered as a homogeneous body. However, instead of deriving a suitable material model, which describes the overall behavior, a microscopic representative volume element (RVE) is assigned to each macroscopic integration point. This RVE reflects the properties of a complex realistic heterogeneous microstructure and represents the overall material behavior. The heterogeneous structure could include for example different phases, cavities, or cracks. However, the choice of a suitable RVE is not distinctive and several options exist for a periodic microstructure, see Figure 6.1 for possible RVEs of a heterogeneous composite.

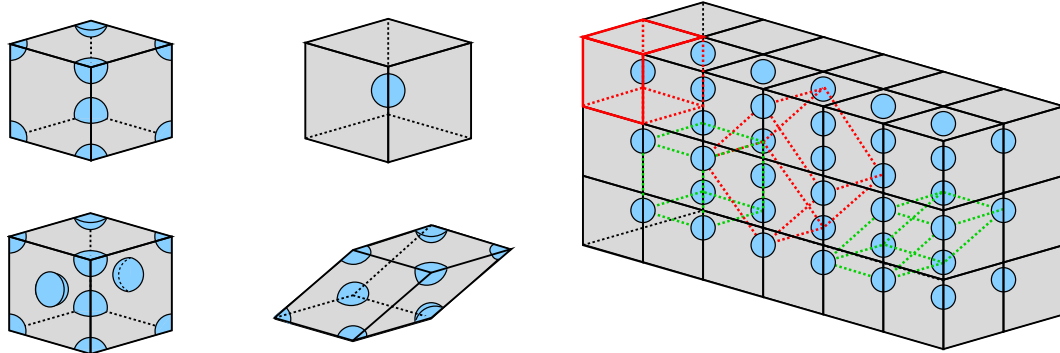


Figure 6.1: Possible representative volume elements (RVEs) for a periodic heterogeneous microstructure.

Based on the solution of a microscopic finite element boundary value problem, using appropriate boundary conditions on the RVE, a subsequent homogenization approach provides the effective properties for the macroscopic constitutive equations. This strategy automatically incorporates the influence of the interactions of the different phases on the microscopic level. In the sense of magneto-electric composites, where different structures generate varying ME effects, the FE^2 -method offers a suitable tool for the simulation of ME composites. The following schedule shows the main steps of the FE^2 -method and is visualized in Figure 6.2.

- (i) The magneto-electro-mechanical boundary conditions are applied on the macroscopic body.
- (ii) In each macroscopic integration point the strains, electric and magnetic fields are localized on the corresponding RVE.
- (iii) The microscopic boundary value problem is solved using suitable boundary conditions.
- (iv) A homogenization step yields the effective properties, including the magneto-electric coefficient, as well as the stresses, electric displacement and magnetic induction, which are given back to the corresponding macroscopic integration point.
- (v) The macroscopic boundary value problem is solved.

For nonlinear problems the steps (ii) to (v) have to be repeated until an equilibrium state on both scales is reached. In the following, the boundary value problems on both

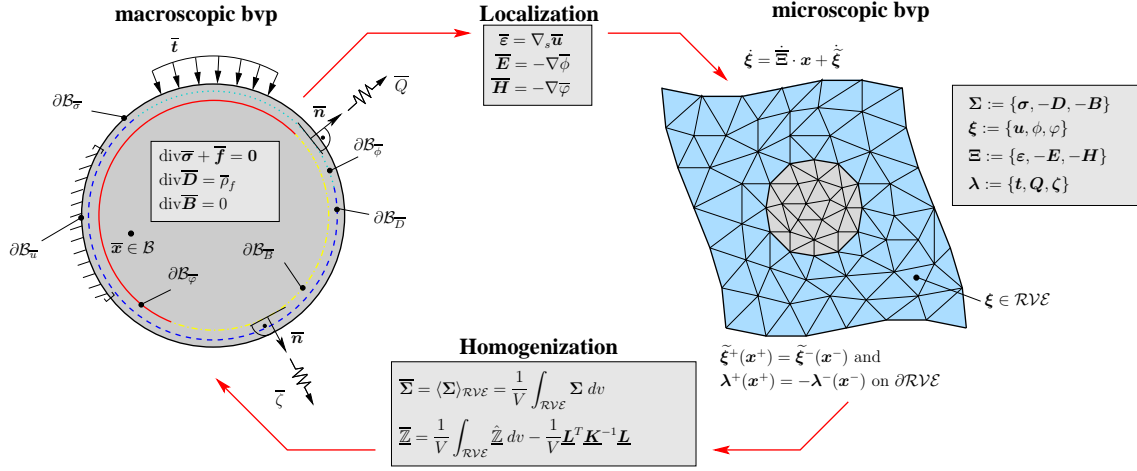


Figure 6.2: Visualization of the FE²-method, where a microscopic representative volume element (RVE) is assigned to each macroscopic integration point. The microscopic boundary value problem is driven by the macroscopic fields, localized on the RVE. A homogenization approach over the microscale provides the effective properties for the macroscopic problem.

scales will be described. The field variables on the microscopic level are denoted without additional labeling (\bullet) and the variables on the macroscale with an overline ($\bar{\bullet}$).

6.2.1 Macroscopic magneto-electro-mechanical boundary value problem

The considered body on the macroscale $\bar{B} \subset \mathbb{R}^3$ is parameterized in the macroscopic Cartesian coordinates \bar{x} . For the magneto-electro-mechanically coupled case the governing balance laws are given by the balance of linear momentum, Gauss' law of electrostatics and Gauss' law of magnetostatics as

$$\text{div}_{\bar{x}}[\bar{\sigma}] + \bar{f}_{mech} + \bar{f}_{em} = 0, \quad \text{div}_{\bar{x}}[\bar{D}] = \bar{\rho}_f \quad \text{and} \quad \text{div}_{\bar{x}}[\bar{B}] = 0 \quad \text{in } \bar{B} \quad (6.2)$$

with the divergence operator $\text{div}_{\bar{x}}$ with respect to the macroscopic variable \bar{x} . Here, we neglect the mechanical body force density \bar{f}_{mech} as well as the electromagnetic Lorentz force density \bar{f}_{em} , since the Maxwell stresses have a negligible influence in dielectric materials. Furthermore, free electric charge carriers $\bar{\rho}_f$ are neglected, since we are considering dielectric materials without free charges. The macroscopic linear strain tensor, the electric field vector and the magnetic field vector are defined as

$$\bar{\varepsilon} = \text{sym}[\text{grad}_{\bar{x}} \bar{u}], \quad \bar{E} = -\text{grad}_{\bar{x}} \bar{\phi} \quad \text{and} \quad \bar{H} = -\text{grad}_{\bar{x}} \bar{\varphi} \quad (6.3)$$

with the gradient operator $\text{grad}_{\bar{x}}$ with respect to the macroscopic variable \bar{x} . The assumption of a scalar magnetic potential is restricted to static problems of uniaxial boundary conditions. Otherwise a vector potential must be used, which would complicate the approach too much. The Dirichlet boundary conditions for the coupled case are given in terms of the displacements, the electric potential and the magnetic potential as

$$\bar{u} = \bar{u}_b \quad \text{on } \partial \bar{B}_u, \quad \bar{\phi} = \bar{\phi}_b \quad \text{on } \partial \bar{B}_\phi \quad \text{and} \quad \bar{\varphi} = \bar{\varphi}_b \quad \text{on } \partial \bar{B}_\varphi. \quad (6.4)$$

The Neumann boundary conditions can be described in terms of the surface tractions, the electric surface charge and the magnetic flux as

$$\bar{t}_b = \bar{\sigma} \cdot \bar{n} \quad \text{on } \partial \bar{B}_\sigma, \quad -\bar{Q}_b = \bar{D} \cdot \bar{n} \quad \text{on } \partial \bar{B}_D \quad \text{and} \quad -\bar{\zeta}_b = \bar{B} \cdot \bar{n} \quad \text{on } \partial \bar{B}_B. \quad (6.5)$$

Here, \bar{n} denotes the outward unit normal vector of the surface $\partial \bar{B}$.

6.2.2 Microscopic magneto-electro-mechanical boundary value problem

In the sense of the FE²-method no macroscopic thermodynamic potential is postulated to obtain the overall material behavior, instead they are obtained through a homogenization step over adjacent representative volume elements, requiring the solution of the microscopic boundary value problem. The adjacent volume elements on the microscopic level $\mathcal{RVE} \subset \mathbb{R}^3$ are parameterized in the microscopic coordinates \mathbf{x} . Since, we suppose a relatively large scale separation between the macro- and the microscopic level, with the proportion of the lengths $l_{macro} \gg l_{micro}$, we can neglect the body forces on microscopic level, such that the balance of linear momentum and Gauss' laws of electrostatics as well as magnetostatics appear as

$$\operatorname{div}_{\mathbf{x}}[\boldsymbol{\sigma}] = \mathbf{0} \ , \quad \operatorname{div}_{\mathbf{x}}[\mathbf{D}] = 0 \quad \text{and} \quad \operatorname{div}_{\mathbf{x}}[\mathbf{B}] = 0 \quad \text{in } \mathcal{RVE} \ . \quad (6.6)$$

Analogously, the free charge carriers in equation (6.2)₂ on the microscopic level are neglected. The microscopic linear strain tensor, the electric field vector and the magnetic field vector are defined as

$$\boldsymbol{\varepsilon} = \operatorname{sym}[\operatorname{grad}_{\mathbf{x}} \mathbf{u}] \ , \quad \mathbf{E} = -\operatorname{grad}_{\mathbf{x}} \phi \quad \text{and} \quad \mathbf{H} = -\operatorname{grad}_{\mathbf{x}} \varphi \ . \quad (6.7)$$

Here, the divergence as well as the gradient operator $\operatorname{div}_{\mathbf{x}}$ and $\operatorname{grad}_{\mathbf{x}}$ are defined with respect to the microscopic variables \mathbf{x} . In order to solve the microscopic boundary value problem, suitable boundary conditions have to be applied on the \mathcal{RVE} , which are derived in the following.

6.2.3 Scale transition and definitions of microscopic boundary conditions

The effective macroscopic properties are determined by a homogenization approach regarding the microscopic quantities. Beforehand, the macroscopic quantities in each macroscopic integration point are distributed on the corresponding \mathcal{RVE} in a localization step. To solve the boundary value problem on the microscale, suitable boundary conditions have to be applied on the \mathcal{RVE} , which are derived from a generalized Hill-Mandel condition. In HILL [67] the Hill condition states that the macroscopic stress power is equal to the volume average of the microscopic stress power. Based on this assumption we derive a generalized macro-homogeneity condition for the magneto-electro-mechanically coupled case as

$$\bar{\boldsymbol{\sigma}} : \dot{\bar{\boldsymbol{\varepsilon}}} - \bar{\mathbf{D}} \cdot \dot{\bar{\mathbf{E}}} - \bar{\mathbf{B}} \cdot \dot{\bar{\mathbf{H}}} = \frac{1}{V} \int_{\mathcal{RVE}} \boldsymbol{\sigma} : \dot{\boldsymbol{\varepsilon}} \, dv - \frac{1}{V} \int_{\mathcal{RVE}} \mathbf{D} \cdot \dot{\mathbf{E}} \, dv - \frac{1}{V} \int_{\mathcal{RVE}} \mathbf{B} \cdot \dot{\mathbf{H}} \, dv \ . \quad (6.8)$$

The latter equation can be satisfied if the individual mechanical, electric and magnetic conditions

$$\begin{aligned} \mathcal{P}_{mech} &= \bar{\boldsymbol{\sigma}} : \dot{\bar{\boldsymbol{\varepsilon}}} - \frac{1}{V} \int_{\mathcal{RVE}} \boldsymbol{\sigma} : \dot{\boldsymbol{\varepsilon}} \, dv \ , \\ \mathcal{P}_{elec} &= \bar{\mathbf{D}} \cdot \dot{\bar{\mathbf{E}}} - \frac{1}{V} \int_{\mathcal{RVE}} \mathbf{D} \cdot \dot{\mathbf{E}} \, dv \ , \\ \mathcal{P}_{magn} &= \bar{\mathbf{B}} \cdot \dot{\bar{\mathbf{H}}} - \frac{1}{V} \int_{\mathcal{RVE}} \mathbf{B} \cdot \dot{\mathbf{H}} \, dv \end{aligned} \quad (6.9)$$

hold independently, see for example SCHRÖDER [182] for the electro-mechanical case. We can rewrite the latter expressions based on the explanations of HILL [69]. By using the balance laws and the definitions of the surface tractions \mathbf{t} , Q and ζ we obtain

$$\begin{aligned}\mathcal{P}_{mech} &= \frac{1}{V} \int_{\partial\mathcal{R}\nu\mathcal{E}} (\mathbf{t} - \bar{\boldsymbol{\sigma}} \cdot \mathbf{n}) \cdot (\dot{\mathbf{u}} - \dot{\bar{\boldsymbol{\varepsilon}}} \cdot \mathbf{x}) \, da , \\ \mathcal{P}_{elec} &= \frac{1}{V} \int_{\partial\mathcal{R}\nu\mathcal{E}} (Q + \bar{\mathbf{D}} \cdot \mathbf{n}) \cdot (\dot{\phi} + \dot{\bar{\mathbf{E}}} \cdot \mathbf{x}) \, da , \\ \mathcal{P}_{magn} &= \frac{1}{V} \int_{\partial\mathcal{R}\nu\mathcal{E}} (\zeta + \bar{\mathbf{B}} \cdot \mathbf{n}) \cdot (\dot{\varphi} + \dot{\bar{\mathbf{H}}} \cdot \mathbf{x}) \, da .\end{aligned}\tag{6.10}$$

From the latter equations we can directly derive the Dirichlet and Neumann conditions

$$\begin{aligned}\mathbf{t} &= \bar{\boldsymbol{\sigma}} \cdot \mathbf{n} \quad \text{or} \quad \dot{\mathbf{u}} = \dot{\bar{\boldsymbol{\varepsilon}}} \cdot \mathbf{x} \quad \text{on} \quad \partial\mathcal{R}\nu\mathcal{E} , \\ Q &= -\bar{\mathbf{D}} \cdot \mathbf{n} \quad \text{or} \quad \dot{\phi} = \dot{\bar{\mathbf{E}}} \cdot \mathbf{x} \quad \text{on} \quad \partial\mathcal{R}\nu\mathcal{E} , \\ \zeta &= -\bar{\mathbf{B}} \cdot \mathbf{n} \quad \text{on} \quad \dot{\varphi} = \dot{\bar{\mathbf{H}}} \cdot \mathbf{x} \quad \text{on} \quad \partial\mathcal{R}\nu\mathcal{E} ,\end{aligned}\tag{6.11}$$

which fulfill the conditions in Equation (6.10). Furthermore, the macro-homogeneity condition can be fulfilled with the constraint conditions by Voigt, which state that $\boldsymbol{\varepsilon} = \bar{\boldsymbol{\varepsilon}}$, $\mathbf{E} = \bar{\mathbf{E}}$ and $\mathbf{H} = \bar{\mathbf{H}}$, respectively, resulting in homogeneous microscopic fields $\boldsymbol{\varepsilon}$, \mathbf{E} and \mathbf{H} . Another assumption is given by the constraint conditions by Reuss. Then the microscopic stresses, dielectric displacement and magnetic induction are equal to their macroscopic counterparts with $\boldsymbol{\sigma} = \bar{\boldsymbol{\sigma}}$, $\mathbf{D} = \bar{\mathbf{D}}$ and $\mathbf{B} = \bar{\mathbf{B}}$, respectively. In this thesis periodic boundary conditions are used, motivated by a periodic arrangement of the volume elements. The boundary conditions are obtained by a decomposition of the microscopic quantities into a constant macroscopic part ($\bar{\bullet}$) and a fluctuation field ($\tilde{\bullet}$) as

$$\boldsymbol{\varepsilon} = \bar{\boldsymbol{\varepsilon}} + \tilde{\boldsymbol{\varepsilon}} , \quad \mathbf{E} = \bar{\mathbf{E}} + \tilde{\mathbf{E}} \quad \text{and} \quad \mathbf{H} = \bar{\mathbf{H}} + \tilde{\mathbf{H}} .\tag{6.12}$$

The displacement fields as well as the electric and magnetic potential are obtained by

$$\mathbf{u} = \bar{\boldsymbol{\varepsilon}} \cdot \mathbf{x} + \tilde{\mathbf{u}} , \quad \phi = \bar{\mathbf{E}} \cdot \mathbf{x} + \tilde{\phi} \quad \text{and} \quad \varphi = \bar{\mathbf{H}} \cdot \mathbf{x} + \tilde{\varphi} .\tag{6.13}$$

Due to the large difference in length scale, the decomposition into a constant homogeneously distributed part depending on the macroscopic quantities can be motivated. However, such constant distribution is not correct for microscopic heterogeneities, which is for instance the case in composite materials. Field variations, which do not coincide with the homogeneous distribution triggered by inhomogeneities, are described by the fluctuation part. Analogous to the decomposition of the quantities in equation (6.12) the microscopic stresses, dielectric displacement, and magnetic induction can be decomposed as

$$\boldsymbol{\sigma} = \bar{\boldsymbol{\sigma}} + \tilde{\boldsymbol{\sigma}} , \quad \mathbf{D} = \bar{\mathbf{D}} + \tilde{\mathbf{D}} \quad \text{and} \quad \mathbf{B} = \bar{\mathbf{B}} + \tilde{\mathbf{B}} .\tag{6.14}$$

Periodicity is postulated as

$$\begin{aligned}\tilde{\mathbf{u}}(\mathbf{x}^+) &= \tilde{\mathbf{u}}(\mathbf{x}^-) \quad \text{and} \quad \mathbf{t}(\mathbf{x}^+) = -\mathbf{t}(\mathbf{x}^-) , \\ \tilde{\phi}(\mathbf{x}^+) &= \tilde{\phi}(\mathbf{x}^-) \quad \text{and} \quad Q(\mathbf{x}^+) = -Q(\mathbf{x}^-) , \\ \tilde{\varphi}(\mathbf{x}^+) &= \tilde{\varphi}(\mathbf{x}^-) \quad \text{and} \quad \zeta(\mathbf{x}^+) = -\zeta(\mathbf{x}^-)\end{aligned}\tag{6.15}$$

for the mechanical, electric and magnetic quantities, see Figure 6.3 for an illustration of periodicity.

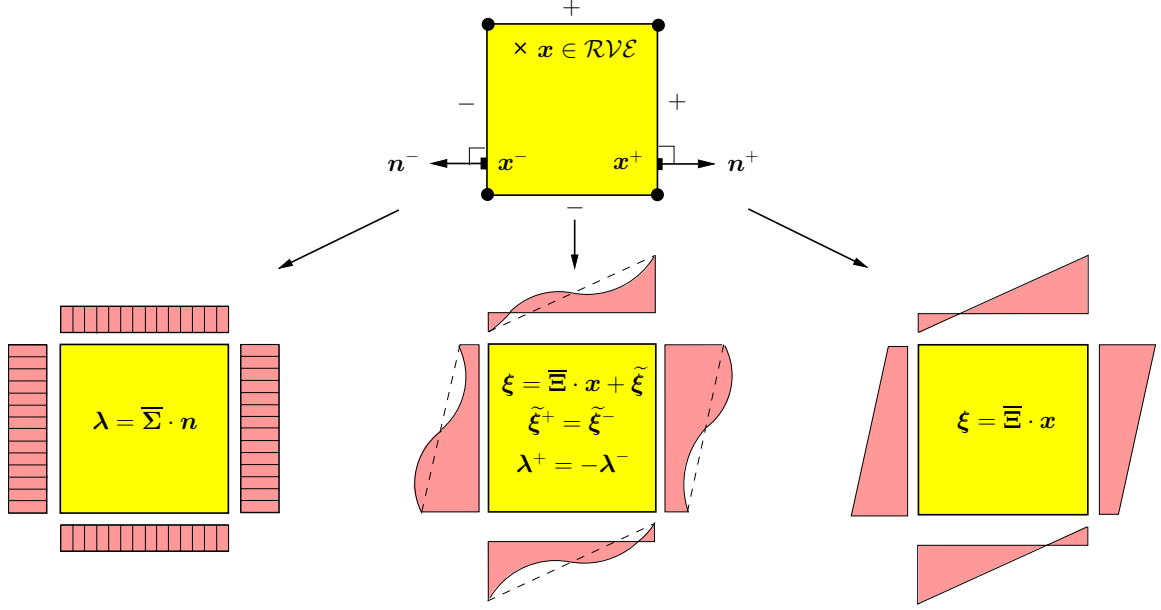


Figure 6.3: Illustration of the microscopic magneto-electro-mechanical boundary conditions with the decomposition of the microscopic fields into a constant part and a fluctuation field.

6.2.4 Consistent linearization of macroscopic field quantities

In the sense of a scale transition within the FE²-method, the boundary value problems on the macro- and microscale have to be solved. To achieve a quadratic convergence of the Newton-Raphson iteration scheme for the solution of the problems on both scales, a consistent linearization of the macroscopic weak forms is required. For magneto-electro-mechanically coupled problems the macroscopic constitutive equations can be written in the following compact notation

$$\underbrace{\begin{bmatrix} \Delta \bar{\sigma} \\ -\Delta \bar{D} \\ -\Delta \bar{B} \end{bmatrix}}_{\Delta \bar{\Sigma}} = \underbrace{\begin{bmatrix} \bar{C} & -\bar{e}^T & -\bar{q}^T \\ -\bar{e} & -\bar{\epsilon} & -\bar{\alpha}^T \\ -\bar{q} & -\bar{\alpha} & -\bar{\mu} \end{bmatrix}}_{\bar{\mathbb{Z}}} \underbrace{\begin{bmatrix} \Delta \bar{\epsilon} \\ \Delta \bar{E} \\ \Delta \bar{H} \end{bmatrix}}_{\Delta \bar{\mathbb{X}}}. \quad (6.16)$$

The effective mechanical, dielectric, magnetic, electro-mechanical, magneto-mechanical and magneto-electric moduli are determined as follows

$$\begin{aligned} \bar{C} &= \partial_{\bar{\epsilon}} \bar{\sigma}, \quad \bar{\epsilon} = \partial_{\bar{E}} \bar{D}, \quad \bar{\mu} = \partial_{\bar{H}} \bar{B}, \quad \bar{e} = \partial_{\bar{\epsilon}} \bar{D} = [-\partial_{\bar{E}} \bar{\sigma}]^T, \\ \bar{q} &= \partial_{\bar{\epsilon}} \bar{B} = [-\partial_{\bar{H}} \bar{\sigma}]^T \quad \text{and} \quad \bar{\alpha} = \partial_{\bar{E}} \bar{B} = [\partial_{\bar{H}} \bar{D}]^T, \end{aligned} \quad (6.17)$$

where $[\{\bar{e}, \bar{q}\}^T]_{ijk} := \{\bar{e}, \bar{q}\}_{kij}$. In the latter three equations Maxwell's relations have been applied, see NYE [153]. Assuming that no cavities or cracks are present on the microscopic level, the macroscopic stress, dielectric displacement and magnetic induction can be computed as simple volume averages over the microscopic counterparts. Thus, the effective

moduli can be reformulated as

$$\begin{aligned}\bar{\mathbb{C}} &= \frac{\partial \langle \boldsymbol{\sigma} \rangle_V}{\partial \bar{\boldsymbol{\epsilon}}}, \quad \bar{\boldsymbol{\epsilon}} = \frac{\partial \langle \mathbf{D} \rangle_V}{\partial \bar{\mathbf{E}}}, \quad \bar{\boldsymbol{\mu}} = \frac{\partial \langle \mathbf{B} \rangle_V}{\partial \bar{\mathbf{H}}}, \\ \bar{\mathbf{e}} = \frac{\partial \langle \mathbf{D} \rangle_V}{\partial \bar{\boldsymbol{\epsilon}}} &= \left[-\frac{\partial \langle \boldsymbol{\sigma} \rangle_V}{\partial \bar{\mathbf{E}}} \right]^T, \quad \bar{\mathbf{q}} = \frac{\partial \langle \mathbf{B} \rangle_V}{\partial \bar{\boldsymbol{\epsilon}}} = \left[-\frac{\partial \langle \boldsymbol{\sigma} \rangle_V}{\partial \bar{\mathbf{H}}} \right]^T, \\ \bar{\boldsymbol{\alpha}} &= \frac{\partial \langle \mathbf{B} \rangle_V}{\partial \bar{\mathbf{E}}} = \left[\frac{\partial \langle \mathbf{D} \rangle_V}{\partial \bar{\mathbf{H}}} \right]^T.\end{aligned}\tag{6.18}$$

Using periodic boundary conditions, the computation of the macroscopic moduli is obviously not straight-forward. With the application of the chain rule and the additive decomposition of the microscopic quantities into a macroscopic and a fluctuation part, we obtain the overall material tangent as

$$\bar{\mathbb{Z}} = \frac{\partial \langle \boldsymbol{\Sigma}(\mathbb{X}) \rangle_V}{\partial \bar{\mathbb{X}}} = \left\langle \frac{\partial \boldsymbol{\Sigma}(\mathbb{X})}{\partial \mathbb{X}} \frac{\partial (\bar{\mathbb{X}} + \tilde{\mathbb{X}})}{\partial \bar{\mathbb{X}}} \right\rangle_V = \underbrace{\langle \mathbb{Z} \rangle_V}_{\mathbb{Z}^{\text{Voigt}}} + \underbrace{\left\langle \mathbb{Z} \frac{\partial \tilde{\mathbb{X}}}{\partial \bar{\mathbb{X}}} \right\rangle_V}_{\mathbb{Z}^{\text{Soft}}}\tag{6.19}$$

with the abbreviations given in equation (6.16). Now, the effective modulus is decomposed into two parts. The first part of the latter equation $\mathbb{Z}^{\text{Voigt}}$ is denoted as the Voigt upper bound of the material tangent and is defined as a simple volume average of the microscopic moduli. The second part contains the partial derivatives of the microscopic fluctuation fields with respect to their macroscopic counterparts. This softening term of the overall tangent will be computed by using the FE discretization of the microscopic boundary value problem. A reformulation of expression (6.16) with the chain rule shown in Equation (6.19) gives the linearized constitutive relations

$$\begin{bmatrix} \Delta \bar{\boldsymbol{\sigma}} \\ -\Delta \bar{\mathbf{D}} \\ -\Delta \bar{\mathbf{B}} \end{bmatrix} = \frac{1}{V} \left(\int_{\mathcal{B}} \begin{bmatrix} \mathbb{C} & -\mathbf{e}^T & -\mathbf{q}^T \\ -\mathbf{e} & -\boldsymbol{\epsilon} & -\boldsymbol{\alpha}^T \\ -\mathbf{q} & -\boldsymbol{\alpha} & -\boldsymbol{\mu} \end{bmatrix} + \begin{bmatrix} \mathbb{C} & -\mathbf{e}^T & -\mathbf{q}^T \\ -\mathbf{e} & -\boldsymbol{\epsilon} & -\boldsymbol{\alpha}^T \\ -\mathbf{q} & -\boldsymbol{\alpha} & -\boldsymbol{\mu} \end{bmatrix} \begin{bmatrix} \frac{\partial \tilde{\boldsymbol{\epsilon}}}{\partial \bar{\boldsymbol{\epsilon}}} \\ \frac{\partial \tilde{\mathbf{E}}}{\partial \bar{\mathbf{E}}} \\ \frac{\partial \tilde{\mathbf{H}}}{\partial \bar{\mathbf{H}}} \end{bmatrix} dv \right) \begin{bmatrix} \Delta \bar{\boldsymbol{\epsilon}} \\ \Delta \bar{\mathbf{E}} \\ \Delta \bar{\mathbf{H}} \end{bmatrix}.\tag{6.20}$$

The microscopic moduli are obtained from a microscopic thermodynamic potential ψ with

$$\begin{aligned}\mathbb{C} &= \frac{\partial^2 \psi}{\partial \boldsymbol{\epsilon} \partial \boldsymbol{\epsilon}}, \quad \boldsymbol{\epsilon} = -\frac{\partial^2 \psi}{\partial \mathbf{E} \partial \mathbf{E}}, \quad \boldsymbol{\mu} = -\frac{\partial^2 \psi}{\partial \mathbf{H} \partial \mathbf{H}}, \\ \mathbf{e} = -\frac{\partial^2 \psi}{\partial \boldsymbol{\epsilon} \partial \mathbf{E}} &= \left[-\frac{\partial^2 \psi}{\partial \mathbf{E} \partial \boldsymbol{\epsilon}} \right]^T, \quad \mathbf{q} = -\frac{\partial^2 \psi}{\partial \boldsymbol{\epsilon} \partial \mathbf{H}} = \left[-\frac{\partial^2 \psi}{\partial \mathbf{H} \partial \boldsymbol{\epsilon}} \right]^T, \\ \boldsymbol{\alpha} &= -\frac{\partial^2 \psi}{\partial \mathbf{E} \partial \mathbf{H}} = -\left[\frac{\partial^2 \psi}{\partial \mathbf{H} \partial \mathbf{E}} \right]^T\end{aligned}\tag{6.21}$$

with $[\{e, q\}^T]_{ijk} := \{e, q\}_{kij}$ again using Maxwell's relations in the latter three equations. In order to derive the overall material tangent the microscopic boundary value problems have to be solved. The weak form of the balance of momentum is given by the expression

$$G_u = - \int_{\mathcal{R} \vee \mathcal{E}} \delta \tilde{\mathbf{u}}^T \cdot \text{div} \boldsymbol{\sigma} \, dv = \int_{\mathcal{R} \vee \mathcal{E}} \delta \tilde{\boldsymbol{\epsilon}} : \boldsymbol{\sigma} \, dv - \int_{\partial \mathcal{R} \vee \mathcal{E}} \delta \tilde{\mathbf{u}} \cdot (\boldsymbol{\sigma} \cdot \mathbf{n}) \, da.\tag{6.22}$$

Analogously, we obtain the microscopic weak form of Gauss' law of electrostatics with

$$G_\phi = - \int_{\mathcal{RV}\mathcal{E}} \delta\tilde{\phi} \operatorname{div} \mathbf{D} \, dv = - \int_{\mathcal{RV}\mathcal{E}} \delta\tilde{\mathbf{E}} \cdot \mathbf{D} \, dv - \int_{\partial\mathcal{RV}\mathcal{E}} \delta\tilde{\phi} (\mathbf{D} \cdot \mathbf{n}) \, da \quad (6.23)$$

and the microscopic weak form of Gauss' law of magnetostatics with

$$G_\varphi = - \int_{\mathcal{RV}\mathcal{E}} \delta\tilde{\varphi} \operatorname{div} \mathbf{B} \, dv = - \int_{\mathcal{RV}\mathcal{E}} \delta\tilde{\mathbf{H}} \cdot \mathbf{B} \, dv - \int_{\partial\mathcal{RV}\mathcal{E}} \delta\tilde{\varphi} (\mathbf{B} \cdot \mathbf{n}) \, da \quad (6.24)$$

with the definitions $\delta\tilde{\boldsymbol{\varepsilon}} := \operatorname{sym}[\operatorname{grad} \delta\tilde{\mathbf{u}}]$, $\delta\tilde{\mathbf{E}} := -\operatorname{grad} \delta\tilde{\phi}$ and $\delta\tilde{\mathbf{H}} := -\operatorname{grad} \delta\tilde{\varphi}$. The linearizations of the above weak forms yield the linear increment of the virtual mechanical work

$$\Delta G_u = \int_{\mathcal{RV}\mathcal{E}} \delta\tilde{\boldsymbol{\varepsilon}} : \mathbb{C} : \Delta\tilde{\boldsymbol{\varepsilon}} \, dv - \int_{\mathcal{RV}\mathcal{E}} \delta\tilde{\boldsymbol{\varepsilon}} : \mathbf{e}^T \cdot \Delta\tilde{\mathbf{E}} \, dv - \int_{\mathcal{RV}\mathcal{E}} \delta\tilde{\boldsymbol{\varepsilon}} : \mathbf{q}^T \cdot \Delta\tilde{\mathbf{H}} \, dv \quad (6.25)$$

the linear increment of the virtual electric work

$$\Delta G_\phi = - \int_{\mathcal{RV}\mathcal{E}} \delta\tilde{\mathbf{E}} \cdot \mathbf{e} : \Delta\tilde{\boldsymbol{\varepsilon}} \, dv - \int_{\mathcal{RV}\mathcal{E}} \delta\tilde{\mathbf{E}} \cdot \boldsymbol{\varepsilon} \cdot \Delta\tilde{\mathbf{E}} \, dv - \int_{\mathcal{RV}\mathcal{E}} \delta\tilde{\mathbf{E}} \cdot \boldsymbol{\alpha}^T \cdot \Delta\tilde{\mathbf{H}} \, dv \quad (6.26)$$

and the linear increment of the virtual magnetic work

$$\Delta G_\varphi = - \int_{\mathcal{RV}\mathcal{E}} \delta\tilde{\mathbf{H}} \cdot \mathbf{q} : \Delta\tilde{\boldsymbol{\varepsilon}} \, dv - \int_{\mathcal{RV}\mathcal{E}} \delta\tilde{\mathbf{H}} \cdot \boldsymbol{\alpha} \cdot \Delta\tilde{\mathbf{E}} \, dv - \int_{\mathcal{RV}\mathcal{E}} \delta\tilde{\mathbf{H}} \cdot \boldsymbol{\mu} \cdot \Delta\tilde{\mathbf{H}} \, dv. \quad (6.27)$$

For the solution of the microscopic boundary value problems, a finite element discretization is performed, which is discussed in detail in Section 5.7. In the following a vector-matrix notation will be used and all appearing vectors and matrices will be labeled with an underline as $(\underline{\bullet})$, see Section 5.4 for the introduction of the Voigt notation. Since the macroscopic strain, electric and magnetic potential are constant throughout the $\mathcal{RV}\mathcal{E}$, only the fluctuation fields are discretized for the solution of the microscopic boundary value problem with

$$\begin{aligned} \{\underline{\tilde{\mathbf{u}}}, \delta\underline{\tilde{\mathbf{u}}}, \Delta\underline{\tilde{\mathbf{u}}}\} &= \sum_{I=1}^{n_{node}} N_u^I \{\underline{\tilde{\mathbf{d}}}_u^I, \delta\underline{\tilde{\mathbf{d}}}_u^I, \Delta\underline{\tilde{\mathbf{d}}}_u^I\}, \\ \{\tilde{\phi}, \delta\tilde{\phi}, \Delta\tilde{\phi}\} &= \sum_{I=1}^{n_{node}} N_\phi^I \{\tilde{d}_\phi^I, \delta\tilde{d}_\phi^I, \Delta\tilde{d}_\phi^I\}, \\ \{\tilde{\varphi}, \delta\tilde{\varphi}, \Delta\tilde{\varphi}\} &= \sum_{I=1}^{n_{node}} N_\varphi^I \{\tilde{d}_\varphi^I, \delta\tilde{d}_\varphi^I, \Delta\tilde{d}_\varphi^I\}, \end{aligned} \quad (6.28)$$

where N^I contains the classical shape-functions associated with node I and the expressions $\{\underline{\tilde{\mathbf{d}}}_u, \underline{\tilde{d}}_\phi, \underline{\tilde{d}}_\varphi\}$ denote the nodal displacement, the electric and magnetic potential. We approximate the actual, virtual, and incremental fluctuation fields of the deformation, the electric as well as the magnetic field with

$$\begin{aligned} \underline{\tilde{\boldsymbol{\varepsilon}}} &= \mathbb{B}_u^e \underline{\tilde{\mathbf{d}}}_u^e, & \delta\underline{\tilde{\boldsymbol{\varepsilon}}} &= \mathbb{B}_u^e \delta\underline{\tilde{\mathbf{d}}}_u^e, & \Delta\underline{\tilde{\boldsymbol{\varepsilon}}} &= \mathbb{B}_u^e \Delta\underline{\tilde{\mathbf{d}}}_u^e \\ \underline{\tilde{\mathbf{E}}} &= \mathbb{B}_\phi^e \underline{\tilde{d}}_\phi^e, & \delta\underline{\tilde{\mathbf{E}}} &= \mathbb{B}_\phi^e \delta\underline{\tilde{d}}_\phi^e, & \Delta\underline{\tilde{\mathbf{E}}} &= \mathbb{B}_\phi^e \Delta\underline{\tilde{d}}_\phi^e, \\ \underline{\tilde{\mathbf{H}}} &= \mathbb{B}_\varphi^e \underline{\tilde{d}}_\varphi^e, & \delta\underline{\tilde{\mathbf{H}}} &= \mathbb{B}_\varphi^e \delta\underline{\tilde{d}}_\varphi^e, & \Delta\underline{\tilde{\mathbf{H}}} &= \mathbb{B}_\varphi^e \Delta\underline{\tilde{d}}_\varphi^e \end{aligned} \quad (6.29)$$

with the $\underline{\mathbb{B}}^e$ -matrices containing the partial derivatives of the shape-functions with respect to the reference coordinates. Substituting the latter approximations into the linear increments of the weak forms yields the discrete representation of the mechanical part

$$\Delta G_u^{int,h} = \sum_{e=1}^{num_{ele}} (\delta \tilde{\underline{\mathbf{d}}}_u)^T \left\{ \underbrace{\int_{\mathcal{RV}\mathcal{E}} (\underline{\mathbb{B}}_u^e)^T \underline{\mathbb{C}} \underline{\mathbb{B}}_u^e dv}_{\underline{\mathbf{k}}_{uu}^e} \Delta \tilde{\underline{\mathbf{d}}}_u - \underbrace{\int_{\mathcal{RV}\mathcal{E}} (\underline{\mathbb{B}}_u^e)^T \underline{\mathbf{e}}^T \underline{\mathbb{B}}_\phi^e dv}_{\underline{\mathbf{k}}_{u\phi}^e} \Delta \tilde{\underline{\mathbf{d}}}_\phi - \underbrace{\int_{\mathcal{RV}\mathcal{E}} (\underline{\mathbb{B}}_u^e)^T \underline{\mathbf{q}}^T \underline{\mathbb{B}}_\varphi^e dv}_{\underline{\mathbf{k}}_{u\varphi}^e} \Delta \tilde{\underline{\mathbf{d}}}_\varphi \right\}, \quad (6.30)$$

the discrete representation of the electric part of the weak form

$$\Delta G_\phi^{int,h} = \sum_{e=1}^{num_{ele}} (\delta \tilde{\underline{\mathbf{d}}}_\phi)^T \left\{ \underbrace{- \int_{\mathcal{RV}\mathcal{E}} (\underline{\mathbb{B}}_\phi^e)^T \underline{\mathbf{e}} \underline{\mathbb{B}}_u^e dv}_{\underline{\mathbf{k}}_{\phi u}^e} \Delta \tilde{\underline{\mathbf{d}}}_u - \underbrace{\int_{\mathcal{RV}\mathcal{E}} (\underline{\mathbb{B}}_\phi^e)^T \underline{\mathbf{e}} \underline{\mathbb{B}}_\phi^e dv}_{\underline{\mathbf{k}}_{\phi\phi}^e} \Delta \tilde{\underline{\mathbf{d}}}_\phi - \underbrace{\int_{\mathcal{RV}\mathcal{E}} (\underline{\mathbb{B}}_\phi^e)^T \underline{\boldsymbol{\alpha}}^T \underline{\mathbb{B}}_\varphi^e dv}_{\underline{\mathbf{k}}_{\phi\varphi}^e} \Delta \tilde{\underline{\mathbf{d}}}_\varphi \right\}, \quad (6.31)$$

and the magnetic part

$$\Delta G_\varphi^{int,h} = \sum_{e=1}^{num_{ele}} (\delta \tilde{\underline{\mathbf{d}}}_\varphi)^T \left\{ \underbrace{- \int_{\mathcal{RV}\mathcal{E}} (\underline{\mathbb{B}}_\varphi^e)^T \underline{\mathbf{q}} \underline{\mathbb{B}}_u^e dv}_{\underline{\mathbf{k}}_{\varphi u}^e} \Delta \tilde{\underline{\mathbf{d}}}_u - \underbrace{\int_{\mathcal{RV}\mathcal{E}} (\underline{\mathbb{B}}_\varphi^e)^T \underline{\boldsymbol{\alpha}} \underline{\mathbb{B}}_\phi^e dv}_{\underline{\mathbf{k}}_{\varphi\phi}^e} \Delta \tilde{\underline{\mathbf{d}}}_\phi - \underbrace{\int_{\mathcal{RV}\mathcal{E}} (\underline{\mathbb{B}}_\varphi^e)^T \underline{\boldsymbol{\mu}} \underline{\mathbb{B}}_\varphi^e dv}_{\underline{\mathbf{k}}_{\varphi\varphi}^e} \Delta \tilde{\underline{\mathbf{d}}}_\varphi \right\}. \quad (6.32)$$

Let now num_{ele} denote the number of finite elements of the microscopic boundary value problem. Then, the FE assembly procedure yields, with the element residual vectors $\underline{\mathbf{r}}_u^e$, $\underline{\mathbf{r}}_\phi^e$, $\underline{\mathbf{r}}_\varphi^e$, the compact notation

$$\sum_{e=1}^{num_{ele}} \begin{bmatrix} \delta \tilde{\underline{\mathbf{d}}}_u^e \\ \delta \tilde{\underline{\mathbf{d}}}_\phi^e \\ \delta \tilde{\underline{\mathbf{d}}}_\varphi^e \end{bmatrix}^T \left(\underbrace{\begin{bmatrix} \underline{\mathbf{k}}_{uu}^e & \underline{\mathbf{k}}_{u\phi}^e & \underline{\mathbf{k}}_{u\varphi}^e \\ \underline{\mathbf{k}}_{\phi u}^e & \underline{\mathbf{k}}_{\phi\phi}^e & \underline{\mathbf{k}}_{\phi\varphi}^e \\ \underline{\mathbf{k}}_{\varphi u}^e & \underline{\mathbf{k}}_{\varphi\phi}^e & \underline{\mathbf{k}}_{\varphi\varphi}^e \end{bmatrix}}_{\underline{\mathbf{k}}^e} \underbrace{\begin{bmatrix} \Delta \tilde{\underline{\mathbf{d}}}_u^e \\ \Delta \tilde{\underline{\mathbf{d}}}_\phi^e \\ \Delta \tilde{\underline{\mathbf{d}}}_\varphi^e \end{bmatrix}}_{\Delta \tilde{\underline{\mathbf{d}}}^e} + \underbrace{\begin{bmatrix} \underline{\mathbf{r}}_u^e \\ \underline{\mathbf{r}}_\phi^e \\ \underline{\mathbf{r}}_\varphi^e \end{bmatrix}}_{\underline{\mathbf{r}}^e} \right) = 0 \quad (6.33)$$

with the definition of the incremental element solution vector $\Delta\tilde{\mathbf{d}}^e$. A standard assembly procedure of the element stiffness matrix $\underline{\mathbf{k}}^e$ and the element residual vector $\underline{\mathbf{r}}^e$ leads to the system of equations

$$\underline{\mathbf{K}}\Delta\tilde{\mathbf{D}} = -\underline{\mathbf{R}} \quad \text{with} \quad \underline{\mathbf{K}} = \mathbf{A} \sum_{e=1}^{num_{ele}} \underline{\mathbf{k}}^e \quad \text{and} \quad \underline{\mathbf{R}} = \mathbf{A} \sum_{e=1}^{num_{ele}} \underline{\mathbf{r}}^e, \quad (6.34)$$

where \mathbf{A} denotes suitable assembly operators, $\underline{\mathbf{K}}$ denotes the global stiffness matrix and $\underline{\mathbf{R}}$ is the global residual vector on the microscopic level. In order to solve the global microscopic problem we compute the global solution vector as

$$\Delta\tilde{\mathbf{D}} = -\underline{\mathbf{K}}^{-1}\underline{\mathbf{R}}. \quad (6.35)$$

In order to derive the complete overall material tangent, the partial derivatives of the microscopic fluctuation fields with respect to their macroscopic counterparts have to be computed. Thus, we linearize the microscopic weak forms at an equilibrium state. For the mechanical weak form, this results in

$$\int_{\mathcal{R}\mathcal{V}\mathcal{E}} \delta\tilde{\boldsymbol{\varepsilon}} : \mathbf{C} : (\Delta\bar{\boldsymbol{\varepsilon}} + \Delta\tilde{\boldsymbol{\varepsilon}}) dv - \int_{\mathcal{R}\mathcal{V}\mathcal{E}} \delta\tilde{\boldsymbol{\varepsilon}} : \mathbf{e}^T \cdot (\Delta\bar{\mathbf{E}} + \Delta\tilde{\mathbf{E}}) dv - \int_{\mathcal{R}\mathcal{V}\mathcal{E}} \delta\tilde{\boldsymbol{\varepsilon}} : \mathbf{q}^T \cdot (\Delta\bar{\mathbf{H}} + \Delta\tilde{\mathbf{H}}) dv = 0. \quad (6.36)$$

Analogously, the electric part yields

$$- \int_{\mathcal{R}\mathcal{V}\mathcal{E}} \delta\tilde{\mathbf{E}} \cdot \mathbf{e} : (\Delta\bar{\boldsymbol{\varepsilon}} + \Delta\tilde{\boldsymbol{\varepsilon}}) dv - \int_{\mathcal{R}\mathcal{V}\mathcal{E}} \delta\tilde{\mathbf{E}} \cdot \boldsymbol{\epsilon} \cdot (\Delta\bar{\mathbf{E}} + \Delta\tilde{\mathbf{E}}) dv - \int_{\mathcal{R}\mathcal{V}\mathcal{E}} \delta\tilde{\mathbf{E}} \cdot \boldsymbol{\alpha}^T \cdot (\Delta\bar{\mathbf{H}} + \Delta\tilde{\mathbf{H}}) dv = 0 \quad (6.37)$$

and the magnetic part is given by

$$- \int_{\mathcal{R}\mathcal{V}\mathcal{E}} \delta\tilde{\mathbf{H}} \cdot \mathbf{q} : (\Delta\bar{\boldsymbol{\varepsilon}} + \Delta\tilde{\boldsymbol{\varepsilon}}) dv - \int_{\mathcal{R}\mathcal{V}\mathcal{E}} \delta\tilde{\mathbf{H}} \cdot \boldsymbol{\alpha} \cdot (\Delta\bar{\mathbf{E}} + \Delta\tilde{\mathbf{E}}) dv - \int_{\mathcal{R}\mathcal{V}\mathcal{E}} \delta\tilde{\mathbf{H}} \cdot \boldsymbol{\mu} \cdot (\Delta\bar{\mathbf{H}} + \Delta\tilde{\mathbf{H}}) dv = 0. \quad (6.38)$$

Inserting the corresponding FE approximations of equation (6.29) we achieve the discrete versions of the above equations. For the mechanical part we obtain

$$\sum_{e=1}^{num_{ele}} \left\{ (\delta\tilde{\mathbf{d}}_u^e)^T \left(\underbrace{\int_{\mathcal{B}^e} (\mathbf{B}_u^e)^T \mathbf{C} dv}_{\underline{\mathbf{l}}_{uu}^e} \Delta\bar{\boldsymbol{\varepsilon}} + \underbrace{\int_{\mathcal{B}^e} (\mathbf{B}_u^e)^T \mathbf{C} \mathbf{B}_u^e dv}_{\underline{\mathbf{k}}_{uu}^e} \Delta\tilde{\mathbf{d}}_u^e \right. \right. \\ \left. \left. - \underbrace{\int_{\mathcal{B}^e} (\mathbf{B}_u^e)^T \mathbf{e}^T dv}_{\underline{\mathbf{l}}_{u\phi}^e} \Delta\bar{\mathbf{E}} - \underbrace{\int_{\mathcal{B}^e} (\mathbf{B}_u^e)^T \mathbf{e}^T \mathbf{B}_\phi^e dv}_{\underline{\mathbf{k}}_{u\phi}^e} \Delta\tilde{\mathbf{d}}_\phi^e \right. \right. \\ \left. \left. - \underbrace{\int_{\mathcal{B}^e} (\mathbf{B}_u^e)^T \mathbf{q}^T dv}_{\underline{\mathbf{l}}_{u\varphi}^e} \Delta\bar{\mathbf{H}} - \underbrace{\int_{\mathcal{B}^e} (\mathbf{B}_u^e)^T \mathbf{q}^T \mathbf{B}_\varphi^e dv}_{\underline{\mathbf{k}}_{u\varphi}^e} \Delta\tilde{\mathbf{d}}_\varphi^e \right) \right\} = 0, \quad (6.39)$$

where we have defined adequate FE matrices $\underline{\mathbf{l}}$. In order to give a more compact expression, we reformulate the above equation as

$$\sum_{e=1}^{num_{ele}} (\delta \tilde{\underline{\mathbf{d}}}_u)^T \left(\underline{\mathbf{l}}_{uu}^e \Delta \underline{\underline{\boldsymbol{\varepsilon}}} + \underline{\mathbf{k}}_{uu}^e \Delta \tilde{\underline{\mathbf{d}}}_u + \underline{\mathbf{l}}_{u\phi}^e \Delta \underline{\underline{\mathbf{E}}} + \underline{\mathbf{k}}_{u\phi}^e \Delta \tilde{\underline{\mathbf{d}}}_\phi + \underline{\mathbf{l}}_{u\varphi}^e \Delta \underline{\underline{\mathbf{H}}} + \underline{\mathbf{k}}_{u\varphi}^e \Delta \tilde{\underline{\mathbf{d}}}_\varphi \right) = 0. \quad (6.40)$$

Analogously, we obtain the discrete form of the electric part as

$$\sum_{e=1}^{num_{ele}} \left\{ (\delta \tilde{\underline{\mathbf{d}}}_\phi)^T \left(\underbrace{- \int_{\mathcal{B}^e} (\underline{\mathbf{B}}_\phi)^T \underline{\mathbf{e}} dv}_{\underline{\mathbf{l}}_{\phi u}^e} \Delta \underline{\underline{\boldsymbol{\varepsilon}}} - \underbrace{\int_{\mathcal{B}^e} (\underline{\mathbf{B}}_\phi)^T \underline{\mathbf{e}} \underline{\mathbf{B}}_u dv}_{\underline{\mathbf{k}}_{\phi u}^e} \Delta \tilde{\underline{\mathbf{d}}}_u \right. \right. \\ \left. \left. - \underbrace{\int_{\mathcal{B}^e} (\underline{\mathbf{B}}_\phi)^T \underline{\boldsymbol{\varepsilon}} dv}_{\underline{\mathbf{l}}_{\phi\phi}^e} \Delta \underline{\underline{\mathbf{E}}} - \underbrace{\int_{\mathcal{B}^e} (\underline{\mathbf{B}}_\phi)^T \underline{\boldsymbol{\varepsilon}} \underline{\mathbf{B}}_\phi dv}_{\underline{\mathbf{k}}_{\phi\phi}^e} \Delta \tilde{\underline{\mathbf{d}}}_\phi \right. \right. \\ \left. \left. - \underbrace{\int_{\mathcal{B}^e} (\underline{\mathbf{B}}_\phi)^T \underline{\boldsymbol{\alpha}}^T dv}_{\underline{\mathbf{l}}_{\phi\varphi}^e} \Delta \underline{\underline{\mathbf{H}}} - \underbrace{\int_{\mathcal{B}^e} (\underline{\mathbf{B}}_\phi)^T \underline{\boldsymbol{\alpha}}^T \underline{\mathbf{B}}_\varphi dv}_{\underline{\mathbf{k}}_{\phi\varphi}^e} \Delta \tilde{\underline{\mathbf{d}}}_\varphi \right) \right\} = 0, \quad (6.41)$$

which can be expressed in the compact notation by

$$\sum_{e=1}^{num_{ele}} (\delta \tilde{\underline{\mathbf{d}}}_\phi)^T \left(\underline{\mathbf{l}}_{\phi u}^e \Delta \underline{\underline{\boldsymbol{\varepsilon}}} + \underline{\mathbf{k}}_{\phi u}^e \Delta \tilde{\underline{\mathbf{d}}}_u + \underline{\mathbf{l}}_{\phi\phi}^e \Delta \underline{\underline{\mathbf{E}}} + \underline{\mathbf{k}}_{\phi\phi}^e \Delta \tilde{\underline{\mathbf{d}}}_\phi + \underline{\mathbf{l}}_{\phi\varphi}^e \Delta \underline{\underline{\mathbf{H}}} + \underline{\mathbf{k}}_{\phi\varphi}^e \Delta \tilde{\underline{\mathbf{d}}}_\varphi \right) = 0. \quad (6.42)$$

Finally, the discrete relation for the magnetic part appears as

$$\sum_{e=1}^{num_{ele}} \left\{ (\delta \tilde{\underline{\mathbf{d}}}_\varphi)^T \left(\underbrace{- \int_{\mathcal{B}^e} (\underline{\mathbf{B}}_\varphi^e)^T \underline{\mathbf{q}} dv}_{\underline{\mathbf{l}}_{\varphi u}^e} \Delta \underline{\underline{\boldsymbol{\varepsilon}}} - \underbrace{\int_{\mathcal{B}^e} (\underline{\mathbf{B}}_\varphi^e)^T \underline{\mathbf{q}} \underline{\mathbf{B}}_u dv}_{\underline{\mathbf{k}}_{\varphi u}^e} \Delta \tilde{\underline{\mathbf{d}}}_u \right. \right. \\ \left. \left. - \underbrace{\int_{\mathcal{B}^e} (\underline{\mathbf{B}}_\varphi^e)^T \underline{\boldsymbol{\alpha}} dv}_{\underline{\mathbf{l}}_{\varphi\phi}^e} \Delta \underline{\underline{\mathbf{E}}} - \underbrace{\int_{\mathcal{B}^e} (\underline{\mathbf{B}}_\varphi^e)^T \underline{\boldsymbol{\alpha}} \underline{\mathbf{B}}_\phi dv}_{\underline{\mathbf{k}}_{\varphi\phi}^e} \Delta \tilde{\underline{\mathbf{d}}}_\phi \right. \right. \\ \left. \left. - \underbrace{\int_{\mathcal{B}^e} (\underline{\mathbf{B}}_\varphi^e)^T \underline{\boldsymbol{\mu}} dv}_{\underline{\mathbf{l}}_{\varphi\varphi}^e} \Delta \underline{\underline{\mathbf{H}}} - \underbrace{\int_{\mathcal{B}^e} (\underline{\mathbf{B}}_\varphi^e)^T \underline{\boldsymbol{\mu}} \underline{\mathbf{B}}_\varphi dv}_{\underline{\mathbf{k}}_{\varphi\varphi}^e} \Delta \tilde{\underline{\mathbf{d}}}_\varphi \right) \right\} = 0 \quad (6.43)$$

with the compact notation

$$\sum_{e=1}^{num_{ele}} (\delta \tilde{\underline{\mathbf{d}}}_\varphi)^T \left(\underline{\mathbf{l}}_{\varphi u}^e \Delta \underline{\underline{\boldsymbol{\varepsilon}}} + \underline{\mathbf{k}}_{\varphi u}^e \Delta \tilde{\underline{\mathbf{d}}}_u + \underline{\mathbf{l}}_{\varphi\phi}^e \Delta \underline{\underline{\mathbf{E}}} + \underline{\mathbf{k}}_{\varphi\phi}^e \Delta \tilde{\underline{\mathbf{d}}}_\phi + \underline{\mathbf{l}}_{\varphi\varphi}^e \Delta \underline{\underline{\mathbf{H}}} + \underline{\mathbf{k}}_{\varphi\varphi}^e \Delta \tilde{\underline{\mathbf{d}}}_\varphi \right) = 0. \quad (6.44)$$

By now using the FE assembly procedure, yielding the global stiffness matrices and the global \mathbf{L} -matrices as

$$\underline{\mathbf{K}}_{ab} = \mathbf{A}_{e=1}^{num_{ele}} \underline{\mathbf{k}}_{ab}^e \quad \text{and} \quad \underline{\mathbf{L}}_{ab} = \mathbf{A}_{e=1}^{num_{ele}} \underline{\mathbf{l}}_{ab}^e \quad \text{for} \quad a, b = \{u, \phi, \varphi\} \quad (6.45)$$

we can write the global representation

$$\underbrace{\begin{bmatrix} \delta \tilde{\mathbf{D}}_u \\ \delta \tilde{\mathbf{D}}_\phi \\ \delta \tilde{\mathbf{D}}_\varphi \end{bmatrix}^T}_{\delta \tilde{\mathbf{D}}^T} \left(\underbrace{\begin{bmatrix} \underline{\mathbf{K}}_{uu} & \underline{\mathbf{K}}_{u\phi} & \underline{\mathbf{K}}_{u\varphi} \\ \underline{\mathbf{K}}_{\phi u} & \underline{\mathbf{K}}_{\phi\phi} & \underline{\mathbf{K}}_{\phi\varphi} \\ \underline{\mathbf{K}}_{\varphi u} & \underline{\mathbf{K}}_{\varphi\phi} & \underline{\mathbf{K}}_{\varphi\varphi} \end{bmatrix}}_{\underline{\mathbf{K}}} \underbrace{\begin{bmatrix} \Delta \tilde{\mathbf{D}}_u \\ \Delta \tilde{\mathbf{D}}_\phi \\ \Delta \tilde{\mathbf{D}}_\varphi \end{bmatrix}}_{\Delta \tilde{\mathbf{D}}} + \underbrace{\begin{bmatrix} \underline{\mathbf{L}}_{uu} & \underline{\mathbf{L}}_{u\phi} & \underline{\mathbf{L}}_{u\varphi} \\ \underline{\mathbf{L}}_{\phi u} & \underline{\mathbf{L}}_{\phi\phi} & \underline{\mathbf{L}}_{\phi\varphi} \\ \underline{\mathbf{L}}_{\varphi u} & \underline{\mathbf{L}}_{\varphi\phi} & \underline{\mathbf{L}}_{\varphi\varphi} \end{bmatrix}}_{\underline{\mathbf{L}}} \underbrace{\begin{bmatrix} \Delta \bar{\boldsymbol{\varepsilon}} \\ \Delta \bar{\mathbf{E}} \\ \Delta \bar{\mathbf{H}} \end{bmatrix}}_{\Delta \bar{\boldsymbol{\varkappa}}} \right) = 0. \quad (6.46)$$

This can be solved for the incremental nodal fluctuations

$$\Delta \tilde{\mathbf{D}} = -\underline{\mathbf{K}}^{-1} \underline{\mathbf{L}} \Delta \bar{\boldsymbol{\varkappa}}. \quad (6.47)$$

Considering Equation (6.20) we need the partial derivatives of the microscopic fluctuation fields with respect to the macroscopic counterparts for the determination of the overall material tangent, which can be computed from the latter equation as

$$\frac{\partial \Delta \tilde{\mathbf{D}}}{\partial \bar{\boldsymbol{\varkappa}}} = -\underline{\mathbf{K}}^{-1} \underline{\mathbf{L}} \frac{\partial \Delta \bar{\boldsymbol{\varkappa}}}{\partial \bar{\boldsymbol{\varkappa}}} = -\underline{\mathbf{K}}^{-1} \underline{\mathbf{L}}. \quad (6.48)$$

From Equation (6.20) we can identify the overall material tangent as

$$\bar{\boldsymbol{\varkappa}} = \frac{1}{V} \left(\int_{RVE} \underline{\mathbb{Z}} + \underline{\mathbb{Z}} \frac{\partial \bar{\boldsymbol{\varkappa}}}{\partial \bar{\boldsymbol{\varkappa}}} dv \right). \quad (6.49)$$

Inserting the general form of the discretizations $\Delta \bar{\boldsymbol{\varkappa}} = \underline{\mathbb{B}}_\xi^e \Delta \tilde{\mathbf{d}}_\xi^e$ in the latter equation with the update $\bar{\boldsymbol{\varkappa}} \leftarrow \bar{\boldsymbol{\varkappa}} + \Delta \bar{\boldsymbol{\varkappa}}$ in consideration of the equilibrium state in the current time step we obtain

$$\bar{\boldsymbol{\varkappa}} = \frac{1}{V} \left(\int_{RVE} \underline{\mathbb{Z}} dv \right) + \frac{1}{V} \left(\int_{RVE} \sum_{e=1}^{num_{ele}} \underline{\mathbb{Z}} \frac{\partial \underline{\mathbb{B}}_\xi^e \Delta \tilde{\mathbf{d}}_\xi^e}{\partial \bar{\boldsymbol{\varkappa}}} dv \right). \quad (6.50)$$

Using the FE assembly procedure, the partial derivative of the microscopic fluctuation fields with respect to their macroscopic counterparts and the definition of the adequate FE matrices $\underline{\mathbf{L}}$ we get the final solution of the overall material tangent as

$$\bar{\boldsymbol{\varkappa}} = \frac{1}{V} \left(\int_{RVE} \underline{\mathbb{Z}} dv \right) + \frac{1}{V} \left(\underline{\mathbf{L}}^T \frac{\partial \Delta \tilde{\mathbf{D}}_\xi^e}{\partial \bar{\boldsymbol{\varkappa}}} \right) = \langle \underline{\mathbb{Z}} \rangle_V - \frac{1}{V} \underline{\mathbf{L}}^T \underline{\mathbf{K}}^{-1} \underline{\mathbf{L}}. \quad (6.51)$$

Since the determination of the second part of the effective material tangent requires high computational cost, the second term is identified as

$$\underline{\mathbf{L}}^T \underline{\mathbf{K}}^{-1} \underline{\mathbf{L}} \quad \text{with} \quad \underline{\mathbf{K}} \boldsymbol{\varkappa} = \underline{\mathbf{L}}, \quad (6.52)$$

where $\boldsymbol{\varkappa}$ is the solution of a system with several right hand sides.

7 Material models

The following chapter deals with the material modeling of magneto-electric composites. Since the magneto-electric properties can be determined by suitable macroscopic models or as a result of the interaction of ferroelectric and ferromagnetic microscopic models, an overview is given of some possible approaches for ferroelectric, magnetostrictive and magneto-electric material models. Afterwards, the used models are described in more detail and a motivation is given for the choice of these models.

A possible method to describe the effective magneto-electric properties are analytical solutions, see e.g. ABOUDI [1], AVELLANEDA AND HARSHE [12], BENVENISTE [17], HUANG [73], HUANG AND KUO [74], KUO AND KUO [107], KUO ET AL. [108], LI [123], LI AND DUNN [124], NAN [150], WU AND HUANG [222] or KRANTZ AND GERKEN [104]. Such analytical solutions are for example based on the Mori-Tanaka-Method or Eshelby's equivalent eigenstrain solutions but often restricted to specific inclusion geometries and simple boundary value problems. However, the ME properties change through a modification of the microstructure while the volume fractions of the constituents remain the same. Such microscopic variations are mostly not captured within analytical approaches.

Finite element simulations of linear magneto-electro-mechanically coupled composite materials were for instance performed in LEE ET AL. [121]. In this work, the material behavior for the electro- and magneto-active phases was approximated as a linear piezoelectric as well as piezomagnetic behavior.

As a possible approach to describe the hysteresis behavior of the ferroelectric and ferromagnetic phases more precisely, the Preisach model was developed in 1935 by F. Preisach, see PREISACH [159]. Originally it was derived as a scalar-valued formulation and later extended to multidimensional problems. Some applications to ferroelectric and ferromagnetic materials are for example given in HEGEWALD ET AL. [62], HUGHES AND WEN [77], KALTENBACHER ET AL. [88], MAYERGOYZ [134], MAYERGOYZ AND FRIEDMAN [135], ROBERT ET AL. [170], SONG ET AL. [195], STANCU ET AL. [202], YU ET AL. [225] and BERMÚDEZ ET AL. [18]. In all cases the hysteresis curves are approximated by a superposition of multiple hysterons, which show a rectangular hysteresis loop. Due to different switching thresholds to their *up* and *down* positions, the macroscopic hysteresis is characterized by a stepwise increase or decrease of the magnetization.

A further approach for the simulation of the ferroelectric hysteresis behavior is given in HWANG ET AL. [79]. Therein, the effective polarization is based on multiple microscopic remanent polarizations, which can change their directions due to a switching criterion based on the change in the free energy. The switching criterion considers influences by electric fields or mechanical stresses, resulting in effective dielectric and butterfly hysteresis curves. Based on this model and on micro-mechanically motivated switching processes the reader is referred to the works of MENZEL ET AL. [136], MICHELITSCH AND KREHER [138] or KEIP [93]. In AVAKIAN ET AL. [11] a ferroelectric model, based on this switching criterion, is used to determine the magneto-electric coupling in two-phase composites. However, interactions between neighboring domains are not considered in this model.

In order to incorporate effects through domain interactions, phase field models based on the Ginzburg-Landau equation are a powerful tool. The simulated phase transformation and domain wall movements are a result of the minimization process of the total free energy. WANG ET AL. [214] presented effective polarization and strain hysteresis loops by averaging the microscopic polarization state obtained by a phase field model. For the

application of phase field models to ferroelectric materials and the study of domain structures and polarization switching we refer for example to KOYAMA [103], MIEHE AND ETHIRAJ [140], SCHRADER ET AL. [180] or KEIP ET AL. [96].

Ferroelectric phenomena as domain wall or boundary effects can also be modeled using molecular statics (MS) simulations, molecular dynamics (MD) or density functional theory (DFT). Therein, the atoms are considered as individual particles, which can interact with each other. The dynamical state of the system in molecular dynamics is determined using potentials, such as the Lennard-Jones potential. In density functional theory the atomic forces are calculated by approximating the Schrödinger equation. However, the simulations are restricted to very small length scales and require high computational cost. Furthermore, models on higher scales simulate the macroscopic ferroelectric behavior more exactly. In ENDRES AND STEINMANN [42] a ferroelectric hysteresis is determined using molecular statics simulations.

Simulations of the material behavior of magnetorheological elastomers are performed in KEIP AND RAMBAUSEK [94; 95], using the FE²-method. On the microscopic level, the magnetic particles are described by an extension of a classical neo-Hookean energy function, which is enhanced by a term accounting for the magnetic saturation behavior. The neo-Hookean energy function is motivated by the fact that such particles, embedded in an elastic matrix, undergo finite rigid-body rotations. Further simulations of magnetorheological elastomers can be found in KALINA ET AL. [87] or METSCH ET AL. [137].

Large deformations of ionic electro-active polymers were investigated in the framework of the theory of porous media (TPM) in BLUHM ET AL. [20]. In this work additional balance equations related to electric fields and the electroneutrality condition are taken into account. The large deformations of these EAPs are a result of the displacements of electrically charged ions, which is incorporated with a concentration equation.

Based on thermally or magnetically induced phase transitions, strains of up to 10% can be obtained in magnetic shape memory alloys. A suitable modeling approach for the simulation of such alloys is based on the concept of energy relaxation in the context of non-convex free energy landscapes. Applications of this theory to magnetic shape memory alloys are for example given in TICKLE ET AL. [206] or KIEFER ET AL. [99]. Further approaches are for instance given in KIEFER AND LAGOUDAS [97] or KIEFER ET AL. [98]. A different approach is based on the theory of plasticity, where an evolution equation is derived for the plastic strains. The electric polarization is represented by an internal variable. First approaches based on this theory were applied for ferroelectric ceramics in BASSIOUNY ET AL. [14]. Further applications for dissipative magnetostriction are e.g. given in MIEHE ET AL. [146] or for magneto-electro-mechanics in MIEHE ET AL. [147]. Macroscopic phenomenological models describe the material behavior based on parameters of experimental measurements. In HOM AND SHANKAR [71] and HOM AND SHANKAR [72] the nonlinear behavior of the electric polarization was approximated by a hyperbolic tangent, which suitably depicts the experimental results. A phenomenological model for ferromagnetic shape memory alloys was derived in KIEFER AND LAGOUDAS [97]. In this context the work of AVAKIAN AND RICOEUR [10] has to be highlighted, where inter alia a phenomenological ferromagnetic model is combined with a ferroelectric model, based on the switching of unit cells on the microscopic level. Both models were used to simulate the magneto-electric coupling in two phase composites. Furthermore, in the same work a physically motivated ferromagnetic model was derived, which is based on a switching criterion (HWANG ET AL. [79]) depending on the dissipative work of Bloch wall motions.

In the following section an overview of possible material models for the simulation of magneto-electric composites is given. For this, four different models are introduced. At the beginning a linear model is used to describe the electro-active and magneto-active phases. For ferroelectric materials it is a common approach to simulate the material behavior after a polarization process, when the microscopic remanent polarizations are aligned in one direction. In this state, the material shows approximately a linear behavior, when the centers of the positive and negative charged ions only move in linear dependence on the applied electric field or mechanical stress and not due to a reorientation of the polarization direction. For ferromagnetic materials this approach can also be used. In the case of the investigated cobalt ferrite, the linear behavior is not fitted to the material response after a magnetization process since the material only shows a small hysteresis. Instead, the parameters are fitted to the steepest curve at the beginning of the hysteresis loops. In this field region the hysteresis curve can roughly be approximated by a linear function. However, this approach is only applicable for a small magnetic field region and can not depict the nonlinear behavior of the magnetization and magnetostriction. Numerical examples show, that further assumptions, as different polarization directions and a factorization of piezoelectric coupling moduli, yield a more accurate prediction of measured magneto-electric coefficients, see LABUSCH ET AL. [111; 115]. Nevertheless, to predict the ME coupling more precisely nonlinear models have to be taken into account. Therefore, we consider in the second approach a nonlinear magnetostrictive model, see SCHRÖDER ET AL. [187]. It is capable of describing the hysteresis loops of the magnetization and the magnetostriction and is able to incorporate a reorientation of the magnetization direction. Numerical simulations with this model demonstrate the necessity of using nonlinear models for the simulation of ME coefficients. Thus, we consider in the third approach a ferroelectric/-elastic switching model, see KEIP [93], based on the work of HWANG ET AL. [79]. Based on a switching criterion for remanent polarization vectors on the microscopic level, the nonlinear properties of the hysteresis loops are described. This model is extended to the three dimensional space by using an orientation distribution function based on the construction of a geodesic dome, see KURZHÖFER [109]. In numerical examples the nonlinear properties of the magneto-electric coupling can be shown, see LABUSCH ET AL. [112; 114; 116], SCHRÖDER ET AL. [188]. The material model last implemented is a three-dimensional Preisach model. The Preisach model approximates the magnetization by a superposition of multiple relays, which simulate the behavior of microscopic magnetic moments. These microscopic relays switch their direction depending on specific switching thresholds. Thus, the magnetization and magnetostriction hysteresis curves can be fitted to arbitrary continuous functions. This is used for the description of the material behavior of cobalt ferrite, see section 4.1.3. However, the classical Preisach model is a scalar valued model. In this thesis, the model is extended to the three-dimensional space. In a first approach the model was extended to 3D by applying the Preisach operator in each direction of an orientation distribution function (ODF). In SCHRÖDER AND LABUSCH [186] this approach was first applied for ferroelectric materials and simulations of two-phase magneto-electric composites were performed. However, the high number of relays in each direction of the ODF yields very time consuming computations. Therefore, in a second approach the Preisach operator was multiplied with one direction vector, which depicts the current magnetization direction, see LABUSCH ET AL. [117]. However, a direct switching of the magnetization vector into the direction of the microscopic magnetic field could cause numerical instabilities, since a direct reorientation

of the magnetization yields switching of the Preisach relays. This could involve again a reorientation of the magnetization direction resulting in back and forth switching of the vector and the Preisach relays. In order to prevent such instabilities the magnetization vector slowly, which means in multiple time steps, rotates into the new direction. With this approach the model is capable of describing the nonlinear hysteresis loops for cobalt ferrite. Finally, the ferroelectric/-elastic switching model and the ferromagnetic Preisach model are combined for the simulation of two-phase magneto-electric composites and show promising results in the prediction of ME coefficients.

7.1 Linear piezoelectric/piezomagnetic material model

For the description of the piezoelectric and piezomagnetic material model one general model is used, where either the piezoelectric coupling modulus or the piezomagnetic coupling modulus is activated. Therefore, we use a coordinate-invariant formulation of a magneto-electro-mechanically coupled enthalpy function ψ_1 , based on the work of SCHRÖDER AND GROSS [184]. Since mostly polarized or magnetized materials are considered to depict the linear behavior of such ferroic materials, a transversely isotropic formulation is used as a suitable approximation. It is given as

$$\begin{aligned} \psi_1 = & \underbrace{\frac{1}{2}\lambda I_1^2 + \mu I_2 + \omega_1 I_5 + \omega_2 I_4^2 + \omega_3 I_1 I_4}_{\psi_1^{mech}} + \underbrace{\beta_1 I_1 J_2^e + \beta_2 I_4 J_2^e + \beta_3 K_1^e}_{\psi_1^{pe}} \\ & + \underbrace{\kappa_1 I_1 J_2^m + \kappa_2 I_4 J_2^m + \kappa_3 K_1^m}_{\psi_1^{pm}} + \underbrace{\gamma_1 J_1^e + \gamma_2 (J_2^e)^2}_{\psi_1^{diel}} + \underbrace{\xi_1 J_1^m + \xi_2 (J_2^m)^2}_{\psi_1^{magn}}, \end{aligned} \quad (7.1)$$

where the individual parts represent the purely mechanical (ψ_1^{mech}), the piezoelectric (ψ_1^{pe}), the piezomagnetic (ψ_1^{pm}), the purely electric (ψ_1^{diel}), and the purely magnetic behavior (ψ_1^{magn}). The used invariants are defined as follows

$$\begin{aligned} I_1 &= \text{tr}[\boldsymbol{\varepsilon}], & I_2 &= \text{tr}[\boldsymbol{\varepsilon}^2], & I_4 &= \text{tr}[\boldsymbol{\varepsilon}\mathbf{m}], & I_5 &= \text{tr}[\boldsymbol{\varepsilon}^2\mathbf{m}], \\ J_1^e &= \text{tr}[\mathbf{E} \otimes \mathbf{E}], & J_2^e &= \text{tr}[\mathbf{E} \otimes \mathbf{a}], & K_1^e &= \text{tr}[\boldsymbol{\varepsilon}(\mathbf{E} \otimes \mathbf{a})], \\ J_1^m &= \text{tr}[\mathbf{H} \otimes \mathbf{H}], & J_2^m &= \text{tr}[\mathbf{H} \otimes \mathbf{a}], & K_1^m &= \text{tr}[\boldsymbol{\varepsilon}(\mathbf{H} \otimes \mathbf{a})], \end{aligned} \quad (7.2)$$

where \mathbf{a} denotes the preferred direction indicating the orientation of the remanent polarization or magnetization and \mathbf{m} denotes the structural tensor with $\mathbf{m} = \mathbf{a} \otimes \mathbf{a}$. The derivations of the energy function with respect to the process variables as

$$\begin{aligned} \mathbb{C} &= \partial_{\boldsymbol{\varepsilon}\boldsymbol{\varepsilon}}^2 \psi_1, & \boldsymbol{\varepsilon} &= \partial_{\mathbf{E}\mathbf{E}}^2 \psi_1, & \boldsymbol{\mu} &= \partial_{\mathbf{H}\mathbf{H}}^2 \psi_1, \\ \mathbf{e} &= \partial_{\boldsymbol{\varepsilon}\mathbf{E}}^2 \psi_1 = [-\partial_{\mathbf{E}\boldsymbol{\varepsilon}}^2 \psi_1]^T & \text{and} & \quad \mathbf{q} &= \partial_{\boldsymbol{\varepsilon}\mathbf{H}}^2 \psi_1 = [-\partial_{\mathbf{H}\boldsymbol{\varepsilon}}^2 \psi_1]^T \end{aligned} \quad (7.3)$$

yield the following constitutive magneto-electro-mechanical moduli as

$$\begin{aligned} \mathbb{C} &= \lambda \mathbf{1} \otimes \mathbf{1} + 2\mu \mathbb{I} + \omega_3 [\mathbf{1} \otimes \mathbf{m} + \mathbf{m} \otimes \mathbf{1}] + 2\omega_2 \mathbf{m} \otimes \mathbf{m} + \omega_1 \boldsymbol{\Xi}, \\ \mathbf{e} &= -\beta_1 \mathbf{a} \otimes \mathbf{1} - \beta_2 \mathbf{a} \otimes \mathbf{m} - \beta_3 \boldsymbol{\theta}, \\ \mathbf{q} &= -\kappa_1 \mathbf{a} \otimes \mathbf{1} - \kappa_2 \mathbf{a} \otimes \mathbf{m} - \kappa_3 \boldsymbol{\theta}, \\ \boldsymbol{\varepsilon} &= -2\gamma_1 \mathbf{1} - 2\gamma_2 \mathbf{m}, \\ \boldsymbol{\mu} &= -2\xi_1 \mathbf{1} - 2\xi_2 \mathbf{m}, \end{aligned} \quad (7.4)$$

where the following third and fourth order tensors are introduced

$$\theta_{ijk} = \frac{1}{2}(a_j\delta_{ik} + a_k\delta_{ij}), \quad \mathbb{I}_{ijkl} = \frac{1}{2}(\delta_{ik}\delta_{jl} + \delta_{il}\delta_{jk}), \quad \text{and} \quad \Xi_{ijkl} = a_i\delta_{jk}a_l + a_k\delta_{il}a_j. \quad (7.5)$$

Based on these moduli the compact notation of the constitutive relations can be given as

$$\begin{bmatrix} \underline{\boldsymbol{\sigma}} \\ -\underline{\boldsymbol{D}} \\ -\underline{\boldsymbol{B}} \end{bmatrix} = \begin{bmatrix} \underline{\mathbb{C}} & -\underline{\boldsymbol{e}}^T & -\underline{\boldsymbol{q}}^T \\ -\underline{\boldsymbol{e}} & -\underline{\boldsymbol{\epsilon}} & \underline{\mathbf{0}} \\ -\underline{\boldsymbol{q}} & \underline{\mathbf{0}} & -\underline{\boldsymbol{\mu}} \end{bmatrix} \begin{bmatrix} \underline{\boldsymbol{\epsilon}} \\ \underline{\boldsymbol{E}} \\ \underline{\boldsymbol{H}} \end{bmatrix}, \quad (7.6)$$

where the underline ($\underline{\bullet}$) denotes a vector-matrix notation. The magneto-electric modulus, denoted as $\underline{\boldsymbol{\alpha}}$, is not present in the individual phase, such that holds $\underline{\boldsymbol{\alpha}} = \underline{\mathbf{0}}$. The piezoelectric or piezomagnetic modulus $\underline{\boldsymbol{e}}$ or $\underline{\boldsymbol{q}}$ are zero in the corresponding other phase.

7.2 Nonlinear magnetostrictive material model

For the description of the magnetostrictive material behavior the material model proposed by MIEHE ET AL. [146; 147] is used. In the considered approach, a reversible, linear piezomagnetic response is assumed to exist at a given state of remanent magnetization \boldsymbol{M} . Nonlinearity and dissipation enter the formulation through their direct association with the evolution of this vector-valued internal state variable. More specifically, in analogy to Perzyna-type overstress models in viscoplasticity, the dissipation functional

$$\phi_\eta(\dot{\boldsymbol{M}}) = \sup_{\mathcal{H}} \left[\mathcal{H} \cdot \dot{\boldsymbol{M}} - \frac{H_c}{\eta(n+1)} \langle f(\mathcal{H}) \rangle^{n+1} \right] \quad (7.7)$$

is introduced governing the evolution of the effective remanent magnetization vector, with the coercive threshold value H_c . Here, $\langle x \rangle = \frac{1}{2}(x + |x|)$ denotes the ramp function. The dissipation functional (7.7) can be interpreted as the approximate penalty-type solution of the nonlinear inequality-constrained maximization problem

$$\phi_\eta(\dot{\boldsymbol{M}}) = \sup_{\mathcal{H} \in \mathbb{E}} \left[\mathcal{H} \cdot \dot{\boldsymbol{M}} \right], \quad (7.8)$$

where $\mathbb{E} := \{\mathcal{H} | f(\mathcal{H}) := |\mathcal{H}|/H_c - 1 < 0\}$, with $|\mathcal{H}| := (\mathcal{H} \cdot \mathcal{H})^{1/2}$, defines the reversible range in terms of the thermodynamic driving force

$$\mathcal{H} = -\frac{\partial \psi_2(\boldsymbol{\epsilon}, \boldsymbol{H}, \boldsymbol{M})}{\partial \boldsymbol{M}} \quad (7.9)$$

with the critical threshold value H_c . In this viscous regularization of the rate-dependent dissipation function, the constants $\eta > 0$ and $n > 0$ are material parameters associated with the viscosity of the magnetostrictive response. For $n < 1$ one obtains the phenomenological characteristics of a Norton-Bailey-type creep response. For $\eta \rightarrow 0$ the rate-independent case is recovered. Even though a small rate-dependence is sometimes introduced in computational material modeling to improve the numerical behavior of the constitutive algorithm, actual rate-dependence is observed in ferroelectric and magnetostrictive response, see KAMLAH [90], ZHOU ET AL. [228] or MIEHE AND ROSATO [142]. However, careful considerations are necessary when assessing whether rate-dependence

enters the constitutive or the system level. To give an example for the magnetic case, time-dependent magnetic diffusion due to eddy currents induced on the sample or device level may give the appearance of rate-dependence, even for rate-independent constitutive behavior. The necessary condition associated with the maximum principle (7.7) yields the evolution equation

$$\dot{\mathbf{M}} = \frac{H_c}{\eta} \langle f(\mathcal{H}) \rangle^n \frac{\partial f(\mathcal{H})}{\partial \mathcal{H}} = \frac{1}{\eta} \left\langle \frac{|\mathcal{H}|}{H_c} - 1 \right\rangle^n \frac{\mathcal{H}}{|\mathcal{H}|}. \quad (7.10)$$

Based on the implicit Euler integration of this equation, in combination with the driving force \mathcal{H} in (7.9), one may define the nonlinear residual expression

$$\mathbf{r}_{n+1}(\mathbf{v}_{n+1}) := \left[\begin{array}{c} \mathcal{H}_{n+1} + \partial_{\mathbf{M}} \psi_{n+1}^m \\ \mathbf{M}_{n+1} - \mathbf{M}_n - \frac{\Delta t}{\eta} \left(\frac{|\mathcal{H}_{n+1}|}{H_c} - 1 \right)^n \frac{\mathcal{H}_{n+1}}{|\mathcal{H}_{n+1}|} \end{array} \right] = \mathbf{0} \quad (7.11)$$

with $\Delta t := t_{n+1} - t_n$, in terms of the unknowns $\mathbf{v}_{n+1} := [\mathbf{M}_{n+1}, \mathcal{H}_{n+1}]^T$. Computing the nonlinear and loading-history dependent evolution of the remanent magnetization thus reduces to the nonlinear root-finding problem (7.11). A summary of all central constitutive relations of the model is given in Table 7.1.

Table 7.1: Constitutive relations for the dissipative magnetostrictive model.

1. Magneto-electro-mechanical enthalpy function:

$$\begin{aligned} \psi_2(\boldsymbol{\varepsilon}, \mathbf{H}, \mathbf{M}) &= \frac{1}{2} (\boldsymbol{\varepsilon} - \boldsymbol{\varepsilon}_r) : \mathbb{C} : (\boldsymbol{\varepsilon} - \boldsymbol{\varepsilon}_r) - (\boldsymbol{\varepsilon} - \boldsymbol{\varepsilon}_r) : \frac{|\mathbf{M}|}{M_s} \mathbf{q}^T \cdot \mathbf{H} \\ &\quad - \frac{1}{2} \mathbf{H} \cdot \boldsymbol{\beta} \cdot \mathbf{H} - \mathbf{H} \cdot \mathbf{M} + \psi_2^{mag}(\mathbf{M}) - \frac{1}{2} \mathbf{E} \cdot \boldsymbol{\varepsilon} \cdot \mathbf{E} \end{aligned} \quad (7.12)$$

with the elastic stiffness, piezomagnetic, magnetic permeability and electric permittivity moduli

$$\begin{aligned} \mathbb{C} &= \lambda \mathbf{1} \otimes \mathbf{1} + 2\mu \mathbb{I}^{sym} \quad \text{with} \quad \mathbb{I}^{sym} = \frac{1}{2} (\delta_{ik} \delta_{jl} + \delta_{il} \delta_{jk}), \\ \mathbf{q} &= \text{sym}^{12} [q_0 \mathbf{a} \otimes \mathbf{a} \otimes \mathbf{a} + q_{\perp} \mathbf{1} \otimes \mathbf{a} + q_{-} \mathbf{a} \otimes \mathbf{1}], \\ \boldsymbol{\beta} &= \mu_m \mathbf{1}, \\ \boldsymbol{\varepsilon} &= -\epsilon_{11} \mathbf{1} - (\epsilon_{22} - \epsilon_{11}) \mathbf{a} \otimes \mathbf{a} \end{aligned} \quad (7.13)$$

with the symmetrization operator for a third-order tensor w.r.t. the first two base vectors as

$$\text{sym}^{12} [\mathbf{a}] = \frac{1}{2} (\mathbf{a} + \mathbf{a}^T) \quad \text{respectively} \quad [\mathbf{a}]_{ijk} = \frac{1}{2} (\mathbf{a}_{ijk} + \mathbf{a}_{jik}) \quad (7.14)$$

and with the remanent strains caused by the remanent magnetization as

$$\boldsymbol{\varepsilon}_r = \frac{3}{2} \epsilon_s \frac{|\mathbf{M}|}{M_s} \text{dev}[\mathbf{a} \otimes \mathbf{a}]. \quad (7.15)$$

Table 7.1: Constitutive relations for the dissipative magnetostrictive model.

2. Determination of the stresses, magnetic induction, dielectric displacement, and driving force

$$\begin{aligned}
\boldsymbol{\sigma} &= \frac{\partial \psi_2}{\partial \boldsymbol{\varepsilon}} = \mathbb{C} : (\boldsymbol{\varepsilon} - \boldsymbol{\varepsilon}_r) - \frac{|\mathbf{M}|}{M_s} \mathbf{q}^T \cdot \mathbf{H} , \\
\mathbf{B} &= -\frac{\partial \psi_2}{\partial \mathbf{H}} = -\frac{|\mathbf{M}|}{M_s} \mathbf{q} : (\boldsymbol{\varepsilon} - \boldsymbol{\varepsilon}_r) - \boldsymbol{\beta} \cdot \mathbf{H} - \mathbf{M} , \\
\mathbf{D} &= -\frac{\partial \psi_2}{\partial \mathbf{E}} = -\boldsymbol{\varepsilon} \cdot \mathbf{E} , \\
\mathcal{H} &= -\frac{\partial \psi_2}{\partial \mathbf{M}} = -\boldsymbol{\sigma} : \frac{\partial \boldsymbol{\varepsilon}_r}{\partial \mathbf{M}} - \frac{1}{M_s} [(\boldsymbol{\varepsilon} - \boldsymbol{\varepsilon}_r) : \mathbf{q} \cdot \mathbf{H}] \mathbf{a} \\
&\quad - \frac{1}{M_s} (\mathbb{H} \cdot \mathbf{H}) : (\boldsymbol{\varepsilon} - \boldsymbol{\varepsilon}_r) - \mathbf{H} + \frac{\partial \psi_2^{mag}(\mathbf{M})}{\partial \mathbf{M}} .
\end{aligned} \tag{7.16}$$

The determination of $\frac{\partial \boldsymbol{\varepsilon}_r}{\partial \mathbf{M}}$, the expression of \mathbb{H} and the hysteresis shape are given by

$$\begin{aligned}
\frac{\partial \boldsymbol{\varepsilon}_r}{\partial \mathbf{M}} &= \frac{3}{2} \frac{\varepsilon_s}{M_s} \left(-\mathbf{a} \otimes \mathbf{a} \otimes \mathbf{a} + 2 \text{sym}^{12} [\mathbf{a} \otimes \mathbf{1}] - \frac{1}{3} \mathbf{1} \otimes \mathbf{a} \right) , \\
\mathbb{H} &= q_0 \left(-3 \mathbf{a} \otimes \mathbf{a} \otimes \mathbf{a} \otimes \mathbf{a} + \mathbf{1} \underline{\otimes} (\mathbf{a} \otimes \mathbf{a}) + (\mathbf{a} \otimes \mathbf{a}) \overline{\otimes} \mathbf{1} \right. \\
&\quad \left. + (\mathbf{a} \otimes \mathbf{a}) \otimes \mathbf{1} \right) + q_{\perp} \left(\mathbf{1} \otimes \mathbf{1} - \mathbf{1} \otimes \mathbf{a} \otimes \mathbf{a} \right) \\
&= q_{=} \left(\mathbb{I}^{sym} - \text{sym}^{12} [\mathbf{a} \otimes \mathbf{1}] \otimes \mathbf{a} \right) , \\
\frac{\partial \psi_2^{mag}(\mathbf{M})}{\partial \mathbf{M}} &= \frac{\partial \psi_2^{mag}}{\partial |\mathbf{M}|} \mathbf{a} = \frac{1}{2c} \ln \left(\frac{1 + \frac{|\mathbf{M}|}{M_s}}{1 - \frac{|\mathbf{M}|}{M_s}} \right) \mathbf{a} ,
\end{aligned} \tag{7.17}$$

where the following dyadic product notation is introduced

$$\begin{aligned}
[\mathbf{A} \overline{\otimes} \mathbf{B}]_{ijkl} &= A_{ik} B_{jl} , \\
[\mathbf{A} \underline{\otimes} \mathbf{B}]_{ijkl} &= A_{il} B_{jk} .
\end{aligned} \tag{7.18}$$

Table 7.1: Constitutive relations for the dissipative magnetostrictive model.

3. Update relation for the internal variable:

(a) For $|\mathcal{H}_{n+1}| < H_c$ the response is reversible and piezomagnetic, which yields

$$\mathcal{H}_{n+1} = \mathcal{H}_n, \quad \mathbf{M}_{n+1} = \mathbf{M}_n. \quad (7.19)$$

In the first iteration \mathcal{H}_{n+1} represents a trial value computed based on the internal variables of the previous time step.

(b) For $|\mathcal{H}_{n+1}| \geq H_c$ the iterative Newton-Raphson solution of the implicit Euler integration

$$\mathbf{r}_{n+1}(\mathbf{v}_{n+1}) = \begin{bmatrix} r_{1,n+1} \\ r_{2,n+1} \end{bmatrix} = \begin{bmatrix} \mathcal{H}_{n+1} + \frac{\partial \psi_{2,n+1}}{\partial \mathbf{M}} \\ \mathbf{M}_{n+1} - \mathbf{M}_n - \frac{\Delta t}{\eta} \left(\frac{|\mathcal{H}_{n+1}|}{H_c} - 1 \right)^n \mathbf{n}_{n+1} \end{bmatrix} = \mathbf{0} \quad (7.20)$$

with $\mathbf{v}_{n+1} = [\mathbf{M}_{n+1}, \mathcal{H}_{n+1}]^T$ and $\mathbf{n}_{n+1} = \mathcal{H}_{n+1}/|\mathcal{H}_{n+1}|$, yields the update relation

$$\mathbf{v}_{n+1} = \mathbf{v}_n - \mathbf{j}_{n+1}^{-1} \mathbf{r}_{n+1}. \quad (7.21)$$

The associated Jacobian $\mathbf{j}_{n+1} = \frac{\partial \mathbf{r}_{n+1}}{\partial \mathbf{v}}$ is given by

$$\mathbf{j}_{n+1} = \begin{bmatrix} \frac{\partial^2 \psi_{2,n+1}}{\partial \mathbf{M} \partial \mathbf{M}} & \mathbf{1} \\ \mathbf{1} & \mathbf{J}_{22} \end{bmatrix}, \quad (7.22)$$

where

$$\mathbf{J}_{22} = -\frac{n\Delta t}{\eta H_c} \left(\frac{|\mathcal{H}_{n+1}|}{H_c} - 1 \right)^{n-1} \mathbf{N}_{n+1} - \frac{\Delta t}{\eta |\mathcal{H}_{n+1}|} \left(\frac{|\mathcal{H}_{n+1}|}{H_c} - 1 \right)^n (\mathbf{1} - \mathbf{N}_{n+1}) \quad (7.23)$$

with $\mathbf{N}_{n+1} = \mathbf{n}_{n+1} \otimes \mathbf{n}_{n+1}$.

4. Global algorithmic tangent:

$$\mathbb{C}_{n+1} = \frac{\partial^2 \psi_{2,n+1}}{\partial \boldsymbol{\xi} \partial \boldsymbol{\xi}} - \begin{bmatrix} \frac{\partial^2 \psi_{2,n+1}}{\partial \boldsymbol{\xi} \partial \mathbf{M}} \\ \frac{\partial^2 \psi_{2,n+1}}{\partial \boldsymbol{\xi} \partial \mathcal{H}} \end{bmatrix}^T \mathbf{j}_{n+1}^{-1} \begin{bmatrix} \frac{\partial \mathbf{r}_{1,n+1}}{\partial \boldsymbol{\xi}} \\ \frac{\partial \mathbf{r}_{2,n+1}}{\partial \boldsymbol{\xi}} \end{bmatrix} \quad (7.24)$$

with the compact notation $\boldsymbol{\xi} = [\boldsymbol{\varepsilon}, \mathbf{H}]^T$.

7.3 Ferroelectric/-elastic switching model

In order to describe the nonlinear hysteresis curves of the ferroelectric material barium titanate as well as the strain-induced magneto-electric coupling behavior, which depend on the nonlinear properties of the electric and magnetic phase, a ferroelectric/ferroelastic switching model is used. This model is based on the previous works of KEIP [93] and HWANG ET AL. [79]. The idea of this model is to determine the effective properties of multiple barium titanate unit cells. Based on the domain structure of ferroelectric materials an orientation distribution function (ODF) is taken into account, which represents the different remanent polarization directions of the domains, see Figure 7.1. In order to start with an unpoled electric material which can be polarized in each direction in the three dimensional space, an ODF is used based on the construction of a geodesic dome. Each direction of this ODF represents one barium titanate unit cell which can switch its orientation with regard to the current microscopic electric field. For the construction of the distribution function and the application to ferroelectric materials see the works of KURZHÖFER [109] and KURZHÖFER ET AL. [110].

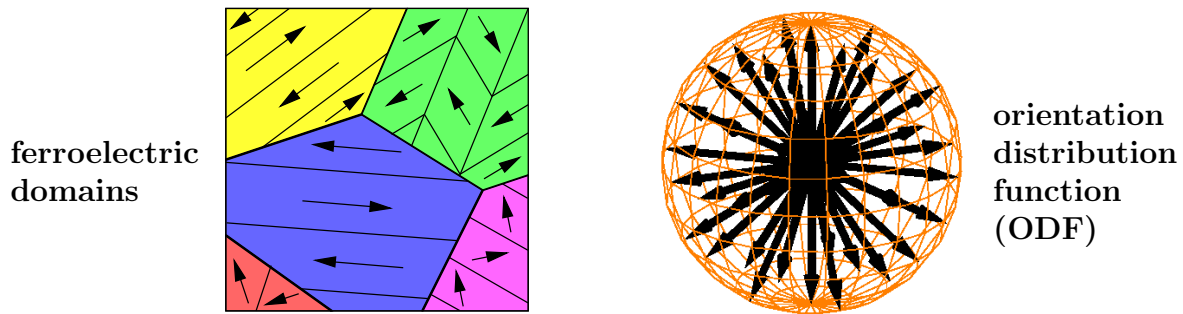


Figure 7.1: Representation of the ferroelectric domain structure with an orientation distribution function (ODF), adopted from KEIP [93] and KURZHÖFER [109].

Therefore, we consider an icosahedron which is a three dimensional polyhedron consisting of 20 triangular surfaces and 12 corners. The individual orientation vectors then point from the center of the icosahedron to the corners, yielding 12 orientations. By subdividing each triangle uniformly into multiple triangles the number of corners, and thus orientations, can be increased. Thereby, the new corners were projected onto the surface of the surrounding sphere. The segmentation of the surfaces into smaller triangles is described by frequencies, such that the frequencies of 2, 3, 4 or 10 result in 42, 92, 162 or 1002 orientations. The more triangles are used the closer is the approximation to a spherical shape. Furthermore, a higher number of orientations improves the approximation of the nonlinear hysteresis curves. However, at the initial distribution of the orientations and without a switching of the individual unit cells, the material has no overall electromechanical coupling and no hysteresis is observed. Therefore, a model with a suitable switching criterion for the spontaneous polarizations has to be derived. We start with a magneto-electric enthalpy function representing the tetragonal symmetry of a barium titanate unit cell as

$$\psi_3 = \psi_3^{mech} + \psi_3^{pe} + \psi_3^{diel} + \psi_3^{magn} \quad (7.25)$$

where the individual parts of the enthalpy function are defined as

$$\begin{aligned}
\psi_3^{mech} &= \frac{1}{2}\lambda\hat{I}_1^2 + \mu\hat{I}_2 + \frac{1}{2}\omega_1\hat{I}_5^2 + \omega_2\hat{I}_1\hat{I}_5 + \frac{1}{2}\omega_3(\hat{I}_6^2 + \hat{I}_7^2) + \frac{1}{2}\omega_4(\hat{I}_3^2 + \hat{I}_4^2 + \hat{I}_5^2), \\
\psi_3^{pe} &= \beta_1\hat{K}_1 + \beta_2\hat{I}_1\hat{J}_2^e + \beta_3\hat{I}_5\hat{J}_2^e, \\
\psi_3^{diel} &= \frac{1}{2}\gamma_1\hat{J}_1^e + \frac{1}{2}(\gamma_2 - \gamma_1)(\hat{J}_2^e)^2 - \hat{J}_2^e\hat{P}_1, \\
\psi_3^{magn} &= \frac{1}{2}\xi_1\hat{J}_1^m + \frac{1}{2}(\xi_2 - \xi_1)(\hat{J}_2^m)^2.
\end{aligned} \tag{7.26}$$

The above functions are formulated in terms of invariants. Due to the determination of the microscopic effective properties through an orientation distribution function, we introduce the nanoscale which is denoted as (\bullet) . The invariants are then given by

$$\begin{aligned}
\hat{I}_1 &= \text{tr}[\hat{\boldsymbol{\varepsilon}}_e], \quad \hat{I}_2 = \text{tr}[(\hat{\boldsymbol{\varepsilon}}_e)^2], \quad \hat{I}_3 = \text{tr}[\hat{\boldsymbol{\varepsilon}}_e\hat{\boldsymbol{M}}_{11}], \quad \hat{I}_4 = \text{tr}[\hat{\boldsymbol{\varepsilon}}_e\hat{\boldsymbol{M}}_{22}], \quad \hat{I}_5 = \text{tr}[\hat{\boldsymbol{\varepsilon}}_e\hat{\boldsymbol{M}}_{33}], \\
\hat{I}_6 &= \text{tr}[\hat{\boldsymbol{\varepsilon}}_e\hat{\boldsymbol{\Xi}}_1], \quad \hat{I}_7 = \text{tr}[\hat{\boldsymbol{\varepsilon}}_e\hat{\boldsymbol{\Xi}}_2], \quad \hat{J}_1^e = \text{tr}[\mathbf{E} \otimes \mathbf{E}], \quad \hat{J}_1^m = \text{tr}[\mathbf{H} \otimes \mathbf{H}], \\
\hat{J}_2^e &= \text{tr}[\mathbf{E} \otimes \hat{\boldsymbol{c}}], \quad \hat{J}_2^m = \text{tr}[\mathbf{H} \otimes \hat{\boldsymbol{c}}], \quad \hat{K}_1 = \text{tr}[\mathbf{E} \otimes (\hat{\boldsymbol{\Xi}}_3 : \hat{\boldsymbol{\varepsilon}}_e)], \quad \hat{P}_1 = \text{tr}[\hat{\boldsymbol{P}}_r \otimes \hat{\boldsymbol{c}}]
\end{aligned} \tag{7.27}$$

with the vector of spontaneous polarization $\hat{\boldsymbol{P}}_r$ of one unit cell in its preferred direction. Based on the tetragonal symmetry of barium titanate, the crystal is defined by three unit vectors $\hat{\boldsymbol{a}}_1$, $\hat{\boldsymbol{a}}_2$ and $\hat{\boldsymbol{a}}_3$, where the latter one describes the direction of remanent polarization $\hat{\boldsymbol{c}} = \hat{\boldsymbol{a}}_3$ and the other ones $\hat{\boldsymbol{a}}_1$ and $\hat{\boldsymbol{a}}_2$ are perpendicular to $\hat{\boldsymbol{a}}_3$. Additionally, we define the second-order structural tensors

$$\hat{\boldsymbol{M}}_{ij} = \hat{\boldsymbol{a}}_i \otimes \hat{\boldsymbol{a}}_j, \quad \hat{\boldsymbol{\Xi}}_1 = (\hat{\boldsymbol{M}}_{13} + \hat{\boldsymbol{M}}_{31}) \quad \text{and} \quad \hat{\boldsymbol{\Xi}}_2 = (\hat{\boldsymbol{M}}_{23} + \hat{\boldsymbol{M}}_{32}) \tag{7.28}$$

and the third order structural tensor

$$\hat{\boldsymbol{\Xi}}_3 = \sum_{i=1}^3 (\hat{\boldsymbol{a}}_i \otimes \hat{\boldsymbol{a}}_i \otimes \hat{\boldsymbol{c}} + \hat{\boldsymbol{a}}_i \otimes \hat{\boldsymbol{c}} \otimes \hat{\boldsymbol{a}}_i). \tag{7.29}$$

The invariants now depend on the elastic strains, which is motivated by the additive decomposition of the total strains and total dielectric displacement into an elastic part (\bullet_e) and a remanent part (\bullet_r) as

$$\hat{\boldsymbol{D}} = \hat{\boldsymbol{D}}_e + \hat{\boldsymbol{P}}_r \quad \text{and} \quad \hat{\boldsymbol{\varepsilon}} = \hat{\boldsymbol{\varepsilon}}_e + \hat{\boldsymbol{\varepsilon}}_r, \tag{7.30}$$

where the polarization $\hat{\boldsymbol{P}}_r$ depend on the material specific property P_s and the remanent strains are defined through the spontaneous strain $\hat{\boldsymbol{\varepsilon}}_s$ and the preferred direction $\hat{\boldsymbol{c}}$ as

$$\hat{\boldsymbol{P}}_r = \hat{P}_s\hat{\boldsymbol{c}} \quad \text{and} \quad \hat{\boldsymbol{\varepsilon}}_r = \frac{3}{2}\hat{\boldsymbol{\varepsilon}}_s\text{dev}(\hat{\boldsymbol{c}} \otimes \hat{\boldsymbol{c}}). \tag{7.31}$$

Based on the enthalpy function ψ_3 the constitutive moduli are determined as

$$\begin{aligned}
\hat{\mathbb{C}} &= \lambda\mathbf{1} \otimes \mathbf{1} + 2\mu\mathbb{I} + \omega_1\hat{\boldsymbol{M}}_{33} \otimes \hat{\boldsymbol{M}}_{33} + \omega_2(\mathbf{1} \otimes \hat{\boldsymbol{M}}_{33} + \hat{\boldsymbol{M}}_{33} \otimes \mathbf{1}) \\
&\quad + \omega_3(\hat{\boldsymbol{\Xi}}_1 \otimes \hat{\boldsymbol{\Xi}}_1 + \hat{\boldsymbol{\Xi}}_2 \otimes \hat{\boldsymbol{\Xi}}_2) + \omega_4 \sum_{i=1}^3 \hat{\boldsymbol{M}}_{ii} \otimes \hat{\boldsymbol{M}}_{ii}, \\
\hat{\boldsymbol{e}} &= -\beta_1\hat{\boldsymbol{\Xi}}_3 - \beta_2\hat{\boldsymbol{c}} \otimes \mathbf{1} - \beta_3\hat{\boldsymbol{c}} \otimes \hat{\boldsymbol{c}} \otimes \hat{\boldsymbol{c}}, \\
\hat{\boldsymbol{\varepsilon}} &= -\gamma_1\mathbf{1} - (\gamma_2 - \gamma_1)\hat{\boldsymbol{c}} \otimes \hat{\boldsymbol{c}}, \\
\hat{\boldsymbol{\mu}} &= -\xi_1\mathbf{1} - (\xi_2 - \xi_1)\hat{\boldsymbol{c}} \otimes \hat{\boldsymbol{c}}.
\end{aligned} \tag{7.32}$$

As mentioned above, the properties of the individual orientations are defined on the nanoscopic level. In order to determine the microscopic effective properties a homogenization approach based on the orientation distribution is utilized. Therefore, in each microscopic integration point an ODF with n orientations is attached. The corresponding effective properties on the microscopic level are determined through the homogenized quantities as

$$\boldsymbol{\lambda} = \frac{1}{n} \sum_{i=1}^n \hat{\boldsymbol{\Sigma}}^{(i)} \quad \text{with} \quad \hat{\boldsymbol{\lambda}}^{(i)} = \{\hat{\boldsymbol{\sigma}}^{(i)}, \hat{\boldsymbol{D}}^{(i)}, \hat{\boldsymbol{B}}^{(i)}, \hat{\mathbb{C}}^{(i)}, \hat{\boldsymbol{e}}^{(i)}, \hat{\boldsymbol{\epsilon}}^{(i)}, \hat{\boldsymbol{\mu}}^{(i)}, \hat{\boldsymbol{\epsilon}}^{(i)}, \hat{\boldsymbol{P}}_{r,(i)}\}. \quad (7.33)$$

However, this homogenization approach has to be repeated, if one or more orientations have switched their directions. Based on HWANG ET AL. [79] and KEIP [93] a switching criterion is used, which is motivated by the incremental change of the free energy with

$$\Delta\psi_3 = \Delta\psi_3^{elec} + \Delta\psi_3^{mech} = \boldsymbol{E} \cdot \Delta\hat{\boldsymbol{P}}_r + \boldsymbol{\sigma} : \hat{\boldsymbol{\epsilon}}_r. \quad (7.34)$$

In this equation the incremental parts are obtained by a reorientation of the unit cells. Possible changes of the remanent polarization direction of a single orientation due to a ferroelectric switching, based on an applied electric field, are

$$\begin{aligned} \Delta\hat{\boldsymbol{P}}_{r,1} &= -2\hat{P}_s\hat{\boldsymbol{c}}, & \Delta\hat{\boldsymbol{P}}_{r,2} &= \hat{P}_s(\hat{\boldsymbol{a}}_1 - \hat{\boldsymbol{c}}), & \Delta\hat{\boldsymbol{P}}_{r,3} &= \hat{P}_s(\hat{\boldsymbol{a}}_2 - \hat{\boldsymbol{c}}) \\ \Delta\hat{\boldsymbol{P}}_{r,4} &= \hat{P}_s(-\hat{\boldsymbol{a}}_1 - \hat{\boldsymbol{c}}), & \Delta\hat{\boldsymbol{P}}_{r,5} &= \hat{P}_s(-\hat{\boldsymbol{a}}_2 - \hat{\boldsymbol{c}}), \end{aligned} \quad (7.35)$$

where $\hat{\boldsymbol{P}}_{r,1}$ describes the 180° and $\hat{\boldsymbol{P}}_{r,2-5}$ the 90° switching options. The spontaneous strain is independent of the sign of the spontaneous polarization, such that only the following two ferroelastic switching options, based on applied or occurring mechanical stresses, are possible

$$\Delta\hat{\boldsymbol{\epsilon}}_{r,2,4} = \frac{3}{2}\hat{\boldsymbol{\epsilon}}_s \text{dev}(\hat{\boldsymbol{a}}_1 \otimes \hat{\boldsymbol{a}}_1 - \hat{\boldsymbol{c}} \otimes \hat{\boldsymbol{c}}) \quad \text{and} \quad \Delta\hat{\boldsymbol{\epsilon}}_{r,3,5} = \frac{3}{2}\hat{\boldsymbol{\epsilon}}_s \text{dev}(\hat{\boldsymbol{a}}_2 \otimes \hat{\boldsymbol{a}}_2 - \hat{\boldsymbol{c}} \otimes \hat{\boldsymbol{c}}). \quad (7.36)$$

In order to specify the energy thresholds for the 90° and 180° ferroelectric and ferroelastic switching options the amount of dissipated work during switching is considered and approximated as

$$\mathcal{W}_{elec,180^\circ}^{diss} = 2\hat{P}_s\hat{E}_c, \quad \mathcal{W}_{elec,90^\circ}^{diss} = \hat{P}_s\hat{E}_c \quad \text{and} \quad \mathcal{W}_{elas,90^\circ}^{diss} = \frac{3}{2}\varepsilon_s\sigma_c. \quad (7.37)$$

These switching thresholds yield the normalized switching criterion

$$\frac{\boldsymbol{E} \cdot \Delta\hat{\boldsymbol{P}}_{r,1}}{\mathcal{W}_{elec,180^\circ}^{diss}} \geq 1 \quad \text{and} \quad \frac{\boldsymbol{E} \cdot \Delta\hat{\boldsymbol{P}}_{r,k}}{\mathcal{W}_{elec,90^\circ}^{diss}} + \frac{\boldsymbol{\sigma} : \Delta\hat{\boldsymbol{\epsilon}}_{r,k}}{\mathcal{W}_{elas,90^\circ}^{diss}} \geq 1 \quad \text{for } k = 2, \dots, 5. \quad (7.38)$$

If two or more orientations fulfill this criterion, the switching options are sorted concerning their highest dissipation. Then, the orientations with the highest amount of dissipation switch first. In the case of equal amounts of dissipation of two or more criteria the choice which orientation switches first is taken randomly. However, a direct switching of single orientations result in an update of the microscopic constitutive mechanical, piezoelectric, dielectric, and magnetic moduli, which can cause algorithmic difficulties. If "too many" orientations switch at the same time, which can be interpreted as a significant change in the material tangent, a back-and-forth switching of multiple polarizations can occur.

In order to avoid this numerical instability as well as unnatural behavior, a step-wise switching process is performed. In detail, if the criteria are fulfilled for multiple orientations in one load step, only n_{swit} orientations are allowed to change its directions in the first *iteration*. Thereby, n_{swit} was chosen between 2 and 4 for 42 or 92 orientations, respectively. During this *iteration* the microscopic effective properties are determined and the microscopic and macroscopic boundary value problems are solved. After this step, the switching criteria for all orientations are checked again and updated.

Table 7.2: Algorithmic box for the ferroelectric/-elastic switching model.

<p>(i) Next macroscopic load step.</p> <p>(ii) While macroscopic equilibrium is not found do</p> <div style="border: 1px solid black; padding: 10px; margin: 10px 0;"> <p>(a) In each macroscopic Gauss point: compute electric field $\bar{\mathbf{E}}$ and strain $\bar{\boldsymbol{\epsilon}}$.</p> <p>(b) Update boundary conditions along $\partial\mathcal{R}\mathcal{V}\mathcal{E}$.</p> <p>(c) In each microscopic Gauss point: compute microscopic quantities $\boldsymbol{\sigma}$, \mathbf{D}, \mathbf{B}, \mathbb{C}, \mathbf{e}, $\boldsymbol{\epsilon}$, and $\boldsymbol{\mu}$ see (7.33).</p> <p>(d) Solve microscopic BVP and determine homogenized quantities.</p> <p>(e) Solve macroscopic BVP.</p> </div> <p>Else (equilibrium is found): Go to (iii) and check if switching is possible.</p> <p>(iii) In each microscopic Gauss point: compute microscopic stress $\boldsymbol{\sigma}$, electric displacement \mathbf{D} and magnetic induction \mathbf{B}.</p> <p>(iv) In each microscopic Gauss point and for each of the attached orientations $\{\hat{\mathbf{a}}_1, \hat{\mathbf{a}}_2, \hat{\mathbf{c}}\}^n$, where n is the number of orientations: compute all possible changes in remanent polarization $\Delta\hat{\mathbf{P}}_i^n$ ($i = 1, \dots, 5$) and remanent strain $\Delta\hat{\boldsymbol{\epsilon}}_i^n$ ($i = 2, 3$) and evaluate switching criteria (7.38).</p> <p>(v) Store evaluated switching criteria per Gauss point which meet the criteria (7.38) from highest to lowest dissipation in <code>list</code>. Store its number of entries in n_{list}.</p> <p>(vi) If $n_{\text{list}} > 0$ (dissipative step) then</p> <div style="border: 1px solid black; padding: 10px; margin: 10px 0;"> <p>(a) Choose number $n_{\text{swit}} \leq n_{\text{list}}$ of spontaneous polarizations allowed to switch simultaneously.</p> <p>(b) Perform update of the first n_{swit} polarization directions associated with the entries stored in <code>list</code>.</p> <p>(c) Save new orientation directions and compute new material tangents $\hat{\mathbb{C}}$, $\hat{\mathbf{e}}$, $\hat{\boldsymbol{\epsilon}}$, and $\hat{\boldsymbol{\mu}}$ for the new state of orientations $\{\hat{\mathbf{a}}_1, \hat{\mathbf{a}}_2, \hat{\mathbf{c}}\}^n$.</p> <p>(d) Go to (ii).</p> </div> <p>Else (switching criterion is no longer fulfilled): Go to (i).</p>

If multiple criteria are still fulfilled, n_{swit} orientations switch their directions followed by an update of the microscopic effective properties and the solution of the boundary value problems. This procedure is repeated in each load step until the switching criterion is no longer fulfilled for any orientation. The algorithmic step-by-step procedure is documented in Table 7.2. In the following the quality of the approximated hysteresis loops depending on the number of orientations is demonstrated. Since only one orientation shows a rectangular-shaped hysteresis loop an increasing number of orientations should depict the nonlinear characteristics.

Table 7.3: Material parameters used for the simulations of single crystal BaTiO₃, $[\hat{C}] = [\hat{\sigma}_c] = \frac{N}{\text{mm}^2}$, $[\hat{\epsilon}] = [\hat{P}_s] = \frac{C}{\text{m}^2}$, $[\hat{\epsilon}] = \frac{\text{mC}}{\text{kVm}}$, $[\hat{\epsilon}_s] = [\hat{\mu}^r] = [\hat{\epsilon}^r] = 1$, $[\hat{E}_c] = \frac{\text{kV}}{\text{mm}}$, $[\hat{\mu}] = \frac{N}{\text{kA}^2}$, see ZGONIK ET AL. [226]. We roughly assumed the value of the coercive stress σ_c .

\hat{C}_{1111}	\hat{C}_{1122}	\hat{C}_{1133}	\hat{C}_{3333}	\hat{C}_{1212}	\hat{C}_{1313}	$\hat{\epsilon}_{11}$ ($\hat{\epsilon}_{11}^r$)	$\hat{\epsilon}_{33}$ ($\hat{\epsilon}_{33}^r$)
222000	108000	111000	151000	134000	61000	0.019 (2146)	0.000496 (56)
$\hat{\epsilon}_{311}$	$\hat{\epsilon}_{333}$	$\hat{\epsilon}_{131}$	$\hat{\mu}_{11}$ ($\hat{\mu}_{11}^r$)	$\hat{\mu}_{33}$ ($\hat{\mu}_{33}^r$)	\hat{E}_c	$\hat{\sigma}_c$	$\hat{\epsilon}_s$
-0.7	6.7	34.2	1.26 (1)	1.26 (1)	1.0	100	0.00834

Here, we consider five different orientation distribution functions with 15, 42, 92, 162 and 1002 directions. The first one with 15 directions is obtained by an error function which minimizes the difference between an average of distributed transversely isotropic properties with isotropic properties, see KURZHÖFER [109]. The other four considered distributions are obtained by the construction of a geodesic dome based on an icosahedron. The material parameters used are summarized in Table 7.3. They are taken from ZGONIK ET AL. [226] and describe the material behavior of single crystal barium titanate, such that they are used for the individual orientations.

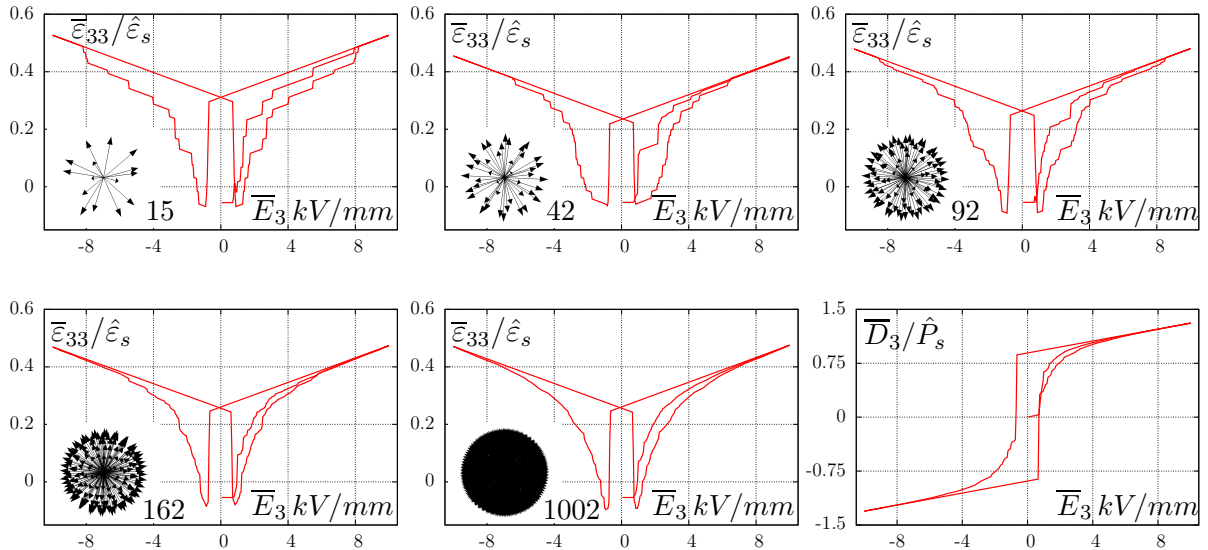


Figure 7.2: Macroscopic butterfly hysteresis loop using 15, 42, 92, 162 and 1002 orientations and a dielectric hysteresis loop for 1002 orientations. Taken from LABUSCH ET AL. [112].

For the comparison of the different ODFs a macroscopic purely ferroelectric cubic body is

considered which is homogeneously loaded with an electric field E_3 in vertical direction. The following Figure 7.2 depicts the resulting macroscopic butterfly hysteresis curves for 15, 42, 92, 162 and 1002 orientations as well as the dielectric hysteresis curve for 1002 orientations. In these results the switching of the individual directions can be clearly seen by the cascade increase and decrease of the deformation and polarization. Furthermore, an increase of the homogenized piezoelectric coupling modulus e can be observed, which becomes larger when the orientations switch into the same direction. This increase is noticeable in the higher slopes of steps in the butterfly hysteresis for larger electric fields. Comparing the different ODFs, it can be pointed out that the hysteresis loops become smoother and converge against a specific shape for an increasing number of directions. For the following simulations 92 orientations should be used to depict the main characteristics. However, due to the huge computational cost, which is necessary for a stable calculation without back-and-forth switchings as well as the complex microstructural morphologies of the two-phase composites, also 42 orientations are used in some simulations.

7.4 Three-dimensional Preisach model

As mentioned before, several models have been developed for the description of ferroelectric and ferromagnetic material behavior. In the following section a three-dimensional Preisach model is derived to describe the ferromagnetic characteristics. It was pointed out that the characteristic shape of the magneto-electric coupling, for instance the change of its sign for an increasing magnetic field, depends on the specific material behavior of cobalt ferrite, which shows a reduction of the magnetostriction for rising magnetic fields in polycrystalline samples. The description of such nonlinearities is an algorithmically challenging task. In order to describe the characteristic behavior of cobalt ferrite a three-dimensional Preisach model is derived, in which the remanent parts of the magnetization as well as magnetostriction can be fitted to arbitrary functions. Therefore, the magnetic induction and strains are additively decomposed into an elastic part (\bullet_e) and a remanent part (\bullet_r), analogous to the previously described switching model. The linear part is described by a transversely isotropic linear material law, whereas the nonlinear magnetization is modeled by the Preisach operator. This Preisach operator is determined depending on a preferred orientation defined by the magnetization direction. Due to inhomogeneities on the microscopic level the magnetization aligns to the microscopic magnetic field distribution. Therefore, the magnetization vector rotates into the direction of the microscopic magnetic fields, where the magnitude of the magnetization is determined by the Preisach operator. In the following a description of the classical Preisach model and the extension to the three dimensional space are given.

7.4.1 Classical Preisach model

The idea of the classical Preisach model goes back to the early work of PREISACH [159] in the year 1935. Further approaches of the Preisach model are for example given in HEGEWALD ET AL. [62], HUGHES AND WEN [77], KALTENBACHER ET AL. [88], MAYERGOYZ [134], MAYERGOYZ AND FRIEDMAN [135], ROBERT ET AL. [170], SONG ET AL. [195], STANCU ET AL. [202], YU ET AL. [225] and BERMÚDEZ ET AL. [18]. The Preisach model can either be used for ferromagnetic or ferroelectric materials. Therefore, the remanent magnetization \mathbf{M}_r or the remanent polarization \mathbf{P}_r are computed by a scalar

hysteresis operator \mathbf{p} , which depends on a finite number of so called hysterons. Each hysteron is characterized by a rectangular hysteresis cycle representing one microscopic magnetic moment or spontaneous polarization. The output value γ , which is either $+1$ or -1 , depends on the *up* and *down* switching thresholds α and β , see Figure 7.3, describing the direction of the microscopic magnetic moment or electric polarization. A superposition of multiple hysterons with different switching thresholds result in the Preisach operator, which describes the nonlinear hysteresis loop. Depending on the input variable, which in the case of magnetostrictive solids is the current magnetic field, the Preisach operator \mathbf{p} is defined as

$$\mathbf{p}(H) = \int_{\beta} \int_{\alpha} \omega(\alpha, \beta) \gamma(\alpha, \beta) H(t) \, d\alpha \, d\beta, \quad (7.39)$$

where the input field H is considered to be a scalar value since the classical Preisach model is a scalar valued approach. The single hysterons are multiplied with a weight function $\omega(\alpha, \beta)$ in order to match the experimentally measured hysteresis loops. Methods to identify the weight function from experimental measurements are for example given in KALTENBACHER ET AL. [88]. In the three-dimensional model used here the switching thresholds α and β are not fitted to measurements. Instead, it is assumed that

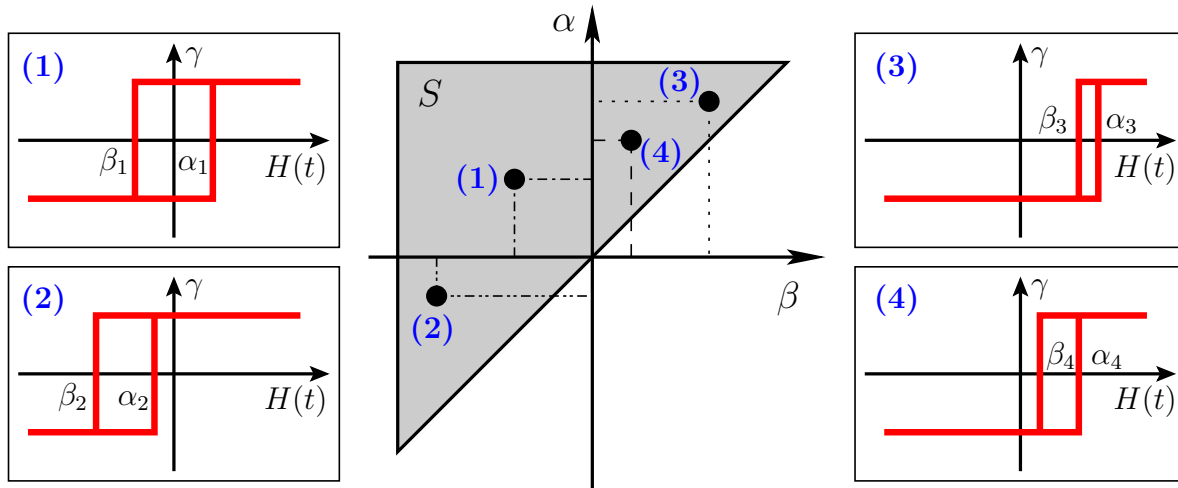


Figure 7.3: Visualization of the Preisach plane S with $S = \{ (\alpha, \beta) \in \mathbb{R}^2 \mid \beta \geq \alpha \}$ and possible hysterons with individual switching thresholds $\alpha_{(1-4)}$ and $\beta_{(1-4)}$, respectively. Taken from LABUSCH ET AL. [117].

the magnitude of the magnetization can be approximated with a hyperbolic tangent as $\mathbf{M}_r \approx \tanh(\mathbf{H})$, such that the switching thresholds depend on this function. Due to the fact that closed hysteresis loops are considered, the set of possible *up* and *down* switching thresholds can be visualized to a Preisach plane $S = \{ (\alpha, \beta) \in \mathbb{R}^2 \mid \beta \geq \alpha \}$, see figure 7.3. In general, with a suitable distribution of switching thresholds, it is also possible to describe minor hysteresis loops.

7.4.2 Application of the Preisach operator to ferroelectrics

Analogous to the linear piezoelectric material model, a generalized coordinate-invariant formulation of a magneto-electro-mechanical enthalpy function ψ_4 for transversely

isotropic solids, as adopted from SCHRÖDER AND GROSS [184], is used

$$\begin{aligned} \psi_4 = & \frac{1}{2}\lambda I_1^2 + \mu I_2 + \omega_1 I_5 + \omega_2 I_4^2 + \omega_3 I_1 I_4 + \kappa_1 I_1 J_2^e + \kappa_2 I_4 J_2^e + \kappa_3 K_1^e \\ & + \xi_1 J_1^m + \xi_2 (J_2^m)^2 + \gamma_1 J_1^e + \gamma_2 (J_2^e)^2 - J_2^e P_1^e, \end{aligned} \quad (7.40)$$

where the invariant functions are formulated in terms of the following invariants

$$\begin{aligned} \hat{I}_1 &= \text{tr}[\hat{\boldsymbol{\varepsilon}}_e], & \hat{I}_5 &= \text{tr}[\hat{\boldsymbol{\varepsilon}}_e^2 \hat{\boldsymbol{m}}], & \hat{J}_1^m &= \text{tr}[\mathbf{H} \otimes \mathbf{H}], & \hat{P}_1^e &= \text{tr}[\hat{\mathbf{P}}_r \otimes \hat{\mathbf{a}}], \\ \hat{I}_2 &= \text{tr}[\hat{\boldsymbol{\varepsilon}}_e^2], & \hat{J}_1^e &= \text{tr}[\mathbf{E} \otimes \mathbf{E}], & \hat{J}_2^m &= \text{tr}[\mathbf{H} \otimes \hat{\mathbf{a}}], & \hat{K}_1^e &= \text{tr}[\hat{\boldsymbol{\varepsilon}}_e(\mathbf{E} \otimes \hat{\mathbf{a}})], \\ \hat{I}_4 &= \text{tr}[\hat{\boldsymbol{\varepsilon}}_e \hat{\boldsymbol{m}}], & \hat{J}_2^e &= \text{tr}[\mathbf{E} \otimes \hat{\mathbf{a}}] \end{aligned} \quad (7.41)$$

with the structural tensor \boldsymbol{m} and the remanent electric polarization $\hat{\mathbf{P}}_r$. Since the material law is applied on each individual direction of the ODF on the nanoscopic level, the invariants are denoted with a hat ($\hat{\bullet}$), see Section 7.3. For the resulting dielectric displacement as well as the strains for each nanoscopic orientation we assume an additive decomposition into an elastic (reversible) part ($\hat{\bullet}_e$) and a remanent (irreversible) part ($\hat{\bullet}_r$), according to KAMLAH AND TSAKMAKIS [92], as

$$\hat{\mathbf{D}} = \hat{\mathbf{D}}_e + \hat{\mathbf{P}}_r \quad \text{and} \quad \hat{\boldsymbol{\varepsilon}} = \hat{\boldsymbol{\varepsilon}}_e + \hat{\boldsymbol{\varepsilon}}_r, \quad (7.42)$$

where the remanent electric polarization vector $\hat{\mathbf{P}}_r$ is determined by the Preisach operator $\mathbf{p}(\mathbf{E})$, depending on the electric field. The remanent strains $\hat{\boldsymbol{\varepsilon}}_r$ depend on the current polarization state as

$$\hat{\mathbf{P}}_r = \mathbf{p}(\mathbf{E})\hat{\mathbf{a}} \quad \text{and} \quad \hat{\boldsymbol{\varepsilon}}_r = \frac{3}{2}\varepsilon_s \frac{1}{P_s^2} \text{dev}(\hat{\mathbf{P}}_r \otimes \hat{\mathbf{P}}_r) \quad (7.43)$$

with the spontaneous polarization P_s and spontaneous strain ε_s . Here the Preisach operator is based on the scalar product of the current electric field and the individual direction $\hat{\mathbf{a}}$ of the ODF as input variables and is given by

$$\mathbf{p}(\mathbf{E}, \hat{\mathbf{a}}) = \int_{\beta} \int_{\alpha} \boldsymbol{\omega}(\alpha, \beta) \gamma(\alpha, \beta) \mathbf{E}(t) \cdot \hat{\mathbf{a}} \, d\alpha d\beta. \quad (7.44)$$

For a suitable approximation of the typical ferroelectric polarization behavior, the Preisach weight function $\boldsymbol{\omega}(\alpha, \beta)$ as well as the switching thresholds α and β are in this case adjusted to the hyperbolic tangent. However, a Preisach operator is defined on a fixed preferred direction, where the individual hysterons switch to their *up* and *down* positions at the individual orientation. In order to extend the classical Preisach model to the three-dimensional space, several Preisach operators are applied on multiple orientations on the nanoscopic level, which are distributed in the three dimensional space. The distribution of the individual directions of the ODF is based on the same approach as in Section 7.3. After the determination of the individual Preisach operators, which depend on the current local microscopic electric field in the corresponding direction, the constitutive quantities on the microscopic level are calculated by a homogenization over all nanoscopic orientations n_{orient} as

$$\boldsymbol{\lambda} = \frac{1}{n_{orient}} \sum_{i=1}^{n_{orient}} \hat{\boldsymbol{\lambda}}_i \quad \text{with} \quad \hat{\boldsymbol{\lambda}}_i = \{\hat{\boldsymbol{\sigma}}_i, \hat{\mathbf{D}}_i, \hat{\mathbf{B}}_i, \hat{\mathbb{C}}_i, \hat{\boldsymbol{\varepsilon}}_i, \hat{\boldsymbol{\varepsilon}}_i, \hat{\boldsymbol{\mu}}_i, \hat{\boldsymbol{\varepsilon}}_{r,i}, \hat{\mathbf{P}}_{r,i}\}. \quad (7.45)$$

Then the microscopic constitutive equations of the ferroelectric phase are computed via (7.45) with the constitutive quantities related to the individual orientations of the ODF as

$$\begin{aligned}\boldsymbol{\sigma} &= \mathbb{C} : (\boldsymbol{\varepsilon} - \boldsymbol{\varepsilon}_r) - \mathbf{e}^T \cdot \mathbf{E} \\ \mathbf{D} &= \mathbf{e} : (\boldsymbol{\varepsilon} - \boldsymbol{\varepsilon}_r) + \boldsymbol{\varepsilon} \cdot \mathbf{E} + \mathbf{P}_r \\ \mathbf{B} &= \boldsymbol{\mu} \cdot \mathbf{H} .\end{aligned}\quad (7.46)$$

In order to incorporate a dependence of the electro-mechanical coupling intensity on the current polarization state, the piezoelectric tensor \mathbf{e} is multiplied by $\|\mathbf{P}_r\|/P_s$, see for example KAMLAH [90]. The following numerical example highlights the influence of the ODF on the effective dielectric and butterfly hysteresis curve compared to one orientation. A purely ferroelectric body is considered which is loaded with an alternating electric field. The boundary value problem is depicted in Figure 7.4(a) with the loading path of the electric field in Figure 7.4(b).

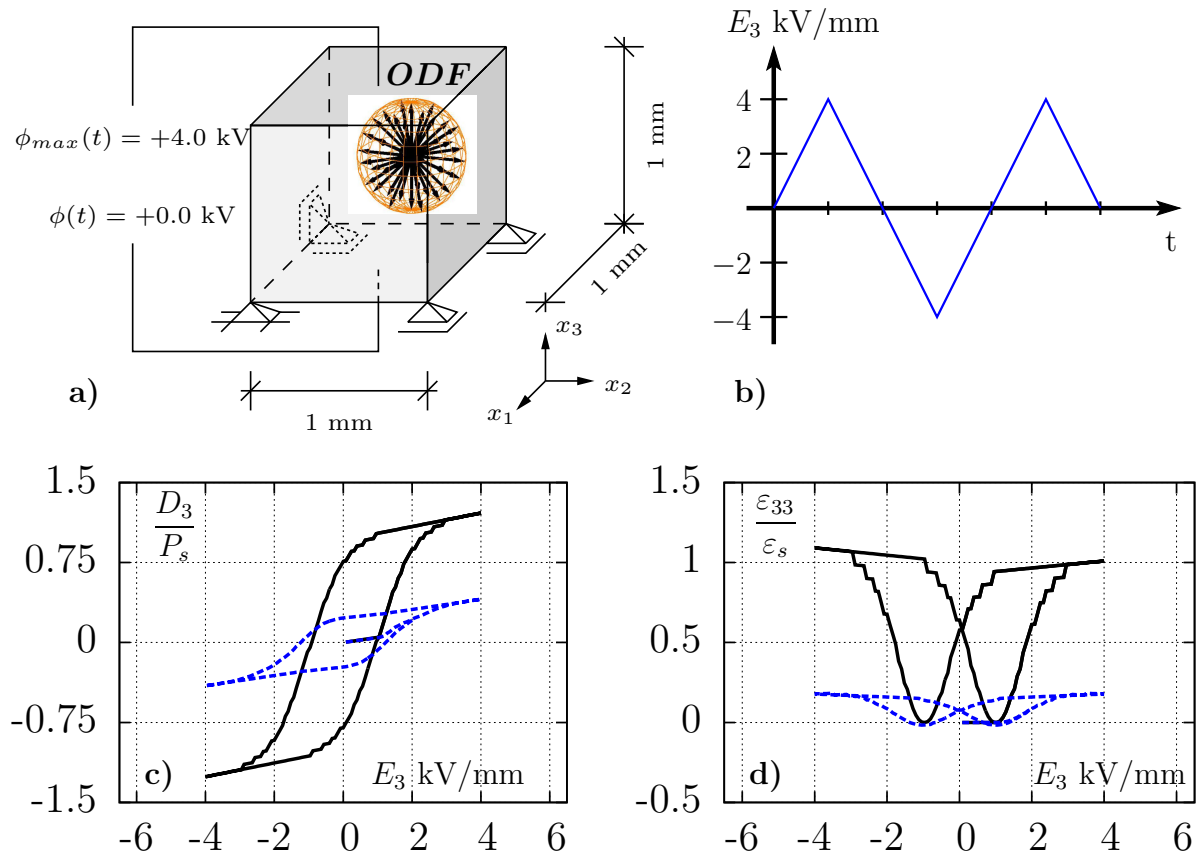


Figure 7.4: a) Macroscopic boundary value problem. The ferroelectric material is loaded with an alternating electric field in vertical direction. b) Loading path of the electric field. Comparison of the c) dielectric and d) butterfly hysteresis curve for 1 (solid black line) and 42 (dashed blue line) orientations. Taken from SCHRÖDER AND LABUSCH [186].

An orientation distribution function is used in each integration point, where a Preisach operator is applied on the individual directions. The corresponding microscopic constitutive quantities are determined through a homogenization over all orientations. Taking a look at the response of the dielectric and butterfly hysteresis curves, in Figure 7.4(c) and (d), a reduction of the maximum polarization and deformation values can be observed. The hysteresis loops of the orientation along the external field axis are highlighted by the

black solid line. The response using the ODF is depicted by the dashed blue line. Due to the homogenization over multiple orientations pointing in different directions in the three dimensional space, a decrease of the saturation values can be explained, see for example LANDIS ET AL. [119] or KURZHÖFER [109]. In contrast to a single orientation, 50 rays on each direction of the ODF are sufficient to generate smooth hysteresis curves. In the following this Preisach model is applied to the simulation of magneto-electric composites. An alternating electric field is applied in vertical direction on the macroscopic body, see Figure 7.5(a).

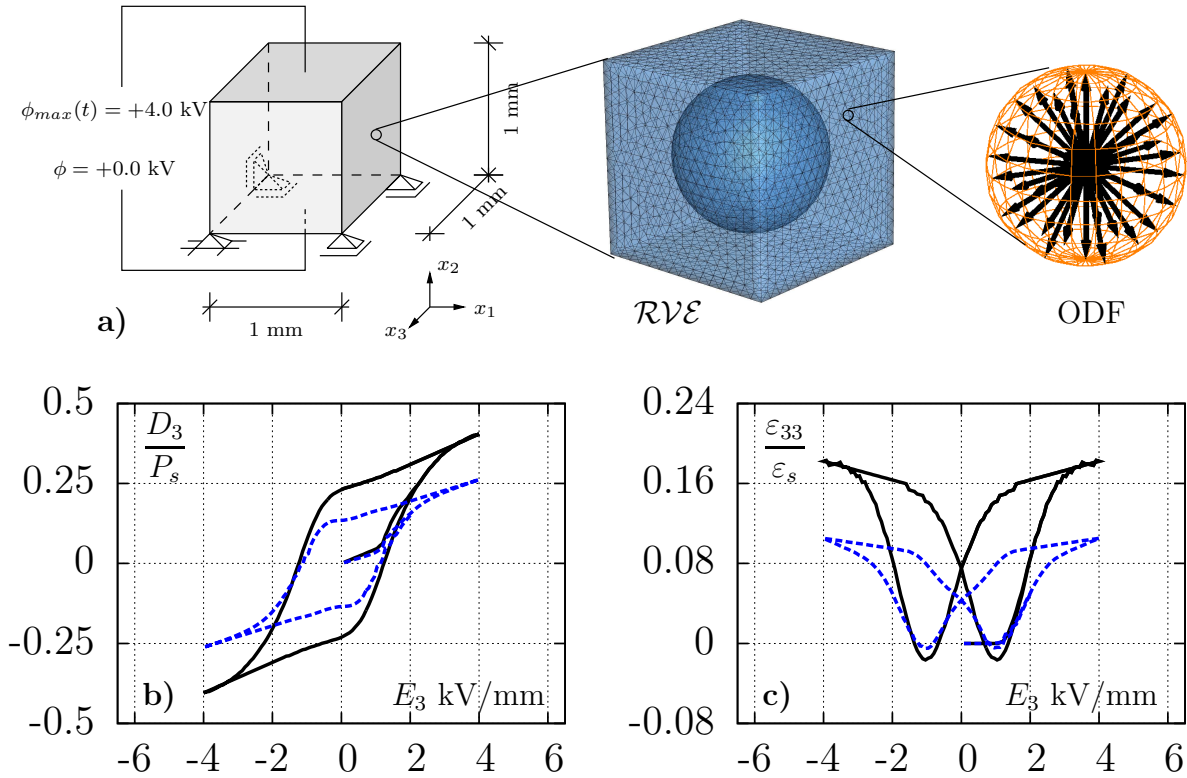


Figure 7.5: a) Macroscopic bvp with attached \mathcal{RVE} and further assigned ODF. Comparison of the b) dielectric and c) butterfly hysteresis loops for a single phase ferroelectric material (solid black line) and a two-phase composite (dashed blue line). Taken from SCHRÖDER AND LABUSCH [186].

A representative volume element is used in each macroscopic integration point, which is characterized by a ferroelectric matrix with spherical piezomagnetic inclusions. An ODF using the Preisach operators is assigned to each microscopic integration point of the ferroelectric matrix. Figures 7.5(b) and (c) illustrate the response of a purely ferroelectric body (solid black curve) to a composite material (dashed blue curve), using an ODF in both cases. A reduction of the maximum saturation values of the composite compared to a single ferroelectric phase is observable. The reason for this decrease is due to the reduced volume fraction of the electric phase. Furthermore, it can be noticed that the slope of the butterfly hysteresis after the poling process ($4 \geq E_3(t) \geq 2$) is flatter than the piezoelectric slope of a single-phase body in the same electric field range. Due to the inhomogeneous microscopic morphology, some areas in the microstructure with local electric field minima are not completely saturated, which explains the reduced piezoelectric slope. Overall this approach is capable of describing suitable material responses for single-phase

and composite materials. However, due to the multiple orientations, which are necessary to describe an accurate behavior in all space directions, and the resulting large number of Preisach relays, the computations are highly time consuming. In view of combining this Preisach approach with a nonlinear model for the other phase of two-phase composites, the calculation time and memory space are too high. Therefore, a second approach of the Preisach model using only one orientation which rotates into the corresponding direction is presented.

7.4.3 Magnetostrictive Preisach model

For the magnetostrictive three-dimensional model the Preisach operator \mathfrak{p} is applied on one preferred direction \mathbf{a} , which is assumed to coincide with the direction of remanent magnetization. Due to the additive decomposition into a linear elastic and a nonlinear remanent part, a generalized coordinate-invariant formulation of a magneto-electro-mechanical enthalpy function ψ_4 for transversely isotropic solids in the style of SCHRÖDER AND GROSS [184] is used with

$$\begin{aligned} \psi_5 = & \frac{1}{2}\lambda I_1^2 + \mu I_2 + \omega_1 I_5 + \omega_2 J_4^2 + \omega_3 I_1 I_4 + \kappa_1 I_1 J_2^m + \kappa_2 I_4 J_2^m + \kappa_3 K_1^m \\ & + \gamma_1 J_1^e + \gamma_2 (J_2^e)^2 + \xi_1 J_1^m + \xi_2 (J_2^m)^2 - J_2^m M_1^m, \end{aligned} \quad (7.47)$$

where the invariant functions are formulated in terms of the following invariants

$$\begin{aligned} I_1 &= \text{tr}[\boldsymbol{\varepsilon}_e], & I_5 &= \text{tr}[\boldsymbol{\varepsilon}_e^2 \mathbf{m}], & J_1^m &= \text{tr}[\mathbf{H} \otimes \mathbf{H}], & M_1^m &= \text{tr}[\mathbf{M}_r \otimes \mathbf{a}], \\ I_2 &= \text{tr}[\boldsymbol{\varepsilon}_e^2], & J_1^e &= \text{tr}[\mathbf{E} \otimes \mathbf{E}], & J_2^m &= \text{tr}[\mathbf{H} \otimes \mathbf{a}], & K_1^m &= \text{tr}[\boldsymbol{\varepsilon}_e(\mathbf{H} \otimes \mathbf{a})], \\ I_4 &= \text{tr}[\boldsymbol{\varepsilon}_e \mathbf{m}], & J_2^e &= \text{tr}[\mathbf{E} \otimes \mathbf{a}] \end{aligned} \quad (7.48)$$

with the structural tensor \mathbf{m} and the remanent magnetization \mathbf{M}_r depending on the magnetic field described by the Preisach operator $\mathfrak{p}(\mathbf{H})$. Analogous to the latter model, the invariants depend on the elastic part of the strains $\boldsymbol{\varepsilon}_e$, due to the decomposition into an elastic (reversible) and remanent part, according to KAMLAH AND TSAKMAKIS [92],

$$\mathbf{B} = \mathbf{B}_e + \mathbf{M}_r \quad \text{and} \quad \boldsymbol{\varepsilon} = \boldsymbol{\varepsilon}_e + \boldsymbol{\varepsilon}_r, \quad (7.49)$$

where the remanent magnetization is determined through the Preisach operator and the remanent strains depend on the current magnetization state as

$$\mathbf{M}_r = \mathfrak{p}(\mathbf{H})\mathbf{a} \quad \text{and} \quad \boldsymbol{\varepsilon}_r^{CFO} = \frac{3}{2} \frac{\varepsilon_s}{M_s^2} \left[\text{dev}(\mathbf{M}_r \otimes \mathbf{M}_r) - \frac{1}{2} \text{dev}(\mathbf{M}_r^{soft} \otimes \mathbf{M}_r^{soft}) \right] \quad (7.50)$$

with the saturation magnetization M_s and the saturation strain ε_s . Commonly, the remanent strains are assumed to be proportional to the squared remanent magnetization vector \mathbf{M}_r^2 as $\boldsymbol{\varepsilon}_r = (3\varepsilon_s)/(2M_s^2)\text{dev}(\mathbf{M}_r \otimes \mathbf{M}_r)$. However, the strain hysteresis curve can also be modeled by an extended hysteresis operator which describes a more complex behavior. As in the case of cobalt ferrite (CFO), where a softening behavior can be observed in the magnetostriction for increasing magnetic fields, an extended approach is used for the remanent strains, where a softening magnetization $\mathbf{M}_r^{soft} = \mathfrak{p}^{soft}(\mathbf{H})\mathbf{a}$ is introduced to reduce magnetostriction. This softening magnetization is determined by a further set

of Preisach relays, which do not affect the overall magnetization but influence the overall remanent strains. The Preisach operator is determined through

$$\mathbf{p}(\mathbf{H}, \mathbf{a}) = \int_{\beta} \int_{\alpha} \omega(\alpha, \beta) \gamma(\alpha, \beta) \mathbf{H}(t) \cdot \mathbf{a} \, d\alpha \, d\beta, \quad (7.51)$$

which now depends on the current magnetic field vector as well as the preferred orientation \mathbf{a} . Since the Preisach relays should switch their values due to the magnetic field in magnetization direction, the scalar product of \mathbf{H} and \mathbf{a} is included. In order to extend this approach to the three dimensional space the preferred orientation aligns with the direction of the microscopic magnetic field. This involves an update of the material tangent moduli, depending on the preferred direction \mathbf{a} , as well as switchings of the corresponding Preisach relays. However, a direct switching of the orientation \mathbf{a} could yield a large shift of the material tangent moduli. The solution of the boundary value problem with these updated properties could result in a largely changed microscopic magnetic field distribution, leading to a back-and-forth oscillation of the preferred direction \mathbf{a} and the Preisach relays. In order to prevent these numerical instabilities, the orientation *slowly* rotates into the direction of the microscopic magnetic field. In this context, the term *slowly* means that the rotation is assumed to be a time dependent process, where a fraction of the total angle θ_{total} defines the rotation angle θ_{rot} during one load step with

$$\theta_{total} = \arccos \left[\frac{\mathbf{a}_n \cdot \mathbf{H}}{\|\mathbf{a}_n\| \cdot \|\mathbf{H}\|} \right] \quad \text{and} \quad \theta_{rot} = -\tanh[\kappa_{\theta} \cdot \tilde{t}] \cdot \theta_{total}, \quad (7.52)$$

where κ_{θ} denotes the rotation speed depending on the time step dt and the index n the current time step. The virtual time \tilde{t} is set to zero for each new load step, such that the magnetization can rotate after changing the load for several time steps. A rotation matrix \mathbf{R}^M uses the determined angle to rotate the magnetization direction \mathbf{a}_n of the last time step into the new direction \mathbf{a}_{n+1} with

$$\mathbf{a}_{n+1} = \mathbf{R}^M(\theta_{rot}) \mathbf{a}_n. \quad (7.53)$$

This time dependent rotation results in a stepwise update of the material tangent moduli and Preisach relays, without numerical instabilities. It has to be mentioned that a slow rotation of the magnetization direction yields stable calculations but results in an unnatural behavior of the hysteresis for a 180° rotation of the applied magnetic field. Then, the magnetization does not switch its direction at the coercivity field, but several load steps beyond. Therefore, a further criterion is implemented, which checks, whether the magnetization wants to switch into the opposite direction for several load steps. This is only the case for a reversal of the applied field into the opposite direction. If the criterion is fulfilled, the magnetization performs a rotation of the full angle θ_{total} . After this full rotation the angle θ_{rot} is used for the following change of the magnetization direction as before. A further approach to adjust the model to the natural material behavior, is to multiply the magneto-mechanical coupling modulus \mathbf{q} with a factor depending on the current magnetization state, here defined as

$$\mathbf{q} = \left(2 \frac{\|\mathbf{M}_r\|}{M_s} \left[1 - \left(\frac{\|\mathbf{M}_r\|}{M_s} \right)^2 \right] - \frac{\|\mathbf{M}_r^{soft}\|}{M_s} \left[1 - \left(\frac{\|\mathbf{M}_r^{soft}\|}{M_s} \right)^2 \right] \right) \hat{\mathbf{q}}. \quad (7.54)$$

The coupling tensor $\hat{\mathbf{q}}$ includes the maximum magneto-mechanical coupling parameters. Commonly, the coupling tensor is given as $\mathbf{q} = \|\mathbf{M}_r\|/M_s \hat{\mathbf{q}}$, see for example KAMLAH [90], and is for instance used to describe a ferroelectric material behavior, where the maximum electro-mechanical coupling is reached for the saturation polarization and the piezoelectric characteristics are dominant. However, this approach does not capture the complex magnetostrictive response of cobalt ferrite. Therefore, a factorization is used, which considers, on the one hand, no further increase of the magnetostriction after saturation and, on the other hand, the so called softening behavior, such that the coupling tensor is defined as in Equation (7.54). The microscopic constitutive equations are then given as

$$\begin{aligned}\boldsymbol{\sigma} &= \mathbb{C} : \boldsymbol{\varepsilon}_e - \mathbf{q}^T \cdot \mathbf{H} , \\ \mathbf{B} &= \mathbf{q} : \boldsymbol{\varepsilon}_e + \boldsymbol{\mu} \cdot \mathbf{H} + \mathbf{M}_r .\end{aligned}\tag{7.55}$$

Although a large number of relays is necessary to describe a smooth hysteresis loop, it requires large memory space and strongly reduces the calculation speed. Therefore, a suitable number of relays has to be chosen to reduce the calculation time and simultaneously generate a smooth hysteresis curve. The dependence of the number of relays on the approximation of the material behavior is demonstrated by considering a purely ferromagnetic body, which is loaded with an alternating magnetic field in vertical direction H_3 , see Figure 7.6. The number of relays is increased in each simulation in order to approximate the overall hysteresis loops more precisely.

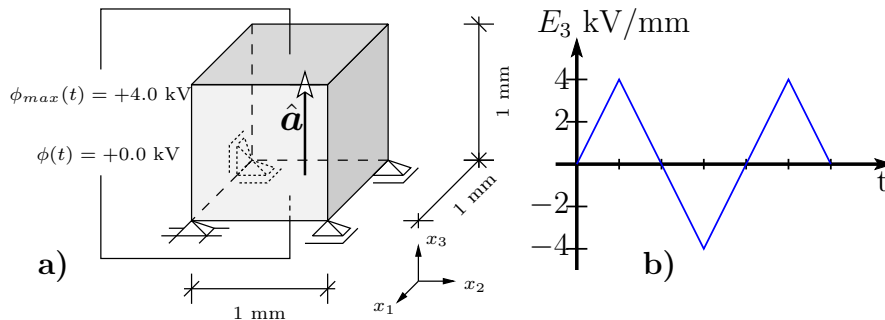


Figure 7.6: a) Unit cell calculation: the ferroelectric phase is loaded with an electric field E_3 in vertical direction and the preferred direction $\hat{\mathbf{a}}$ is also oriented in vertical direction. b) Loading path of the alternating electric field.

Figure 7.7 exemplarily depicts the overall strain hysteresis curve for 10, 100, and 250 relays. After reaching the coercive field, the relays switch into the *up* position and cause a contraction of the material in the applied field direction. Due to the different switching thresholds of the individual relays, a cascaded increase of the magnetostriction is observed below a field strength of 1 kA/mm. For a further increase of the magnetic field, the magnetostriction decreases due to the assumed softening behavior. The slope of the individual steps, between the switching of the Preisach relays, is driven by the magneto-mechanical coupling modulus \mathbf{q} , which can clearly be seen in Figure 7.7(a). After reaching the saturation magnetostriction, the coupling modulus \mathbf{q} vanishes and the slope of the steps is equal zero. However, to reach a suitable approximation of \mathbf{q} the number of Preisach relays has to be increased. Figure 7.7(b) depicts the effective magnetostrictive response for 100 relays. The complete hysteresis curve matches the realistic behavior well, although the cascaded change of magnetostriction is still visible. A smooth curve is obtained with about

250 relays, shown in Figure 7.7(c). The material parameters used for the simulation of cobalt ferrite are listed in Table 7.4. Based on the work of BALKE AND SUCHANECK [13] we used the following set of material parameters to describe the behavior of cobalt ferrite. The elastic stiffness moduli of CoFe_2O_4 are taken from LI ET AL. [125]. Due to the decomposition of the magnetic induction $\mathbf{B} = \mu_0\mathbf{H} + \mathbf{M}_r$ and the application of the Preisach model, we use the vacuum permeability μ_0 for the magnetic permeability μ_{11} and μ_{33} , whereas the magnetic susceptibility, resulting in the nonlinear increase of the magnetization, is captured by the Preisach operator.

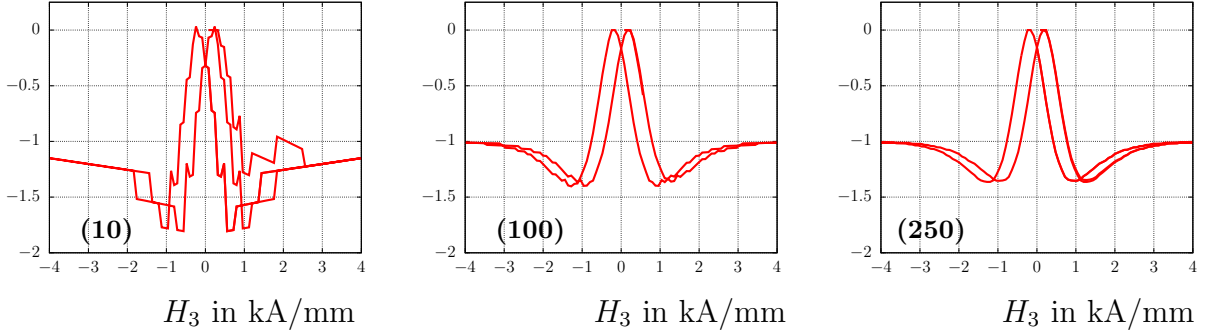


Figure 7.7: Magnetostrictive hysteresis loop for 10 relays, 100 relays and 1000 relays.

The electric permittivity is taken from LEE ET AL. [121]. In order to characterize the nonlinear magnetostrictive behavior we fitted the coupling parameters q_{311} and q_{333} to experimental measurements of the strain hysteresis curve of cobalt ferrite. However, we neglected the value of q_{113} since the properties of the shear deformations are not fitted to experimental measurements. Furthermore, a stress-induced switching criterion is not implemented in the Preisach operator, such that we neglect the value of $\hat{\sigma}_c$. The coercive magnetic field \hat{H}_c and the saturation magnetization are taken from KAMBALE ET AL. [89]. For the characterization of the saturation magnetostriction, we fitted the value of $\hat{\epsilon}_s$ to experimental results. In order to depict the hysteresis curves in an appropriate manner, we used 200 Preisach relays for the simulation of the two-phase composite in Section 8.4.

Table 7.4: Material parameters of cobalt ferrite (CoFe_2O_4). The relative magnetic permeability $\mu^r = \mu/\mu_0$ and dielectric permittivity $\epsilon^r = \epsilon/\epsilon_0$ are determined with the vacuum permeability $\mu_0 = 4\pi \cdot 10^{-7} \text{ N/A}^2$ and the vacuum permittivity $\epsilon_0 = 8.854 \cdot 10^{-6} \text{ mC/kVm}$.

Parameter	Unit	CoFe_2O_4	Parameter	Unit	CoFe_2O_4
\mathbb{C}_{1111}	N/mm^2	$25.71 \cdot 10^4$	μ_{11} (μ_{11}^r)	N/kA^2 (-)	1.256 (1)
\mathbb{C}_{1122}	N/mm^2	$15.00 \cdot 10^4$	μ_{33} (μ_{33}^r)	N/kA^2 (-)	1.256 (1)
\mathbb{C}_{1133}	N/mm^2	$15.00 \cdot 10^4$	ϵ_{11} (ϵ_{11}^r)	mC/kVm (-)	$0.80 \cdot 10^{-4}$ (9.04)
\mathbb{C}_{3333}	N/mm^2	$25.71 \cdot 10^4$	ϵ_{33} (ϵ_{33}^r)	mC/kVm (-)	$0.93 \cdot 10^{-4}$ (10.5)
\mathbb{C}_{1212}	N/mm^2	$5.36 \cdot 10^4$	$\hat{\sigma}_c$	N/mm^2	0.0
\mathbb{C}_{1313}	N/mm^2	$8.53 \cdot 10^4$	\hat{H}_c	kA/mm	0.12
q_{311}	N/Am	5.0	\hat{M}_s	N/kAmm	0.71
q_{333}	N/Am	-12.0	$\hat{\epsilon}_s$	-	-0.00016
q_{113}	N/Am	0.0	relays	-	200

8 Numerical examples

The goal of the following section is to take a closer look at several numerical simulations of magneto-electric composites and compare the accuracy of the predicted ME coefficient with experimental measurements. On the one hand, different material models for the ferroelectric and magnetostrictive phase are used in order to make a statement which approach is suitable for the prediction of the magneto-electric coupling. On the other hand, influences such as defects or the microstructural morphology, are investigated. First, we start with a purely piezoelectric and piezomagnetic model for the corresponding phases. Thereby the resulting ME coefficient for different pre-polarization states is investigated. In the second part a nonlinear magnetostrictive model in combination with a linear piezoelectric model is used to show the nonlinear influences on the magneto-electric coupling. Third, the nonlinear properties of the ferroelectric phase are simulated in combination with a linear piezomagnetic model. In the fourth part, the Preisach model, is used to simulate the particular behavior of cobalt ferrite. In combination with the nonlinear ferroelectric model the resulting nonlinear magneto-electric coupling is investigated. After showing the impact of different material models, further influences on the ME coupling, such as pores at the interfaces and microscopic morphologies are taken into account.

8.1 Piezomagnetic-piezoelectric composite

In the first subsection we examine the magneto-electric coupling by taking into account purely linear piezoelectric and piezomagnetic behaviors for both phases, which is shown in LABUSCH ET AL. [111]. The used material parameters are listed in Table 8.1 and were taken from LEE ET AL. [121]. However, referring to LEE ET AL. [121] two material parameters were changed. The modified parameters are the magnetic permeability $\mu_{11} = 157 \text{ N/kA}^2$ and the piezomagnetic coefficient $q_{33} = -699.7 \text{ N/kAmm}$.

Table 8.1: Piezoelectric/-magnetic material parameters used for barium titanate (BaTiO_3) and cobalt ferrite (CoFe_2O_4), taken from LEE ET AL. [121]. The following two parameters were changed, $\mu_{11} = 157 \text{ N/kA}^2$ and $q_{33} = -699.7 \text{ N/kAmm}$, see Chapter 4.1.3.

Para.	Unit	BaTiO_3	CoFe_2O_4	Para.	Unit	BaTiO_3	CoFe_2O_4
\mathbf{C}_{11}	N/mm^2	$16.6 \cdot 10^4$	$28.60 \cdot 10^4$	q_{31}	N/kAmm	0.0	580.3
\mathbf{C}_{12}	N/mm^2	$7.7 \cdot 10^4$	$17.30 \cdot 10^4$	q_{33}	N/kAmm	0.0	-699.7
\mathbf{C}_{13}	N/mm^2	$7.8 \cdot 10^4$	$17.05 \cdot 10^4$	q_{15}	N/kAmm	0.0	550.0
\mathbf{C}_{33}	N/mm^2	$16.2 \cdot 10^4$	$26.95 \cdot 10^4$	ϵ_{11}	mC/kVm	$112 \cdot 10^{-4}$	$0.80 \cdot 10^{-4}$
\mathbf{C}_{44}	N/mm^2	$4.3 \cdot 10^4$	$4.53 \cdot 10^4$	ϵ_{33}	mC/kVm	$126 \cdot 10^{-4}$	$0.93 \cdot 10^{-4}$
e_{31}	C/m^2	-4.4	0.0	μ_{11}	N/kA^2	5.0	157.0
e_{33}	C/m^2	18.6	0.0	μ_{33}	N/kA^2	10.0	157.0
e_{15}	C/m^2	11.6	0.0				

A detailed explanation and fitting of the material parameters to experimental measurements of cobalt ferrite is given in Chapter 4.1.3. For a comparison of the simulated magneto-electric coefficients with experimental measurements we first take into account

the work of ETIER ET AL. [45]. In order to include the effect of microstructural morphology on the magneto-electric coupling, a realistic microstructure is used consisting of 80% weight fraction of barium titanate and 20% weight fraction of cobalt ferrite ($0.2\text{CoFe}_2\text{O}_4 - 0.8\text{BaTiO}_3$). Therefore, a microscopic image is taken from a real composite, see Figure 8.1, where the brighter areas (gray) represent the matrix material barium titanate and the darker parts (black) represent the inclusion material cobalt ferrite.

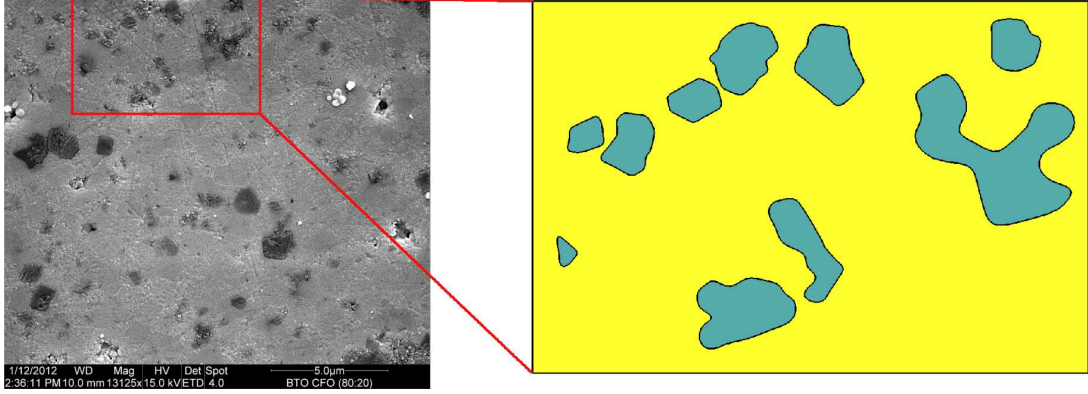


Figure 8.1: Real composite microstructure with selected representative volume element. Taken from LABUSCH ET AL. [111].

The microscopic image is only a very small part of the sample and the surface fraction of the inclusion material does not match the complete volume fraction of cobalt ferrite exactly. In order to match with the originally used volume fractions a rectangular representative volume element of the image is chosen, which is highlighted with a red frame in Figure 8.1. At this point it has to be mentioned, that a conversion from volume fractions to surface fractions is not taken into account, see EXNER [48]. The selected part of the microstructure is discretized with 5324 quadratic triangular finite elements, see Figure 8.2.

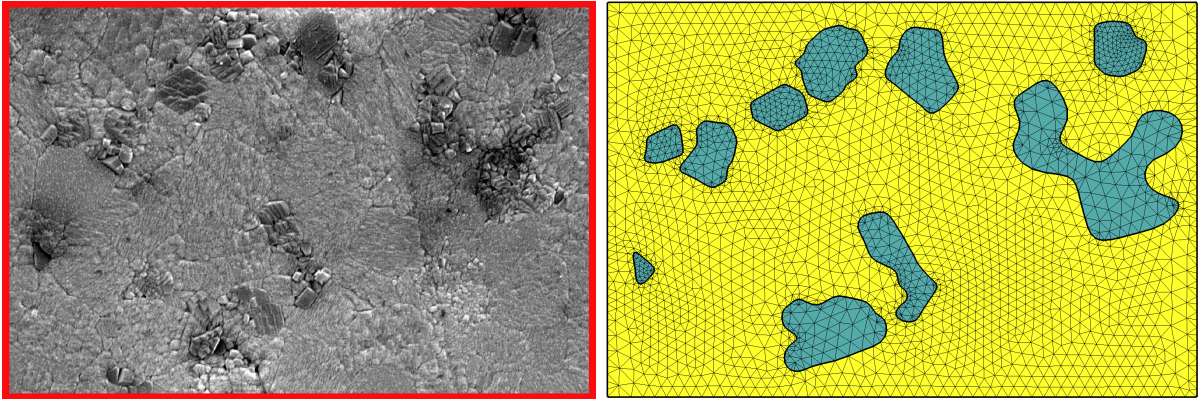


Figure 8.2: (left) Electron microscopy image of the composite microstructure and (right) finite element discretization. Taken from LABUSCH ET AL. [111].

Periodic boundary conditions are used in the numerical simulation, since a periodic multiplication of the chosen \mathcal{RVE} in the two spatial directions is imagined as an approximation of the real microstructure. The body is loaded with a macroscopic vertical electric field $\bar{\mathbf{E}} = [0, \bar{E}_2, 0]^T$. Since we use a transversely isotropic material model for both phases

a preferred direction has to be defined in each Gauss point, which is set to point in positive vertical direction. With the used material parameters from Table 8.1 a magneto-electric coupling coefficient of $\bar{\alpha}_{22} = 10.9 \cdot 10^{-10}$ s/m is obtained. This value is a huge overestimation compared to the experimental value of $\bar{\alpha}_{22} = 4.4 \cdot 10^{-12}$ s/m taken from ETIER ET AL. [45]. The large difference between both results has several reasons. A deviation of the ME-coefficient is given by the simplification to the two-dimensional space, where the shape of the inclusion with the same volume fraction is different to the three-dimensional space. A further influence is given by the used material models. In this example linear material behavior is considered for both phases, where the material parameters are fitted to the behavior after a poling and a magnetization step, respectively. Therefore, the models represent fully polarized electric and fully magnetized magnetic materials with the best achievable piezoelectric as well as piezomagnetic properties. However, these perfectly polarized and magnetized materials are unrealistic in magneto-electric composites since microstructural inhomogeneities may prevent the rotation of the electric polarization or magnetization in the most advantageous direction. This yields a further simplification in the simulation, which is the orientation of the preferred direction. For both phases the preferred direction, which describes the direction of the best piezoelectric/-magnetic coupling, points in positive vertical direction parallel to the direction of the applied macroscopic electric field. As mentioned above, such a polarization as well as magnetization state in composite materials is hardly achievable in reality.

In the following numerical simulations, the listed simplifications which affect the determination of the magneto-electric coupling in a negative manner should be avoided by using more appropriate assumptions as well as nonlinear material models. We start with a pre-polarization step of the electric matrix material due to an applied macroscopic electric field. On the one hand, this pre-polarization step should determine the microscopic polarization directions in each integration point resulting in a more realistic polarization state of the different regions on the microscopic level instead of assuming a uniform polarization over the complete microstructure in vertical direction. On the other hand, the microscopic electric fields resulting from the applied macroscopic field determine the intensity of the piezoelectric coupling. In those areas, where the microscopic electric field is low, the piezoelectric coupling is also low correspondingly, since an electric field intensity for a saturation polarization in this area is not reached. In those areas, where the microscopic field is high enough to assume a saturation polarization the piezoelectric coupling modulus reaches its maximum value. The approach of an incorporation of a pre-polarization step is listed in Table 8.2 and done in the following way.

Table 8.2: Determination of the piezoelectric coupling properties on the microscale.

-
1. Set initial preferred direction $\mathbf{a}_0 = [0, 1, 0]$
 2. Neglect constitutive couplings: set piezoelectric moduli equal zero $\mathbf{e} = \mathbf{0}$
 3. Apply macroscopic electric field $\bar{\mathbf{E}} = [0, \bar{E}_2, 0]$; compute local distribution of \mathbf{E}
 4. Choose preferred directions \mathbf{a} for each Gauss point with $\mathbf{a} = \mathbf{E}/\|\mathbf{E}\|$
 5. Estimate relative amplitude of remanent polarization $p_s = \tanh(c \cdot \|\mathbf{E}\|) \in [0, 1)$
 6. Determine piezoelectric moduli $\mathbf{e} = p_s(-\beta_1 \mathbf{a} \otimes \mathbf{1} - \beta_2 \mathbf{a} \otimes \mathbf{a} \otimes \mathbf{a} - \beta_3 \hat{\mathbf{e}})$ with $\hat{e}_{kij} = \frac{1}{2}[a_i \delta_{kj} + a_j \delta_{ki}]$
-

First, the initial preferred direction in each integration point, representing the polarization orientation, is set to point in vertical direction as $\mathbf{a}_0 = [0, 1, 0]$. To avoid an interaction between the electric fields and microscopic stresses during poling, the piezoelectric coupling is set to zero at the beginning. Then, a macroscopic electric field is applied to the microstructure with $\overline{\mathbf{E}} = [0, \overline{E}_2, 0]$, $\boldsymbol{\varepsilon} = \mathbf{0}$ and $\mathbf{H} = \mathbf{0}$. Due to the heterogeneous microstructure an inhomogeneous distribution of the microscopic electric fields is obtained. This distribution is used to determine the polarization direction in each microscopic integration point with $\mathbf{a} = \mathbf{E}/\|\mathbf{E}\|$. Furthermore, the piezoelectric modulus \mathbf{e} in each microscopic integration point depends on the magnitude of the corresponding local electric field. Since the piezoelectric coupling correlates with the polarization state, we estimate the dimensionless relative amplitude of the remanent local polarization with

$$p_s = \tanh(c \cdot \|\mathbf{E}\|) \in [0, 1) . \quad (8.1)$$

It is assumed that the polarization due to an increasing electric field can be described by the function of a hyperbolic tangent, which depends on the slope c and the norm of the electric field $\|\mathbf{E}\|$. In the following examples the value of c is set to 2 mm/kV in order to approximate the polarization behavior of barium titanate. This function saturates against the value 1 which describes the state of a saturated polarization. Since we do not take into account remanent polarizations in this model, we use the assumed polarization state for the determination of the piezoelectric modulus with

$$\mathbf{e} = p_s(-\beta_1 \mathbf{a} \otimes \mathbf{1} - \beta_2 \mathbf{a} \otimes \mathbf{a} \otimes \mathbf{a} - \beta_3 \hat{\mathbf{e}}) \quad (8.2)$$

and $\hat{e}_{kij} = \frac{1}{2}[a_i \delta_{kj} + a_j \delta_{ki}]$. This strategy ensures that the piezoelectric material parameters, obtained from a polarized barium titanate sample, are multiplied with the value 1 for saturated polarization. Before the saturation of the polarization is reached, the piezoelectric material parameters are scaled with a value between 0 and 1. The following Figure 8.3 shows the resulting microscopic polarization directions and the scaling values p_s for applied macroscopic electric fields $\overline{E}_2 = 0.5$ kV/mm and $\overline{E}_2 = 1.0$ kV/mm.

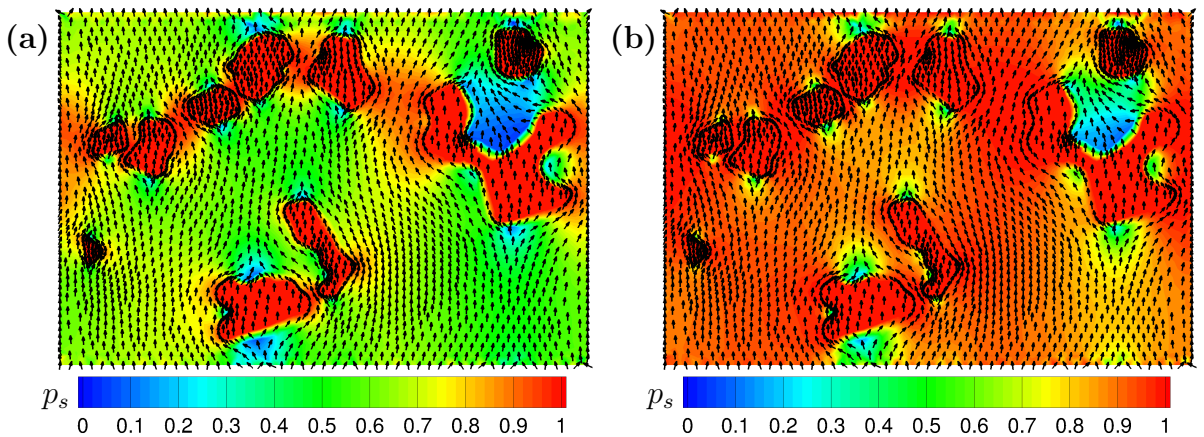


Figure 8.3: Distribution of p_s (contour) with preferred directions \mathbf{a} (vectors) for the applied electric fields $\overline{E}_2 = 0.5$ kV/mm (a) and $\overline{E}_2 = 1.0$ kV/mm (b). Taken from LABUSCH ET AL. [111].

For an applied electric field of $\overline{E}_2 = 0.5$ kV/mm, shown in Figure 8.3(a), the matrix material shows a scaling value between approximately 0.4 and 0.7 in most areas. Due to

the higher electric permittivity of the electric matrix we observe a field concentration of the microscopic electric fields at the left and right boundaries of the magnetic inclusions. As a consequence, the assumed polarization in these areas is almost saturated with $p_s \approx 1$. However, at the upper and lower boundaries of the inclusions we obtain a reduced assumed polarization resulting in a value of p_s between approximately 0 and 0.2. Figure 8.3(b) shows the distribution of p_s as a consequence of an applied macroscopic electric field $\overline{E}_2 = 1.0$ kV/mm. Now, most areas of the electric matrix show a value of $p_s = 1$. The regions of the matrix material at the upper and lower boundaries of the magnetic inclusions still show a non-saturated state, which means that the piezoelectric modulus is scaled with a value lower than 1. For the following investigation of the magneto-electric coupling, different simulations were performed with applied macroscopic electric fields in the range of 0.01 kV/mm and 3.0 kV/mm, which will lead to different pre-polarization states. After this pre-polarization processes, for the different electric field strengths, the microscopic preferred directions and the corresponding scaling factors for each microscopic integration point are stored and used for the next boundary value problem. Now, with the incorporation of the preferred directions and scaling factors, a new macroscopic electric field $\overline{E}_2 = 1.0$ kV/mm is applied to the microstructure to determine the ME coefficient. Due to the piezoelectric coupling of the matrix, its deformations are transferred to the magnetic inclusions, leading to a strain-induced magneto-electric coupling. Figures 8.4(a) and 8.4(b) show the microscopic distribution of the electric potential ϕ (contour) with the electric field directions \mathbf{E} (vectors) as well as the distribution of the magnetic potential φ (contour) with the direction vectors of the magnetic induction (vectors), respectively.

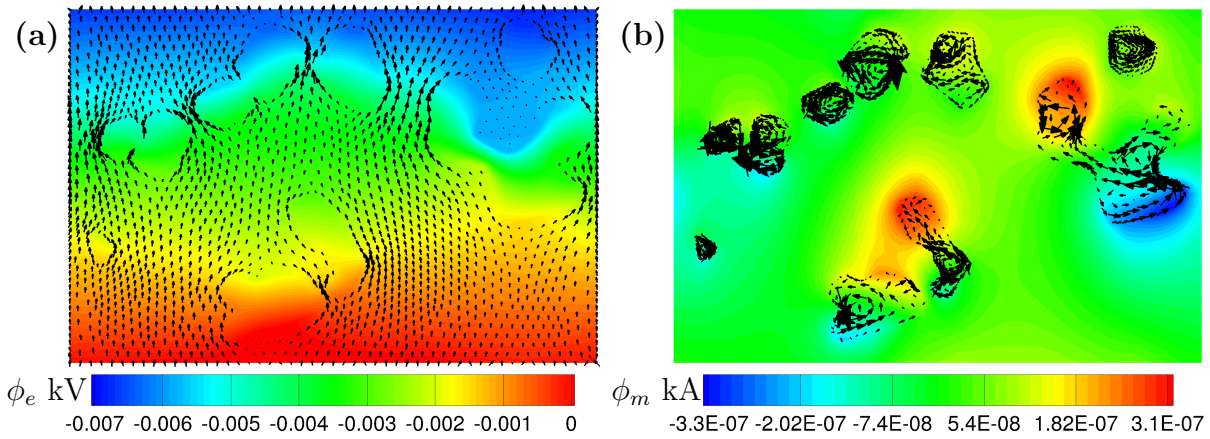


Figure 8.4: (a) Electric potential ϕ (contour) with electric field vectors \mathbf{E} (vectors) in the piezoelectric matrix and (b) magnetic potential φ (contour) with magnetic flux density vectors \mathbf{B} (vectors) in the inclusions for $\overline{E}_2 = 1.0$ kV/mm. Taken from LABUSCH ET AL. [111].

The effects of the transferred piezoelectric strains on the magnetic inclusions are shown in Figure 8.4(b). Due to the piezomagnetic coupling an arising distribution of the magnetic potential and magnetic induction can be observed. Figure 8.5 shows the resulting ME coefficient (y-axis) with respect to the electric field strength (x-axis) of the pre-polarization step. It can be clearly seen, that the ME coefficient depends on the increasing piezoelectric properties and thus on the hyperbolic tangent. For a saturation polarization of the complete matrix material an ME coefficient of $\overline{\alpha}_{22} = 8.04 \cdot 10^{-10}$ s/m is obtained. The ME coupling is decreased for lower electric fields during poling.

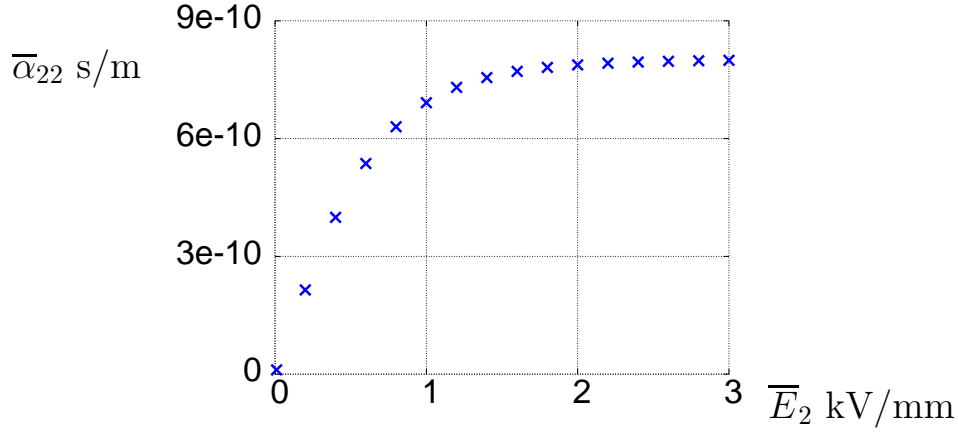


Figure 8.5: Magneto-electric coupling coefficient $\bar{\alpha}_{22}$ in s/m for different electric fields \bar{E}_2 in kV/mm for the pre-polarization. Taken from LABUSCH ET AL. [111].

It can be concluded that this approach is helpful for a more exact prediction of the ME coefficient, since a perfect polarization is hardly feasible. Since, each pre-polarization state can be simulated, it is possible to obtain a wide range of ME coefficients. However, if we compare the numerical results with the experimental measurement of ETIER ET AL. [46], who obtained a magneto-electric coupling of $\bar{\alpha}^{exp} = 4.4 \cdot 10^{-12}$ s/m, we can see a huge overestimation of the coupling coefficient for a saturated polarization state. This value can also be obtained with a pre-polarization based on a small electric field of about $\bar{E}_2 \approx 0.01$ kV/mm. But the resulting polarization distribution does not represent a realistic polarization state. Due to this approach it is shown that the microscopic polarization state has a significant influence on the ME coupling. Furthermore, with the simplified assumption of a linear model a good approximation of the material behavior can be given at a saturation state but is too inaccurate for different polarization states and applied field strengths. Thus, the following examples demonstrate the influence of nonlinear material models for the ferroelectric and magnetostrictive phases on the ME coupling.

8.2 Magnetostrictive-piezoelectric composite

In this numerical example we use a nonlinear magnetostrictive material model in order to depict more precisely the qualitative behavior of the magneto-electric coupling coefficient. In this example a different composite is investigated and a comparison with the experimentally measured magnitude of the ME coefficient is not done.

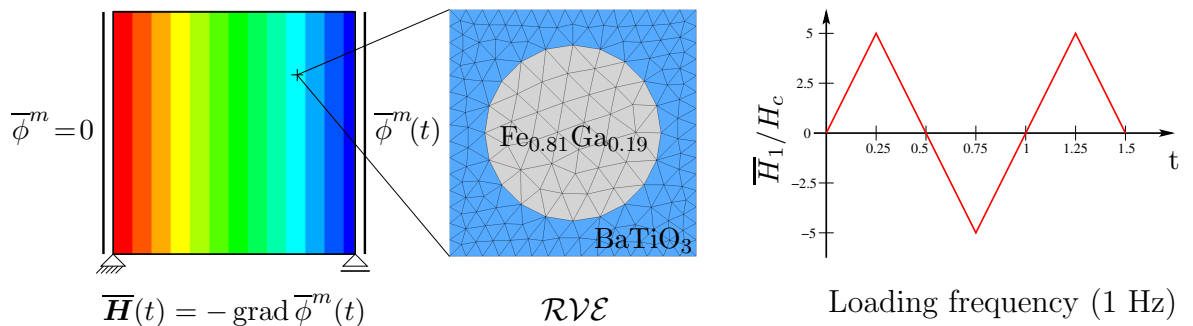


Figure 8.6: Macroscopic boundary value problem with attached \mathcal{RVE} and loading path. Taken from SCHRÖDER ET AL. [187].

A closer look is taken on the qualitative prediction of the ME coupling with respect to different magnetic field strengths. We consider a macroscopic composite, which is loaded with an alternating magnetic field in horizontal direction, see Figure 8.6. A representative volume element consisting of a piezoelectric barium titanate matrix with a circular magnetostrictive galfenol ($\text{Fe}_{0.81}\text{Ga}_{0.19}$) inclusion, is assigned to each macroscopic integration point. The piezoelectric phase has a surface fraction of 60%, whereas the magnetic phase has a surface fraction of 40%.

Table 8.3: Material Parameters for $\text{Fe}_{0.81}\text{Ga}_{0.19}$ (Galfenol) and BaTiO_3 (Barium Titanate) LABUSCH ET AL. [111], LEE ET AL. [121].

Param.	Unit	Name	BaTiO ₃	Param.	Unit	Name	Fe _{0.81} Ga _{0.19}
\mathbf{C}_{11}	N/mm ²	elasticity modulus	166000	λ	N/mm ²	Lamé parameter	15000
\mathbf{C}_{12}	N/mm ²	elasticity modulus	77000	μ	N/mm ²	Lamé parameter	10000
\mathbf{C}_{13}	N/mm ²	elasticity modulus	78000	M_s	N/(kAmm)	sat. magnetization	1.48
\mathbf{C}_{33}	N/mm ²	elasticity modulus	162000	ε_s	—	sat. remanent strain	0.0245%
\mathbf{C}_{44}	N/mm ²	elasticity modulus	43000	H_c	kA/mm	coercive field strength	0.002
ε_{11}	mC/kVm	dielectric modulus	0.0112	ε_{11}	mC/kVm	dielectric modulus	11.2
ε_{33}	mC/kVm	dielectric modulus	0.0126	ε_{33}	mC/kVm	dielectric modulus	12.6
μ_{11}	N/kA ²	magn. permeability	5.0	μ_M	N/kA ²	magn. permeability	4.5
μ_{33}	N/kA ²	magn. permeability	10.0	c	kA ² /N	hysteresis shape para.	300
q_0	N/(kAmm)	piezomagnetic mod.	0.0	q_0	N/(kAmm)	piezomagnetic mod.	73.3
q_{\perp}	N/(kAmm)	piezomagnetic mod.	0.0	q_{\perp}	N/(kAmm)	piezomagnetic mod.	-180.0
$q_{=}$	N/(kAmm)	piezomagnetic mod.	0.0	$q_{=}$	N/(kAmm)	piezomagnetic mod.	121.8
e_{31}	C/m ²	piezoelectric mod.	-4.4	η	(kAmm)/(Ns)	viscosity coefficient	10 ⁻⁶
e_{33}	C/m ²	piezoelectric mod.	18.6	n	—	viscosity exponent	2
e_{15}	C/m ²	piezoelectric mod.	11.6				

To obtain a distinct ME coupling the preferred orientation of the matrix material point in the direction of the applied magnetic field. The material parameters used for both phases are listed in Table 8.3. We assume an electric conductivity for galfenol which is 1000 times higher than the conductivity of barium titanate. The resulting material response due to the applied magnetic field is shown in Figure 8.7, where we depict the magnetization and magnetostriction hysteresis curves.

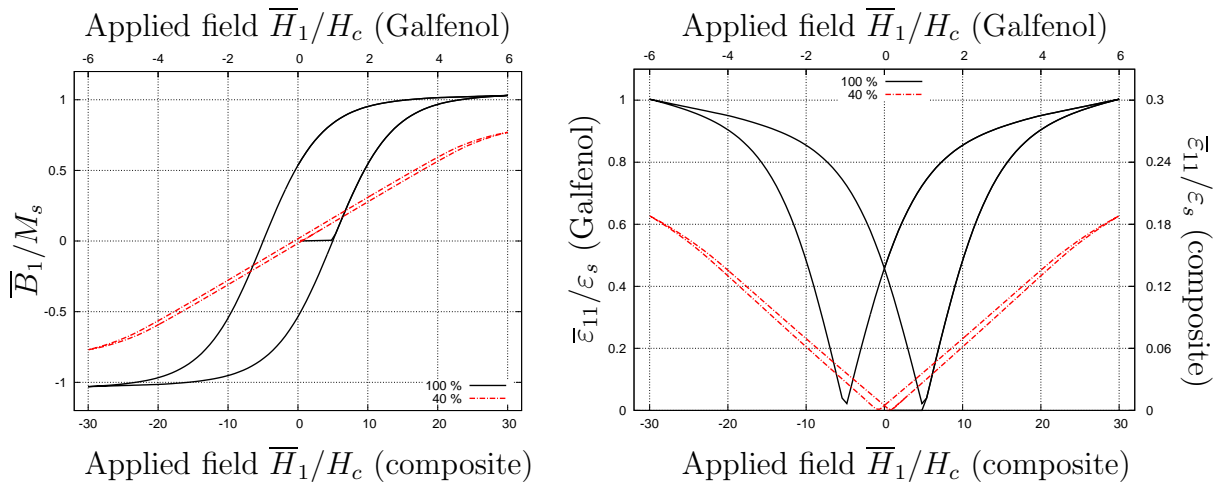


Figure 8.7: Relative magnetization and relative strain hysteresis curves for pure Galfenol and the composite depending on the applied relative magnetic field \overline{H}_1/H_c . Taken from SCHRÖDER ET AL. [187].

In order to compare the effective hysteresis loops of the composite material with a purely magnetostrictive material we plotted the response of both simulations. The black solid curve describes the behavior of pure galfenol and provides a benchmark for the magnetization and magnetostrictive behavior. Smooth effective hysteresis curves are obtained with a saturation for magnetic fields above the relative magnetic field of about $5 \bar{H}_1/H_c$. In contrast to this, the response of the magneto-electric composite material is depicted with the dashed red curves. To reach the saturation magnetization, much higher magnetic fields have to be applied. This is caused by the demagnetization effect, see also MIEHE ET AL. [146] or SCHMITZ-ANTONIAK [177]. In the case of a sphere the demagnetization factor is $N_{xx} = N_{yy} = N_{zz} = 1/3$. Then, the magnetic field inside the material is smaller than the applied field, which is reduced by the magnetic field caused by its magnetization. Additionally, the maximum values of the magnetization and magnetostriction are reduced due to the smaller surface fraction of the magnetic material.

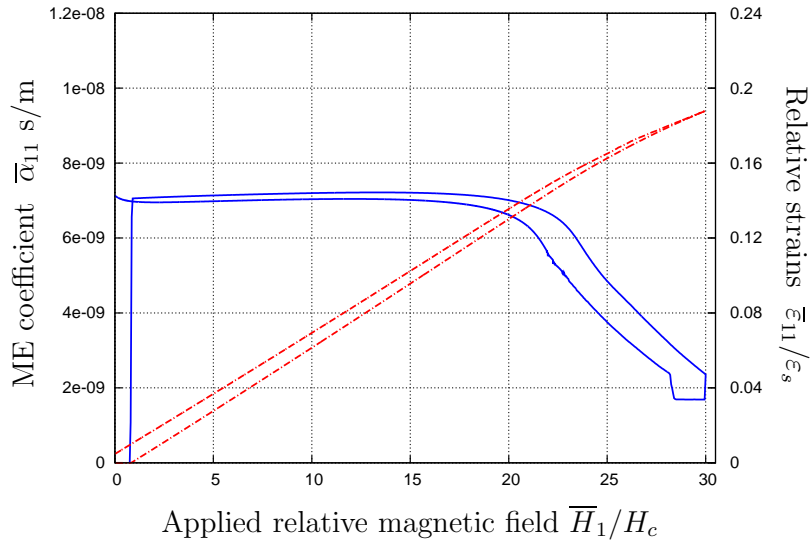


Figure 8.8: Macroscopic magneto-electric coupling coefficient $\bar{\alpha}_{11}$ (blue curve) and strain hysteresis loop (dashed red curve) for a composite with 40% volume fraction of the magnetostrictive phases. Taken from SCHRÖDER ET AL. [187].

Taking a closer look at the magneto-electric response, depicted in Figure 8.8, we see a nonlinear behavior due to the nonlinear properties of the magnetic phase. To better show the correlation between the strains and the ME coefficient we additionally plot one half of the magnetostrictive hysteresis curve in Figure 8.8. The strain hysteresis curve shows a symmetric curve with respect to the y-axis and the ME coefficient curve a more or less point symmetric behavior with respect to the origin of the coordinate system. Comparing both curves we can clearly understand the occurring strain-induced ME behavior. The coupling coefficient is determined by the increment of the dielectric displacement divided by the increment of the magnetic field. Due to the linear piezoelectric material, the dielectric displacement is a linear function of the transferred strains of the magnetostrictive phase. Consequently, the incremental dielectric displacement can be roughly imagined as the tangent of the strain hysteresis loop. The maximum value of the ME coefficient is therefore obtained at the maximum slope of the strain hysteresis loop at $\bar{H}_1/H_c \approx 13.5$, with an ME coefficient of $\bar{\alpha}_{11} \approx 7.22 \cdot 10^{-9}$ s/m. The following decrease of the hysteresis slope after the inflection point explains the observed decrease of the ME coefficient. The jump of the coupling coefficient at $\bar{H}_1/H_c \approx 30$ is caused by the changed slope of

the strain hysteresis loop after the unloading process. At this point the ME coefficient is approximately reduced by 30% to $\bar{\alpha}_{11} \approx 1.69 \cdot 10^{-9}$ s/m. Because of some convergence problems of the Newton iteration for magnetic fields close to the saturation magnetization, the applied magnetic field was not further increased, such that the magnetization of the magnetostrictive phase is not completely saturated. After completely reducing the magnetic field to zero, we obtain an ME coefficient of $\bar{\alpha}_{11} = 7.13 \cdot 10^{-9}$ s/m. We have seen that the nonlinear properties of the magnetostrictive phase significantly influence the behavior of the ME properties. In the next section we investigate the influence of a nonlinear ferroelectric model.

8.3 Ferroelectric/ferroelastic-piezomagnetic composite

As shown in the previous section, nonlinear material models are necessary to describe the realistic magneto-electric properties. Therefore, we consider a nonlinear ferroelectric material model, which is able to capture the hysteretic behavior of barium titanate. In combination with a linear piezomagnetic model, we investigate the influence of the nonlinear ferroelectric behavior on the magneto-electric coupling coefficient. We use the magneto-electro-mechanical boundary value problem as follows. A macroscopic cubic body is loaded with an applied alternating electric field $\bar{E}_3^{max} = 2.0$ kV/mm through the electric potentials at the upper and lower surfaces of the macroscopic body, see Figure 8.9 (macro bvp). The applied electric field is first linearly increased until the maximum load is reached. Afterwards, the field is linearly decreased until the maximum field points into the opposite direction, which is followed by a further increase to the maximum value and a reduction to zero. With this load curve it is ensured that the electric polarization goes through the complete hysteresis loop and all effects on the magneto-electric coupling can be investigated.

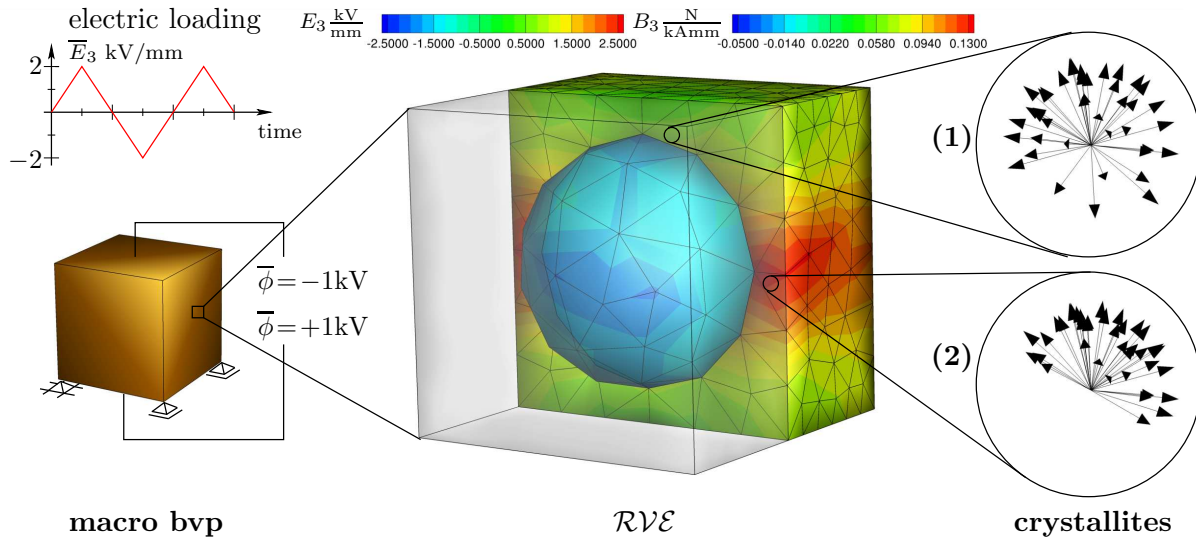


Figure 8.9: Macroscopic bvp with attached \mathcal{RVE} and BaTiO₃ unit cell distributions. Taken from SCHRÖDER ET AL. [188].

For the calculation of the ME coefficient we attached a representative volume element at each macroscopic integration point. The \mathcal{RVE} consists of a cubic ferroelectric matrix with a spherical piezomagnetic inclusion with 25 % volume fraction. Furthermore, at

each microscopic integration point of the ferroelectric matrix an orientation distribution function based on 92 orientations is attached. In the initial state all orientations are isotropically distributed in the three dimensional space.

Table 8.4: Material parameters for tetragonal barium titanate (BaTiO_3), $[\mathbf{C}] = [\sigma_c] = \text{N/mm}^2$, $[\mathbf{e}] = [P_s] = \text{C/m}^2$, $[\mathbf{e}] = \text{mC/kVm}$, $[\varepsilon_s] = [\mu^r] = [\epsilon^r] = 1$, $[E_c] = \text{kV/mm}$, $[\mu] = \text{N/kA}^2$, see ZGONIK ET AL. [226].

$\hat{\mathbf{C}}_{1111}$	$\hat{\mathbf{C}}_{1122}$	$\hat{\mathbf{C}}_{1133}$	$\hat{\mathbf{C}}_{3333}$	$\hat{\mathbf{C}}_{1212}$	$\hat{\mathbf{C}}_{1313}$	$\hat{\epsilon}_{11}$ ($\hat{\epsilon}_{11}^r$)	$\hat{\epsilon}_{33}$ ($\hat{\epsilon}_{33}^r$)
222000	108000	111000	151000	134000	61000	0.019 (2145.9)	0.000496 (56.0)
\hat{E}_c	$\hat{\sigma}_c$	$\hat{\epsilon}_s$	$\hat{\epsilon}_{311}$	$\hat{\epsilon}_{333}$	$\hat{\epsilon}_{131}$	$\hat{\mu}_{11}$ ($\hat{\mu}_{11}^r$)	$\hat{\mu}_{33}$ ($\hat{\mu}_{33}^r$)
1.0	100	0.00834	-0.7	6.7	34.2	1.26 (1)	1.26 (1)

For the electric matrix material barium titanate, the material parameters listed in Table 8.4 are used. To demonstrate the switching behavior of the individual orientations of the orientation distribution functions, Figure 8.9 shows an example of a loaded $\mathcal{RV}\mathcal{E}$. The depicted $\mathcal{RV}\mathcal{E}$ is used as an example to describe the microscopic switching behavior. For further calculations, where we compare the numerical results with experimental measurements, a much more refined mesh was used. In the simulation presented in Figure 8.9 the $\mathcal{RV}\mathcal{E}$ displays the results for a macroscopic electric field of $\bar{E}_3 = 2.0 \text{ kV/mm}$. The contour plot of the matrix reveals the distribution of the microscopic vertical electric fields E_3 , whereas the contour plot of the inclusion shows the distribution of the microscopic vertical magnetic induction B_3 . Due to the inhomogeneous microstructure and the different electric permittivities of the phases, a concentration of the microscopic electric field can be seen at the horizontal boundaries of the inclusion. Thus, the electric field increases to over 2.5 kV/mm in these areas (point 2), whereas the local electric field at the upper boundary of the magnetic inclusion is slightly above 1.0 kV/mm (point 1). The two integration points (1) and (2) were chosen to demonstrate the influence of the different local electric fields on the microscopic properties of the matrix material.

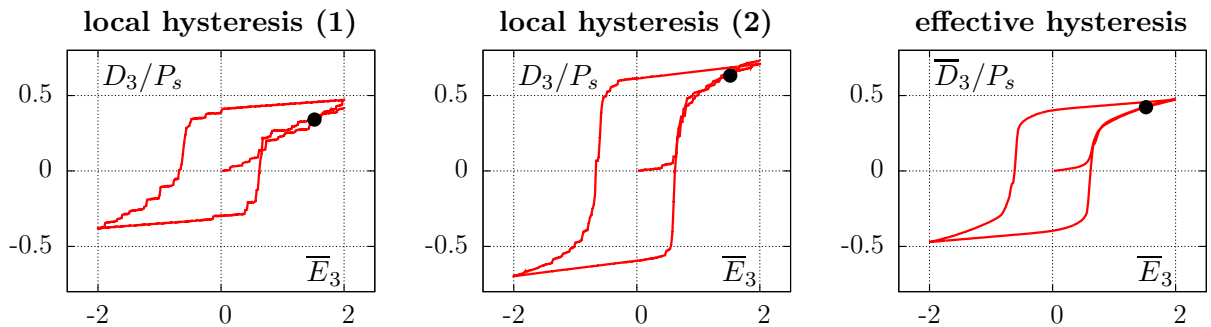


Figure 8.10: Local dielectric response in two microscopic Gauss points and effective macroscopic dielectric hysteresis curves. Taken from SCHRÖDER ET AL. [188].

Based on the higher local microscopic electric field at point (2) the switching criterion for most of the unit cells is fulfilled such that these orientations point roughly into the direction of the electric field. In contrast, the lower electric field in point (1) does not reach the switching thresholds for all orientations, such that some orientations still point

in negative vertical direction. The complete hysteresis loops at point (1), point (2), and the effective macroscopic hysteresis, as obtained by the homogenization over the $\mathcal{RV}\mathcal{E}$ after the application of an alternating electric field can be seen in Figure 8.10. Two major characteristics can be observed. First, the local hysteresis loops show a cascade change of the relative dielectric displacement. Such stepwise increase and decrease is a result of the switching of the single orientations into their new direction. As opposed to this, the effective hysteresis reveals a smooth evolution due to the different switching processes across the whole microstructure and the homogenization over the $\mathcal{RV}\mathcal{E}$. The second major characteristic is the different amplitude of the relative dielectric displacements at the locations (1) and (2). In point (1) the local electric field is lower compared to the local electric field in point (2), such that the switching criterion for less orientations is fulfilled in point (1). This results in a lower amplitude of the dielectric hysteresis in point (1) compared with point (2). The amplitude of the effective dielectric hysteresis is a result of the homogenization process. This example shows, that the microscopic morphology affects the local and effective hysteresis and thus the strain-induced magneto-electric coupling. For the simulations depicted in Figure 8.11 we used a refined mesh for the microscopic $\mathcal{RV}\mathcal{E}$ s with quadratic tetrahedrons.

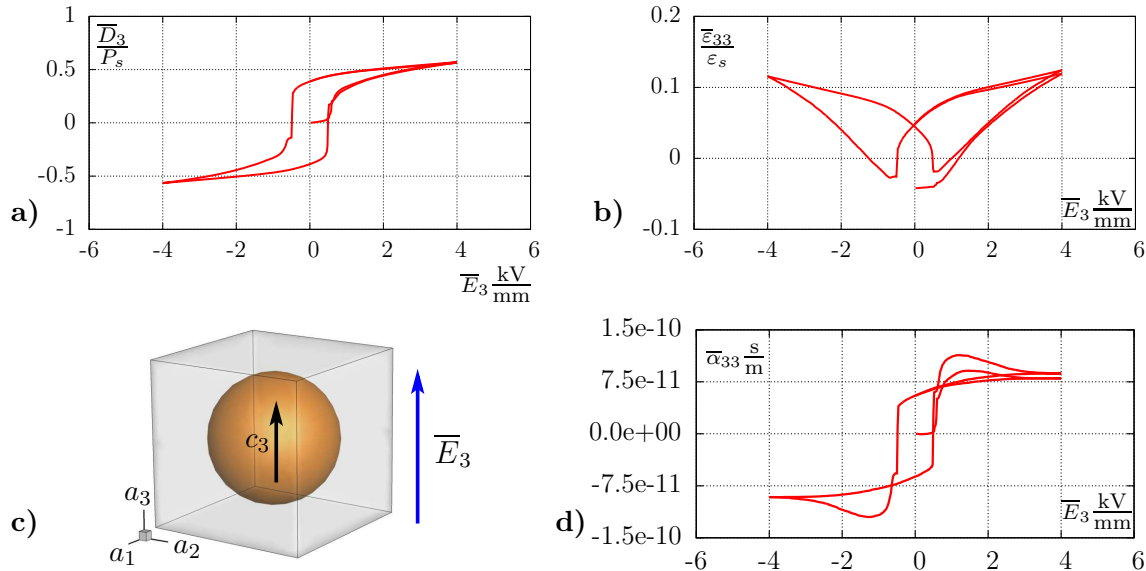


Figure 8.11: Effective response of the ME composite as a result of alternating electric-field loading: a) effective dielectric hysteresis curve b) effective butterfly hysteresis curve, c) preferred direction of the piezomagnetic inclusion and direction of the applied electric field, d) effective magneto-electric coefficient α_{33} . The remanent ME coefficient is half the one predicted with the linear constitutive models. Taken from SCHRÖDER ET AL. [188].

Furthermore, the applied macroscopic electric field was increased to $\bar{E}_3 = 4.0$ kV/mm in order to ensure an efficient polarization of the matrix material. The preferred direction of the piezomagnetic inclusion points in the direction of the applied electric field to obtain the maximum magneto-electric coupling. If the preferred direction of piezomagnetism is orthogonal to the applied electric field we obtain a remanent ME coupling of $\bar{\alpha}_{33} = 0.7944 \cdot 10^{-11}$ s/m, which is approximately one order of magnitude lower than the remanent ME coupling for a parallel alignment. Here, the remanent ME coupling denotes the value when the applied electric field vanishes. After the application of an alternating macroscopic electric field we obtain the complete dielectric and butterfly hysteresis curves

and the magneto-electric coupling shown in Figure 8.11. Analogously to the previous example, we obtain smooth effective hysteresis curves after the homogenization approach. Taking a closer look at the dielectric hysteresis loop in Figure 8.11(a) we can observe that the saturation polarization is more or less reached, since only a linear increase of the dielectric displacement is obtained. Due to the ferroelectric volume fraction of 75 %, the effective saturation polarization does not reach the maximum value of P_s . Furthermore, most orientations of the distribution function do not exactly point in the electric field direction resulting in a further reduction of the effective polarization. Both effects can also be seen in the butterfly hysteresis. Analogously to the example in section 8.2 the magneto-electric coefficient corresponds to the butterfly hysteresis. At the highest slope of the strain curve the ME value reaches its maximum of $\bar{\alpha}_{33}^{max} = 9.29 \cdot 10^{-11}$ s/m. After reaching the ferroelectric polarization, the linear piezoelectric effect is dominant and the ME coefficient converges against the value of $\bar{\alpha}_{33} = 8.04 \cdot 10^{-11}$ s/m. By removing the electric field a remanent ME coefficient of $\bar{\alpha}_{33}^{rem} = 5.66 \cdot 10^{-11}$ s/m is visible. Using the ferroelectric model demonstrates the influence on the behavior of the ME coefficient for alternating electric fields. In addition, the model depicts more exactly the ME coefficient after the polarization process with $\bar{\alpha}_{33}^{rem} = 5.66 \cdot 10^{-11}$ s/m, which is more than 10 times lower than the result based on the linear models ($\bar{\alpha}_{33}^{lin} = 8.04 \cdot 10^{-10}$ s/m).

In order to demonstrate the performance and reliability of the ferroelectric/-elastic switching model we investigate the magneto-electric coupling of a more complex microstructure with two ellipsoidal magnetic inclusions in a ferroelectric matrix. The \mathcal{RVE} is discretized with 5358 quadratic tetrahedrons and the magnetic inclusions have a total volume fraction of 10%. In each microscopic integration point of the ferroelectric matrix 42 orientations are attached. Figure 8.12 depicts the macroscopic boundary value problem with the corresponding \mathcal{RVE} .

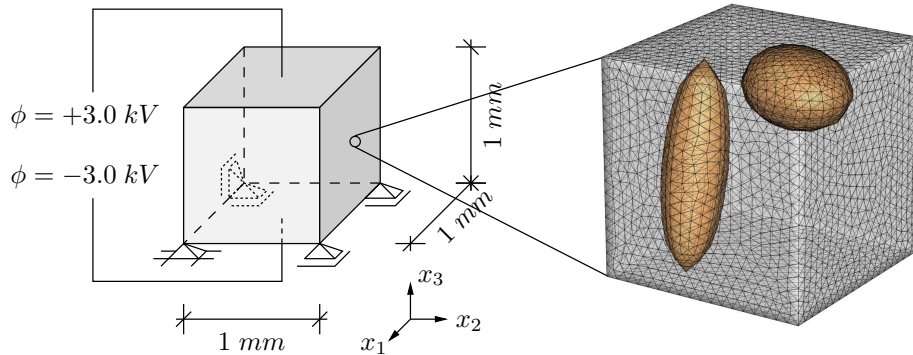


Figure 8.12: Macroscopic bvp ($\bar{E}_3^{max} = 6$ kV/mm) with attached \mathcal{RVE} . Taken from LABUSCH ET AL. [114].

The macroscopic cube is loaded with an alternating electric field with a maximum field strength of $\bar{E}_3 = 6$ kV/mm. We take a closer look at the distribution of the microscopic electric and magnetic fields as well as at the dispersion of the stresses in vertical direction, which are shown in Figure 8.13 at a maximum applied field of $\bar{E}_3 = 6$ kV/mm. It can be clearly observed that at the vertical boundaries of the inclusions microscopic electric field concentrations occur, see Figure 8.13(a), which cause an alignment of the attached orientations in field direction. As a consequence the piezoelectric properties in these regions increase, such that the piezoelectric effect yields higher strains, resulting

in strain-induced ME properties. Due to the large interface between the matrix and the inclusion at the vertical ellipsoid, higher magnetic fields can be observed in this inclusion, compare Figure 8.13(c). However, microscopic vertical stresses could lead to a ferroelastic switching of the orientations perpendicular to the direction of the applied electric field.

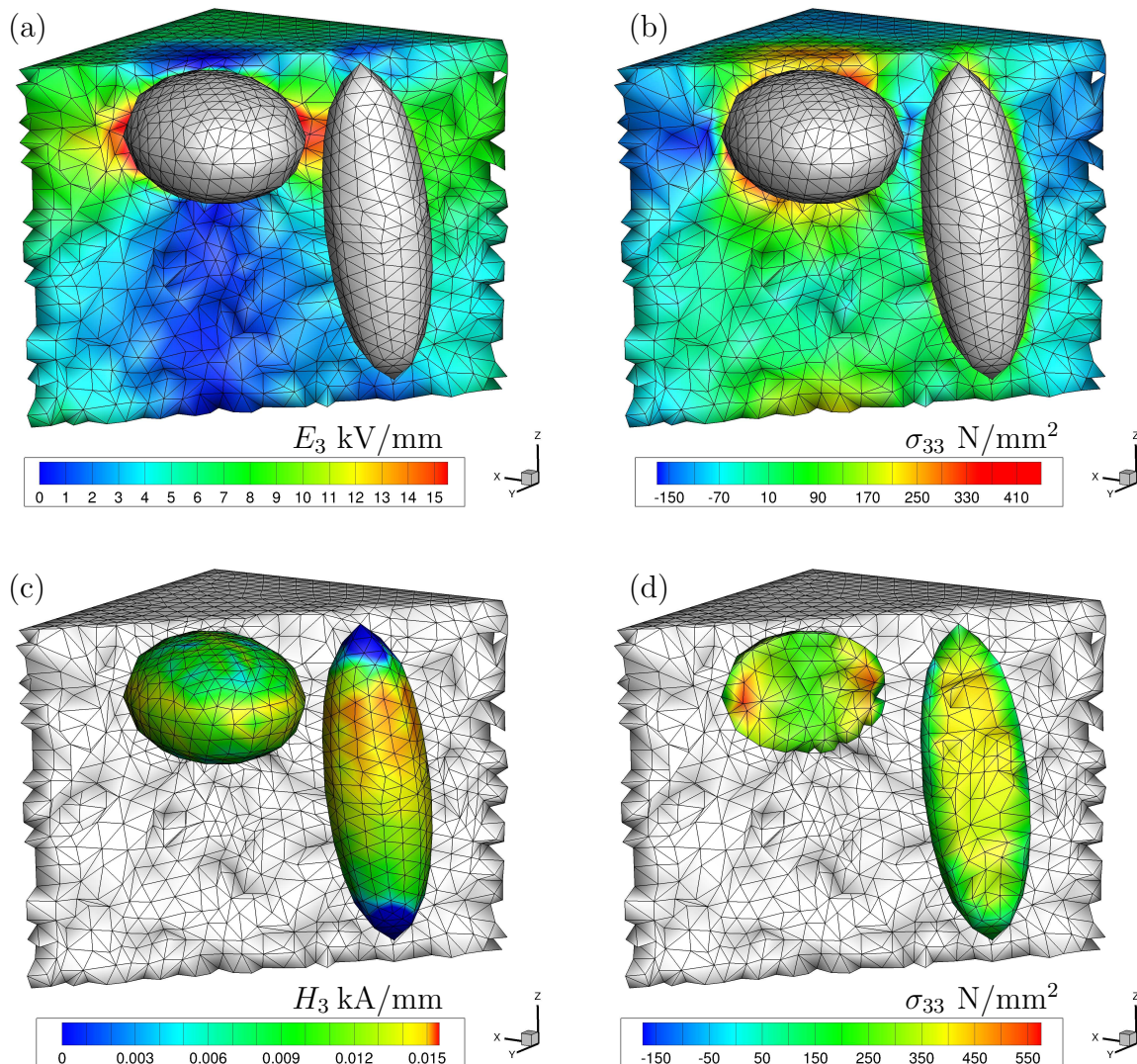


Figure 8.13: Distributions of the microscopic vertical (a) electric field E_3 and (b) stresses σ_{33} in the matrix material, as well as (c) magnetic field H_3 and (d) stresses σ_{33} in the inclusion material. Taken from LABUSCH ET AL. [114].

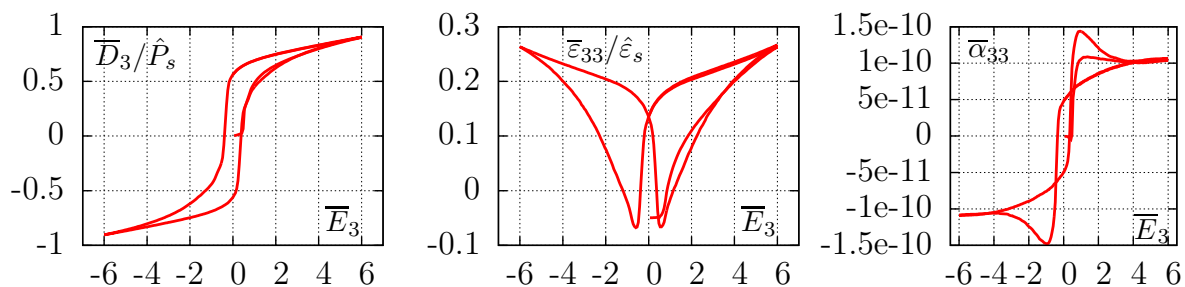


Figure 8.14: Effective dielectric \bar{D}_3/\hat{P}_s and butterfly $\bar{\epsilon}_{33}/\hat{\epsilon}_s$ hysteresis and ME coefficient $\bar{\alpha}_{33}$ in s/m, depending on an electric field \bar{E} in kV/mm. Taken from LABUSCH ET AL. [114].

This switching could decrease the piezoelectric properties in field direction and may yield a negative effect on the ME coefficient. The σ_{ss} -stress distribution in the matrix material is depicted in Figure 8.13(b). A similar effect of the mechanical stresses can reduce the magneto-mechanical properties in the inclusions. Such stresses can also cause a re-orientation of microscopic remanent magnetizations. The overall effective properties of the composite are shown in Figure 8.14, where the dielectric and butterfly hysteresis as well as the ME coefficient are displayed. As in the previous simulation smooth effective hysteresis loops are obtained on the macroscopic level. After the polarization process at $\bar{E}_3 = 0$ kV/mm the remaining ME coefficient is $\bar{\alpha}_{33}^{rem} = 4.78 \cdot 10^{-11}$ s/m, whereas the maximum ME coefficient gets a value of $\bar{\alpha}_{33}^{max} = 10.88 \cdot 10^{-11}$ s/m. Compared with the previous example the remanent ME coefficient is slightly reduced whereas the maximum ME coefficient is even higher, although the volume fraction of the two ellipsoidal inclusions is only 10% compared to the 20% in the previous example. This unproportional relation demonstrates the influence of the microscopic morphology on the overall magneto-electric coupling, which is investigated in more detail in section 8.5. In the next step, nonlinear models are used for both phases.

8.4 Magnetostrictive-ferroelectric/ferroelastic composite

In section 8.2 a dissipative model for magnetostrictive materials was derived. However, this model is not capable of describing the magnetostriction of cobalt ferrite, which causes the specific curve of the ME coefficient. Therefore, a suitable three dimensional Preisach model is derived in this section. The 3D Preisach model is used for the two-scale simulation of two-phase magneto-electric composites, where we combine the Preisach model for the magnetic inclusion with a ferroelectric/-elastic switching model on the microscopic level. The results are compared with experimental measurements of the magneto-electric coupling coefficient. Therefore, a fiber-induced (1-3) magneto-electric composite is considered, which consists of a piezoelectric barium titanate (BaTiO_3) matrix with cylindrical nanopillars of cobalt ferrite (CoFe_2O_4). For an experimental synthesis of magneto-electric composites with square-shaped nanopillars we refer to SCHMITZ-ANTONIAK ET AL. [178].

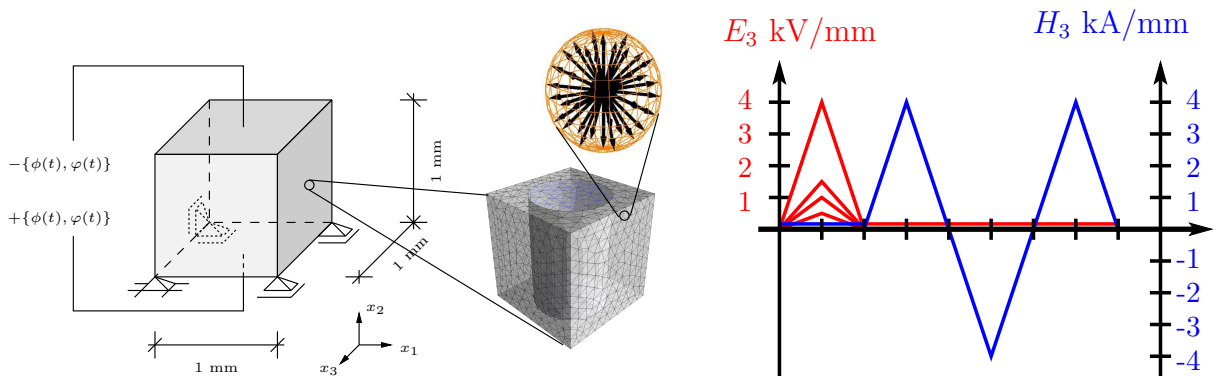


Figure 8.15: (a) Macroscopic bvp with attached \mathcal{RVE} . In each macroscopic integration point of the electric matrix, an ODF is attached. (b) Different electric field paths for four simulations and subsequent magnetic loading path. Taken from LABUSCH ET AL. [117].

The behaviors of both materials are simulated with nonlinear material models on the microscopic level. The piezoelectric matrix is described by the ferroelectric/ferroelastic switching model whereas the magnetostrictive nanopillars are described by the three-dimensional Preisach model. An explanation of both material models is given in Chapter 7. The material parameters used for the electric matrix are given in Table 8.4 and for the magnetic nanopillars in Table 7.4. The macroscopic magneto-electro-mechanical boundary value problem is presented in Figure 8.15. Here, we examine a macroscopic cubic magneto-electric body which is first loaded with an electric field \overline{E}_3 and afterwards loaded with an alternating magnetic field \overline{H}_3 in vertical direction. In each macroscopic integration point we attached a representative volume element ($\mathcal{RV}\mathcal{E}$), consisting of a ferroelectric matrix material and a cylindrical vertical aligned magnetostrictive inclusion. Further on, we add an orientation distribution function based on 92 orientations to each microscopic integration point of the ferroelectric matrix. The applied electric field is used in order to polarize the ferroelectric matrix in vertical direction. Since the ME coupling is a strain-induced product property, different polarization states can change the magnitude of the ME coefficient. To compare the influence of the pre-polarization state of the electric matrix material on the overall magneto-electric coupling, four simulations with different electric field strengths were performed, see Figure 8.15(b). The different electric field strengths of \overline{E}_3 are 0.5, 1.0, 1.5 and 4.0 kV/mm. After this polarization process the electric field vanishes and an alternating magnetic field is applied. Taking a closer look at the resulting different dielectric and strain hysteresis curves of the composite illustrated in Figure 8.16(a) and Figure 8.16(b) four different paths are recognizable.

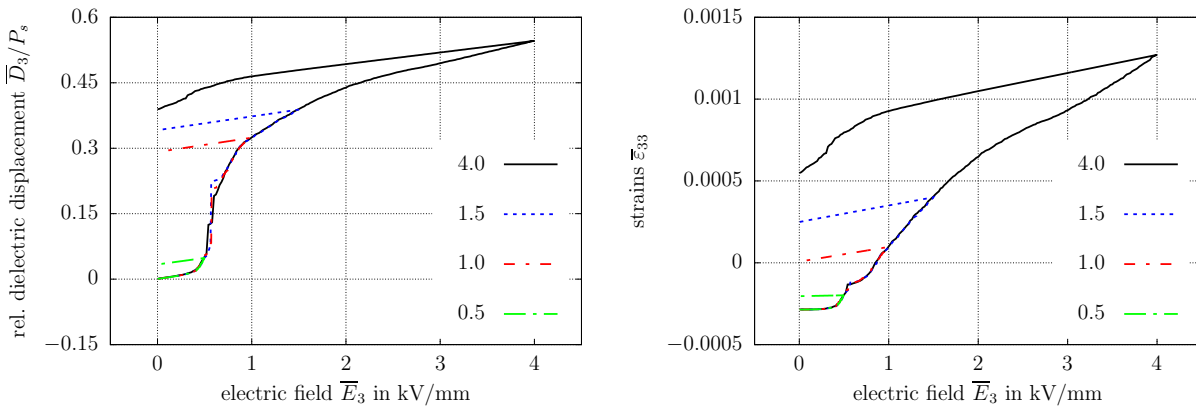


Figure 8.16: (a) Relative overall dielectric displacement \overline{D}_3/P_s for four different electric loading scenarios ($\overline{E}_3 = 0.5$; $\overline{E}_3 = 1.0$; $\overline{E}_3 = 1.5$; $\overline{E}_3 = 4.0$). (b) Macroscopic relative strains $\overline{\epsilon}_{33}/\epsilon_s$ due to the four electric loading cases. Taken from LABUSCH ET AL. [117].

In the initial state the material reveals no polarization since all unit cells are uniformly distributed in the three dimensional space. For an increasing electric field the switching criterion for some unit cells is fulfilled on the microscale, such that the polarization starts to increase, see Figure 8.16(a). However, for the smallest applied electric field of $\overline{E}_2 = 0.5$ kV/mm the polarization increases slightly and is far below the saturation polarization. A remanent relative electric polarization of $\overline{D}_3/P_s = 0.034$ is observable. Additionally, due to the reorientation of the switched unit cells the material is deformed, which results in a difference between the initial and the new deformation of $\Delta \overline{\epsilon}_{33}/\epsilon_s = 8.13 \cdot 10^{-5}$. Here it has to be mentioned, that the composite is contracted in the initial state. This is caused

by the associated orientation distribution function on the microscale, where the individual orientations do not have five corresponding unit cells, which point into the opposite or perpendicular directions and thus cancel out the contractions and elongations of one individual unit cell. After this electric polarization process an alternating vertical magnetic field \overline{H}_3 is applied, see the blue load curve in Figure 8.15(b). Due to the magnetostrictive nanopillars the composite reacts with a contraction in vertical direction, such that the magnetic field generates the magnetostrictive hysteresis curve depicted in Figure 8.17(a).

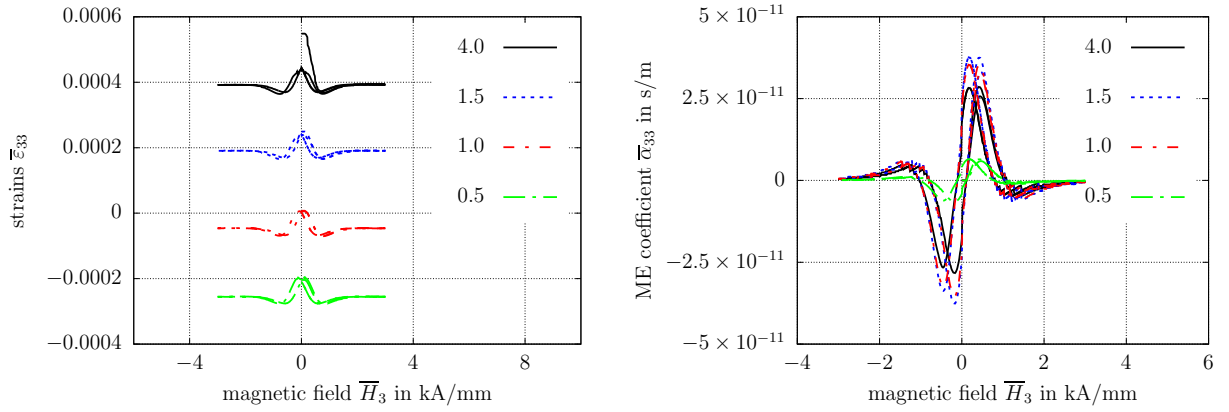


Figure 8.17: (a) Overall magnetostrictive hysteresis loops for different pre-polarization states of the electric matrix. The values 0.5; 1.0; 1.5 and 4.0 denote the before used electric field strengths. (b) Resulting effective strain-induced magneto-electric coupling coefficient $\overline{\alpha}_{33}$. Taken from LABUSCH ET AL. [117].

As a result of the pre-polarization and the ferroelectric deformations, the magnetostrictive strain curve also starts with a non-zero deformation. The overall magnetostrictive strain curve shows the characteristics of the strain curve of pure cobalt ferrite, with the amplitude of the composite's strain curve being lower than the curve of pure cobalt ferrite since the volume fraction of the magnetic phase is reduced. The strains of the magnetic inclusion are transferred to the ferroelectric matrix, which reacts with a change of the dielectric displacement. However, the change of the dielectric displacements depend on the piezoelectric coupling, which in addition depends on the polarization state. Taking into account the low polarization state based on an applied electric field of $\overline{E}_3 = 0.5$ kV/mm, we also obtain a low piezoelectric coupling coefficient. Thus, the magneto-electric coupling of the composite only reaches a maximum value of $\overline{\alpha}_{33}^{max,0.5} = 6.46 \cdot 10^{-12}$ s/m, see Figure 8.17(b). The shape of the magneto-electric coupling curve depends on the magnetostrictive strain curve and can be explained in the following way. Past the very low coercive field of $H_c = 0.3$ kA/mm the nanopillars begin to contract and the magneto-electric coefficient starts to rise. The maximum slope of the magnetostrictive strain curve describes the maximum value of the magneto-electric coupling. Once the maximum magnetostriction is reached and no further strains are transferred among the phases, the ME coefficient vanishes and afterwards reach a negative ME value. This negative value is caused by the softening behavior of cobalt ferrite, whose polycrystalline magnetostriction slightly reduces for higher magnetic fields resulting in a negative slope of the magnetostrictive strain curve. Reaching the saturation magnetostriction of cobalt ferrite, changes in the deformation behavior are not observable anymore, such that the magneto-electric coupling converges to zero.

The behavior of the ME coefficient is point symmetric with respect to the origin of the coordinate system. Now, we take a closer look at the polarization state for applications of higher electric fields and its influence on the magneto-electric coupling. For a macroscopic electric field of $\overline{E}_3 = 1.0$ kV/mm the remanent relative polarization reaches the value of $\overline{D}_3/P_s = 0.291$ and an elongation of the composite of $\Delta\overline{\epsilon}_{33}/\epsilon_s = 2.93 \cdot 10^{-4}$ in vertical direction is observable, such that the magnetostrictive strain curve starts at this deformation state. Due to the fact that in each microscopic integration point more unit cells are aligned in the direction of the microscopic electric fields, the piezoelectric modulus increases. Independent of the pre-polarization process, the alternating magnetic field causes the same magnitude of the magnetostrictive hysteresis curve for $\overline{E}_3 = 1.0$ kV/mm. Since the magnitude of the magnetostrictive deformations are the same compared to the simulation with $\overline{E}_3 = 0.5$ kV/mm the increased magneto-electric response can be explained by the enhanced piezoelectric coupling modulus. At this point no ferroelastic switching criterion is included for the Preisach relays. Therefore, the amplitude of the magnetostrictive hysteresis loops is the same for all polarization states. For $\overline{E}_3 = 1.0$ kV/mm the maximum value of the ME coefficient reaches the value of $\overline{\alpha}_{33}^{max,1.0} = 3.52 \cdot 10^{-11}$ s/m. This maximum value can be further increased by a pre-polarization using $\overline{E}_3 = 1.5$ kV/mm. In this case a magneto-electric coefficient of $\overline{\alpha}_{33}^{max,1.5} = 3.75 \cdot 10^{-11}$ s/m is obtained. At this point the electric matrix has not reached its saturation polarization. With a higher applied electric field of for example $\overline{E}_3 = 4.0$ kV/mm the ferroelectric matrix is saturated concerning its polarization and the piezoelectric modulus achieves its maximum. However, against the expectations, the magneto-electric coupling does not increase further to the maximum value. Instead, the maximum value of the ME coefficient $\overline{\alpha}_{33}^{max,4.0} = 2.86 \cdot 10^{-11}$ s/m is slightly lower than the maximum ME value for $\overline{E}_3 = 1.0$ kV/mm. The reason for this behavior is the ferroelastic switching of several barium titanate unit cells due to internal stresses. Some unit cells, which are orientated in vertical direction after the polarization process, have performed 90° switchings after the maximum magnetostriction is reached and are then orientated in a horizontal direction. Such reoriented unit cells do not affect the ME modulus in vertical direction any longer, resulting in a reduced maximum ME value.

Taking account of the nonlinear ferroelectric/ferroelastic switching model and the nonlinear magnetostrictive Preisach model, we can analyze the simulated qualitative behavior of the magneto-electric coupling for applied bipolar magnetic fields as well as the magnitude of the arising ME coefficient with experimental measurements. Therefore, we compare the simulations with the magneto-electric measurements of the work ETIER ET AL. [45], which measured a magneto-electric coefficient of $0.44 \cdot 10^{-11}$ s/m. It can be seen that the used models are capable of describing the qualitative ME behavior including the peak, the change of the sign for an increasing magnetic field, the saturation of the ME coupling to zero for a further increase of the applied field and the influence of the electric pre-polarization state. Especially the advantage of the Preisach model, which can capture the magnetostrictive softening behavior of cobalt ferrite, is important to depict the change of the sign in the magneto-electric coupling curve. Also the predictions of the magnitude of the magneto-electric coefficient are better than our previous predictions in LABUSCH ET AL. [111] and SCHRÖDER ET AL. [188]. The maximum ME coefficient for purely linear models for both phases is $\overline{\alpha}_{33} = 8.04 \cdot 10^{-10}$ s/m in LABUSCH ET AL. [111]. Using the nonlinear ferroelectric/-elastic switching model in combination with a linear magnetostrictive model the maximum ME coefficient reduces to $\overline{\alpha}_{33} = 12.2 \cdot 10^{-11}$

s/m, see SCHRÖDER ET AL. [188]. Finally, in this contribution the ME value reduces to $\bar{\alpha}_{33} = 3.75 \cdot 10^{-11}$ s/m for the combination of the ferroelectric/-elastic switching model with the magnetostrictive Preisach model. The still deviating prediction of the simulated ME coefficient compared to experimental measurements can be explained by the following reason. Microscopic defects, for example pores, can influence the polarization of the matrix material in a negative manner and reduce the piezoelectric coupling and therefore the magneto-electric coefficient. If the pores are located at the interfaces, they directly interrupt the connection between both phases and the deformations are not transferred from one phase to the other. Since the magneto-electric coefficient is a strain-induced property, such pores can significantly reduce the ME coupling. Therefore, we refer to LABUSCH ET AL. [113] where the influence of a porous composite on the magneto-electric coupling is investigated. A further impact on the coupling is given by the microscopic morphology. This was already briefly discussed in LABUSCH ET AL. [112] and will be shown in the following and investigated in more detail in future works.

8.5 Influence of the microstructure on the magneto-electric coupling

As already mentioned in Section 8.1 and Section 8.3 the heterogeneous microstructure of the composite and the resulting inhomogeneous distribution of the local microscopic electric fields play a significant role on the local polarization states. Regions inside the microstructure with low electric field distributions have accordingly small electro-mechanical properties, which decreases the strain-induced magneto-electric coupling. To investigate the influence of the microscopic morphology on the ME-coefficient we performed 25 simulations with composites, consisting of a piezoelectric matrix with different ellipsoidal piezomagnetic inclusions with varying volume fractions. Here, we restricted the simulations to two-dimensional boundary value problems and purely transversely isotropic linear material models.

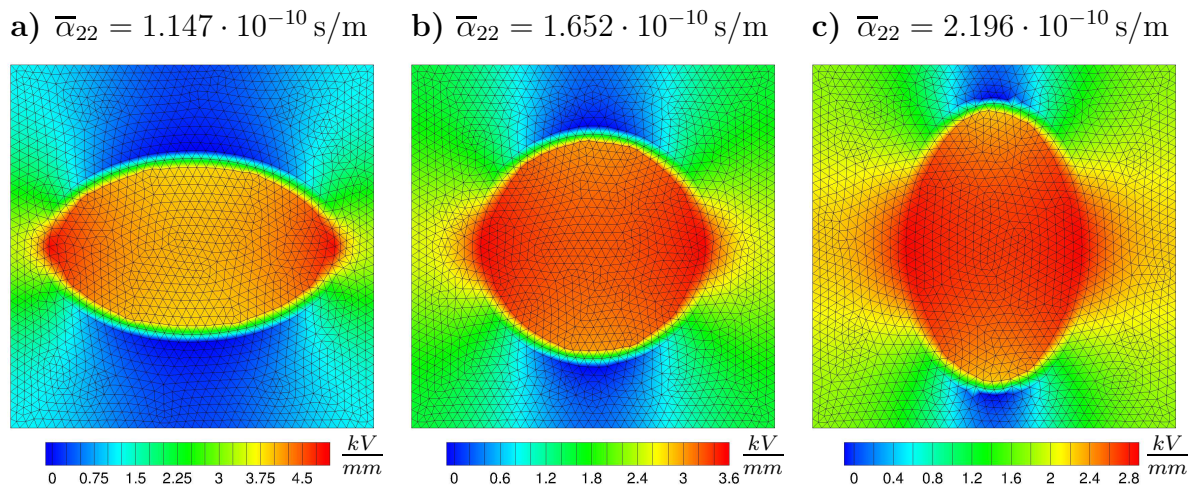


Figure 8.18: Electric field distribution E_2 for three example microstructures with 30 % inclusion volume fraction. Taken from LABUSCH ET AL. [112].

The material parameters used for polycrystalline barium titanate and cobalt ferrite are listed in Table 8.1. In all simulations a macroscopic vertical electric field of $E_2 = 2$ kV/mm is applied and periodic boundary conditions are used on the \mathcal{RVE} . Figure 8.18 shows three

example microstructures with different inclusion geometries but equal volume fractions. The longitudinal expansions of the ellipsoids with varying volume fractions are kept constant to enable a comparison with the different microstructures. Additionally, the microscopic electric field distributions E_2 of the composites are plotted. We can clearly observe that due to the different electric permittivity of the magnetic inclusion, concentrations of the electric fields occur at the left and right boundary of the inclusion. Simultaneously, very low microscopic electric fields, in comparison to the applied macroscopic field strength, appear at the vertical boundaries. For a high magneto-electric coupling the electro-mechanical strains have to be transferred in a wide area of the interface to the inclusions. In these areas the electro-mechanical coupling should be maximized, which is achieved at the saturation polarization due to a high microscopic electric field. By comparing the three depicted microstructures in Figure 8.18 it can be seen in Figure 8.18(c) that, in the case of ellipsoidal inclusions pointing along the direction of the applied electric field, high microscopic electric fields are present in a wide range around the interface. Such electric field distributions are beneficial for the electro-mechanical and thus for the magneto-electric properties. In the case of a horizontally aligned ellipsoidal inclusion (Figure 8.18(a)) the electro-mechanical coupling is low at the interface due to the small microscopic electric fields. As a consequence, the ME-coefficient for the three depicted composites raised from $\bar{\alpha}_{22} = 1.147 \cdot 10^{-10} \text{ s/m}$ (a) over $\bar{\alpha}_{22} = 1.652 \cdot 10^{-10} \text{ s/m}$ (b) to $\bar{\alpha}_{22} = 2.196 \cdot 10^{-10} \text{ s/m}$ (c). A visualization of the ME-coefficients of all 25 considered microstructures is given in Figure 8.19.

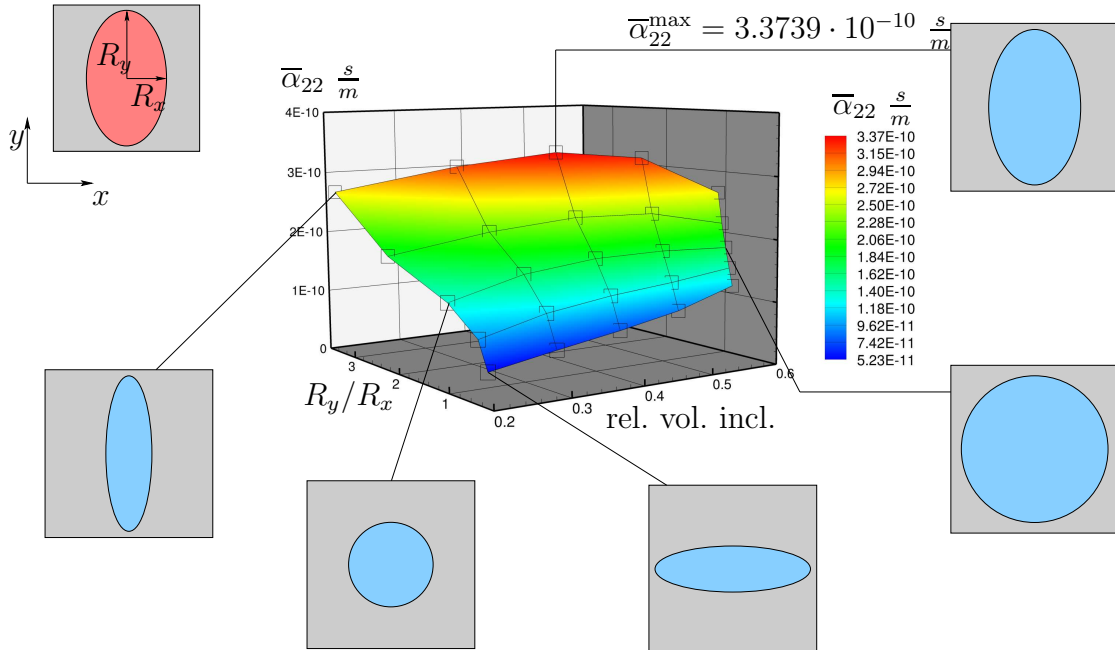


Figure 8.19: Three-dimensional visualization of the ME-coefficients for different inclusion geometries and volume fractions. Taken from LABUSCH ET AL. [112].

The resulting ME-coefficients are plotted against the relative volume fraction of the inclusion and the ratio between the horizontal and vertical radius of the ellipsoidal inclusion, which yield a three-dimensional plot, where the highest point of the surface describes the maximum ME-coefficient. Taking a closer look at the surface plot we obtain the highest ME value for a circular inclusion with 50% volume fraction of both phases. However,

the ME coupling also depends on the shape of the inclusions. As demonstrated in Figure 8.18 the ME coupling increases by changing the inclusion shape to an ellipsoid and the alignment in the direction of the applied electric field. Thus, the highest ME coefficient $\bar{\alpha}_{22}^{max} = 3.374 \cdot 10^{-10}$ s/m is obtained for a microstructure with a vertical aligned ellipsoidal inclusion with 40% volume fraction.

8.6 Simulation of a porous magneto-electric composite

A further important investigation which has to be made is the influence of microscopic defects on the ME coefficient. Pores or other defects included in magneto-electric composites and arise during the manufacturing process, can significantly influence the properties of the individual constituents as well as the effective properties of the composite. Additionally, the reliability and durability of ferroic devices, which is of great importance in technical applications, can be influenced in a negative manner. Such defects can reduce the stiffness of the corresponding phase and distribute the internal fields unevenly, namely the mechanical stresses, or the electric, and magnetic fields. Furthermore, each individual pore alters the electric field and reduces the electric permittivity and the magnetic permeability in its direct environment. In the case of a pore at the interface, the electrically induced strains of the matrix material are not transferred to the inclusion. This breakup of the direct contact between both phases influences the strain-induced magneto-electric coupling negatively. Therefore, we take a look at a microscopic image in Figure 8.20, which shows a two-phase ME composite consisting of a barium titanate matrix (gray) with cobalt ferrite inclusions (dark gray), including multiple pores (black).

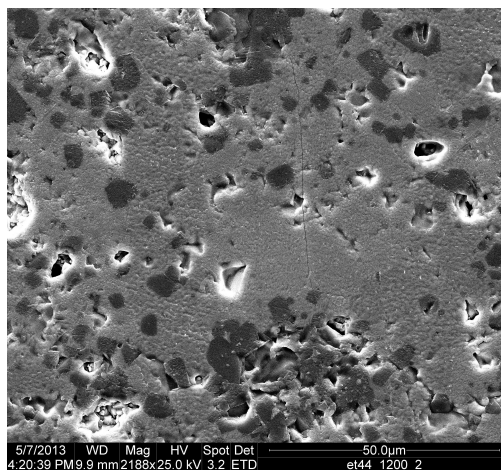


Figure 8.20: Microscope image of a two-phase magneto-electric composite, consisting of barium titanate (gray), cobalt ferrite (dark gray) and pores (black). Taken from LABUSCH ET AL. [116].

Due to the fact that a composite without defects is hard to realize and an overestimation of the overall magneto-electric coupling in numerical simulations is predicted, the microscopic image is a good motivation to investigate the influence of pores on the ME coupling. For that reason, we performed simulations with porous ME composites consisting of an electric matrix and a spherical magnetic inclusion with 79.7% and 20 % volume fractions, respectively. The remaining 0.3% volume fraction are described by a pore at the interface between the ferroelectric matrix and the magnetostrictive inclusion, see Figure 8.21.

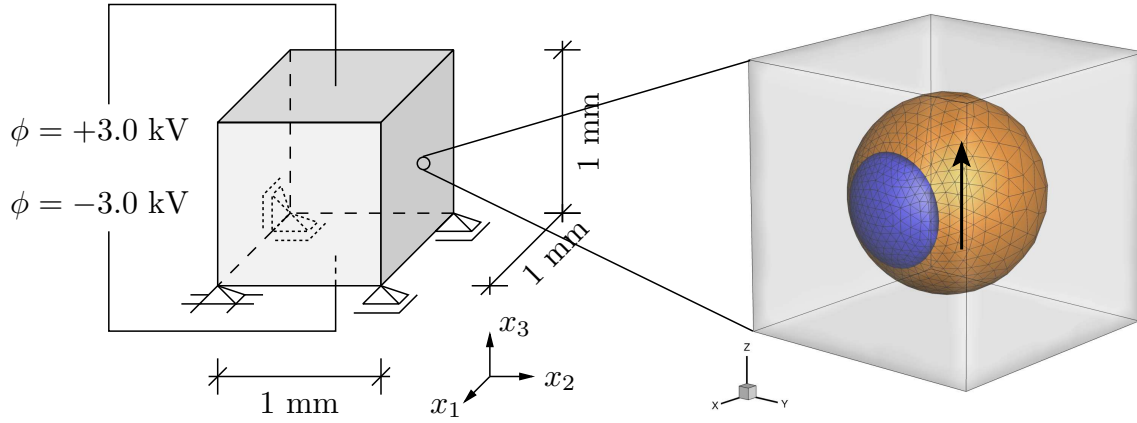


Figure 8.21: Macroscopic bvp with attached porous \mathcal{RVE} , consisting of a ferroelectric matrix (grey) with a piezomagnetic inclusion (brown) and a pore (blue) at the interface. Taken from LABUSCH ET AL. [116].

The used material parameters are summarized in Table 8.5. The elasticity of the air is assumed to be very small instead of zero in order to avoid zero entries on the main diagonal of the material tangent and therefore numerical instabilities.

Various locations of the pore can influence the strain-induced properties to different degrees, since the position of the defect impairs the amount of transferred deformations. Therefore, two microstructures are considered, where the position of the pore is at two different locations of the interface between both composite materials. In the first composite (1) the pore is located in the region where the highest microscopic electric fields and thus the highest amount of deformations in the matrix material are expected. Based on the previous simulations in Section 8.3 the highest electric fields should occur in the area surrounding the magnetic inclusion orthogonal to the applied electric field.

Table 8.5: Material parameters used for BaTiO_3 , CoFe_2O_4 and air.

Para.	Unit	BaTiO_3	CoFe_2O_4	air	Para.	Unit	BaTiO_3	CoFe_2O_4
\mathcal{C}_{1111}	$\frac{\text{N}}{\text{mm}^2}$	$22.2 \cdot 10^4$	$21.21 \cdot 10^4$	$1 \cdot 10^{-8}$	e_{311}	$\frac{\text{C}}{\text{m}^2}$	-0.7	0.0
\mathcal{C}_{1122}	"	$10.8 \cdot 10^4$	$7.45 \cdot 10^4$	0.0	e_{333}	"	6.7	0.0
\mathcal{C}_{1133}	"	$11.1 \cdot 10^4$	$7.45 \cdot 10^4$	0.0	e_{131}	"	34.2	0.0
\mathcal{C}_{3333}	"	$15.1 \cdot 10^4$	$21.21 \cdot 10^4$	$1 \cdot 10^{-8}$	q_{311}	$\frac{\text{N}}{\text{Am}}$	0.0	580.3
\mathcal{C}_{1212}	"	$13.4 \cdot 10^4$	$6.88 \cdot 10^4$	0.0	q_{333}	"	0.0	-699.7
\mathcal{C}_{1313}	"	$6.1 \cdot 10^4$	$6.88 \cdot 10^4$	0.0	q_{131}	"	0.0	550.0
ϵ_{11}	$\frac{\text{mC}}{\text{kVm}}$	0.019	$8.0 \cdot 10^{-5}$	$8.86 \cdot 10^{-6}$	E_c	$\frac{\text{kV}}{\text{mm}}$	1.0	0.0
ϵ_{33}	"	0.000496	$9.8 \cdot 10^{-5}$	$8.86 \cdot 10^{-6}$	σ_c	$\frac{\text{N}}{\text{mm}^2}$	100.0	0.0
μ_{11}	$\frac{\text{N}}{\text{kA}^2}$	1.26	157.0	1.26	ϵ_s	1	0.00834	0.0
μ_{33}	"	1.26	157.0	1.26				

Thus, in the first example, the defect is located at the left boundary of the inclusion, see Figure 8.21. In the second example (composite (2)), the pore is placed in a region with slightly lower electric fields at the upper left boundary. In the following, we compare the influence of both positions on the ME coupling by applying an alternating vertical electric

field on the macroscopic body. The preferred direction of the magnetic phase point in vertical direction to obtain a maximum ME coupling. In each microscopic integration point of the matrix material we attached 92 barium titanate unit cells in form of an orientation distribution function. In the initial state the orientations are uniformly distributed in the three dimensional space. Figure 8.22 shows the resulting microscopic electric field distribution in a cross section of the considered \mathcal{RVE} (composite (1)) for an applied macroscopic field of $\bar{E}_3 = 6 \text{ kV/mm}$.

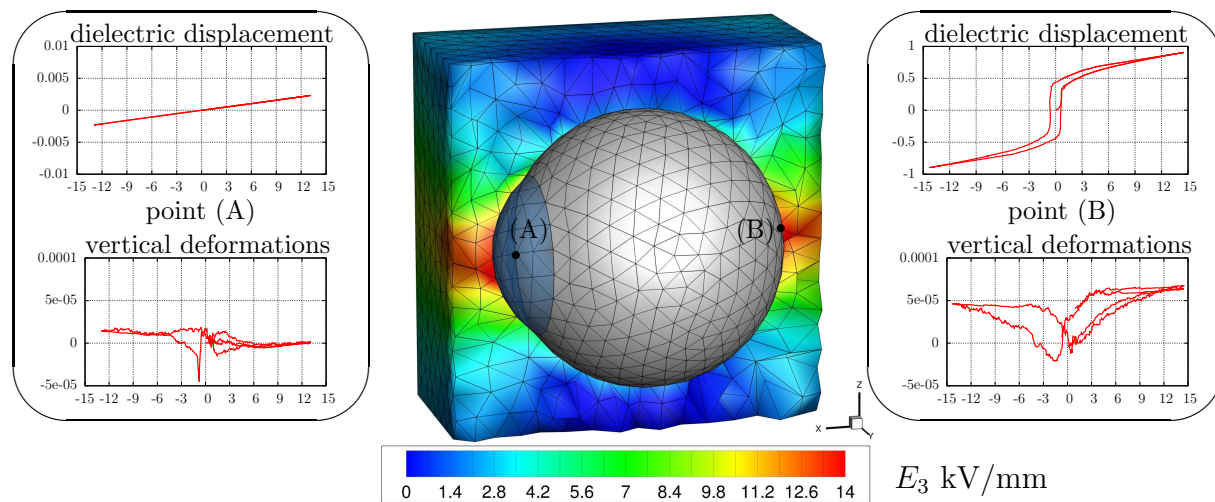


Figure 8.22: Electric field distribution in a cross section of an \mathcal{RVE} . The dielectric and butterfly hysteresis loops are shown for two different points (A) and (B) in the microstructure. Taken from LABUSCH ET AL. [116].

It is clearly observable that due to the inhomogeneous microstructure high electric fields arise in the equatorial plane in the middle of the \mathcal{RVE} around the magnetic inclusion. In these areas, in contrast to the regions with lower electric fields, the switching criteria for more or less all of the assumed orientations are fulfilled, such that the unit cells are aligned in vertical direction.

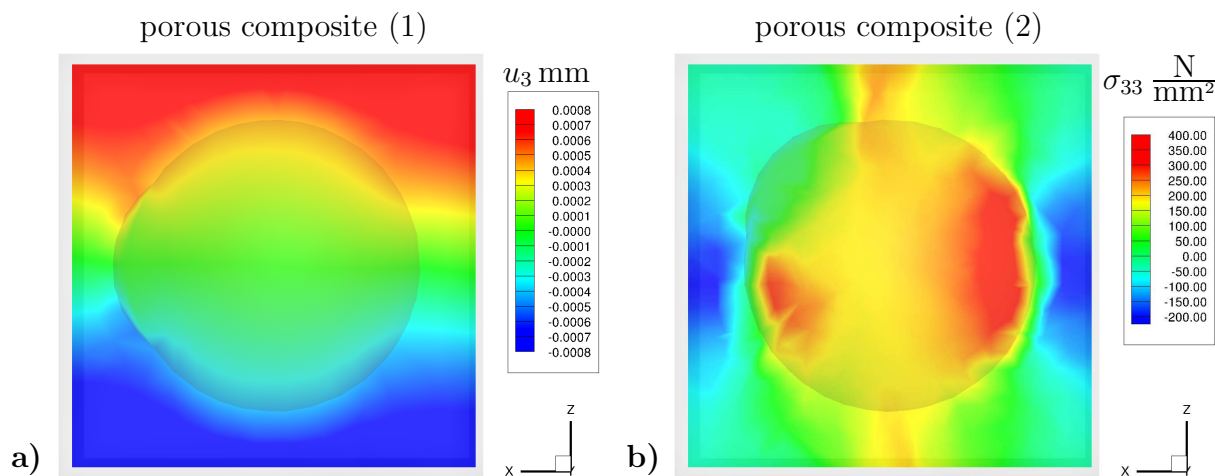


Figure 8.23: a) Microscopic strain and b) stress distribution due to an applied macroscopic electric field $\bar{E}_3 = 6 \text{ kV/mm}$. Taken from LABUSCH ET AL. [116].

As a consequence, the electro-mechanical deformations reach their maximum and transfer to the magnetic inclusion at the interfaces without defects completely. However, in a porous composite with a pore at the interface, the connection between both constituents is interrupted. A visualization of the influence of a pore on the microscopic local electric hysteresis curves is given in Figure 8.22, where the dielectric displacement and the deformations at two points of the interface are plotted. Point (A) is located at the left interface between the pore and the magnetic inclusion, whereas point (B) describes a position between the intact interface at the opposite right side. At the second point (B) all deformations of the matrix material are transferred to the inclusion, such that we observe a butterfly hysteresis loop as well as a dielectric hysteresis. Here it has to be emphasized that due to the switching of the single orientations on the nanoscopic level the hysteresis loops have a cascade characteristic. After the homogenization process the macroscopic effective hysteresis loops show a smooth behavior, see Figure 8.24. However, at point (A) the deformations of the matrix material are interrupted due to the pore and not transferred to the magnetic inclusion, so that only a linear increase of the dielectric displacement is visible, caused by the vacuum permittivity. Furthermore, a butterfly hysteresis loop is not obtained and the small remaining displacements are caused by the deformation of the whole inclusion. Figure 8.23a) visualizes the distribution of the vertical strains in a cross section of an \mathcal{RVE} of composite (1). It can be seen that the strains of the matrix material are not transferred at the pore and the deformations in the inclusion in this region are strongly reduced. At the interface at the opposite side we observe a smooth transition of the vertical displacements between the matrix and the inclusion. Figure 8.23(b) shows the microscopic vertical stress distribution σ_{33} in the second composite (2) for an applied electric field of $\overline{E}_3 = 6 \text{ kV/mm}$, where the pore is located at the upper left boundary. Again, the impact of the interrupted transferred deformations becomes visible. In the inclusion the microscopic stresses σ_{33} strongly decrease in the region around the pore. A comparison of the influence of both pores on the overall dielectric and butterfly hysteresis curve as well as on the magneto-electric coupling is shown in Figure 8.24. The behavior of the intact composite without defects is depicted with the black curve, the composite with the defect on the upper left side of the inclusion (composite (2)) with the dashed blue curve and the composite with the defect at the left interface (composite (1)) by the dotted red curve. Due to the small volume fraction of the pore we can see almost no influence on the effective dielectric displacement, see Figure 8.24(a). However, the position of the pore can affect the overall butterfly hysteresis curves, which are depicted in Figure 8.24(b). Slightly higher overall deformations can be observed in the composite with the defect at the upper left interface (composite (2)). In this region around the pore the matrix could expand much easier in comparison to an intact composite due to the interrupted connection to the inclusion. Nevertheless, the increased overall deformations do not yield an increased effective magneto-electric response, since the deformations are not transferred to the magnetic inclusion, see Figure 8.24(c). The missing connection between both phases only causes a very small reduction of the ME coefficient, because the highest amount of the deformations are in this case transferred in the horizontal areas around the inclusion, where the interface is still intact. A reduction of the effective ME coupling to 98.4% of the value of an intact composite is obtained for composite (2). In case the defect is located at the left interface, where the maximum ferroelectric strains occur, we observe a much larger impact on the effective magneto-electric behavior, whereas we see no larger impacts on the overall butterfly hysteresis. However, due to the fact that the

deformations of the matrix material are not transferred to the magnetic inclusion in the region where the highest ferroelectric strains occur, we observe a significant decrease of the ME coefficient.

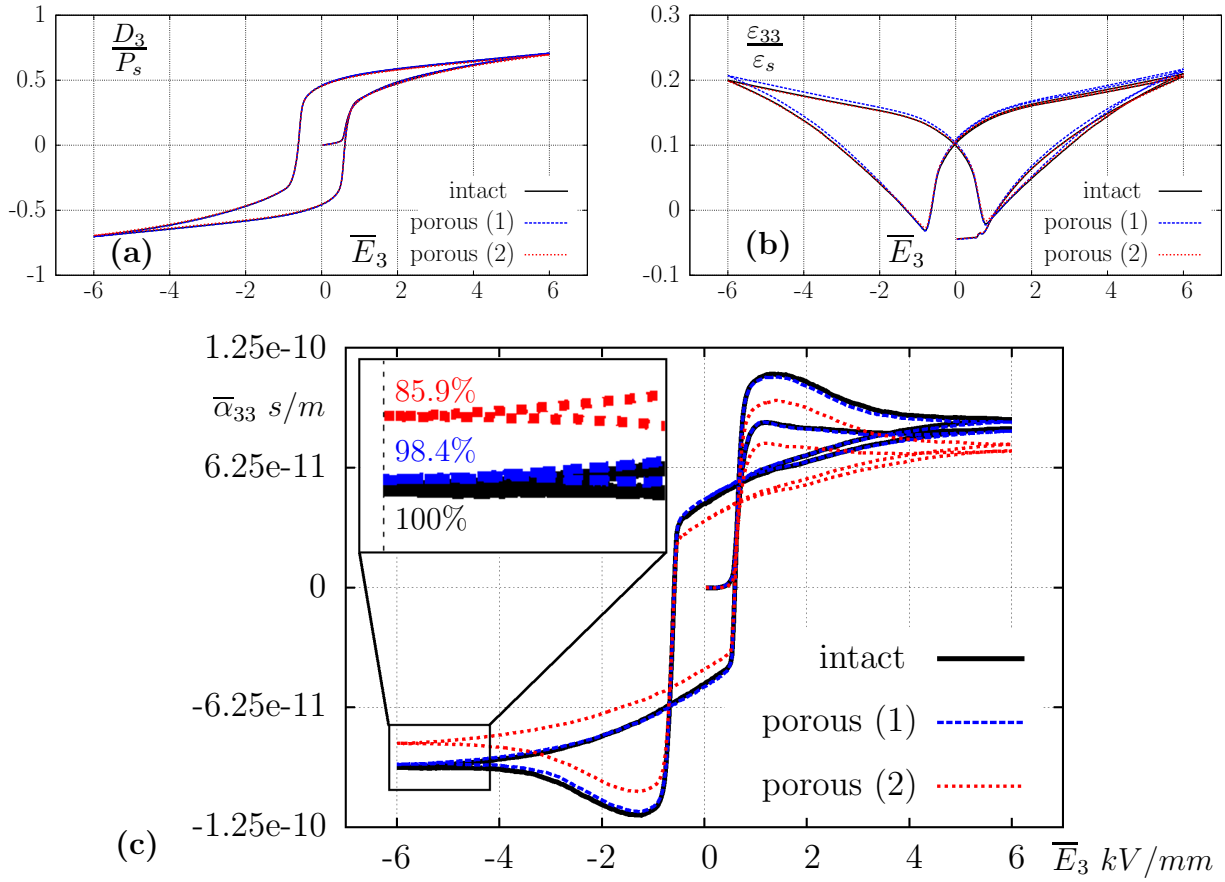


Figure 8.24: Effective (a) dielectric and (b) butterfly hysteresis loop as well as (c) magneto-electric coefficient of a porous ME composite. Taken from LABUSCH ET AL. [116].

For an applied electric field of $\bar{E}_3 = -6$ kV/mm the ME coefficient of the composite (1) decreases to 85.9% of the value of an intact composite. Due to this large impact of a pore on the overall properties and the overestimation of the simulated ME coupling values, the consideration of pores is a good assumption for a more realistic prediction of the composite behavior. In order to give a statement of the influence of multiple pores on the effective properties, a realistic morphology of the microstructure as shown in Figure 8.20 has to be taken into account.

9 Conclusion and Outlook

In this work a two-scale homogenization approach was performed for the determination of magneto-electric product properties in composite materials. First, some technical applications of ME materials were explained to motivate the investigation of such materials. To understand the magneto-electric coupling effect in single-phase and composite materials the physical background to magneto-electro-statics including the fundamental Maxwell equations and the origin of magnetism as well as the characteristics of electro-mechanically and magneto-mechanically coupled materials was given. Afterwards, the basic principles of the continuum mechanics, the Finite Element formulation and the two-scale homogenization approach were outlined. The main focus of this work was to determine the magneto-electric coefficient with the application of appropriate material models and furthermore to evaluate the accuracy of such models for the prediction of ME properties. For this, different material models were derived for simulations of ME composites. We started with purely linear piezoelectric and piezomagnetic models for both phases and performed two dimensional simulations considering realistic microstructures. Compared with experimental measurements we obtained an ME coefficient almost 200 times higher than the measured value. Due to this huge overestimation we included a pre-polarization step, by which a more realistic polarization of the electric phase was simulated instead of a perfectly polarized material. With this approach it was indeed shown that the polarization has a significant influence on the ME coefficient but the pre-polarization has to be decreased to much to approach the measured values. Thus, we focused on nonlinear material models, which were capable of describing the hysteretic behavior of the corresponding phases. With an implemented dissipative magnetostrictive material model we simulated a more precise qualitative behavior of the ME coupling without performing an electric pre-polarization step. A combination of assumed pre-polarizations and nonlinear hysteresis curves was given by a ferroelectric/-elastic polarization switching model. Then, the ME coefficient was strongly decreased and about 30 times higher than the measured value. A further decrease and a reliable prediction of the qualitative ME behavior was given by the magnetostrictive Preisach model. A combination of the latter model with the polarization switching model yield on the one hand a good prediction of the ME coupling, being about 15 times higher than in experiments, and on the other hand the nonlinear characteristics of the coupling properties due to the incorporation of the softening behavior in the magnetostrictive phase. However, next to the used material models further influences on the product properties were shown by investigating porous composite materials as well as different microscopic morphologies. It was shown that a pore, located at the interface between both phases, could reduce the ME coupling by about 14%. Since composites without defects are hardly realizable, the consideration of pores is an important approach. Furthermore, the dependence of the microscopic morphology was shown by including different shapes and volume fractions of the magnetic inclusion. However, there are still further topics to investigate in order to improve the prediction of the ME properties.

As pointed out in the numerical simulations, the shape of the magnetic inclusions, the volume fractions of the phases as well as microscopic defects, such as pores at the interface, play a significant role in the generation of the magneto-electric coupling. It is therefore important in future works to use a **realistic three dimensional microstructure**, which includes all three mentioned influences, for the numerical simulations. Figure 9.1 shows

an example of the complex magnetic inclusion geometries of a realistic microscopic morphology obtained by a Focused ion beam (FIB) technique.

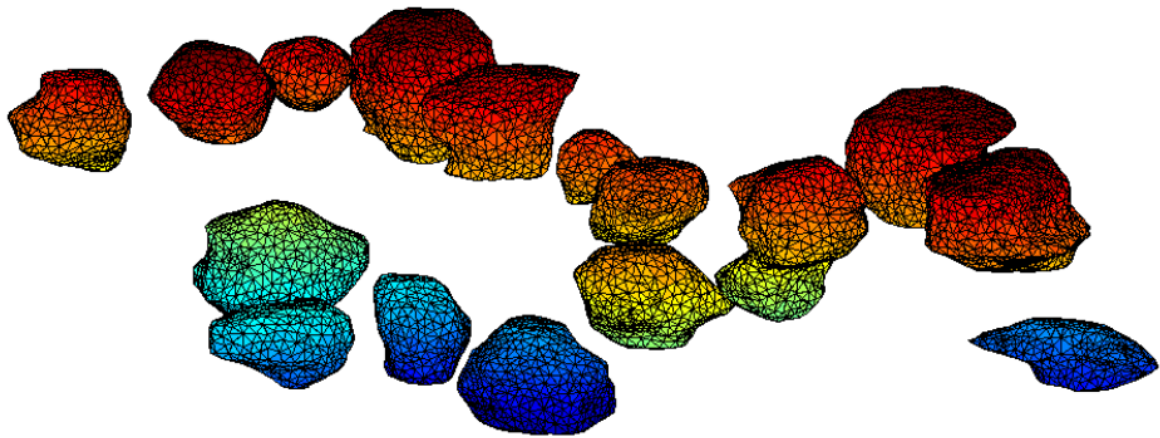


Figure 9.1: Distribution of magnetic particles in a realistic two-phase composite obtained by a Focused Ion Beam (FIB) technique. Measurement performed by the European Synchrotron Radiation Facility (ESRF) in Grenoble.

A special thank goes to the European Synchrotron Radiation Facility (ESRF) in Grenoble for the measurement of such composite samples. A further important aspect, which should be considered in future works is a detailed and exact **parameter fitting** for the magnetostrictive Preisach model. In the framework of this contribution the magnetization curve was adjusted to a hyperbolic tangent, which is a simplified approximation. A fitting to experimental measurements gives a more exact determination of the magnetization and a simulation of minor hysteresis loops will be possible. However, this Preisach model is fitted to macroscopic measurements neglecting complex microscopic processes due to, for example, quantum mechanical exchange energies, stray field energies, magnetic anisotropies or magnetic dipole-dipole interactions. The incorporation of **imperfect interfaces** regarding such interactions could further improve the prediction of the magneto-electric characteristics.

References

- [1] J. Aboudi. Micromechanical analysis of fully coupled electro-magneto-thermo-elastic multiphase composites. *Smart Materials and Structures*, 10:867–877, 2001.
- [2] J. Aboudi. *Mechanics of Composite Materials: A Unified Micromechanical Approach*. Elsevier, 2013.
- [3] K. Aizu. Possible Species of Ferromagnetic, Ferroelectric, and Ferroelastic Crystals. *Physical Review B*, 2:754–772, 1970.
- [4] B. V. Aken, J.-P. Rivera, H. Schmid, and M. Fiebig. Observation of ferrotoroidic domains. *Nature*, 449:702–705, 2007.
- [5] H. Allik and T. Hughes. Finite element method for piezoelectric vibration. *International Journal for Numerical Methods in Engineering*, 2:151–157, 1970.
- [6] B. Al’shin and D. Astrov. Magnetoelectric effect in titanium oxide Ti_2O_3 . *Soviet Physics JETP*, 17:809–811, 1963.
- [7] E. Ascher, H. Rieder, H. Schmid, and H. Stössel. Some Properties of Ferromagnetoelectric Nickel-Iodine Boracite, $\text{Ni}_3\text{B}_7\text{O}_{13}\text{I}$. *Journal of Applied Physics*, 37:1404–1405, 1966.
- [8] D. Astrov. The Magnetoelectric effect in Antiferromagnetics. *Soviet Physics JETP*, 38:984–985, 1960.
- [9] D. Astrov. Magnetoelectric effect in chromium oxide. *Journal of Experimental and Theoretical Physics*, 40:1035–1041, 1961.
- [10] A. Avakian and A. Ricoeur. Constitutive modeling of nonlinear reversible and irreversible ferromagnetic behaviors and application to multiferroic composites. *Journal of Intelligent Material Systems and Structures*, 27(18):2536–2554, 2016.
- [11] A. Avakian, R. Gellmann, and A. Ricoeur. Nonlinear modeling and finite element simulation of magnetoelectric coupling and residual stress in multiferroic composites. *Acta Mechanica*, 226:2789–2806, 2015.
- [12] M. Avellaneda and G. Harshe. Magnetoelectric Effect in Piezoelectric/Magnetostrictive Multilayer (2-2) Composites. *Journal of Intelligent Material Systems and Structures*, 5:501–513, 1994.
- [13] H. Balke and G. Suchanek. Commentary: On the linear coupling of mechanical and magnetic fields in magnetoelectrical composites. *AIP Advances*, 7:060901, 2017.
- [14] E. Bassiouny, A. Ghaleb, and G. Maugin. Thermodynamical formulation for coupled electromechanical hysteresis effects - I. Basic equations. *International Journal of Engineering Science*, 26:1279–1295, 1988.
- [15] G. Bayreuther. Einführung in den Magnetismus. Vorlesungs-Skript, 2007.
- [16] A. Benjeddou. Advances in piezoelectric finite element modeling of adaptive structural elements: a survey. *Computers and Structures*, 76:347–363, 2000.

-
- [17] Y. Benveniste. Magnetolectric effect in fibrous composites with piezoelectric and piezomagnetic phases. *Physical Review B*, 51:16424–16427, 1995.
- [18] A. Bermúdez, L. Dupré, D. Gómez, and P. Venegas. Electromagnetic computations with Preisach hysteresis model. *Finite Elements in Analysis and Design*, 126:65–74, 2017.
- [19] M. Bibes and A. Barthélémy. Multiferroics: Towards a magnetolectric memory. *Nature Materials*, 7(6):425–426, 2008. ISSN 1476-1122.
- [20] J. Bluhm, S. Serdas, and J. Schröder. Theoretical framework of modeling of ionic EAPs within the Theory of Porous Media. *Archive of Applied Mechanics*, 86:3–19, 2016.
- [21] W. Boas. Zur Berechnung des Torsionsmoduls quasiisotroper Vielkristalle aus den Einkristallkonstanten. *Helvetica Physica Acta*, 8:674–681, 1935.
- [22] J.-P. Boehler. A Simple Derivation of Representations for Non-Polynomial Constitutive Equations in Some Cases of Anisotropy. *Zeitschrift für angewandte Mathematik und Mechanik*, 59:157–167, 1979.
- [23] J. V. D. Boomgaard and R. Born. A sintered magnetolectric composite material BaTiO₃-Ni(Co,Mn) Fe₂O₄. *Journal of Materials Science*, 13:1538–1548, 1978.
- [24] J. V. D. Boomgaard, A. V. Run, and J. V. Suchtelen. Magnetolectricity in piezoelectric-magnetostrictive composites. *Ferroelectrics*, 10:295–298, 1976.
- [25] J. V. D. Boomgaard, A. V. Run, and J. V. Suchtelen. Piezoelectric-piezomagnetic composites with magnetolectric effect. *Ferroelectrics*, 14:727–728, 1976.
- [26] L. D. Broglie. Waves and Quanta. *Nature*, 112:540, 1923.
- [27] D. Bruggeman. Berechnung der elastischen Moduln für die verschiedenen Texturen der regulären Metalle. *Zeitschrift für Physik*, 92:561–588, 1934.
- [28] B. Budiansky. On the elastic moduli of some heterogeneous materials. *Journal of the Mechanics and Physics of Solids*, 13:223–227, 1965.
- [29] N. Cai, C.-W. Nan, J. Zhai, and Y. Lin. Large high-frequency magnetolectric response in laminated composites of piezoelectric ceramics, rare-earth iron alloys and polymer. *Applied Physics Letters*, 84:3516–3518, 2004.
- [30] S. Chikazumi. *Physics of magnetism*. John Wiley & Sons, 1964.
- [31] R. Christensen. *Mechanics of Composite Materials*. Courier Corporation, 2012.
- [32] R. Christensen and K. Lo. Solutions for effective shear properties in three phase sphere and cylinder models. *Journal of the Mechanics and Physics of Solids*, 27: 315–330, 1979.
- [33] R. Cohen. Origin of ferroelectricity in perovskite oxides. *Nature*, 358:136–138, 1992.
- [34] O. Crottaz, J.-P. Rivera, B. Revaz, and H. Schmid. Magnetolectric effect of Mn₃B₇O₁₃I boracite. *Ferroelectrics*, 204:125–133, 1997.

- [35] C. Davisson and L. Germer. Diffraction of electrons by a crystal of nickel. *Physical Review*, 30:705–740, 1927.
- [36] P. Debye. Bemerkung zu einigen neuen Versuchen über einen magneto-elektrischen Richteffekt. *Zeitschrift für Physik*, 36:300–301, 1926.
- [37] S. Dong, J.-F. Li, and D. Viehland. Giant Magneto-Electric Effect in Laminate Composites. *IEEE Transactions on Ultrasonic, Ferroelectrics, and Frequency Control*, 50(10):1236–1239, 2003.
- [38] S. Dong, J. Zhai, J. Li, and D. Viehland. Near-ideal magnetoelectricity in high-permeability magnetostrictive/piezofiber laminates with a (2-1) connectivity. *Applied Physics Letters*, 89:252904, 2006.
- [39] I. Dzyaloshinskii. On the magneto-electrical effect in antiferromagnets. *Soviet Physics JETP-USSR*, 37:881–882, 1959.
- [40] W. Eerenstein, N. D. Mathur, and J. F. Scott. Multiferroic and magnetoelectric materials. *Nature*, 442(7104):759–765, 2006.
- [41] W. Eerenstein, M. Wiora, J. Prieto, J. F. Scott, and N. Mathur. Giant sharp and persistent converse magnetoelectric effects in multiferroic epitaxial heterostructures. *Nature Materials*, 6(5):348–351, May 2007.
- [42] F. Endres and P. Steinmann. Molecular statics simulations of ferroelectric barium titanate in the rhombohedral phase. *GAMM-Mitteilungen*, 38:132–146, 2015.
- [43] A. Eringen and G. Maugin. *Electrodynamics of Continua I - Foundations and Solid Media*. Springer Verlag, 1989.
- [44] J. Eshelby. The determination of the elastic field of an ellipsoidal inclusion, and related problems. *Proceedings of the Royal Society A*, 241:376–396, 1957.
- [45] M. Etier, Y. Gao, V. V. Shvartsman, D. C. Lupascu, J. Landers, and H. Wende. Magnetoelectric properties of 0.2CoFe₂O₄-0.8BaTiO₃ composite prepared by organic method. pages 1–4, 2012.
- [46] M. Etier, V. Shvartsman, Y. Gao, J. Landers, H. Wende, and D. Lupascu. Magnetoelectric Effect in (0-3) CoFe₂O₄-BaTiO₃ (20/80) Composite Ceramics Prepared by the Organosol Route. *Ferroelectrics*, 448:77–85, 2013.
- [47] M. Etier, C. Schmitz-Antoniak, S. Salamon, H. Trivedi, Y. Gao, A. Nazrabi, J. Landers, D. Gautam, M. Winterer, D. Schmitz, H. Wende, V. Shvartsman, and D. Lupascu. Magnetoelectric coupling on multiferroic cobalt ferrite-barium titanate ceramic composites with different connectivity schemes. *Acta Materialia*, 90:1–9, 2015.
- [48] H. Exner. *Einführung in die quantitative Gefügeanalyse*. Verlag Oberursel: DGM-Informationsges.-Verl., 1986.
- [49] M. Fabrizio and A. Morro. *Electromagnetism of Continuous Media*. Oxford Science Publications, 2003.

-
- [50] M. Fiebig. Revival of the magnetoelectric effect. *Journal of Physics D: Applied Physics*, 38:R123–R152, 2005.
- [51] M. Fiebig and N. A. Spaldin. Current trends of the magnetoelectric effect. *The European Physical Journal B*, 71:293–297, 2009.
- [52] V. Folen, G. Rado, and E. Stalder. Anisotropy of the magnetoelectric effect in Cr_2O_3 . *Physical Review Letters*, 6:607–608, 1961.
- [53] H. Frohne. *Elektrische und magnetische Felder*. B. G. Teubner Stuttgart, 1994.
- [54] M. Geers, V. Kouznetsova, and W. Brekelmans. Gradient-enhanced computational homogenization for the micro-macro scale transition. *Journal de Physique IV*, 11: 145–152, 2001.
- [55] M. Geers, V. Kouznetsova, and W. Brekelmans. Multi-scale first-order and second-order computational homogenization of microstructures towards continua. *International Journal for Multiscale Computational Engineering*, 1:371–386, 2003.
- [56] M. G. D. Geers, V. G. Kouznetsova, and W. A. M. Brekelmans. Multi-scale computational homogenization: Trends and challenges. 234(7):2175–2182, 2010. Fourth International Conference on Advanced Computational Methods in Engineering (ACOMEN 2008).
- [57] S. Ghosh, K. Lee, and S. Moorthy. Multiple scale analysis of heterogeneous elastic structures using homogenization theory and voronoi cell finite element method. *International Journal of Solids and Structures*, 32(1):27–62, 1995.
- [58] H. Greve, E. Woltermann, H.-J. Quenzer, B. Wagner, and E. Quandt. Giant magnetoelectric coefficients in $(\text{Fe}_{90}\text{Co}_{10})_{78}\text{Si}_{12}\text{B}_{10}$ -AlN thin film composites. *Applied Physics Letters*, 96, 2010.
- [59] J. M. Guedes and N. Kikuchi. Preprocessing and postprocessing for materials based on the homogenization method with adaptive finite element methods. *Computer Methods in Applied Mechanics and Engineering*, 83:143–198, 1990.
- [60] Z. Hashin. Analysis of Composite Materials - A Survey. *Journal of Applied Mechanics*, 50:481–505, 1983.
- [61] Z. Hashin and S. Shtrikman. A variational approach to the theory of the elastic behaviour of multiphase materials. *Journal of the Mechanics and Physics of Solids*, 11:127–140, 1963.
- [62] T. Hegewald, B. Kaltenbacher, M. Kaltenbacher, and R. Lerch. Efficient Modeling of Ferroelectric Behavior for the Analysis of Piezoceramic Actuators. *Journal of Intelligent Material Systems and Structures*, 2008.
- [63] W. Heisenberg. Über den anschaulichen Inhalt der quantentheoretischen Kinematik und Mechanik. *Zeitschrift für Physik*, 43:172–198, 1927.
- [64] W. Heitler and F. London. Wechselwirkung neutraler Atome und homöopolare Bindung nach der Quantenmechanik. *Zeitschrift für Physik*, 44:455–472, 1927.

-
- [65] N. Hill. Why are there so few Magnetic Ferroelectrics? *Journal of Physical Chemistry B*, 104:6694–6709, 2000.
- [66] R. Hill. The Elastic Behaviour of a Crystalline Aggregate. *Proceedings of the Physical Society A*, 65:349–354, 1952.
- [67] R. Hill. Elastic properties of reinforced solids – some theoretical principles. *Journal of the Mechanics and Physics of Solids*, 11:357–372, 1963.
- [68] R. Hill. A self-consistent mechanics of composite materials. *Journal of the Mechanics and Physics of Solids*, 13:213–222, 1965.
- [69] R. Hill. On macroscopic effects of heterogeneity in elastoplastic media at finite strain. *Mathematical Proceedings of the Cambridge Philosophical Society*, 95:481–494, 1984.
- [70] G. Holzapfel. *Nonlinear Solid Mechanics - A continuum Approach for Engineering*. John Wiley & Sons, LTD, 2000.
- [71] C. Hom and N. Shankar. A Fully Coupled Constitutive Model for Electrostrictive Ceramic Materials. *Journal of Intelligent Material Systems and Structures*, 5:795–801, 1994.
- [72] C. Hom and N. Shankar. A finite element method for electrostrictive ceramic devices. *International Journal of Solids and Structures*, 33(12):1757–1779, 1996.
- [73] J. Huang. Analytical predictions for the magnetoelectric coupling in piezomagnetic materials reinforced by piezoelectric ellipsoidal inclusions. *Physical Review B*, 58:12–15, 1998.
- [74] J. H. Huang and W.-S. Kuo. The analysis of piezoelectric/piezomagnetic composite materials containing ellipsoidal inclusions. *Journal of Applied Physics*, 81:1378–1386, 1997.
- [75] A. Huber and E. Schmid. Bestimmung der elastischen Eigenschaften quasiisotroper Vielkristalle durch Mittelung. *Helvetica Physica Acta*, 7:621–627, 1934.
- [76] A. Hubert and R. Schäfer. *Magnetic Domains - The Analysis of Magnetic Microstructures*. Springer, 1938.
- [77] D. Hughes and J. Wen. Preisach modeling of piezoceramic and shape memory alloy hysteresis. *Smart Materials and Structures*, 6:287–300, 1997.
- [78] T. Hughes. *The Finite Element Method: Linear Static and Dynamic Finite Element Analysis*. Courier Corporation, 2012.
- [79] S. Hwang, C. Lynch, and R. McMeeking. Ferroelectric/Ferroelastic interaction and a polarization switching model. *Acta Metallurgica et Materialia*, 43:2073–2084, 1995.
- [80] N. Ida and J. Bastos. *Electro-Magnetics and Calculation of Fields*. Springer, 1997.

-
- [81] R. Islam and S. Priya. Effect of piezoelectric grain size on magnetoelectric coefficient of $\text{Pb}(\text{Zr}_{0.52}\text{Ti}_{0.48})\text{O}_3\text{-Ni}_{0.8}\text{Zn}_{0.2}\text{Fe}_2\text{O}_4$ particulate composites. *Journal of Materials Science*, 43:3560–3568, 2008.
- [82] R. Islam, Y. Ni, A. Khachaturyan, and S. Priya. Giant magnetoelectric effect in sintered multilayered composite structures. *Journal of Applied Physics*, 104:044103, 2008.
- [83] E. Jäger and R. Perthel. *Magnetische Eigenschaften von Festkörpern*. Akademie-Verlag, 1996.
- [84] J.D.Jackson. *Klassische Elektrodynamik*. Walter de Gruyter, 2006.
- [85] D. Jiles. *Introduction to magnetism and magnetic materials*. Chapman and Hall, 1991.
- [86] L. Kaczmarczyk, C. J. Pearce, and N. Bićanić. Scale transition and enforcement of RVE boundary conditions in second-order computational homogenization. *International Journal for Numerical Methods in Engineering*, 74:506–522, 2008.
- [87] K. Kalina, P. Metsch, and M. Kästner. Microscale modeling and simulation of magnetorheological elastomers at finite strains: A study on the influence of mechanical preloads. *International Journal of Solids and Structures*, pages 286–296, 2016.
- [88] M. Kaltenbacher, B. Kaltenbacher, T. Hegewald, and R. Lerch. Finite Element Formulation for Ferroelectric Hysteresis of Piezoelectric Materials. *Journal of Intelligent Material Systems and Structures*, 2010.
- [89] R. C. Kambale, P. A. Shaikh, C. H. Bhosale, K. Y. Rajpure, and Y. D. Kolekar. The effect of Mn substitution on the magnetic and dielectric properties of cobalt ferrite synthesized by an autocombustion route. *Smart Materials and Structures*, 18:115028, 2009.
- [90] M. Kamlah. Ferroelectric and ferroelastic piezoceramics - modeling of electromechanical hysteresis phenomena. *Continuum Mechanics and Thermodynamics*, 13: 219–268, 2001.
- [91] M. Kamlah and U. Böhle. Finite element analysis of piezoceramic components taking into account ferroelectric hysteresis behavior. *International Journal of Solids and Structures*, 38:605–633, 2001.
- [92] M. Kamlah and C. Tsakmakis. Phenomenological modeling of the non-linear electro-mechanical coupling in ferroelectrics. *International Journal of Solids and Structures*, 36:669–695, 1999.
- [93] M.-A. Keip. *Modeling of Electro-Mechanically Coupled Materials on Multiple Scales*. PhD thesis, University of Duisburg-Essen, 2012.
- [94] M.-A. Keip and M. Rambašek. A multiscale approach to the computational characterization of magnetorheological elastomers. *International Journal For Numerical Methods In Engineering*, 107:338–360, 2016.

-
- [95] M.-A. Keip and M. Rambausek. Computational and analytical investigation of shape effects in the experimental characterization of magnetorheological elastomers. *International Journal of Solids and Structures*, 2017.
- [96] M.-A. Keip, D. Schrade, H. N. M. Thai, J. Schröder, B. Svendsen, R. Müller, and D. Gross. Coordinate-invariant phase-field modeling of ferroelectrics, part II: Application to composites and poly-crystals. *GAMM-Mitteilungen*, 38(1):115–131, 2015.
- [97] B. Kiefer and D. Lagoudas. Phenomenological modeling of ferromagnetic shape memory alloys. In *Proc. SPIE, Smart Structures and Materials*, volume 5387, 2004.
- [98] B. Kiefer, H. Karaca, D. Lagoudas, and I. Karaman. Characterization and modeling of the magnetic field-induced strain and work output in Ni₂MnGa magnetic shape memory alloys. *Journal of magnetism and magnetic materials*, 312:164–175, 2007.
- [99] B. Kiefer, K. Buckmann, and T. Bartel. Numerical energy relaxation to model microstructure evolution in functional magnetic materials. *GAMM Mitteilungen*, 38:171–195, 2015.
- [100] T. Kimura, T. Goto, H. Shintani, K. Ishizaka, T. Arima, and Y. Tokura. Magnetic control of ferroelectric polarization. *Nature*, 426:55–58, 2003.
- [101] V. Kouznetsova, W. Brekelmans, and F. Baaijens. An approach to micro-macro modeling of heterogeneous materials. *Computational Mechanics*, 27:37–48, 2001.
- [102] V. Kouznetsova, M. G. D. Geers, and W. A. M. Brekelmans. Multi-scale constitutive modelling of heterogeneous materials with a gradient-enhanced computational homogenization scheme. *International Journal for Numerical Methods in Engineering*, 54(8):1235–1260, 2002.
- [103] T. Koyama. Phase-field modeling of microstructure evolutions in magnetic materials. *Science and Technology of Advanced Materials*, 9:013006, 2008.
- [104] M. Krantz and M. Gerken. Theory of magnetoelectric effect in multilayer nanocomposites on a substrate: Static bending-mode response. *AIP Advances*, 3:022103, 2013.
- [105] B. Krichevtsov, V. Pavlov, and R. Pisarev. Giant linear magnetoelectric effect in garnet ferrite films. *Journal of Experimental and Theoretical Physics Letters*, 49:466–469, 1989.
- [106] E. Kröner. Berechnung der elastischen Konstanten des Vielkristalls aus den Konstanten des Einkristalls. *Zeitschrift für Physik*, 151:504–518, 1958.
- [107] H.-Y. Kuo and Y.-M. Kuo. Magnetoelectricity in multiferroic particulate composites with arbitrary crystallographic orientation. *Smart Materials and Structures*, 21, 2012.
- [108] H.-Y. Kuo, A. Slinger, and K. Bhattacharya. Optimization of magnetoelectricity in piezoelectric-magnetostrictive bilayers. *Smart Materials and Structures*, 19:125010, 2010.

-
- [109] I. Kurzhöfer. *Mehrskalens-Modellierung polykristalliner Ferroelektrika basierend auf diskreten Orientierungsverteilungsfunktionen*. PhD thesis, University of Duisburg-Essen, 2007.
- [110] I. Kurzhöfer, J. Schröder, and H. Romanowski. Simulation of polycrystalline ferroelectrics based on discrete orientation distribution functions. *Proceedings in Applied Mathematics and Mechanics*, 5:307–308, 2005.
- [111] M. Labusch, M. Etier, D. Lupascu, J. Schröder, and M.-A. Keip. Product properties of a two-phase magneto-electric composite: Synthesis and numerical modeling. *Computational Mechanics*, 54:71–83, 2014.
- [112] M. Labusch, M.-A. Keip, V. Shvartsman, D. Lupascu, and J. Schröder. On the Influence of Ferroelectric Polarization States on the Magneto-electric Coupling in Two-phase Composites. *Technische Mechanik*, 36:73–87, 2016.
- [113] M. Labusch, J. Schröder, and D. Lupascu. Multiscale homogenization of magneto-electric porous two-phase composites. In *Insights and Innovations in Structural Engineering, Mechanics and Computation*, 2017.
- [114] M. Labusch, J. Schröder, and M.-A. Keip. An FE²-Scheme for Magneto-Electro-Mechanically Coupled Boundary Value Problems. In J. Schröder and D. Lupascu, editors, *Ferroc Functional Materials - Experiment, Modeling and Simulation*, volume 581 of *CISM Courses and Lectures*, pages 227–262. Springer, 2018.
- [115] M. Labusch, V. Lemke, C. Schmitz-Antoniak, J. Schröder, S. Webers, and H. Wende. FEM-analysis of multiferroic nanocomposite - Comparison of experimental data and numerical simulation. *Archive of Applied Mechanics*, 2018 (submitted).
- [116] M. Labusch, J. Schröder, and D. C. Lupascu. A two-scale homogenization analysis of porous magneto-electric two-phase composites. *Archive of Applied Mechanics*, 2018 (submitted).
- [117] M. Labusch, J. Schröder, and D. C. Lupascu. Derivation of a 3D magnetostrictive Preisach model for the analysis of magneto-electric composites. *Archive of Applied Mechanics*, 2018 (submitted).
- [118] L. Landau and E. Lifshitz. *Electrodynamics of continuous media*. Pergamon Press, 1960.
- [119] C. Landis, J. Wang, and J. Sheng. Micro-electromechanical Determination of the Possible Remanent Strain and Polarization States in Polycrystalline Ferroelectrics and the Implications for Phenomenological Constitutive Theories. *Journal of Intelligent Material Systems and Structures*, 15:513–525, 2004.
- [120] G. Lawes, A. Harris, T. Kimura, N. Rogado, R. Cava, A. Aharony, O. Entin-Wohlman, T. Yildirim, M. Kenzelmann, C. Broholm, and A. Ramirez. Magnetically Driven Ferroelectric Order in Ni₃V₂O₈. *Physical Review Letters*, 95:087205, 2005.
- [121] J. S. Lee, J. G. Boyd, and D. C. Lagoudas. Effective properties of three-phase electro-magneto-elastic composites. *International Journal Of Engineering Science*, 43(10):790–825, 2005.

-
- [122] G. Lehner. *Elektromagnetische Feldtheorie*. Springer, 1990.
- [123] J. Li. Magnetoelastic multi-inclusion and inhomogeneity problems and their applications in composite materials. *International Journal of Engineering Science*, 38:1993–2011, 2000.
- [124] J. Li and M. Dunn. Micromechanics of Magnetoelastic Composite Materials: Average Fields and Effective Behavior. *Journal of Intelligent Material Systems and Structures*, 9:404–416, 1998.
- [125] Z. Li, S. Fischer, J. Liu, and M. Nevitt. Single-crystal elastic constants of Co-Al and Co-Fe spinels. *Journal of Materials Science*, 26:2621–2624, 1991.
- [126] M. Lines and A. Glass. *Principles and Applications of Ferroelectrics and Related Materials*. Oxford: Clarendon Press, 1977.
- [127] D. Lupascu, I. Anusca, M. Etier, Y. Gao, G. Lackner, A. Nazrabi, M. Sanliyalp, H. Trivedi, N. Ul-Haq, and J. Schröder. Semiconductor Effects in Ferroelectrics. In J. Schröder and D. C. Lupascu, editors, *Ferroic Functional Materials - Experiment, Modeling and Simulation*. Springer, 2018.
- [128] J. Ma, Z. Shi, and C.-W. Nan. Magnetolectric Properties of Composites of Single Pb(Zr,Ti)O₃ Rods and Terfenol-D/Epoxy with a Single-Period of 1-3-Type Structure. *Advanced Materials*, 19:2571–2573, 2007.
- [129] J. Ma, J. Hu, Z. Li, and C.-W. Nan. Recent Progress in Multiferroic Magnetolectric Composites: from Bulk to Thin Films. *Advanced Materials*, 23:1062–1087, 2011.
- [130] J. Mackerle. Sensors and actuators: finite element and boundary element analyses and simulations. a bibliography (1997-1998). *Finite Elements in Analysis and Design*, 33:209–220, 1999.
- [131] T. Martin and J. Anderson. Magneto-electric annealing effects of Cr₂O₃. *Physics Letters*, 2:109–110, 1964.
- [132] S. D. Matteo and A. Jansen. Magnetolectricity in V₂O₃. *Physical Review B*, 66:100402–1–100402–4, 2002.
- [133] G. Maugin. *Continuum mechanics of electromagnetic solids*. Elsevier Science Publishers B.V., 1988.
- [134] I. Mayergoyz. Mathematical models of hysteresis. *IEEE Transactions on Magnetics*, 22:603–608, 1986.
- [135] I. Mayergoyz and G. Friedman. Generalized preisach model of hysteresis. *IEEE Transactions on Magnetics*, 24:212–217, 1988.
- [136] A. Menzel, A. Arockiarajan, and S. Sivakumar. Two models to simulate rate-dependent domain switching effects - application to ferroelastic polycrystalline ceramics. *Smart Materials and Structures*, 17, 2008.

-
- [137] P. Metsch, K. Kalina, C. Spieler, and M. Kästner. A numerical study on magnetostrictive phenomena in magnetorheological elastomers. *Computational Materials Science*, 124:364–374, 2016.
- [138] T. Michelitsch and W. Kreher. A simple model for the nonlinear material behavior of ferroelectrics. *Acta Materialia*, 46(14):5085–5094, 1998.
- [139] C. Miehe and C. Bayreuther. On multiscale FE analyses of heterogeneous structures: from homogenization to multigrid solvers. *International Journal for Numerical Methods in Engineering*, 71:1135–1180, 2007.
- [140] C. Miehe and G. Ethiraj. A geometrically consistent incremental variational formulation for phase field models in micromagnetics. *Computer Methods in Applied Mechanics and Engineering*, 245–246:331–347, 2012.
- [141] C. Miehe and A. Koch. Computational micro-to-macro transitions of discretized microstructures undergoing small strains. *Archive of Applied Mechanics*, 72:300–317, 2002.
- [142] C. Miehe and D. Rosato. A rate-dependent incremental variational formulation of ferroelectricity. *International Journal of Engineering Science*, 49:466–496, 2011.
- [143] C. Miehe, J. Schotte, and J. Schröder. Computational micro-macro transitions and overall moduli in the analysis of polycrystals at large strains. *Computational Materials Science*, 16(1-4):372–382, 1999.
- [144] C. Miehe, J. Schröder, and J. Schotte. Computational homogenization analysis in finite plasticity. Simulation of texture development in polycrystalline materials. *Computer Methods in Applied Mechanics and Engineering*, 171:387–418, 1999.
- [145] C. Miehe, Schröder, and C. Bayreuther. On the homogenization analysis of composite materials based on discretized fluctuations on the micro-structure. *Acta Mechanica*, 155:1–16, 2002.
- [146] C. Miehe, B. Kiefer, and D. Rosato. An incremental variational formulation of dissipative magnetostrictive at the macroscopic continuum level. *International Journal of Solids and Structures*, 48:1846–1866, 2011.
- [147] C. Miehe, D. Rosato, and B. Kiefer. Variational principles in dissipative electromagneto-mechanics: A framework for the macro-modeling of functional materials. *International Journal For Numerical Methods In Engineering*, 86:1225–1276, 2011.
- [148] K. Mori and M. Wuttig. Magnetolectric coupling in Terfenol-D/polyvinylidenedifluoride composites. *Applied Physics Letters*, 81:100–101, 2002.
- [149] C. Nan, M. Li, and J. Huang. Calculations of giant magnetolectric effects in ferroic composites of rare-earth-iron alloys and ferroelectric polymers. *Physical Review B*, 63:144415, 2001.
- [150] C.-W. Nan. Magnetolectric effect in composites of piezoelectric and piezomagnetic phases. *Physical Review B*, 50:6082–6088, Sep 1994.

-
- [151] C.-W. Nan, L. Liu, N. Cai, J. Zhai, Y. Ye, and Y. Lin. A three-phase magnetoelectric composite of piezoelectric ceramics, rare-earth iron alloys, and polymer. *Applied Physics Letters*, 81:3831–3833, 2002.
- [152] C.-W. Nan, M. I. Bichurin, S. Dong, D. Viehland, and G. Srinivasan. Multiferroic magnetoelectric composites: Historical perspective, status, and future directions. *Journal of Applied Physics*, 103(3):031101, 2008.
- [153] J. Nye. *Physical Properties of Crystals: Their Representation by Tensors and Matrices Paperback*. Oxford University Press, 1985.
- [154] T. O’Dell. An Induced Magneto-electric Effect in Yttrium Iron Garnet. *Philosophical Magazine*, 16:487–494, 1967.
- [155] I. Özdemir, W. Brekelmans, and M. Geers. FE² computational homogenization for the thermo-mechanical analysis of heterogeneous solids. *Computer Methods in Applied Mechanics and Engineering*, 198:6, 2008.
- [156] N. Papasimakis, V. Fedotov, V. Savinov, T. Raybould, and N. Zheludev. Electromagnetic toroidal excitations in matter and free space. *Nature Materials*, 15:263–271, 2016.
- [157] A. Planes, T. Castán, and A. Saxena. Recent progress in the thermodynamics of ferrotoroidic materials. *Multiferroic Materials*, 1:9–22, 2014.
- [158] B. Ponomarev, S. Ivanov, Y. Popov, and V. Negrii. Magnetoelectric properties of some rare earth molybdates. *Ferroelectrics*, 161:43–48, 1994.
- [159] F. Preisach. über die magnetische Nachwirkung. *Zeitschrift für Physik*, 94:277–302, 1935.
- [160] S. Priya, R. Islam, S. Dong, and D. Viehland. Recent advancements in magnetoelectric particulate and laminate composites. *Journal of Electroceramics*, 19(1):147–164, 2007.
- [161] K. M. Rabe. Response with a twist. *Nature*, 449:674–675, 2007.
- [162] G. Rado. Observation and possible mechanisms of magnetoelectric effects in a ferromagnet. *Physical Review Letters*, 13:335–337, 1964.
- [163] G. Rado and V. Folen. Observation of the magnetically induced magnetoelectric effect and evidence for antiferromagnetic domains. *Physical Review Letters*, 7:310–311, 1961.
- [164] G. Rado, J. Ferrari, and W. Maisch. Magnetoelectric susceptibility and magnetic symmetry of magnetoelectrically annealed TbPO₄. *Physical Review B*, 29:4041–4048, 1984.
- [165] E. Ressouche, M. Loire, V. Simonet, R. Ballou, A. Stunault, and A. Wildes. Magnetoelectric MnPS₃ as a candidate for ferrotoroidicity. *Physical Review B*, 82:100408, 2010.

-
- [166] A. Reuss. Berechnung der Fließgrenze von Mischkristallen auf Grund der Plastizitätsbedingung für Einkristalle. *Zeitschrift für Angewandte Mathematik und Mechanik*, 9:49–58, 1929.
- [167] J.-P. Rivera. On definitions, units, measurements, tensor forms of the linear magnetoelectric effect and on a new dynamic method applied to Cr-Cl boracite. *Ferroelectrics*, 161:165–180, 1994.
- [168] J.-P. Rivera. The linear magnetoelectric effect in LiCoPO_4 Revisited. *Ferroelectrics*, 161:147–164, 1994.
- [169] J.-P. Rivera and H. Schmid. On the birefringence of magnetoelectric BiFeO_3 . *Ferroelectrics*, 204:23–33, 1997.
- [170] G. Robert, D. Damjanovic, N. Setter, and A. Turik. Preisach modeling of piezoelectric nonlinearity in ferroelectric ceramics. *Journal of Applied Physics*, 89:5067–5074, 2001.
- [171] W. Röntgen. Ueber die durch Bewegung eines im homogenen elektrischen Felde befindlichen Dielectricums hervorgerufene electrodynamische Kraft. *Annalen der Physik*, 271:264–270, 1888.
- [172] A. V. Run, D. Terrell, and J. Scholing. An in situ grown eutectic magnetoelectric composite material. *Journal of Materials Science*, 9:1710–1714, 1974.
- [173] J. Ryu, A. V. Carazo, K. Uchino, and H.-E. Kim. Magnetoelectric Properties in Piezoelectric and Magnetostrictive Laminate Composites. *Japanese Journal of Applied Physics*, 40:4948–4951, 2001.
- [174] J. Ryu, A. V. Carazo, K. Uchino, and H.-E. Kim. Piezoelectric and Magnetoelectric Properties of Lead Zirconate Titanate/Ni-Ferrite Particulate Composites. *Journal of Electroceramics*, 7:17–24, 2001.
- [175] J. Ryu, S. Priya, A. V. Carazo, and K. Uchino. Effect of the Magnetostrictive Layer on Magnetoelectric Properties in Lead Zirconate Titanate/Terfenol-D Laminate Composites. *Journal of the American Ceramic Society*, 84:2905–2908, 2001.
- [176] J. Ryu, S. Priya, K. Uchino, and H. E. Kim. Magnetoelectric effect in composites of magnetostrictive and piezoelectric materials. *Journal of Electroceramics*, 8:107–119, 2002.
- [177] C. Schmitz-Antoniak. Grundlagen des magnetismus (lecture notes), 2012/13.
- [178] C. Schmitz-Antoniak, D. Schmitz, P. Borisov, F. de Groot, S. Stienen, A. Warland, B. Krumme, R. Feyerherm, E. Dudzik, W. Kleemann, and H. Wende. Electric in-plane polarization in multiferroic CoFe_2O_4 - BaTiO_3 nanocomposite tuned by magnetic fields. *Nature Communications*, 4, 2013.
- [179] P. Scholten. Which SI? *Journal of Magnetism and Magnetic Materials*, 149:57–59, 1995.

-
- [180] D. Schrade, M.-A. Keip, H. Thai, J. Schröder, B. Svendsen, R. Müller, and D. Gross. Coordinate-invariant phase field modeling of ferroelectrics, part I: Model formulation and single-crystal simulations. *GAMM-Mitteilungen*, 38(1):102–114, 2015.
- [181] J. Schröder. *Homogenisierungsmethoden der nichtlinearen Kontinuumsmechanik unter Beachtung von Instabilitäten*. Habilitation, Bericht aus der Forschungsreihe des Instituts für Mechanik (Bauwesen), Lehrstuhl I, Universität Stuttgart, 2000.
- [182] J. Schröder. Derivation of the localization and homogenization conditions for electromechanically coupled problems. *Computational Materials Science*, 46(3):595–599, 2009.
- [183] J. Schröder. Anisotropic polyconvex energies. In J. Schröder and P. Neff, editors, *Poly-, Quasi- and Rank-one Convexity in Applied Mechanics*, volume 516 of *CISM Courses and Lectures*, pages 53–105. Springer, 2010.
- [184] J. Schröder and D. Gross. Invariant formulation of the electromechanical enthalpy function of transversely isotropic piezoelectric materials. *Archive of Applied Mechanics*, 73:533–552, 2004.
- [185] J. Schröder and M.-A. Keip. Two-scale homogenization of electromechanically coupled boundary value problems. *Computational Mechanics*, 50:229–244, 2012.
- [186] J. Schröder and M. Labusch. *A 3D Magnetostrictive Preisach Model for the Simulation of Magneto-Electric Composites on Multiple Scales*, pages 303–327. Springer International Publishing, 2018.
- [187] J. Schröder, M. Labusch, M.-A. Keip, B. Kiefer, D. Brands, and D. Lupascu. Computation of non-linear magneto-electric product properties of 0-3 composites. *GAMM-Mitteilungen*, 2015.
- [188] J. Schröder, M. Labusch, and M.-A. Keip. Algorithmic two-scale transition for magneto-electro-mechanically coupled problems - FE²-scheme: Localization and Homogenization. *Computer Methods in Applied Mechanics and Engineering*, 302:253–280, 2016.
- [189] E. Schrödinger. Quantisierung als Eigenwertproblem. *Annalen der Physik*, pages 437–490, 1926.
- [190] J. Scott. Applications of magnetoelectrics. *Journal of Materials Chemistry*, 22:4567–4574, 2012.
- [191] V. V. Shvartsman, F. Alawneh, P. Borisov, D. Kozodaev, and D. C. Lupascu. Converse magnetoelectric effect in CoFe₂O₄-BaTiO₃ composites with a core-shell structure. *Smart Materials and Structures*, 20, 2011.
- [192] R. Smit, W. Brekelmans, and H. Meijer. Prediction of the mechanical behavior of nonlinear heterogeneous systems by multi-level finite element modeling. *Computer Methods in Applied Mechanics and Engineering*, 155:181–192, 1998.
- [193] G. Smith. On isotropic Integrity Bases. *Archive for Rational Mechanics and Analysis*, pages 282–292, 1965.

-
- [194] G. Smith. On isotropic functions of symmetric tensors, skew-symmetric tensors and vectors. *International Journal of Engineering Science*, 9:899–916, 1971.
- [195] G. Song, J. Zhao, X. Zhou, and J. D. Abreu-García. Tracking Control of a Piezoceramic Actuator With Hysteresis Compensation Using Inverse Preisach Model. *IEEE/ASME Transactions on Mechatronics*, 10:198–209, 2005.
- [196] N. Spaldin and M. Fiebig. The Renaissance of Magnetoelectric Multiferroics. *Science*, 309:391–392, 2005.
- [197] N. Spaldin, M. Fiebig, and M. Mostovoy. The toroidal moment in condensed-matter physics and its relation to the magnetoelectric effect. *Journal of Physics: Condensed Matter*, 20:434203, 2008.
- [198] A. Spencer. Part III - Theory of Invariants. In *Mathematics*, pages 239–353. Academic Press, 1971. doi: <https://doi.org/10.1016/B978-0-12-240801-4.50008-X>.
- [199] G. Srinivasan. Magnetoelectric Composites. *Annual Review of Materials Research*, 40:1–26, 2010.
- [200] G. Srinivasan, V. Laletsin, R. Hayes, N. Puddubnaya, E. Rasmussen, and D. Fekel. Giant magnetoelectric effects in layered composites of nickel zinc ferrite and lead zirconate titanate. *Solid State Communications*, 124:373–378, 2002.
- [201] G. Srinivasan, E. Rasmussen, B. Levin, and R. Hayes. Magnetoelectric effects in bilayers and multilayers of magnetostrictive and piezoelectric perovskite oxides. *Physical Review B*, 65:134402, 2002.
- [202] A. Stancu, P. Bissell, and R. Chantrell. Interparticle interactions in magnetic recording media as obtained from high-order measurements by a Preisach model. *Journal of Applied Physics*, 87:8645–8652, 2000.
- [203] K. Tanaka and T. Mori. Note on volume integrals of the elastic field around an ellipsoidal inclusion. *Journal of Elasticity*, 2:199–200, 1972.
- [204] I. Temizer and P. Wriggers. On the computation of the macroscopic tangent for multiscale volumetric homogenization problems. *Computer Methods in Applied Mechanics and Engineering*, 198:495–510, 2008.
- [205] K. Terada, M. Hori, T. Kyoya, and N. Kikuchi. Simulation of the multi-scale convergence in computational homogenization approach. *International Journal of Solids and Structures*, 37:2285–2311, 2000.
- [206] R. Tickle, D. James, T. Shield, M. Wuttig, and V. Kokorin. Ferromagnetic Shape Memory in the NiMnGa System. *IEEE Transactions on Magnetism*, 35:4301–4310, 1999.
- [207] P. Tipler. *Physics for scientists and engineers 4th editions*. W.H. Freeman and Company, 1999.
- [208] P. Tolédano, M. Ackermann, L. Bohatý, P. Becker, T. Lorenz, N. Leo, and M. Fiebig. Primary ferrotoroidicity in antiferromagnets. *Physical Review B*, 92:094431, 2015.

- [209] C. Truesdell and W. Noll. *The Non-Linear Field Theories of Mechanics*. Springer, 2004.
- [210] J. van Suchtelen. Product properties: a new application of composite materials. *Philips Research Reports*, 27:28–37, 1972.
- [211] K. R. Vignesh, A. Soncini, S. K. Langley, W. Wernsdorfer, K. S. Murray, and G. Rajaraman. Ferrotoroidic ground state in a heterometallic $\{\text{Cr}^{III}\text{Dy}^{III}\}$ complex displaying slow magnetic relaxation. *nature communications*, 2017.
- [212] W. Voigt. *Lehrbuch der Kristallphysik*. B. G. Teubner, 1910.
- [213] M. Vopsaroiu, J. Blackburn, and M. Cain. A new magnetic recording read head technology based on the magneto-electric effect. *Journal of Physics D: Applied Physics*, 40:5027–5033, 2007.
- [214] J. Wang, S.-Q. Shi, L.-Q. Chen, Y. Li, and T.-Y. Zhang. Phase field simulations of ferroelectric/ferroelastic polarization switching. *Acta Materialia*, 52:749–764, 2004.
- [215] Y. Wang, J. Hu, Y. Lin, and C.-W. Nan. Multiferroic magnetoelectric composite nanostructures. *NPG asia materials*, 2(2):61 – 68, 2010.
- [216] T. Watanabe and K. Kohn. Magnetoelectric effect and low temperature transition of $\text{PbFe}_{0.5}\text{Nb}_{0.5}\text{O}_3$ single crystal. *Phase Transitions*, 15:57–68, 1989.
- [217] H. Wiegmann, A. Jansen, P. Wyder, J.-P. Rivera, and H. Schmid. Magnetoelectric effect of Cr_2O_3 in strong static magnetic fields. *Ferroelectrics*, 162:141–146, 1994.
- [218] J. Willis. Bounds and self-consistent estimates for the overall properties of anisotropic composites. *Journal of the Mechanics and Physics of Solids*, 25:185–202, 1977.
- [219] H. Wilson. On the Electric Effect of Rotating a Dielectric in a Magnetic Field. *Philosophical Transactions of the Royal Society of London*, 204:121–137, 1905.
- [220] A. Wineman and A. Pipkin. Material Symmetry Restrictions on Constitutive Equations. *Archive for Rational Mechanics and Analysis*, pages 184–214, 1964.
- [221] P. Wriggers. *Nonlinear Finite Element Methods*. Springer, 2008.
- [222] T.-L. Wu and J. Huang. Closed-form solutions for the magnetoelectric coupling coefficients in fibrous composites with piezoelectric and piezomagnetic phases. *International Journal of Solids and Structures*, 37:2981–3009, 2000.
- [223] Y. Yamasaki, S. Miyasaka, Y. Kaneko, J.-P. He, T. Arima, and Y. Tokura. Magnetic Reversal of the Ferroelectric Polarization in a Multiferroic Spinel Oxide. *Physical Review Letters*, 96:207204, 2006.
- [224] Z.-G. Ye, J.-P. Rivera, H. Schmid, M. Haida, and K. Kohn. Magnetoelectric effect and magnetic torque of chromium chlorine boracite $\text{Cr}_3\text{B}_7\text{O}_{13}\text{Cl}$. *Ferroelectrics*, 161: 99–110, 1994.

-
- [225] Y. Yu, Z. Xiao, N. Naganathan, and R. Dukkipati. Dynamic Preisach modelling of hysteresis for the piezoceramic actuator system. *Mechanics and Machine Theory*, 37:75–89, 2002.
- [226] M. Zgonik, P. Bernasconi, M. Duelli, R. Schlessler, and P. Günter. Dielectric, elastic, piezoelectric, electro-optic, and elasto-optic tensors of BaTiO₃ crystals. *Physical Review B*, 50(9):5941–5949, 1994.
- [227] Q.-S. Zheng and D.-X. Du. An explicit and universally applicable estimate for the effective properties of multiphase composites which accounts for inclusion distribution. *Journal of the Mechanics and Physics of Solids*, 49:2765–2788, 2001.
- [228] D. Zhou, M. Kamlah, and D. Munz. Rate Dependence of Soft PZT Ceramics under Electric Field Loading. In *Proceedings of SPIE*, volume 4333, pages 64–70, 2001.
- [229] A. Zimmermann, D. Meier, and M. Fiebig. Ferroic nature of magnetic toroidal order. *Nature Communications*, 5:4796, 2014.

Der Lebenslauf ist in der Online-Version
aus Gründen des Datenschutzes nicht enthalten.

In dieser Schriftenreihe bisher erschienene Berichte:

- Nr. 1 (2004) *Ein Modell zur Beschreibung finiter anisotroper elastoplastischer Deformationen unter Berücksichtigung diskreter Rissausbreitung*, J. Löblein, Dissertation, 2004.
- Nr. 2 (2006) *Polyconvex Anisotropic Energies and Modeling of Damage applied to Arterial Walls*, D. Balzani, Dissertation, 2006.
- Nr. 3 (2006) *Kontinuumsmechanische Modellierung ferroelektrischer Materialien im Rahmen der Invariatentheorie*, H. Romanowski, Dissertation, 2006.
- Nr. 4 (2007) *Mehrskalen-Modellierung polykristalliner Ferroelektrika basierend auf diskreten Orientierungsverteilungsfunktionen*, I. Kurzhöfer, Dissertation, 2007.
- Nr. 5 (2007) *Proceedings of the First Seminar on the Mechanics of Multifunctional Materials*, J. Schröder, D.C. Lupascu, D. Balzani (Ed.), Tagungsband, 2007.
- Nr. 6 (2008) *Zur Modellierung und Simulation diskreter Rissausbreitungsvorgänge*, O. Hilgert, Dissertation, 2008.
- Nr. 7 (2009) *Least-Squares Mixed Finite Elements for Solid Mechanics*, A. Schwarz, Dissertation, 2009.
- Nr. 8 (2010) *Design of Polyconvex Energy Functions for All Anisotropy Classes*, V. Ebbing, Dissertation, 2010.
- Nr. 9 (2012) *Modeling of Electro-Mechanically Coupled Materials on Multiple Scales*, M.-A. Keip, Dissertation, 2012.
- Nr. 10 (2012) *Geometrical Modeling and Numerical Simulation of Heterogeneous Materials*, D. Brands, Dissertation, 2012.
- Nr. 11 (2012) *Modeling and simulation of arterial walls with focus on damage and residual stresses*, S. Brinkhues, Dissertation, 2012.
- Nr. 12 (2014) *Proceedings of the Second Seminar on the Mechanics of Multifunctional Materials*, J. Schröder, D.C. Lupascu, M.-A. Keip, D. Brands (Ed.), Tagungsband, 2014.
- Nr. 13 (2016) *Mixed least squares finite element methods based on inverse stress-strain relations in hyperelasticity*, B. Müller, Dissertation, 2016.
- Nr. 14 (2016) *Electromechanical Modeling and Simulation of Thin Cardiac Tissue Constructs*, R. Frotscher, Dissertation, 2016.
- Nr. 15 (2017) *Least-squares mixed finite elements for geometrically nonlinear solid mechanics*, K. Steeger, Dissertation, 2017.

- Nr. 16 (2017) *Scale-Bridging of Elasto-Plastic Microstructures using Statistically Similar Representative Volume Elements*, L. Scheunemann, Dissertation, 2017.
- Nr. 17 (2018) *Modeling of Self-healing Polymers and Polymeric Composite Systems*, S. Specht, Dissertation, 2017.
- Nr. 18 (2018) *Proceedings of the Third Seminar on the Mechanics of Multifunctional Materials*, J. Schröder, D.C. Lupascu, H. Wende, D. Brands (Ed.), Tagungsband, 2018.
- Nr. 19 (2018) *Least-squares finite element methods with applications in fluid and solid mechanics*, C. Nisters, Dissertation, 2018.